Use of genome editing in human phagocytic cells to elucidate the role of the NLRP3 inflammasome in *L. major* infection

Dissertation

zur Erlangung des Grades

Doktor der Naturwissenschaften

am Fachbereich Biologie

der Johannes Gutenberg-Universität Mainz

Kerren Volkmar

geb. am 09.08.1994 in Holzminden

Mainz, 2023

Diese Doktorarbeit wurde vom 01.01.2020-01.05.2023 in der Abteilung Immunologie am Paul-Ehrlich-Institut, Bundesinstitut für Impfstoffe und biomedizinische Arzneimittel erstellt. Die experimentelle Arbeit wurde betreut durch…

1. Betreuer:

2. Betreuer:

Dekan: Prof. Dr. Eckhard Thines

                         Institut für Molekular Physiologie

                         Johannes Gutenberg-Universität Mainz

1. Berichterstatter:

2. Berichterstatter:

Tag der mündlichen Prüfung:

Table of contents

List of figures

List of tables

Abbreviations

°C	degree Celsius
%	percent
% (v/v)	volume percent
% (w/v)	mass per volume percent
µl	microliter
µm	micrometer
AAM	Alexander's amastigote medium
AIM-2	absent in melanoma 2
AP-1	activator protein 1
ASC	apoptosis-associated speck-like protein containing a caspase recruitment domain
ATP	adenosine triphosphate
BM	BLaER1 medium
BM-DMEM	BLaER1 medium based on DMEM high glucose
B-ALL	B cell acute lymphoblastic leukemia
CARD	caspase recruitment domain
Cas9	CRISPR-associated protein 9
CD	cluster of differentiation
CEBPα	CCAAT/enhancer-binding protein
CL	cutaneous leishmaniasis
CLR	C-type lectin receptor
CM	complete medium
cPLA2	phospholipase A2
DAMP	damage-associated molecular pattern
DC	dendritic cell
DEPC	diethyl pyrocarbonate
DHE	dihydroethidium
DMSO	dimethyl sulfoxide
DPI	diphenyleneiodonium chloride
eGFP	enhanced green fluorescent protein
ER	estrogen receptor

Abbreviations

FADD	FAS-associated death domain protein
FCS	fetal calf serum
g	gram
g	relative centrifugal force
GOI	gene of interest
GSDMD	gasdermin D
h	hour
HIF-1α	hypoxia-inducible factor 1α
hMDM	human monocyte-derived macrophages
HTS	high throughput sampler
IFN-γ	interferon-γ
ILC2	innate lymphoid cell 2
IL-6	interleukin-6
IL-1β	interleukin-1β
IL-1R	interleukin-1 receptor
IL-10	interleukin-10
IL-12	interleukin-12
IL-18	interleukin-18
IL-23	interleukin-23
iNOS	inducible nitric oxide synthase
IRES	internal ribosome entry site
LDH	lactate dehydrogenase
LM	leishmania medium
LPG	lipophosphoglycan
LPS	lipopolysaccharide
LRR	leucin-rich repeats
MCL	mucocutaneous leishmaniasis
MDA-5	melanoma differentiation-associated protein 5
MFI	mean fluorescence intensity
min	minute
ml	milliliter
mM	millimole per liter

X

MOI	multiplicity of infection
MR	mannose receptor
mtDNA	mitochondrial DNA
M-CSF	macrophage colony-stimulating factor
NADPH	nicotinamide adenine dinucleotide phosphate
NF-κB	nuclear factor κ-light-chain-enhancer
NLR	NOD-like receptor
NLRP1	NLR family pyrin domain containing 1
NLRP3	NLR family pyrin domain containing 3
nM	nanomole per liter
NNN	Novy-MacNeal-Nicolle
NO	nitric oxide
NOD	nucleotide-binding oligomerization domain
NOS2	nitric oxide synthase 2
NOX2	cytochrome b(558) subunit β
PAMP	pathogen-associated molecular pattern
PBMC	peripheral blood mononuclear cells
PDL	poly-D-lysine
pg	picogram
PLO	poly-L-ornithine
PMA	phorbol 12-myristate 13-acetate
PKDL	post kala-azar dermal leishmaniasis
PRR	pattern recognition receptor
PS	phosphatidylserine
PYD	pyrin domain
p.i.	post infection
p.n.	post nucleofection
RIG-1	retinoic acid inducible gene 1
RIPK-1	receptor-interacting serine/threonine-protein kinase 1
RLR	RIG-like receptor
RNP	ribonucleoprotein complex
ROS	reactive oxygen species

Abbreviations

shRNA	short hairpin RNA
STING	stimulator of interferon genes
Syk	spleen tyrosine kinase
tdBM	transdifferentiation BM; BM with transdifferentiation supplements
tdBM-DMEM	transdifferentiation BM-DMEM; BM-DMEM with transdifferentiation supplements
TGF-β	transforming growth factor β
TLR	Toll-like receptor
TNF-α	tumor necrosis factor α
TRM	tissue-resident macrophages
USD	US Dollar
VEGF-α	vascular endothelial growth factor α
VL	visceral leishmaniasis
WGA	wheat germ agglutinin
4PL	4-parameter logistic regression

Abstract

Leishmaniasis is a neglected tropical disease caused by protozoan parasites of the *Leishmania (L.)* genus. The parasite has a digenetic life cycle with a promastigote form in the phlebotomine sand fly and an amastigote form in the mammalian host. Upon inoculation of *Leishmania ssp.* into the mammalian host skin during a sandfly's blood meal, the parasite infects human macrophages, its definite host cell. In order to sustain and propagate infections, the parasites have to complete cycles of exit from its host cells and re-infection of previously uninfected cells. Recent in vivo studies reported pro-inflammatory monocytes as replicative niche of *L. major* and showed prolonged expression of IL-1β at the infection site, indicating an activation of the NLRP3 inflammasome. Therefore, I hypothesized that *L. major* infection activates the human NLRP3 inflammasome and promotes parasite spreading via its downstream effector mechanism pyroptosis. To overcome limitations associated with the use of reverse genetic methods in human primary macrophages, I characterized the transdifferentiating cell line BLaER1 as a model for *L. major* infection. I found that *Leishmania* can infect, activate, and develop in BLaER1 macrophages similar as they can do in primary human macrophages. Utilizing this infection model, BLaER1 cells were used to investigate the role of the human inflammasome in the innate immune response to *L. major*. NLRP3 inflammasome activation by *L. major* was confirmed and found to be dependent on phagolysosomal ROS production and presence of LPG on the parasite surface. In contrast to murine macrophages, infection-dependent inflammasome activation in BLaER1 did not result in parasite restriction. To elucidate the role of pyroptosis in the spread of *L. major* parasites to new host cells, I first found that BLaER1 *GSDMD*$^{-/-}$ cells, which carry a deletion of the pore-forming protein gasdermin D, are more resistant to pyroptotic cell death and, concomitantly, display a strongly delayed release of intracellular parasite. Using this knockout in a co-incubation assay in comparison with wild type BLaER1 cells, I demonstrate that impairment of the pyroptosis pathway leads to lower rates of parasite spread to new host cells, thus, implicating pyroptotic cell death as a possible exit mechanism of *L. major* in pro-inflammatory microenvironments. In summary, this thesis showed that BLaER1 cells are a promising cell line model for investigation of host-pathogen interactions of human macrophages and *L. major*. Moreover, it discovered species-specific differences in the NLRP3 inflammasome response, which are highly relevant for the development of inflammasome-targeting drugs. Furthermore, it makes a strong case for the investigation of pro-inflammatory forms of cell death in the pathogenesis of leishmaniasis.

Zusammenfassung

Leishmaniose ist eine vernachlässigte Tropenkrankheit, die von protozoischen Parasiten der Gattung *Leishmania (L.)* verursacht wird. Der Parasit hat einen digenetischen Lebenszyklus mit einer promastigoten Form im Sandmückenvektor und einer amastigoten Form im Säugetierwirt. Der Biss der infizierten Sandmücke überträgt die Promastigoten in die Haut des Wirtes. Die Parasiten infizieren hier Makrophagen als finale Wirtszelle. Um die Infektion aufrecht zu erhalten und zu verbreiten, müssen Leishmanien Zyklen von Wirtszellaustritt und Neuinfektion durchlaufen. In vivo Studien haben gezeigt, dass *L. major* pro-inflammatorische Monozyten als Reservoir zur Replikation nutzt. Dies geht mit einer anhaltenden Expression von IL-1β einher, was auf eine Aktivierung des NLRP3 Inflammasoms hindeutet. Daher lautete meine Hypothese, dass auch das humane NLRP3 Inflammasom durch eine Leishmanieninfektion aktiviert wird und durch seinen Downstream-Mechanismus, Pyroptose zur Ausbreitung von Parasiten auf neue Wirtszellen beiträgt. Um die Probleme, die mit einer genetischen Veränderung von primären humanen Makrophagen (hMDM) verbunden sind, zu umgehen, habe ich die transdifferenzierende Zelllinie BLaER1 auf ihre Eignung als Modell für die Infektion von Makrophagen mit *L. major* untersucht. *L. major* infizierte, aktivierte und replizierte in BLaER1 Zellen ähnlich wie in hMDM. Ich benutzte dieses Infektionsmodell, um die Aktivierung des humanen Inflammasoms durch *L. major* zu charakterisieren. *L. major* aktivierte das humane NLRP3 Inflammasom in Abhängigkeit von der Produktion phagolysosomaler reaktiver Sauerstoffspezies (ROS) und der Präsenz von LPG auf der Parasitenoberfläche. Im Gegensatz zu murinen Makrophagen führte die Inflammasomaktivierung nicht zu einer Restriktion der intrazellulären Parasiten. Um die Rolle der Pyroptose als Mechanismus der Ausbreitung on *L. major* aufzuklären, stellte ich zunächst fest, dass BLaER1 *GSDMD*$^{-/-}$ Zellen eine erhöhte Pyroptoseresistenz im Vergleich zu BLaER1 Zellen besitzen und damit einhergehend eine stark verzögerte Parasitenfreisetzung aufweisen. Durch den Einsatz dieser Zelllinie in einem Koinkubationsexperiment, konnte ich zeigen, dass Beeinträchtigung des Pyroptosesignalwegs zu einer verminderten Parasitenausbreitung auf neue Wirtszellen führte. Dies bestätigt, dass Pyroptose ein möglicher Austrittsmechanismus von *L. major* in pro-inflammatorischen Mikroumgebungen ist. Insgesamt hat diese Arbeit gezeigt, dass BLaER1 ein vielversprechendes Zelllinienmodell für die Erforschung von Wirts-Pathogen-interaktionen von hMDM und *L. major* ist. Die, in dieser Arbeit demonstrierten, speziesspezifischen Unterschiede in der NLRP3 Inflammasomantwort sind bedeutend für die Entwicklung von Inflammasom-spezifischen Medikamenten. Darüber hinaus, zeigen die Ergebnisse, dass eine Erforschung pro-inflammatorischer Zelltodformen in der Pathogenese der Leishmaniose nötig ist.

1 Introduction

1.1 Leishmaniasis

Leishmaniasis is a neglected tropical disease caused by protozoan parasites of the *Leishmania* genus, which are transmitted by the bite of phlebotomine sandflies [1]. The disease is highly poverty-related as almost 90 % of all affected people live of less than two US dollar (USD) per day [2]. This problem is further compounded by the fact that several poverty-associated circumstances, e.g. malnutrition and poor housing and sanitary conditions, not only increase the exposure to the vector, and, thus, the risk of becoming infected, but also aggravate the outcome of the disease [3]. Based on clinical symptoms three main forms of leishmaniasis are distinguished (**Figure *1***), visceral leishmaniasis, mucocutaneous leishmaniasis and cutaneous leishmaniasis [3,4].

 Figure 1: Clinical manifestations of leishmaniasis.
Three main forms of leishmaniasis are distinguished based on the clinical symptoms. (A-C) cutaneous leishmaniasis causes ulceration of the skin. It occurs in three forms, localized cutaneous leishmaniasis is the most common form of the disease with a single localized lesion at the bite site (A), diffuse cutaneous leishmaniasis is a rare anergic form of the disease with multiple lesions spread across the body (B), and mucocutaneous leishmaniasis affects mucosal surfaces and leads to tissue destruction at nose and mouth (C). (D and E) Visceral leishmaniasis is the most severe form of the disease and leads to weight loss and spleno- and hepatomegaly (D). After visceral leishmaniasis some patients suffer from post-kala-azar dermal leishmaniasis, which manifests as diffuse nodules across the body (E). Images A-C are adapted from *Torres-Guerrero et al.* [5], images D and E are adapted from *Griensven and Diro* [6] .

Visceral leishmaniasis (VL) or kala-azar (**Figure *1*D**) is the also most severe form of the disease with a case-fatality-rate of 95 % when left untreated [3]. The clinical symptoms of VL are fever, spleno- and hepatomegaly, progressive anemia, pancytopenia and hyperglobulinemia [4]. Because of this strong depletion of immune cells, VL is often accompanied by opportunistic infections, which are believed to be the primary cause of death among patients [4]. After one to two years post recovery, approximately 10 % of patients develop non-ulcerative cutaneous lesions termed post kala-azar dermal leishmaniasis (PKDL) that require long and costly treatment (**Figure *1*E**) [4]. Most of the 50,000 to 90,000 annual cases occur in Brazil and India and are caused by *L. chagasi* and *L. donovani* [4].

The mucocutaneous leishmaniasis (MCL) affects the mucosa of the naso-oral and pharyngeal cavities (**Figure *1*C**). The clinical symptoms break out years after the resolution of the initial cutaneous form of the disease and consist of metastatic lesions that lead to disfigurement of the face and greatly reduce the quality of life of the patient [4]. MCL predominantly occurs in South and Central America and is caused by *L. braziliensis* [4].

Cutaneous leishmaniasis (CL) is the most benign form of the disease, but with 600,000 to one million cases per year [3] also the most abundant form of the disease (**Figure *1*A**). After a variable incubation time of few days up to several months, a skin lesion manifests at the site of the sandfly bite [4]. Through influx of macrophages the lesion develops into a granuloma and self-heals usually within six months [1,7].

1.2 *L. major*

The geographical distribution of *Leishmania* species has been classically divided into Old-World and New-World species [4,2,8]. Among the Old-World species of *Leishmania L. major* is one of the most frequent causative agents of cutaneous leishmaniasis that is endemic in North Africa, the Middle East and Northern Asia [4].

1.2.1 *L. major* life cycle

Like all parasites of the genus *Leishmania L. major* has a digenetic life cycle with a flagellated promastigote form in the sand fly vector and an aflagellated amastigote form in the human host (**Figure *2***) [8]. Besides the flagellum, two other major morphological differences between

promastigotes and amastigotes are the cell shape and the cell size. While promastigotes have an elongated cell body with a length of 6-11 µm depending on the exact stage of the life cycle, amastigotes have an ovoid cell shape with a diameter of 2-3 µm [8,9]. So far. these morphological changes are also the only undisputed indicators of the parasite life cycle stage [8,10].
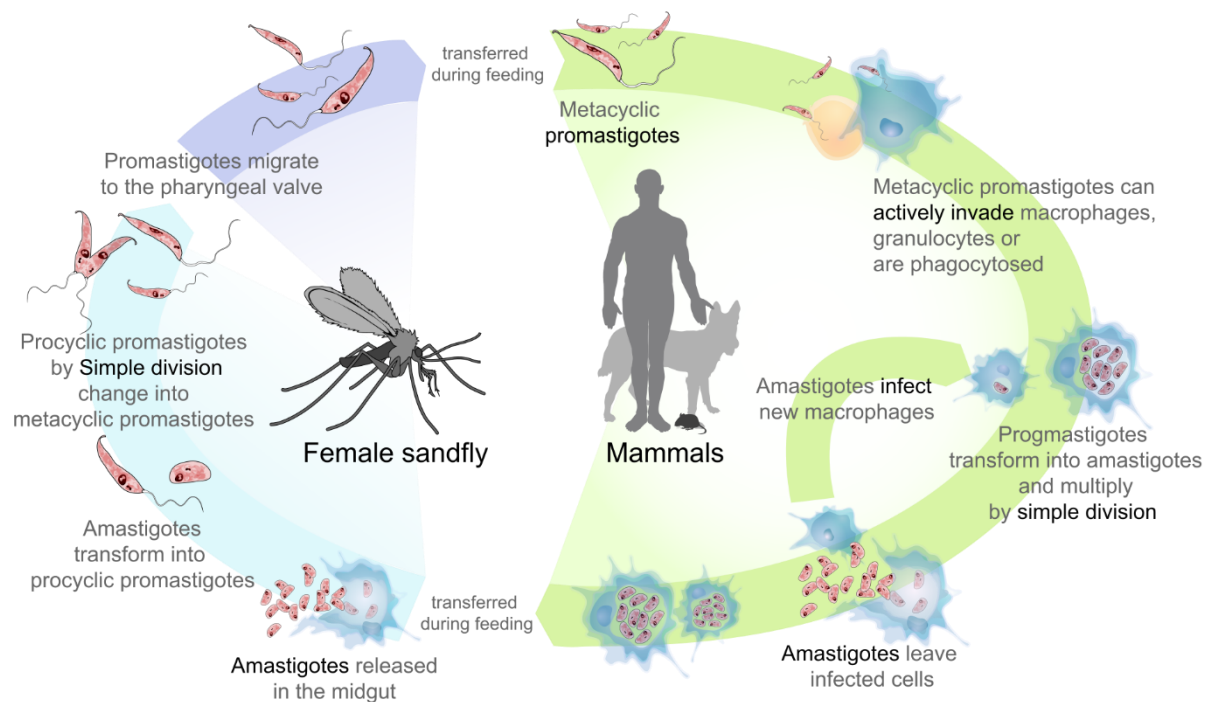
Figure 2: Life cycle of pathogenic *Leishmania ssp.*
Infectious metacyclic promastigotes are regurgitated during the blood meal of a female phlebotomine sandfly. Metacyclic promastigotes are taken up directly by macrophages, or transiently infect neutrophils and are ultimately taken up inside neutrophil apoptotic bodies by macrophages through efferocytosis. Inside of the human macrophage parasites transform to amastigotes and multiply within the phagolysosome. The infection is spread and maintained by infection of other macrophages. The life cycle is completed when infected macrophages are taken up by a female phlebotomine sandfly during a blood meal. Inside of the phlebotomine midgut amastigotes transform to procyclic promastigotes and eventually migrate to the stomodeal valve. Here procyclic promastigotes transform to metacyclic promastigotes. Image adapted from Wikipedia.com [11].

The life cycle begins with the inoculation of the mammalian host by the bite of an infected phlebotomine sand fly. During the blood meal the sand fly regurgitates a mixture of viable and dead metacyclic parasites, sand fly saliva and *Leishmania* proteophosphoglycans into the host [4,12]. After inoculation, metacyclic are rapidly phagocytosed by tissue resident macrophages, or by neutrophils. Mechanistically, this uptake can be facilitated by a plethora of redundant receptors and recognized parasite surface molecules, that are comprehensively reviewed elsewhere [13–16]. After 48 h to 72 h, the neutrophils undergo apoptosis and parasites are taken up within the neutrophilic apoptotic bodies

by their definite host cell, the macrophage, by efferocytosis. ("Trojan horse strategy") [17,18]. After taking residence within the phagolysosome of the macrophage, parasites start to transform into the intracellular amastigote form [4,8,12]. The life cycle of the parasite is completed when amastigotes are ingested by a sand fly during a blood meal [12,19]. While the establishment of the initial infection has been well understood, the spread of the amastigotes to new host cells has remained enigmatic. Frequently speculated to be a passive process mediated by mechanical stress of increasing numbers of intracellular amastigotes [12,20,21], more recent studies have shown, that macrophages can sustain extremely high parasite burdens [22]. Additionally, it has been shown that dendritic cells (DC), which are refractory to promastigote infection [23,24] become an important subset of infected cells, as early as five days post infection [25]. This points towards parasite spread as a more active and regulated process, a paradigm shift, which is also taking place in research on multiple other intracellular pathogens[26].

1.3 Macrophages

Macrophages were first described in 1883 by the Russian immunologist Ellie Metchnikoff during his studies of the larvae of starfish which lack an adaptive immune response [27,28]. This makes macrophages the oldest precisely identified cell of the immune system, predating the distinction of lymphocytes into B and T cells in the 1960s by almost 100 years [29]. While phagocytosis was initially believed to be a process predominantly involved in tissue homeostasis and nutrient acquisition, Metchnikoff proposed phagocytosis as an effector mechanism against pathogens, pioneering not only the concept of cell-mediated immunity, but also the concept of innate immunity [27]. Macrophages were initially believed to be a simple phagocytic effector cell, like neutrophils, that extravasates into inflamed tissues [30]. This view changed with the discovery of tissue-resident macrophages in healthy tissues [29–31], and was expanded by the finding of *Mills et al.* that macrophages from C57BL/6 mice and BALB/C mice directed the T cell response towards a T_h1 response or a T_h2 response, respectively, upon activation with either IFN-γ or LPS (classical activation) or IL-4 (alternative activation) [32,33]. Because these differences were attributed to differences in the arginine metabolism of the mouse strains, this capability was believed to be an intrinsic characteristic of different macrophages subsets [32]. Analogous to the name of the different subsets of T cells they induced, Mills termed these macrophages M1 and M2 macrophages [32]. M1 macrophages were characterized by secretion of IL-12, TNF-α, IL-1β, IL-18 and IL-23 and induction of oxidative burst, while M2 macrophages were characterized by increased mannose receptor activity and secretion of TGF-β and IL-10 [32,34] . Additionally, M2 polarization has been associated with tissue remodeling and maintenance of

homeostasis in a variety of tissues [30,34,35]. While this skew in macrophage metabolism and T cell response was later found to be a property of the genetic backgrounds of these mice strains, and Mills proposed nomenclature was largely overturned, the terms M1 and M2 persist as the extremes of pro-inflammatory and anti-inflammatory macrophage activation, respectively [36,37]. The nomenclature has remained a subject of controversial debate ever since (reviewed in [36]. The clear identification of macrophage subsets is further complicated by their high plasticity and capability to polarize depending on the signals of the respective microenvironment i.e., switch from a pro-inflammatory to an anti-inflammatory phenotype, or assume the phenotype of the tissue-specific resident macrophages [36,38–41].

Along with the identification of multiple tissue-resident macrophage (TRM) populations, advances in the understanding of pattern recognition receptors have further changed the view on macrophages and highlighted their role as an important sentinel cell in healthy tissues [27,29][29,27]. Macrophages express a large variety of toll-like receptors (TLRs), RIG-like receptors (RLRs) and NOD-like receptors (NLRs) [29]. Notably, macrophages are the only cell type that expresses all known TLRs i.e., TLR1-9, and can therefore sense a broad range of pathogen-associated molecular patterns (PAMPs) that consists of lipomannans, lipoproteins, lipoteichoic acids, cell wall β-glucans, double- and single-stranded RNA flagellin, LPS and bacterial DNA [29]. Furthermore, macrophages express the RLRs STING, MDA-5 and RIG-1, that sense viral RNA and DNA in the cytoplasm [29]. Finally, macrophages also express NLRs, like NLRP3, NLRP1, pyrin, and AIM-2 [29,42,43]. Interestingly, several NLRs have been shown to detect damage-associated molecular pattern (DAMPs), like K^+ efflux, reactive oxygen species (ROS), or aberrant cytoskeleton dynamics rather than PAMPs [43,44]. Therefore, NLRs play an important role in inflammatory conditions in absence of infection and have been identified to contribute to several chronic inflammatory diseases [43,44]. In summary, the understanding of macrophages has evolved from simple phagocytes to a highly plastic, sophisticated signal transducer cell that shapes the immune response and is involved in a plethora of processes of tissue remodeling, homeostasis, and metabolism.

1.3.1 Role of macrophages in immunity to *Leishmania*

As mentioned above, the investigation of macrophage and T cell polarization are linked, because these concepts were first discovered in the murine infection models for *L. major* infection [32,33,45]. The role of macrophages in leishmaniasis is particularly manifold, because macrophages are not only responsible for directing the immune response as an important signal transducer, but also act as

replicative niche for parasites and important effector cell in the resolution of the disease [46]. Upon inoculation of the mammalian host, parasites are rapidly taken up by tissue-resident macrophages and neutrophils during the first 24 h of the infection [19,46,25]. The tissue-resident macrophages were shown to express an anti-inflammatory i.e., M2-like phenotype (CD11b$^+$Ly6C$^{-/int}$CD64$^+$CD206$^+$) [25,46]. Notably, these cells do not induce oxidative burst nor the production of nitric oxide (NO) upon infection with *L. major* and are, therefore a promising replicative niche for the parasite [46,47]. In the following acute phase of the infection (up to 3 weeks post infection), monocytes are recruited via the cytokines CCL2, MCP-1, CXCL9 and CXCL10 and pro-inflammatory monocytes and monocyte-derived DCs become important host cells [48,49]. In the murine system, these pro-inflammatory monocytes were identified by their CD11b$^+$Ly6C$^+$CCR2$^+$CX3CR1$^+$CD64$^+$CD24^{low} marker profile and monocyte-derived DCs by their CD11c$^+$Ly6C$^+$CCR2$^+$F4/80$^+$ phenotype [48–50]. Interestingly, these cells have been identified as an important replicative niche by employing a photoconvertible fluorescent protein, despite the pro-inflammatory polarization of these cells and their production of leishmanicidal effectors like NO [48–50]. This somewhat paradoxical finding can be explained by the IFN-γ dependent secretion of the monocyte-recruiting MCP-1, CXCL9 and CXCL10 [48,49]. Hence, the T$_h$1 response via IL-12 secretion and subsequent production of IFN-γ compensates the activation of leishmanicidal effector mechanisms, and concomitant parasite restriction, by the augmentation of the host cell reservoir by recruitment of pro-inflammatory monocytes [48,50]. Staying true to the plasticity of the cell type, a subset of the recruited monocytes re-polarizes to an anti-inflammatory phenotype characterized by Arg1$^+$MHCII$^+$PDL2$^+$ [48].

While the induction of a leishmanicidal T$_h$1 response seems to be initially compensated by the recruitment of monocytes, infiltration of CD4$^+$, IFN-γ producing T$_h$1 cells and the subsequent activation of macrophages for intracellular killing of parasites ultimately resolves the infection [46]. The activation of macrophages by these T cells, however, remains enigmatic. First, macrophages cannot be sufficiently activated by IFN-γ alone in the absence of T$_h$1 cells, suggesting cell-cell-contact, but the activating effect of T cells has been shown to extend to bystander cells [51–54]. Furthermore, activation by T cells does not seem to activate different effector mechanisms than the ones already active during innate immunity, which fail to resolve the infection in that phase [52–54].

1.3.2 Differences between human and murine macrophages

To a large extend the great understanding of the dynamics of the early *L. major* infection can be attributed to the advances in intravital microscopy and flow cytometry. However, it is openly

acknowledged in the field that all these findings were made in the murine system and do not necessarily translate to human cutaneous leishmaniasis [46]. The reasons for this are the manifold differences between the human and the murine immune system. A multifaceted review of multiple differences can be found in [55]. In accordance with the focus of my thesis, I will focus on the differences between murine and human macrophages and their importance for cutaneous leishmaniasis.

The most important difference, and subject of ongoing controversy, is the production of nitric oxide by the enzyme inducible nitric oxide synthase (iNOS), mediated by the transcription factors NFkB and AP-1, in response to pro-inflammatory activation by IFN-γ in vivo or LPS+IFN-γ in vitro [56]. Upon activation, iNOS metabolizes the amino acid L-arginine to L-citrulline and the reactive effector molecule NO, in a tetrahydrobiopterin (H_4B) dependent way [56,57]. While this pathway has been well characterized and can be reliably induced in murine monocytes and macrophages, results from human cells have been inconsistent (reviewed in [58–60,57,55,61]). Aside from the debate around presence of absence of this pathway, it is well established that iNOS-mediated NO production is a prominent effector mechanism of the murine innate immunity, while it does not have this function in human monocytes and macrophages [19,59,61]. The latter employ the production of reactive oxygen species (ROS) via the NAPDH oxidase enzyme complex [29]. The resulting redundancy of effector mechanisms in mice compared to the focus on ROS in human cells leads to profound phenotypical differences between humans and mice. One example is the redundancy of the Nos2 (iNOS) and the Nox2 (NADPH oxidase) gene in mice, that allows $Nox2^{-/-}$ mice to control intracellular parasites as long as Nos2 is still functional [19,62]. Another example is the weak or absent phenotype of chronic granulatomous disease mouse models i.e., mice with knocked out components of ROS producing NADPH oxidase complex, while this disease leads to high susceptibility to bacterial infections in humans [62,63]. On the other hand, no disease associated with a non-functional NOS2 gene is known in humans [64].

Since macrophages are the primary host cells of *L. major*, important initiators of the immune response and also important effector cells in the later stages of the disease, the different effector mechanisms affect several aspects of metabolism, parasite restriction and disease phenotypes between the two species. First, murine macrophages regulate their arginine metabolism based on pro- or anti-inflammatory activation [32,34,61]. Upon pro-inflammatory activation murine macrophages display strong iNOS activity, which depletes L-arginine and generates NO, which in turn stimulates IL-12 secretion inducing a T_h1 response [32,46,65]. Upon anti-inflammatory activation, murine macrophages

display a strong arginase-1 activity, which converts L-arginine to L-ornithine, which is in turn converted to polyamines [61]. Polyamines are assumed to play a role in tissue repair, an important anti-inflammatory macrophages function, but also support the intracellular growth of *L. major* parasites [40,66]. This differential regulation of arginine metabolism is not observed in human macrophages, which display neither strong iNOS activity upon pro-inflammatory activation nor arginase-1 activity upon anti-inflammatory activation [61,67]. Second, the production of NO has an impact on the ATP metabolism of murine macrophages, because of the high affinity of NO for the Fe-S cluster at the center of most enzymes involved in the oxidative phosphorylation [56,67]. Hence, upon pro-inflammatory activation murine macrophages switch their ATP metabolism towards glycolysis, a property that has not been observed for human macrophages [67]. Because *Leishmania* infection take place in tissues with already reduced oxygen concentrations and hypoxia-induced transcription factors like hypoxia-inducible factor 1α (HIF-1α) and vascular endothelial growth factor A (VEGF-A), this metabolic difference is likely to lead to differential gene regulation of human and murine macrophages during *Leishmania* infection [46]. Third, it is well established that NO is a far more potent effector against several intracellular pathogens, especially *Mycobacteria* and *Leishmania* species, than ROS [59,62,64]. A consequence of this is that mice are highly resistant against these human pathogens e.g., *L. major* infections are resolved up to six times faster by commonly used C57BL/6 mice than by human patients[7,68].

Regarding the role of mouse models, it should furthermore be noted that the investigation of *L. major* infections is dominated by the use of two mouse strains, the C57BL/6 strain and the BALB/c strain [36,37]. These mice strongly differ in their arginine metabolism and T cell response. C57BL/6 have high iNOS activity and skew towards T_h1 responses while BALB/c have strong arginase-1 activity and skew towards T_h2 responses BALB/c [32,33,36,37]. These traits are not only strongly conserved in the genetic backgrounds of the strains and largely refractory to experimental interventions but they also lead to vastly different outcomes of L. major infection. As mentioned earlier, C57BL/6 resolve the infection very fast while BALB/c mice are unable to control the infection, develop a visceral leishmaniasis and ultimately succumb to the infection [69]. Since the BALB/c disease phenotype does not correspond to the one of human patients, which would be a hallmark of a good animal model [70], the use of this strain is increasingly depreciated in the field.

In summary, human macrophages differ greatly from their murine counterparts in regard to metabolism (L-arginine depletion, polyamine synthesis) and predominantly employed effector

mechanism (ROS compared to NO and ROS in murine macrophages), which both have a huge impact on the outcome of *L. major* infection. Additionally, these commonly used mice strains skew strongly towards a beneficial T_h1 or detrimental T_h2 response, while T cell polarization in humans is more heterogenous [4,40] (summarized in **Table 1**).

Table 1: Differences of human and murine hosts in leishmaniasis
The table list phenotypical differences between humans and the two most frequently used mouse strains in *L. major* research.

	host		
	Mouse (C57BL/6)	**Mouse (BALB/c)**	**human**
sensitivity to endotoxin	low [71,72]	low [71,72]	high [71,72]
disease phenotype	CL [69]	VL [69]	CL [4,7]
time until disease resolution	approx. 3 months [69,68]	fatal disease [69]	approx. 18 months [7,68]
T-cell response	T_h1 bias [32,33]	T_h2 bias [32,33]	heterogenous [4]
arginine metabolism	iNOS >> arginase-1 [32]	arginase-1 >> iNOS [32]	low to absent activity of both enzymes in monocytes/macrophages [67,73,74]
antimicrobial effector mechanism	ROS, NO and antimicrobial peptides [29]	ROS, NO and antimicrobial peptides [29]	ROS, LL-37 [74,75]
ATP metabolism during inflammation	glycolysis [67]	glycolysis [67]	oxidative phosphorylation [67]

1.3.3 Genome editing in macrophages

Considering the differences between murine and human macrophages and their implications for the investigation of leishmaniasis, the question arises why most studies are still conducted in the mouse model. One of the reasons for this is that, while over the years a sophisticated toolkit of reverse genetic methods and reporters was built for mouse models [70,76], the methods for genome editing in primary human macrophages are limited [77]. One reason for this is the previously mentioned role of macrophages as signal transducing cell with a vast repertoire of pattern recognition receptors (PRRs), which sense both PAMPs and DAMPs. Because most genetic methods rely on the introduction of either DNA or RNA into the cell, an activation of the endosomal TLRs 3, 7, 8 and 9, as well as the cytosolic nucleic acid receptors RIG-1, STING and MDA-5 are possible [29,78]. Furthermore, if the introduction into the cell is facilitated by a method that causes membrane damage e.g., electroporation, DAMP sensing receptors like inflammasomes can also be activated. Since macrophages express PRRs for foreign nucleic acids even in the nucleus, the problem is persisting even after successful delivery of DNA into this compartment [29,79]. The result of this are high off-target effects, presumably due to

pro-inflammatory activation of the macrophages and poor viability. Because Cas9-based approaches for genome editing do not address the problem of PRR activation, the advent of this technology did not revolutionize the field of primary human macrophage research to the same extend as it did for example the modification of primary human T cells [80–82]. However, several recent studies showed, that modification of freshly isolated monocytes with Cas9-containing ribonucleotide-protein complexes (RNP) and using the subsequent differentiation to macrophages as a rest period can be employed to address this problem [83,84]. An unresolved limitation of these methods is the quiescence of macrophages that requires repeated modification by RNPs of every batch of macrophages that is used for experimentation. The resulting macrophages are a mixture of successfully transduced macrophages with varying shares of partial and complete knockouts and untransduced macrophages with wild type expression of the protein of interest. This means that the efficiency of every batch of modified macrophages needs to be determined on DNA and protein level. In summary, there is currently no way to generate knockouts in primary human macrophages. While it is technically not a knockout approach, it should be noted, that lentiviral transduction of stable short hairpin RNA (shRNA) has also been successfully used to generate of knock-downs in primary human macrophages [85,86]. However, this method is also hampered by the quiescence of macrophages and largely affected by the same drawbacks as the previously described RNP-based method. In conclusion, these approaches are not only laborious and costly, but also include two additional sources of variance, RNP or lentiviral vector preparation, and transduction efficiency into the experiment. Therefore, both approaches rarely used despite their technical feasibility.

1.3.4 Macrophage cell lines and associated problems

An alternative approach to conduct reverse genomic studies in human macrophages is the use of human macrophage cell lines. To understand how the use of cell lines overcomes the difficulties associated with genetic methods in human macrophages, it needs to be emphasized that these cell lines are not really macrophages or monocytes, but resemble myeloblasts i.e., a granulocyte-monocyte precursor cell type in between of stem cells and mature monocytes [87,88]. The reason for this is that cell lines were commonly isolated from human cancer patients and, so far, no monocyte or macrophage cancer cells have been observed in humans [88]. While the exact reason for this remains unknown, it is believed that the strong quiescent nature of these cells is not easily overcome by genetic alterations that lead to cancer in other cell types [89]. Due to their immature state, these cells do not yet express the vast PRR repertoire of mature monocytes or macrophages [87], hence, can be genetically altered without the causing activation as described earlier for macrophages.

However, this immature state is also one of the great disadvantages of these cell lines, as it requires differentiation to a monocyte or macrophage phenotype before experimentation. This is most commonly achieved by stimulation with phorbol-12-myristate-13-acetate (PMA) or vitamin D3. Both substances are activators of protein kinase C signaling, which is involved in a plethora of cellular processes including inflammatory response, cell differentiation, gene expression and cell proliferation [90,91]. In accordance with this unspecific stimulus for the differentiation, the resulting phenotype of the most commonly used cell line THP-1 varies greatly depending on the chosen chemical, concentration, and rest period post stimulation [92–95].

Finally, all commonly used macrophage cell lines have been shown to display deficiencies in expression and or functionality of PRRs [90,96,97]. For example, U937 cells showed considerable differences in the NFκB signaling upon LPS stimulation [97] and THP-1 cells are not only very insensitive to LPS stimulation in general, but also show deficiencies in the NLRP3 inflammasome pathway [77,96].

1.4 BLaER1 cell line

In recent years, BLaER1 cells have emerged as a possible alternative to the commonly used human macrophage cell lines. BLaER1 was created from the B cell acute lymphoblastic leukemia (B-ALL) cell line RCH-ACV [98] by transduction with a lentiviral construct consisting of a fusion protein of the transcription factor CEBPα and an estrogen receptor (ER), an internal ribosome entry side (IRES) and an eGFP protein (entire construct: CEBPαER-IRES-eGFP) [99]. Upon treatment with the ER agonist β-estradiol the master regulator of myeloid cell differentiation CEBPα is translocated to the nucleus and initiates the transdifferentiation of the undifferentiated pre-B BLaER1 cells to a macrophage-like
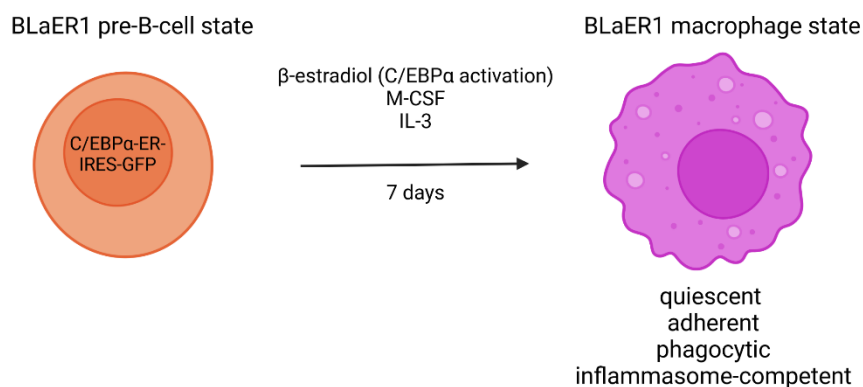
Figure 3: BLaER1 differentiation scheme.
BLaER1 cells can be transdifferentiated to a macrophage-like phenotype by treatment with β-estradiol. The compound binds to the CEBP/αER fusion protein and translocates it to the nucleus. After seven days of β-estradiol treatment BLaER1 cells assume a macrophage-like phenotype i.e., become adherent, quiescent, phagocytic, and express a vast repertoire of PRRs including the NLRP3 inflammasome.

phenotype (**Figure 3**) [99,100]. The resulting transdifferentiated BLaER1 cells increase in size, mostly by increasing their cytoplasm, start to express monocyte/macrophage surface markers like CD11b and CD14, become adherent, quiescent, and phagocytic [99,100]. Additionally, transdifferentiated BLaER1 cells assume a transcriptome that closely resembles the transcriptome of M-CSF derived macrophages [99]. This transcription factor-based differentiation procedure is better defined and more reproducible than the PKC agonist-based differentiation of commonly used human macrophage cell lines mentioned earlier.

BLaER1 cells can be genetically modified in the undifferentiated pre-B cell form using Cas9-based approaches and then be transdifferentiated into a macrophage-like phenotype with the desired genetic alteration for experimentation [77,101]. While this approach is not fundamentally different from the strategy discussed earlier for other human macrophage cell lines, it should be noted that the transcription factor-based transdifferentiation process eliminates the risk of accidentally differentiating cells during genome editing by activation of PRRs – a risk, which at least hypothetically exists in THP-1, U937 and Mono Ma6 cells.

Although BLaER1 cells were originally generated to explore terminal differentiation as a therapy for leukemia [89,99], subsequent studies demonstrated that BLaER1 cells are a promising model cell line for innate immunity research [78,101,102]. Unlike other macrophage cell lines, BLaER1 cells have a high sensitivity for LPS, closely resembling primary human macrophages [77,99], and a fully functional NLRP3 inflammasome [77]. Furthermore, the expression of functional, endosomal TLRs has been demonstrated [100,101].

1.5 NLRP3 inflammasome

NOD-like receptors are PRRs that recognize PAMPs and DAMPs in the cytoplasm [44]. There are 23 NLR family proteins in humans and 34 in mice, of which many have been reported to form inflammasomes [102,103]. Inflammasomes are multimeric protein complexes that consist of a cytosolic PRR (usually an NLR), an adapter protein and an effector caspase [103]. In case of the NOD-like receptor family pyrin domain-containing 3 (NLRP3) inflammasome, NLRP3 acts as cytosolic sensor protein, the apoptosis-associated speck-like protein (ASC) as an adapter protein, and caspase-1 acts as the effector caspase [44,104]. The NLRP3 protein consists of three domains, a carboxy-terminal leucine-rich repeat (LRR) domain that recognizes a vast range of PAMPS (viral RNA, LPS, bacterial cell wall components) and

DAMPS (ATP, aluminum hydroxide, uric acid crystals, β-amyloid peptide), a nucleotide-binding oligomerization domain (NOD or NACHT), and an amino-terminal pyrin (PYD) domain [44,103]. Upon sensing of a PAMP or DAMP via the LRR domain, NLRP3 oligomerizes at the NOD domain, which allows the PYD domain of each NLRP3 monomer to recruit the adapter protein ASC [29]. ASC is a bipartite protein, consisting of an amino-terminal PYD domain and a carboxy-terminal caspase recruitment domain (CARD) domain [29] and is recruited to oligomerized NLRP3 via PYD-PYD interaction, forming polymeric ASC filaments [29]. Recruitment to NLRP3 induces a conformational change in ASC, which allows the recruitment of pro-caspase-1 via CARD-CARD interaction, forming discrete, outward branching pro-caspase-1 filaments [29]. Upon oligomerization of pro-caspase-1, it autocleaves its autoinhibitory domains, producing active caspase-1 [29]. These NLRP3 inflammasome complexes become very large and can incorporate the entire NLRP3, ASC and caspase-1 proteins of a cell ("ASC-speck formation") which can be visualized by electron microscopy [29]. Active caspase-1 then cleaves pro-IL-1β, pro-IL-18, releasing the active cytokines IL-1β and IL18 [29,44]. Further, upon cleavage by caspase-1, the amino-terminal fragment of the protein gasdermin D (GSDMD) inserts into the cell membrane, forming a non-selective pore that facilitates the secretion of IL-1β and IL-18 [105,106].

Due to the large amount of detected PAMPs and DAMPs and the complex activation process, it is not surprising that multiple pathways for the activation of the NLRP3 inflammasome have been described. Currently, three routes of activation, the canonical pathway, the non-canonical pathway, and the alternative pathway, have been identified (**Figure 4**) [44,77].
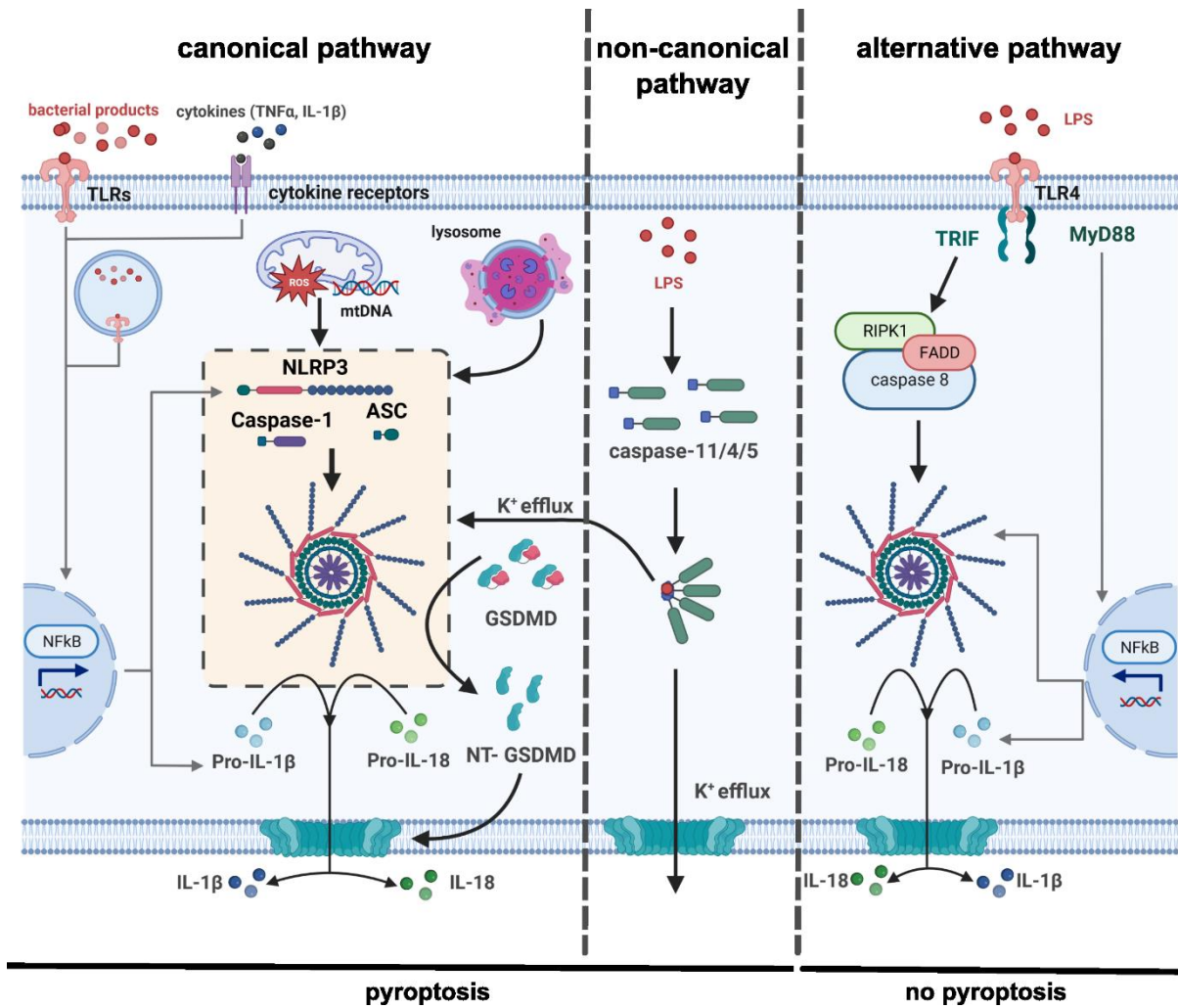
Figure 4: The NLRP3 inflammasome can be activated by three different pathways.
The first pathway is the canonical activation of the NLRP3 inflammasome, which is a two-step process. First, priming by TLR signaling, NLR (not depicted) or cytokine receptors activates NFκB and transcriptionally upregulates NLRP3 and pro-IL-1β. Second, detection of DAMP, like mitochondrial ROS or DNA, lysosomal contents or ion efflux are sensed by NLRP3, which oligomerizes by NOD-NOD interactions and recruits adapter protein ASC by interaction of PYD domains. The resulting ASC filaments recruit pro-caspase-1 by CARD-CARD interaction, which leads to autoactivation of caspase-1. Active caspase-1 converts pro-IL-1β and pro-IL-18 (not shown) to IL-1β and IL-18. Additionally, caspase-1 cleaves GSDMD, whose N-terminal fragment forms a pore in the cell membrane, which releases cytokines and initiates pyroptosis. The second pathway is the non-canonical activation of the NLRP3 inflammasome. Here, cytosolic LPS is directly recognized by caspase-11 or human orthologs caspase-4/5 (not shown). This leads to oligomerization of caspase-4/5/11, which cleaves GSDMD and activates NLRP3 through K$^+$ efflux. The third pathway is the alternative activation by prolonged TLR4 signaling. Signaling through TLR4-MyD88 transcriptionally primes the NLRP3 inflammasome by activation of NFκB, while signaling through TLR4-TRIF activates NLRP3 dependent on RIPK1-FADD-caspase-8 signaling.

The canonical activation of the NLRP3 inflammasome commonly described as a two-step process. The priming step is characterized by stimulation of TLRs (TLR4, TLR2 or TRL7/8), NLRs (NOD1 and NOD2) or cytokine receptors (IL-1 receptor, TNF-α-receptor). Each of these priming stimuli leads to activation of the pro-inflammatory transcription factor NFκB, which induces the upregulation of the not constitutively expressed inflammasome components NLRP3 and pro-IL-1β [102,107–109]. After priming, the NLRP3 inflammasome is activated by of one of the multiple PAMPs or DAMPs [44,102,103,107–109]. While it remains to be determined whether NLRP3 interacts with any of these

ligands directly, and some molecular patterns are still controversial (reviewed in [103]), currently accepted cellular alterations leading to NLRP3 inflammasome activation are (I): K^+ efflux or Ca^{2+} influx caused by cell membrane injury, pore-forming proteins (GSDMD), or ionophors (P2X7 activated by extracellular ATP, nigericin) [109–112], (II): Mitochondrial dysfunction detected by release of ROS or mitochondrial DNA (mtDNA) [113,114] and (III): Lysosomal rupture detected by release of ROS, lysosomal proteins of the cathepsin family and H^+ [115–120].

The second pathway of inflammasome activation is the non-canonical activation mediated by cytosolic LPS [103]. Cytosolic LPS binds directly to the CARD domain of murine caspase-11 or its human orthologs caspase-4 and caspase-5 , which induces oligomerization [121–123]. Oligomerized caspase-4/5/11 akin to caspase-1 autoactivate by autocleavage and subsequently, process GSDMD and pannexin-1, which transports ATP to the extracellular space [123–125]. Here, ATP activates the K^+ ionophore P2X7 and the K^+ efflux caused by P2X7 and the GSDMD pore cause this pathway to converge with the canonical pathway [106,109,123]. Unlike the canonical inflammasome activation, the necessity of a priming step is species-specific and depends on whether the cytosolic sensor caspase is constitutively expressed, which is the case for caspase-4 in human cells, or whether the sensor caspase is upregulated upon pro-inflammatory stimulation, which is the case for murine caspase-11 [122,123].

The last and most recently discovered pathway of NLRP3 inflammasome activation is the alternative activation by extracellular LPS [77]. In human macrophages, prolonged TLR4 activation by LPS leads to upregulation of pro-IL-1β as described for the canonical pathway. However, while the TLR4 signaling using the intracellular signaling protein Myd88 leads to the NFκB-mediated priming, signaling via TRIF and RIPK1-FADD-caspase-8 leads to activation of NLRP3 by a yet unknown mechanism [77]. Alternative inflammasome activation results in secretion of IL-1β, but does not show any classical signs of NLRP3 activation like pyroptosis, dependency on K^+ efflux or formation of ASC speckles [77].

The activation of the NLRP3 inflammasome leads to the secretion of IL-1β and IL-18, which mediate several important effector functions [104].]. IL-18 has been identified as an important mediator of IL-12 and IFN-γ production in bacterial and fungal infections, which are required for induction of T_h1 T cells and activation of macrophages for intracellular pathogen killing. Hence, caspase-1 deficiency leads to an impaired T_h1 response and reduced parasite clearance in infected mice [104,126,127]. IL-1β is a potent endogenous pyrogen and involved in several aspects of the innate and adaptive Immune

response [29,104,126,128,129]. IL-1β is a strong activator of lymphocytes i.e., T cells and B cells, and greatly enhances the CD4+ T cell response [126,129]. Furthermore, IL-1β activates endothelial cells and attracts neutrophils, thus, playing a crucial role in neutrophil recruitment [104,130]. Additionally, IL-1β has been shown to be a potent activator of NO in murine macrophages on par with IFN-γ [128]. Considering the potent activation of intracellular pathogen killing in macrophages and the strong induction of T_h1 T cell responses, it is not surprising that inflammasome activation promotes host protection against a wide range of intracellular pathogens [131].

For the sake of completion it should by mentioned that the beneficial role of the NLRP3 inflammasome in the host response to intracellular pathogens is in strong contrast to its deleterious role in many autoimmune diseases, in which sensing of DAMPs contributes to inflammation (reviewed in [132,133]. However, this aspect of the NLRP3 inflammasome is out of the scope of this thesis and thus, omitted here.

1.5.1 Pyroptosis

Pyroptosis is a form of pro-inflammatory programmed cell death induced by NLRP3 inflammasome activation [44]. Morphological characteristics of pyroptotic cells are chromatin condensation, an intact nucleus, cellular swelling, and membrane rupture [44]. Pyroptosis occurs when a strong activation of the NLRP3 inflammasome produces a large number of GSDMD pores that cannot be controlled by the membrane repair capabilities of the cell [44]. The non-selective GSDMD pores release active IL-1β and IL-18 to the extracellular space but also allow the influx of fluid, leading to cell swelling and ultimately cell rupture [44,106,134]. Lysed cells release all soluble cellular contents into the extracellular space, among them IL-1β, IL-18 and many other cytokines, lactate dehydrogenase (LDH) and DAMPs like ATP [44]. This results in a strong pro-inflammatory activation of bystander cells, which are primed for pyroptosis and recruitment of new effector cells. Thus, pyroptosis can be considered as a powerful pro-inflammatory amplification loop of the innate immune system [104]. So far, no NLRP3 inflammasome-specific effector mechanisms beyond the effects of IL-1β and IL-18 have been reported [134] and therefore, the anti-microbial effects mediated by pyroptosis correspond to the ones of IL-1β and IL-18 described in 1.5.

1.5.2 Differences between human and murine inflammasome

As for macrophages, there are several species-specific differences between the human and the murine NLRP3 inflammasome – some of which have already been mentioned earlier. The most important differences lie in the activation pathways of the NLRP3 inflammasome. First, the alternative activation pathway by prolonged LPS-mediated TLR4 signaling is absent in mice [77]. Together with the much higher LPS sensitivity of human cells compared to murine cells, that ranges from 250-fold if assessed based on IL-6 secretion [71] to more than 1000-fold based on IL-1β [135], it can be assumed that the NLRP3 inflammasome is more easily activated under physiological conditions in humans than in mice. Second, while in mice, inflammasome activation via the canonical and non-canonical pathway is a two-step process, this is not the case for human cells in which the non-canonical pathway can be activated in a one-step process due to the constitutive expression of caspase-4 [123]. Since the non-canonical pathway directly converges into the canonical pathway [44] and the alternative inflammasome activation produces active caspase-1 [77], thus, theoretically retains the ability to trigger K^+ efflux by cleavage of GSDMD, the two-step dogma de facto does not apply to human cells.

Another very important difference is the activation of iNOS by IL-1R signaling, that induces a potent restriction of intracellular pathogens in mice [128]. As described in 1.3.2, this effector mechanism is not activated in human macrophages and I am unaware of any reports describing a similar effect i.e., an IL-1R-mediated oxidative burst, for human cells.

1.5.3 NLRP3 inflammasome in leishmaniasis

It has been known for a long time that macrophages secrete IL-1β in response to *Leishmania spp.* infection [136]. However, it took almost twenty years to show that this cytokine response was mediated by the activation of the NLRP3 inflammasome [128]. *Lima-Junior et al.* showed that the NLRP3 inflammasome activation by *L. amazonensis* is dependent on caspase-1, NLRP3 and ASC and causes a pronounced parasite restriction in vitro and in vivo by induction of iNOS via IL-1R signaling [128]. Activation of the NLRP3 inflammasome by *Leishmania ssp*. was subsequently confirmed by several other studies [130,137,138]. The exact mechanism of NLRP3 inflammasome activation by *Leishmania* is not completely understood but so far, two main branches of activation have been identified (**Figure 5**) [139,140]. The first branch of activation uses the canonical pathway of inflammasome activation and involves signaling via C-type lectin receptors (CLR) Dectin-1 and mannose receptor (MR) as second stimulus [137,141]. CLR activation leads to phosphorylation of the spleen tyrosine kinase (Syk) which is required for phosphorylation of the p47 subunit of the NAPDH

oxidase and subsequent assembly of the NAPDH oxidase enzyme complex resulting in ROS production [137,141]. Accordingly, inhibition of ROS with apocynin or DPI for the first two hours of infection with promastigotes or the first hour of infection with amastigotes abrogated NLRP3 inflammasome activation [141]. While the release of arachnidonic acid from the phospholipids of the inner membrane leaflet has been reported as an intermediate signal transducer between mannose receptor activation and p47 phosphorylation, arachnidonic acid release seems to be dispensable for NLRP3 inflammasome activation, because inhibition of the cPLA2 enzyme responsible for arachnidonic acid release leads only partially impairs IL-1β secretion and signaling via Dectin-1 does not involve it at all [137]. The second branch of inflammasome activation uses the non-canonical signaling pathway and involves lipophosphoglycan (LPG) signaling via the cytosolic LPS sensors caspase-11 (murine) or caspase-4/5 (human). However, unlike LPS, LPG does not bind to these caspases directly [142].
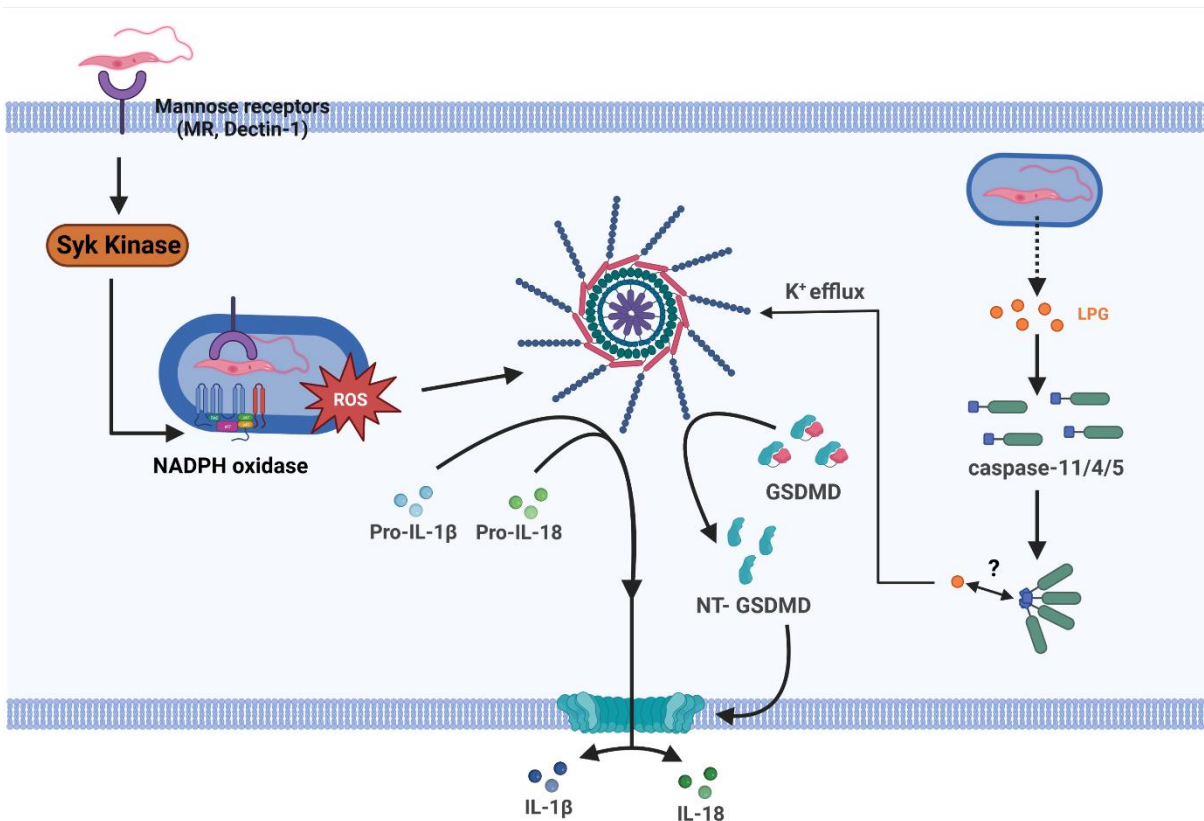
Figure 5: NLRP3 inflammasome activation by *Leishmania ssp.*
The illustration shows the two main branches of Leishmania-mediated NLRP3 inflammasome activation. First, Phagocytosis through a mannose-receptor like Dectin-1 or mannose receptor leads to phosphorylation of Syk, which is required for phosphorylation of p47 subunit of the NADPH oxidase complex. Phagolysosomal ROS produced by NADPH oxidase, then, activates NLRP3. The second branch is the detection of cytosolic LPG by caspase-4/5/11. Unlike detection of cytosolic LPS, LPG is not bound directly by caspase-4/5/11. All shown pathways and corresponding citations are described in detail in the text.

While the parasite restriction in vitro and the better control of the infection observed for *L. amazonensis* and *L. infantum* in vivo were well in line with the protective role of the NLRP3 inflammasome reported for other intracellular pathogens [128,131,134,137,141], the results for *L. major* remain unclear. The reason for this are the biases of the used mouse models mentioned earlier (see 1.3.2). Studies with inflammasome-deficient C57BL/6 mice showed that *L. major* does activate the murine NLRP3 inflammasome similar to *L. amazonensis*, but the inflammasome activation was dispensable for efficient clearance of the infection [128]. NLRP3 inflammasome activation in BALB/C mice, on the other hand, did not only not lead to iNOS-mediated NO production but did also promote a T_h2 response in a IL-18 dependent way, exacerbating the disease phenotype [65,143]. Interestingly, the NLRP3 inflammasome plays a crucial role in the maintenance of tissue-resident macrophages (TRMs) by IL-1β-mediated induction of group 2 innate lymphoid cells (ILC2s). ILC2s produce IL-4, IL-5 and IL-13 and have been shown to be important for the maintenance of eosinophilic granulocytes and TRMs [144,145]. Hence, IL-1β secretion and therefore, presence of the NLRP3 inflammasome is required for the non-healing phenotype of the *L. major* Seidman strain [145,146]. Additionally, continued recruitment of neutrophils by IL-1β is assumed to be responsible for the observed tissue damage [145].

The role of the NRLP3 inflammasome in human leishmaniasis remains unclear because to date, very few studies addressing this signaling pathway have been conducted. The scarce existing data showed that genes of the NLRP3 inflammasome pathway are upregulated during *L. braziliensis* infection [147], and that the serum level of IL-1β is negatively correlated with the severity of CL [148]. Conversely, the IL-1β secretion of *L. mexicana*-infected patients was higher for diffuse cutaneous leishmaniasis patients than for localized cutaneous leishmaniasis patients [149]. However, diffuse cutaneous leishmaniasis is a very rare manifestation of CL that is associated with a defective immune response and should not be considered as more severe phenotype of localized cutaneous leishmaniasis [150–152]. In summary, the scarce data from human leishmaniasis patients points towards a protective role of the NLRP3 inflammasome.

2 Hypotheses and aims

The course of cutaneous leishmaniasis is well understood and many aspects of the disease: from the initial establishment of the infection over the replicative niche during acute infection to the immunological processes and effector mechanisms that lead to its resolution. However, most of this knowledge has been obtained from mouse models and does not translate well to the human patient due to species-specific differences. This is particularly true for the NLRP3 inflammasome – a key player of the innate immune response against intracellular parasites, for which several species-specific differences compound with strain-specific traits of commonly used mouse models. Hence, there is a dire need for mechanistic research of cutaneous leishmaniasis in the human system. So far, this type of research has been impaired by the lack of reverse genetic methods for human macrophages. The project that led to this thesis aims to overcome this problem by using a transdifferentiating human macrophage cell line to characterize the role of the NLRP3 inflammasome in human cutaneous leishmaniasis.

Therefore, the main hypothesis of this project is:

The human NLRP3 inflammasome plays a role in the innate immune response against *L. major*, which contributes to the spread of the infection to new host cells by inducing pyroptotic cell death.

This hypothesis leads to the following aims:

1. Investigation of the potential of the BLaER1 cell line to be used as an infection model for the infection of primary human macrophages with *L. major.*
2. Characterization of the pathogen- or damage-associated molecular pattern that lead to *L. major* mediated activation of the NLRP3 inflammasome
3. Determination of NLRP3 inflammasome mediated parasite restriction and investigation of the leishmanicidal effector mechanism downstream of NLRP3 inflammasome activation
4. Elucidation of the role of pyroptotic cell death in the cell-to-cell spread of *L. major* parasites
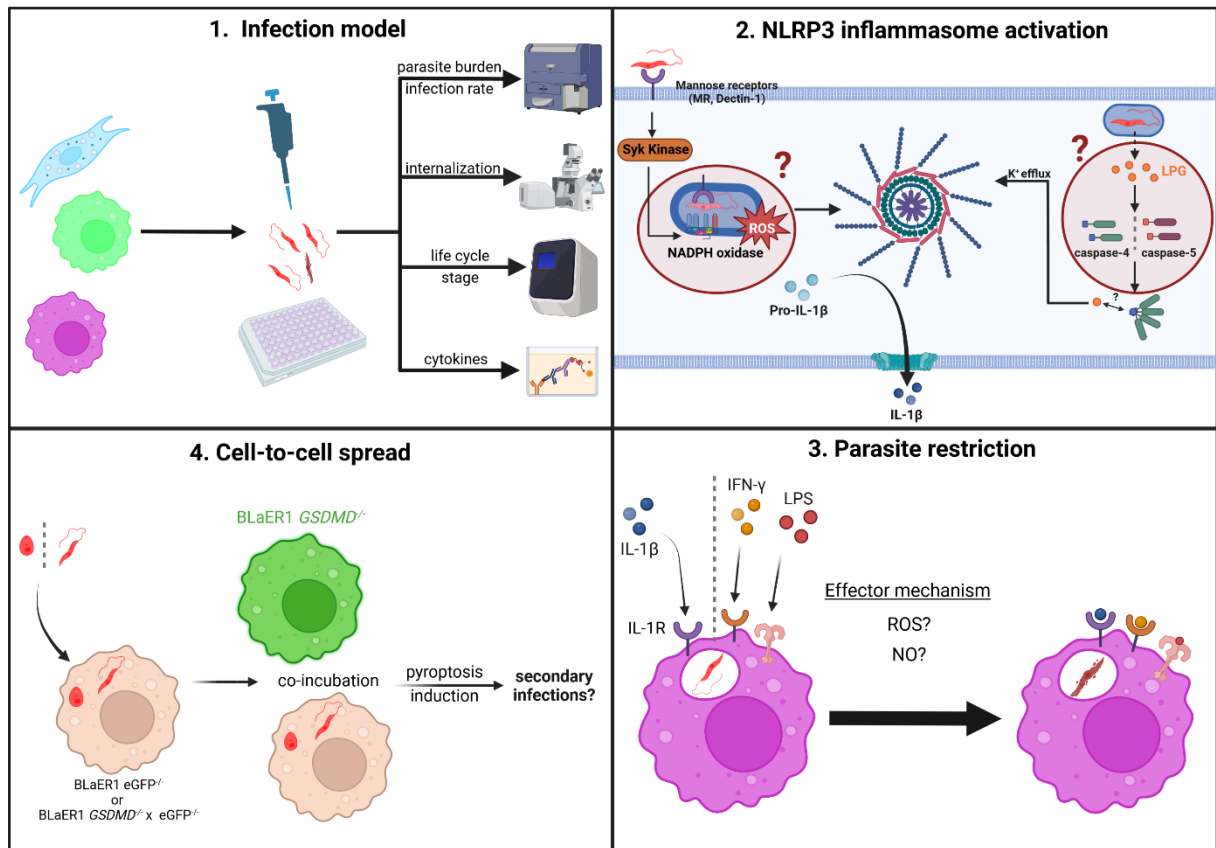
Figure 6: Schematic depiction of the aims of this thesis.
The role of the human NLRP3 inflammasome in the innate immune response against *L. major* was investigated in this thesis. (1. Infection model) To allow the use of reverse genetic methods, the BLaER1 cell line (purple) was tested as a model for GM-CSF-derived (green) and M-CSF-derived hMDMs (blue), by comparison across several important parameters of the *L. major* infection. (2. NLRP3 inflammasome activation) Using inflammasome-deficient knockout BLaER1 cell lines, the *L. major*-mediated inflammasome activation was tested for its dependency on phagolysosomal ROS production and LPG. (3. Parasite restriction) The effect of NLRP3 inflammasome activation on parasite restriction was investigated. (4. Cell-to-cell spread) Finally, pyroptosis was investigated as a possible mechanism of the cell-to-cell spread of L. major in co-incubation assays of eGFP-deficient BLaER1 cell lines (ochre) and eGFP-expressing BLaER1 cell lines (green).

3 Material and methods

3.1 Materials

3.1.1 List of devices

Device	Manufacturer
CASY® Cell Counter Model TT	Roche Innovatis AG
centrifuge 5430 and 5430R	Eppendorf
centrifuge J2-MC	Beckman Coulter
centrifuge Megafuge 40R with BIOLiner swinging bucket rotor and buckets (75003670, 75003668)	Thermo Fisher Scientific
CLARIOstar Plus microplate reader	BMG Labtech
ECL and fluorescence imager Chemostar	Intas
electrophoresis chamber for SDS-PAGE mini-Protean Tetra cell	Bio-Rad
FACSymphony A3 Cell Analyzer	BD Bioscience
Gel Doc XR+	Bio-Rad
Live-7 confocal microscope	Carl Zeiss Microscopy
LSR Fortessa	BD Bioscience
LSR II SORP	BD Bioscience
MACS Chill Rack	Miltenyi Biotec
MACS multistand	Miltenyi Biotec
microscope AxioVert A1	Carl Zeiss Microscopy
microscope Primo Star	Carl Zeiss Microscopy
MidiMACS Magnet	Miltenyi Biotec
MidiMACS separator	Miltenyi Biotec
Mini centrifuge Sprout	Biozym Scientific GmbH
Nalgene Mr. Frosty freezing container	Thermo Fisher Scientific
Neubauer counting chamber improved, depth 0.1mm	VWR
Neubauer counting chamber improved, depth 0.02 mm	VWR
Operetta high content microplate imager	Perkin Elmer
pH meter PB -11	Sartorius
power supply 'PowerPac HC'	Bio-Rad
semi-dry transfer unit OWL HEP-1	Thermo Fisher Scientific
spectrophotometer NanoDrop 2000c	Thermo Fisher Scientific

TCS SP8 confocal fluorescence microscope	Leica Microsystems
thermal cycler S-1000	Bio-Rad
Thermomixer comfort with thermoblock	Eppendorf

3.1.2 List of consumables

Consumable	Manufacturer
CASY tubes	OLS OMNI Life Science
cell culture flasks with filter (25cm^2 and 75cm^2)	Sarstedt
cell culture plates (6 well F-bottom, 24 well F-bottom, 48 well F-bottom, 96 well F/U/ V-bottom), sterile	Sarstedt
cell scraper (S, M), sterile	Sarstedt
chamber slides (8-well, 12-well with removable gasket), sterile	Ibidi
conical tubes, 15ml, 50ml	Greiner Bio-One
Cryo.s Freezing Tube, 2 ml, round bottom	Greiner Bio-One
electroporation cuvettes (2 mm)	VWR
FACS micronic tubes, 1.4 ml, U-bottom	Micronic
FACS tube, 5 ml	BD labware
MACS column, LS	Miltenyi Biotec
microcentrifuge tubes (1.5ml, 2ml)	Eppendorf
microplate, µclear 96 well, F-bottom, black	Greiner Bio-One
pipette filter tips (0.5-10µl, 10-200µl, 100-1000µl)	Nerbe plus
pipette tips SurPhob SafeSeal (0.1-10µl, 10-200µl, 100-1000µl)	Biozym Scientific GmbH
polyvinylidene difluoride (PVDF) membrane	GE Healthcare
serological pipettes, sterile (5ml, 10ml, 25ml)	Greiner Bio-One

3.1.3 List of kits

Kit	Manufacturer
CD14 MicroBead Kit, human	Miltenyi Biotec
DNeasy Blood & Tissue Kit	Qiagen

FLICA 660 caspase-1 assay kit	Immunochemistry Technologies
human B cell nucleofection kit	Lonza
human IL-10 DuoSet ELISA	R&D Systems
human IL-12 ELISA MAX deluxe	Biolegend
human IL-1β ELISA MAX deluxe	Biolegend
human TNF-α DuoSet ELISA	R&D Systems
Im Prom-II Reverse transcription system	Promega
MESA Blue qPCR MasterMix Plus	Eurogentec
nitric oxide generation kit	Biotium
nitric oxide (total) detection kit	Enzo Life Science Inc.
NucleoBond Xtra Maxi Kit	Macherey-Nagel
Qiaprep Spin Miniprep Kit	Qiagen
RNeasy Plus Mini Kit	Qiagen
Wizard SV Gel and PCR clean-up system	Promega

3.1.4 Media

Medium	Composition	Manufacturer
amastigote medium	RPMI-1640 10 % (v/v) 3 mM L-glutamine 100 U/mL penicillin 100 µg/mL streptomycin pH 5.5 sterile filtered	RPMI-1640 from Sigma Aldrich, see 3.1.7 for manufacturers of supplement
BLaER1 DMEM medium	DMEM high glucose 10 % (v/v) FCS 2 mM L-glutamine 100 U/mL penicillin 100 µg/mL streptomycin 10 mM HEPES buffer	DMEM high glucose from Sigma Aldrich, see 3.1.7 for manufacturers of supplement
BLaER1 medium	RPMI 1640 10 % (v/v) FCS 2 mM L-glutamine	RPMI-1640 from Sigma Aldrich, see 3.1.7 for manufacturers of supplement

	100 U/mL penicillin	
	100 µg/mL streptomycin	
	10 mM HEPES buffer	
liquid medium	Medium 199	M199 from Gibco, see 3.1.7 for
	10 % (v/v) FCS	manufacturers of supplement
	100 U/mL penicillin	
	100 µg/mL streptomycin	
	20 mM HEPES buffer	
	100 µM adenine	
	0.05 % hemin (w/v)	
	0.041 % biotin (w/v)	
leishmania medium	RPMI 1640	RPMI-1640 from Sigma Aldrich,
	5% (v/v) FCS	see 3.1.7 for manufacturers of
	2 mM L-glutamine	supplement
	100 U/mL penicillin	
	100 µg/mL streptomycin	
	10 mM HEPES buffer	
	50 µM β-mercaptoethanol	
complete medium	RPMI 1640	RPMI-1640 from Sigma Aldrich,
	10 % (v/v) FCS	see 3.1.7 for manufacturers of
	2 mM L-glutamine	supplement
	100 U/mL penicillin	
	100 µg/mL streptomycin	
	10 mM HEPES buffer	
	50 µM β-mercaptoethanol	
Novy-Nicolle-McNeal agar	16% rabbit blood defibrinated	
	16 % PBS	
	3.44 % brain heart infusion agar (400 ml of 5.2 % stock solution)	
	66.2 U/mL penicillin	
	66.2 µg/mL streptomycin	
LB medium	2. 5% LB bouillon (Miller)	Paul-Ehrlich-Institut

	aqua bidest.	
LB$_{amp}$ agar plates	3.7 % LB agar 100 µg/mL ampicillin aqua bidest.	Paul-Ehrlich-Institut
SOC medium	2.66 % SOB-medium 20 mM D-glucose aqua bidest.	Paul-Ehrlich-Institut

3.1.5 Buffers and solutions

All buffers and solutions that were made by the central laboratory of the Paul-Ehrlich-Institut were listed with "Paul-Ehrlich-Institut" as manufacturer. All buffers that were prepared by myself were listed with the manufacturer column left blank.

Buffer	Composition	Manufacturer
10 % SDS	10 % (w/v) SDS aqua bidest.	Paul-Ehrlich-Institut
ammoniumchloride solution	0.15 M ammoniumchloride aqua bidest.	Paul-Ehrlich-Institut
blocking buffer (microscopy, flow cytometry)	PBS pH 7.1 10% (v/v) FCS 10% (v/v) human AB serum	
blocking buffer (Western blot)	TBS/T 5% (w/v) milk powder	
blotting buffer	50 mM Tris 40 mM glycin 0.0375% SDS (w/v) 2.5% methanol (v/v) aqua bidest.	Paul-Ehrlich-Institut
Coomassie fixing solution	H_2O 20 % (v/v) methanol 1 % (v/v) glacial acetic acid	
Coomassie staining solution	H_2O 20 % (v/v) methanol 20 % (v/v) Rotiblue	

Coomassie washing solution	H$_2$O 25 % (v/v) methanol	
CutSmart buffer (10x)	500 mM potassium acetate 200 mM Tris-acetate 100 mM magnesium acetate 1 mg/ml recombinant albumin pH 7.9	New England Biolabs
cytokine storage buffer	PBS, pH 7.4 0.1 % (w/v) BSA sterile filtered	
electrophoresis running buffer (5x)	125 mM Tris 1.25 M glycine 0.5% (w/v) SDS aqua bidest.	Paul-Ehrlich-Institut
FACS Clean	aqua hypochloric acid concentration not disclosed) sodium hydroxide (concentration not disclosed)	BD Biosciences, Heidelberg, GER
FACS Flow (Sheath Solution)	PBS 0.1 % (v/v) sodium azide	Paul-Ehrlich-Institut
FACS Rinse	no ingredients disclosed	BD Biosciences, Heidelberg, GER
fixing solution	PBS, pH 7.1 4 % (v/v) formaldehyde	
Lämmli buffer (6x)	aqua bidest. 500 mM Tris-HCl pH 6.8 38% glycerol (v/v) 10% SDS (w/v) 600 mM DTT 0.01% bromophenol blue	Paul-Ehrlich-Institut

MACS buffer	0.5% BSA (w/v) 0.5 mM EDTA PBS pH 7.2	Paul-Ehrlich-Institut
NEB buffer r3.1 (10x)	1000 mM NaCl 500 mM Tris-HCl 100 mM MgCl2 1 mg/ml recombinant Albumin pH 7.9	New England Biolabs
1x PBS without Ca^{2+} and Mg^{2+}, pH 7.1 (used for all experiments except for ELISA)	136.9 mM sodium chloride 2.68 mM potassium chloride 1.47 mM potassium dihydrogen orthophosphate 8.1 mM sodium dihydrogen phosphate aqua bidest.	Paul-Ehrlich-Institut
1x PBS without Ca^{2+} and Mg^{2+}, pH 7.4 (used for ELISA)	136.9 mM sodium chloride 2.68 mM potassium chloride 1.47 mM potassium dihydrogen orthophosphate 8.1 mM sodium dihydrogen phosphate aqua bidest.	Paul-Ehrlich-Institut
permeabilization buffer	PBS, pH 7.1 0.1 % (v/v) Triton-X 100	
reagent diluent	PBS, pH 7.4 1 % (w/v) BSA sterile filtered	
Ringer solution	147 mM NaCl 4 mM KCl 2.2 mM CaCl$_2$ aqua bidest.	B. Braun Melsungen AG

RNA loading dye (5x)	5% (v/v) β-mercaptoethanol 0.02 % (w/v) bromphenol blue 30 % (v/v) glycerol 10 % (w/v) SDS Tris-HCl	prepared in lab by unkown experimentator
staining buffer	PBS pH 7.1 1% (v/v) FCS 1% (v/v) human AB Serum	
TAE buffer (20x)	0.8 M Tris-HCl pH 8.0 20 mM EDTA 2.25 % acetic acid aqua bidest.	Paul-Ehrlich-Institut
TBS/T buffer	1 x TBS buffer 0.5% Tween 20 (v/v)	Paul-Ehrlich-Institut
Tris-HCl 0.5 M, pH 6.8	0.5 M Tris(hydroxymethyl)-aminomethane aqua bidest. pH adusted to 6.8 with HCl	Paul-Ehrlich-Institut
Tris-HCl 1.5 M, pH 8.8	1.5 M Tris(hydroxymethyl)-aminomethane aqua bidest. pH adusted to 8.8 with HCl	Paul-Ehrlich-Institut
Trypsin	PBS, pH 7.1 1 % (v/v) EDTA 0.05 % (w/v) trypsin	Paul-Ehrlich-Institut
washing buffer (ELISA)	PBS, pH 7.4 0.05 % (v/v) Tween-20	
washing-buffer (PBMC isolation)	1x PBS without Ca^{2+} and Mg^{2+} pH 7.1	

	10% (v/v) complete medium	
Zimmerman buffer	132 mM NaCl	
	8 mM KCl	
	8 mM Na_2HPO_4	
	1.5 mM KH_2PO_4	
	0.5 mM $MgAc_2$	
	90 µM $CaOAc_2$	
	aqua bidest.	
	pH 7.0	
	sterile filtered	

3.1.6 Antibodies and dyes

All listed antibodies were monoclonal unless indicated otherwise.

Antibody or dye	Isotype	Flurochrome	Host species	Concentration [µl/10^6 cells]	Manufacturer
Alexa-Fluor405	-	-	-	1 µg/ml	Thermo Fisher Scientific
Alexa-Fluor647	-	-	-	1 µg/ml	Thermo Fisher Scientific
annexin V	-	Alexa Fluor647	-	1	Thermo Fisher Scientific
caspase-4	IgG	unconjugated	rabbit	0.568 µg/ml	AbCam
caspase-5	IgG1κ	unconjugated	mouse	1 µg/ml	Biozol
CD115	IgG1κ	PE	rat	2.5	Biolegend
CD116	IgG1κ	PE	mouse	5	Biolegend
CD11b	IgG1κ	PE	mouse	3	BD Pharmingen
CD124	IgG2a,κ	PerCP-Cy5.5	mouse	2.5	Biolegend
CD14	IgG2a,κ	Pacific Blue	mouse	4	Biolegend
CD163	IgG1κ	Brilliant Violet 421	mouse	5	Biolegend
CD18	IgG1κ	APC/Fire	mouse	5	Biolegend
CD19	IgG1κ	PerCP-Cy5.5	mouse	5	Biolegend

CD206	IgG1κ	Brilliant Violet 711	mouse	5	Biolegend
CD209	IgG2b,κ	APC	mouse	20	BD Pharmingen
CD83	IgG1κ	APC	mouse	20	BD Pharmingen
CD86	IgG2b	APC	mouse	5	Biolegend
CellTracker DeepRed	-	-	-	0.5 μM	Thermo Fisher Scientific
CFMDA	-	-	-	5 μM	Thermo Fisher Scientific
CFSE	-	-	-	1 μg/ml	Thermo Fisher Scientific
DAPI	-	-	-	300 nM	
DHE	-	-	-	5 μM	AAT Bioquest
HLA-ABC	IgG2a,κ	PerCP-Cy5.5	mouse	5	Biolegend
HLA-DR	IgG2a,κ	Brilliant Violet 421	mouse	5	Biolegend
phalloidin	-	Alexa-Fluor488	-	50 nM	Thermo Fisher Scientific
polyclonal α-Lm serum	-	unconjugated	mouse	1 μg/ml	
polyclonal α-Lm serum	-	unconjugated	rabbit	1 μg/ml	Uwe Ritter, University Regensburg
propidium iodide	-	-	-	500 ng/ml	Bio-Rad
wheat germ agglutinin CF568	-	-	-	2.5 μg/ml	Biotium
Zombie aqua	-	-	-	1:1000 dilution	Biolegend
α-mouse	IgG	Alexa-Fluor568	donkey	2.5 μg/ml	Thermo Fisher Scientific
α-mouse	IgG	HRP	goat	1 μg/ml	Cell Signaling
α-rabbit	IgG	Alexa-Fluor647	chicken	2.5 μg/ml	Thermo Fisher Scientific

α-rabbit	IgG	HRP	goat	1 μg/ml	Cell Signaling

3.1.7 Reagents

Reagent	Manufacturer
123count eBeads, counting Beads	Thermo Fisher Scientific
2-Propanol	VWR
acrylamide/ bisacrylamide solution 30%	Roth
agarose, LE	Biozym Scientific
ammonium chloride (0.15 M)	Pau-Ehrlich-Institute
ammonium persulfate (APS)	SERVA Electrophoresis
apocynin	Sigma Aldrich
aqua bidest.	Paul-Ehrlich-Institute
blasticidin	InvivoGen
bovine serum albumin (BSA)	Applichem
bromophenol blue	Merck
CASYclean	OLS OMNI Life Sciences
CASYton	OLS OMNI Life Sciences
DEPC-treated aqua bidest	Paul-Ehrlich-Institute
Difco Brain Heart Infusion Agar	Becton Dickenson
dimethyl sulfoxide (DMSO)	AppliChem
diphenylene iodonium chloride (DPI)	Sigma Aldrich
ethanol (EtOH, 96%)	Paul-Ehrlich-Institute
ethidium bromide	
fetal calf serum (FCS)	Sigma-Aldrich, Steinheim, GER
formaldehyde (37 %)	
GeneRuler 100 bp plus DNA ladder	Thermo Fisher Scientific
GeneRuler 1 kb plus DNA ladder	Thermo Fisher Scientific
hemin	Sigma-Aldrich
HEPES, 1 M	Merck
High-purity water	Paul-Ehrlich-Institute
Histopaque 1.077 g/ml	Sigma-Aldrich
human interferon-γ (IFN-γ)	Sigma-Aldrich

human recombinant granulocyte macrophage colony stimulation factor (GM-CSF), Leukine®	Bayer Healthcare Pharmaceutical
human recombinant macrophage colony stimulating factor (M-CSF)	R&D Systems
human serum type AB	Sigma-Aldrich
hydrochloric acid 37%	Roth
hygromycin	InvivoGen
L-glutamine, 200 mM	Biochrom
lipopolysaccharide from *Escherichia coli*	Sigma Aldrich
Luminata Forte Western HRP substrate	Merck
medium 199	Gibco
menadione	Sigma Aldrich
methanol (MeOH)	Paul-Ehrlich-Institute
Mowiol mounting medium	Sigma-Aldrich
nigericin	Biomol
nourseothricin	Jena Bioscience
NOX VII	Sigma Aldrich
PageRuler Plus prestained protein ladder, 10 to 250 kDa	Thermo Fisher Scientific
penicillin, 10000 U/ml/ streptomycin, 10 mg/ml	Biochrom
poly-D-lysine, 0.1 mg/ml	Gibco
poly-L-ornithine, 0.1 mg/ml	Sigma-Aldrich
puromycin	InvivoGen
rabbit blood, defibrinated	Elocin-Lab or Paul-Ehrlich-Institute
recombinant human IL-3	PeproTech
purified Cas9-NLS protein	Horizon Discovery
Resiquimod (R848) Vaccigrade	InvivoGen
RNase AWAY	VWR
Roswell Park Memorial Institute (RPMI) 1640 medium	Sigma-Aldrich
skim-milk powder	EDEKA
sodium dodecyl sulfate (SDS)	Merck
TEMED (tetramethylethylendiamine)	Roth

TriTrack DNA loading dye (6x)	Thermo Fisher Scientific
Ultracomp eBeads compensation beads	Thermo Fisher Scientific
ZVAD-FMK	InvivoGen
β-mercaptoethanol	Sigma-Aldrich

3.1.8 Primers

Target	Orientation	Sequence
NMT	forward	CCGTCGACTGTGATTGGGAA
	reverse	GTGAATGCGCCACGATCAAA
SHERP	forward	GAC GCT CTG CCC TTC ACA TAC
	reverse	TCT CTC AGC TCT CGG ATC TTG TC
ABC transporter homologue	forward	CGG GTT TGT CTT TCA GTC GT
	reverse	CAC CAG AGA GCA TTG ATG GA
GAPDH	forward	CCCCACACACATGCACTTACC
	reverse	TTGCCAAGTTGCCTGTCCTT
HPRT1	forward	CCT GGC GTC GTG ATT AGT GA
	reverse	CGA GCA AGA CGT TCA GTC CT
iNOS	forward	AGGATCCAGTGGTCCAACCT
	reverse	GTGATGGCCGACCTGATGTT
Hnrnpab	forward	GGCCGTGTCATTGACCCTAA
	reverse	TCAATCTCCCCAAACTCGCC
DsRed with overhangs for Gibson assembly	forward	GCTGGTTGCAGCGGCCGTGTCGGTCGACGCTGGCGCCTCTATGGCATCCACC GAGGACG
	reverse	GGCCGCCTAGTGGTGGTGATGGTGGTGGGTACCCTTAAGGCTACAGGAACA GGTGGTGGCGG
SAT	forward	GAAGATTTCGGTGATCCCTGAGCAG
18S-rRNA (*L. major*)	forward	GGCTACCGTTTC GGCTTTTG
	reverse	CTCTCTCTCCCT CCCGCC
blasticidin	forward	GCCGCATCTTCACTGGTGTCAA
	reverse	TCGGCTGTCCATCACTGTCCT
LPG1 CDS	forward	CGGGCACAGAGA CCTTCGAAG
	reverse	GACATCATCAGG GAACCACTTCGC

LPG1 3'-UTR	reverse	GCTGCCGCAAGG AGAGAGG
LPG1 HR	forward	GTGTATCCTTTTC TAGCCAAACCAG TGCCGGTATAAT GCAGACCTGCTG C
	reverse	CGTCGCAATGGC CAGCGAGAGCGT GTGCCGCCAATT TGAGAGACCTGT GC
LPG1 5'-sgRNA	forward	GAAATTAATACGA CTCACTATAGGT GCTCTCTGGTTC GACTAAGGTTTTA GAGCTAGAAATAG C
LPG1 3'-sgRNA	forward	GAAATTAATACGA CTCACTATAGGTT CTGGTCGGGAGT AATGCAGTTTTAG AGCTAGAAATAGC
sgRNA scaffold	reverse	AAAAGCACCGACTCGGTGCCACTTTTTCAAGTTGATAACGGACTAGCCTTATTTTAAC TTGCTATTTCTAGCTCTAAAAC

3.1.9 Plasmids

Plasmid	Insert	Backbone	Resistance marker	Origin
pLEXSY-sat.21	-	pLEXSY-sat.21	nourseothricin	Jena Bioscience
pLEXSY-DsRed-sat2.1	DsRed express	pLEXSY-sat.21	nourseothricin	This thesis
pSSU-DsRed	DsRed express	pSSU-eGFP	hygromycin	Paul-Ehrlich-Institut
pTPuro	-	B6162	puromycin	kind gift of Tom Beneke (university of Oxford)
pTBlast	-	B6162	blasticidin	kind gift of Tom Beneke (university of Oxford)
pCAGGS-Redstar	Redstar	pCAGGS	-	kind gift of Moritz Schüssler (Paul-Ehrlich-Institut)

The red fluorescent protein in encoded all plasmids except for pCAGGS-RedStar, and expressed by all
L. major strains with stable genomic integration of linearized plasmid fragments is DsRed-express. The

protein will be referred to as "DsRed" throughout this thesis for convenience and spatial constrains in figures.

3.1.10 Enzymes

Enzyme	Manufacturer
NEBuilder® HiFi DNA Assembly Master Mix (2x)	New England Biolabs
NheI	New England Biolabs
PWO MasterMix (2x)	Roche
SwaI	New England Biolabs
XbaI	New England Biolabs

3.1.11 Single guide RNAs

Target	Sequence of DNA target	Manufacturer
eGFP	GGCTGAAGCACTGCACGCCGT	Horizon Discovery
Casp4	CCTTAAGTGGCTTTTTTCTG	Horizon Discovery
Casp5	GTCCTGGAGAGACCGCACAA	Horizon Discovery

All sgRNAs were dissolved in nuclease-free aqua bidest. (DEPC-treated) at a concentration of 200 µM in according with the manufacturer's protocol. After addition of nuclease-free aqua bidest., sgRNAs were incubated with shaking for 30 min at room temperature. Afterwards, 5 µl aliquots were prepared in sterile, nuclease-free 200 µl micro-reaction tubes and stored at -80 °C until use.

3.1.12 Human cell lines

Cell line	Origin
BLaER1	Kind gift of Holger Heine (Research Center Borstel)
BLaER1 eGFP⁻/⁻	Kind gift of Holger Heine (Research Center Borstel)
BLaER1 Casp1⁻/⁻	Kind gift of Holger Heine (Research Center Borstel)
BLaER1 NLRP3⁻/⁻	Kind gift of Holger Heine (Research Center Borstel)

BLaER1 *GSDMD*-/-	Kind gift of Holger Heine (Research Center Borstel)
BLaER1 *Casp4*-/-	created from BlaER1 in this thesis
BLaER1 *Casp5*-/-	created from BlaER1 in this thesis
BLaER1 *GSDMD*-/- x eGFP-/-	created from BlaER1 *GSDMD*-/- in this thesis

3.1.13 Primary human cells

Peripheral blood mononuclear cells (PBMCs) were isolated from blood of healthy human donors obtained from the DRK-Blutspendedienst Hessen GmbH.

3.1.14 Primary murine cells

Murine bone-marrow cells were isolated in the lab of Zoe Waibler (Paul-Ehrlich-Institut) from a single B6.SJL-*Ptprc*ᵃ/B6-Cd45.1 mouse.

3.1.15 *Leishmania* strains

The *L. major* isolate MHOM/IL/81/FEBNI strain was isolated from a skin biopsy of an Israeli patient and will be referred to as wild type in this work. All strains in this thesis were derived from this isolate unless indicated otherwise.

Strain	Genetic modification	antibiotic resistance	Origin
L. major	-	-	Skin biopsy of Israeli patient
***L. major* DsRed**	Stable expression of DsRed	hygromycin (20 µg/ml)	Generated by Sabine Förster at Paul-Ehrlich-Institute, Langen
***L. major* T7/Cas9**	Stable expression of Cas9 endonuclease and T7 RNA polymerase	hygromycin (30 µg/ml)	kind gift of Antonio Jiménez Ruiz (Universidad de Alcalá)

L. major **T7/Cas9 DsRed**	Stable expression of Cas9 endonuclease and T7 RNA polymerase and DsRed	hygromycin (30 µg/ml), nourseothricin (100 µg/ml)	Generated from *L. major* T7/Cas9 in this thesis
L. major **T7/Cas9 DsRed LPG1**$^{-/-}$	Stable expression of Cas9 endonuclease and T7 RNA polymerase and DsRed; Knocked-out LPG1 gene	hygromycin (30 µg/ml), nourseothricin (100 µg/ml), blasticidin (10 µg/ml)	Generated from *L. major* T7/Cas9 DsRed in this thesis

3.1.16 Bacteria strains

All transformations were performed using chemically competent *E. coli* TOP10 Prime cells.

3.1.17 Software

Software	Manufacturer
CellProfiler v4.2.1	Broad Institute
Citavi v6.12.0.0	Swiss Academic Software
FACSDiva v9.0.1	BD Biosciences
FlowJo v10.7.1	BD Biosciences
ImageJ (Fiji distribution)	[153]
Image Lab v6.0.1.34	Bio-Rad
Inkscape v1.2.0	The Inkscape Project
LabImage1D	Intas
LAS X v3.5.19976.5	Leica Microsystems
Mars v4.01 R2	BMG Labtech
Office package v2016 and v2019	Microsoft
Prism v9.2.0.332	GraphPad Software Inc.
R v4.2.1	R Foundation
SnapGene v6.0	GSL Biotech LLC
ZenBlue v1.1.1	Carl Zeiss Microscopy

3.2 Methods

3.2.1 Cell culture

All cell culture methods were conducted under sterile conditions under a laminar flow workbench using sterile consumables and autoclaved or sterile filtered buffers, media, and reagents. Primary human cells and human cell lines were incubated at 37 °C, 5 % CO_2. Centrifugation steps were performed at 143 g for 8 min at room temperature for primary human cells and primary murine cells and 100 g for 10 min at room temperature for human cell lines. All used *L. major* strains were incubated at 27 °C, 5 % CO_2 in promastigote form and at 33 °C, 5 % CO_2 in amastigote form. Centrifugation steps for all parasite strains were performed at 2400 g for 8 min at room temperature, irrespective of the life cycle stage of the parasite. All deviations from these experimental conditions are specifically indicated in the method descriptions.

3.2.1.1 Coating of cell culture consumables

Since BLaER1 cells are not as adherent as primary human macrophages, all experiments with transdifferentiated BLaER1 (tdBLaER1) cells were performed in cell culture consumables coated with either poly-D-lysine (PDL) or poly-L-ornithine (PLO) to minimize cell loss. This does not apply for the experiments shown in figure 10, 11 and 13-16 as these experiments were performed before this improvement was implemented.

Coating with PDL was performed by incubating each well of the respective consumable with 0.05 mg/ml PDL solution at room temperature for 1 h followed by three washing steps with PBS (pH 7.1). Coating with PLO was performed by incubating each well of the respective consumable with 0.05 mg/ml PLO solution at 37 °C, 5 % CO_2 for 2 h followed by three washing steps with aqua bidest. The volumes of coating and washing solution for each consumable are listed in **Table 2**.

Table 2: Summary of coating and washing volumes used for different tissue culture consumables.

consumable	coating volume [µl]	washing volume [µl]
96-well plate	50	100
12-well plate	550	1,000
12-well chamber slide	240	300
8-well chamber slide	300	300

3.2.1.2 Cell counting

Undifferentiated, transdifferentiated BLaER1 cells, murine bone-marrow cells and bone-marrow-derived macrophages were stained with Trypan blue to exclude dead cells and subsequently, counted in a Neubauer counting chamber with a depth of 0.1 mm. Four large squares of the counting chamber were counted and the cell density was calculated as follows:

$$\frac{cells}{ml} = \frac{sum\ of\ counted\ cells}{4} * dilution\ factor * 10^4 \tag{1}$$

Alternatively, BLaER1 cells were counted by flow cytometry using a high-throughput sampler (HTS). For this, 10 µl of cell suspension were transferred to a 96-well U bottom plate and adjusted to a volume of 100 µl with MACS buffer. Then, 30 µl of each sample were acquired at a flow rate of 1 µl/s. After quality control gating (see 3.2.4.2) the number of viable cells was calculated as follows:

$$\frac{viable\ cells}{ml} = \frac{sum\ of\ counted\ cells}{30\ \mu l} * 1000\ \mu l * 10 \tag{2}$$

Peripheral blood mononuclear cells (PBMCs), monocytes and primary monocyte-derived macrophages were counted using a CASY cell counter TT with a 150 µm capillary. For this, 10 ml of CASYton buffer were transferred to a CASY tube and mixed with 10 µl of cell suspension (dilution factor: 1,000). The cell suspension was measured in triplicate and cell density and size were determined based on electrical impedance of the cell. Cell viability and cell aggregation of were automatically calculated based on program-specific cell sizes and size distributions. The automatic consideration of cell aggregation was manually reversed by dividing the viable cell density by the aggregation factor.

L. major parasites, irrespective of life cycle stage, were counted in an improved Neubauer counting chamber with a depth of 0.02 mm. Viable and dead parasites were distinguished based on cell morphology and motility. Viable cells display an elongated cell body and visible flagellar beating, whereas dead parasites show a small round cell body and no flagellar beating. Two small squares of each of the four large squares was counted and the cell density was calculated as follows:

$$\frac{parasites}{ml} = \frac{sum\ of\ counted\ parasites_{viable+dead}}{8} * 16 * dilution\ factor * 5 * 10^4 \qquad (3)$$

3.2.1.3 BLaER1 cells

To improve the readability of this section, BLaER1 cells and BLaER1 knockout cell lines are summarized as BLaER1. All experimental procedures described for BLaER1 cells, were performed identically for all BLaER1 knockout cell lines unless indicated otherwise.

BLaER1 cells were cultivated in T-75 flasks in 20 ml of BLaER1 medium (BM) and split two to three times per week to maintain a cell density of $1*10^5$-$4*10^6$ cells/ml. For this, the entire cell suspension was harvested and transferred to a fresh 50 ml falcon tube. Cells were counted, spun down and re-suspended in fresh BM. Cells were seeded into T-75 flasks for further cultivation or used for transdifferentiation. Because a subset of BLaER1 cells adheres to the flask bottom over time, the T-75 flask was replaced every three passages.

3.2.1.3.1 Freezing and thawing of BLaER1 cells

To generate cryo-stocks of BLaER1 cells, cells from low passages were spun down, re-suspended BM supplemented with 20 % FCS and 10 % DMSO at densities of 2-$6*10^6$ cells/ml and transferred to freezing tubes. Cells were subsequently, frozen in a - 80 °C freezer using a Mr. Frosty freezing container for 24 h. Afterwards, cells were stored in liquid nitrogen until use.

BLaER1 cell lines were not used beyond passage 28 and instead, a fresh aliquot of the respective cell line from a low passage was thawed. For this, the cells were removed from the liquid nitrogen and quickly thawed in a 37 °C water bath. Cells were transferred to a 50 ml falcon tube and 19 ml of medium were carefully added over the course of 3 min to lower the DMSO concentration without cell rupture. Cells were spun down, re-suspended in 5 ml of fresh BM and seeded into a T-25 flask. After two to five days of expansion, the cell suspension was transferred to a T-75 flask and the volume was adjusted to 20 ml with fresh BM.

3.2.1.4 Transdifferentiation

For transdifferentiation in 6-well plates, BLaER1 cells were adjusted to a density of $3.33*10^5$ cells per ml with BM and, subsequently supplemented with 10 ng/ml rhIL-3, 10 ng/ml M-CSF and 200 nM β-estradiol. 3 ml of cell suspension per well were seeded into a 6-well plate and incubated for seven days. At day two and day five, 1.5 ml of supernatant were carefully aspirated from each well and 1.5 ml of fresh BM supplemented with 10 ng/ml rhIL-3, 10 ng/ml M-CSF and 200 nM β-estradiol (tdBM) were added. At day seven, the supernatant was discarded and 1 ml of fresh BM was added to each well. Cells were detached by pipetting up and down with a 1,000 μl automatic pipette, transferred to a conical tube and counted. For the analysis of the influence of M-CSF differentiation on the cytokine production of transdifferentiated BLaER1 cells, BLaER1 cells were transdifferentiated as described above, but with 20 ng/ml GM-CSF instead of 10 ng/ml M-CSF.

For transdifferentiation in 96-well plates, BLaER1 cells were adjusted to a density of $5*10^5$ cells per ml with BM and, subsequently supplemented with 10 ng/ml rhIL-3, 10 ng/ml M-CSF and 400 nM β-estradiol. 100 μl of cell suspension per well were seeded into a PLO-coated 96-well plate and incubated for seven days. At day two and day five, the supernatant was discarded from each well and 100 μl of fresh BM supplemented with 10 ng/ml rhIL-3, 10 ng/ml M-CSF and 400 nM β-estradiol were added. At day seven, cells in three non-edge wells were detached by pipetting up and down with a 1000 μl automatic pipette, pooled in a micro-reaction tube and counted to determine the number of transdifferentiated BLaER1 (tdBLaER1) cells per well.

For experiments in which the NO concentration of supernatants was measured, BLaER1 cells were transdifferentiated in BLaER1 DMEM medium (BM-DMEM) by (I): Spinning down the cells, and re-suspending them in BM-DMEM supplemented with transdifferentiation cytokines (tdBM-DMEM) and only using BM-DMEM medium thereafter, (II): Using tdBM-DMEM for the second medium change and only using BM-DMEM medium thereafter, or (III): Discard tdBM after transdifferentiation and perform cell harvest in BM-DMEM medium.

Transdifferentiation efficiency of BLaER1 cell lines was regularly tested by flow cytometric analysis of CD19, CD11b and CD14 expression (see 3.2.4.2) as described in [99].

3.2.1.5 PBMC isolation from buffy coat

Peripheral blood mononuclear cells (PBMCs) were isolated from buffy coats of healthy donors (obtained from German Red Cross blood donation service, Frankfurt am Main) by density gradient centrifugation. For this, blood cell concentrated was adjusted with PBS to a volume of 100 ml, and each 25 ml of diluted buffy coat were carefully layered on top 15 ml of leukocyte separation medium in a 50 ml falcon tube. Samples were centrifuged at 1057 *g* for 30 minutes at room temperature, with reduced acceleration and deceleration. After centrifugation, the interphase was carefully aspirated and washed once with washing buffer. Cells were then spun down and residual erythrocytes re-suspended in 0.15 M ammonium chloride solution to lyse residual erythrocytes. After 10 minutes, lysis was stopped by addition of 40 ml washing buffer. Cells were spun down, re-suspended in complete medium (CM) and counted.

3.2.1.6 Isolation of monocytes from PBMCs

Monocytes were isolated from PBMCs by adherence to tissue cultured plastic surfaces. $1.5*10^8$ PBMCs were seeded into a T-75 flask and the volume adjusted to 20 ml with CM supplemented with 1 % heat-inactivated human serum. After 1 hour of incubation, the supernatant was discarded to separate the non-adherent fraction of the PBMCs from the adherent monocytes.

3.2.1.7 Monocyte differentiation to macrophages

Monocytes were differentiated to macrophages by adding 20 ml of fresh CM supplemented with either 30 ng/ml GM-CSF or 45 ng/ml of M-CSF to generate GM-CSF-derived or M-CSF-derived macrophages, respectively. After seven days of incubation the medium replaced with 10 ml of fresh CM. Afterwards, macrophages were harvested by incubating flasks on ice for 30 minutes to loosen their adherence to the plastic and, then, detached using a cell scraper. The cell suspension was transferred to a conical tube and the macrophages were counted.

3.2.1.8 Differentiation of bone-marrow cells to bone-marrow-derived macrophages

For differentiation to bone-marrow-derived macrophages, $3.61*10^7$ Bone-marrow cells were seeded into a T-75 flask in 15 ml BM supplemented with an additional 10 % of FCS and 40 ng/ml of M-CSF. After two days of incubation, 7 ml of the medium were transferred to a conical tube and centrifuged to precipitate any non-adherent or weakly adherent cells. The supernatant was discarded, the cells were re-suspended in 7 ml of fresh BM supplemented with additional 10 % of FCS and 40 ng/ml of M-

CSF and transferred back to the T-75 flask. After five days of incubation, 10 ml of medium were replaced with 10 ml of fresh BM supplemented with additional 10 % of FCS and 40 ng/ml of M-CSF. After seven days of incubation the medium replaced with 10 ml of fresh CM. After seven days of incubation, differentiated bone-marrow-derived macrophages were harvested as described for primary human macrophages, counted, and seeded into 6-well plates at a density of $3.5*10^6$ cells per well.

3.2.1.9 Preparation of blood agar plates

Autoclaved brain heart infusion agar stock solution was cooled to approx. 55 °C and mixed with PBS preheated to 42 °C in a sterile petri dish with constant stirring by a magnet stirrer. Defibrinated rabbit blood was preheated to 37 °C and added to the mixture of brain heart infusion agar and PBS once it cooled down to approx. 45 °C. After addition of penicillin/streptomycin solution, the resulting Novy-MacNeal-Nicolle (NNN) blood agar was transferred to 96-well plates, by pipetting 50 μl into each well in a 45 ° angle with an automatic multichannel pipette. Plates were sealed in autoclave bags and stored at 4 °C until use.

3.2.1.10 Leishmania culture

L. major wild type promastigotes were cultured in a bi-phasic system comprised of a liquid phase of leishmania medium (LM) and a solid phase NNN blood agar. Parasites were grown in 100 μl LM per well in 96-well blood agar plates. After seven to eight days of incubation, stationary-phase parasites were harvested, counted, and re-seeded into a fresh blood agar plate at a cell density of $1*10^6$/ml. *L. major* strains expressing a fluorescent protein, a T7 RNA polymerase-Cas9 construct or with knocked out genes were cultured in LM supplemented with antibiotics as described in section 3.1.14.

3.2.1.11 Generation of axenic amastigotes

Cell suspension from 16 wells of logarithmic-phase (day three to four) *L. major* promastigote culture was transferred to a T-75 flask, adjusted to a volume of 20 ml with liquid medium and supplemented with an additional 10 % FCS. Genetically modified *L. major* strains were supplemented with their respective antibiotic during this step. Parasites were incubated for three days, spun down and washed in amastigote medium (AAM) three times, finally, re-suspended in 10 ml of AAM. Parasites were counted, adjusted to a cell density of $2-5*10^7$/ml, and seeded into a 24-well plate. After incubation for 7-14 days at 32 °C, the successful transformation of promastigotes to axenic amastigotes was visually

confirmed at an inverse light microscope. The supernatant was discarded to remove dead parasites and residual promastigotes and 1 ml of AAM was added to each well. Afterwards, axenic amastigotes were detached from the well bottom by pipetting up and down with a 1,000 µl pipette, transferred to a falcon tube and counted. If the share of residual promastigotes was smaller than 10 %, axenic amastigotes were used for experimentation.

3.2.1.11.1 Freezing and thawing of Leishmania

To generate cryo-stocks of all used *L. major* strains, axenic promastigotes were spun down, re-suspended in LM, counted, and adjusted to a cell density of $1*10^6$/ml. Axenic amastigotes were subsequently, seeded into a 96-well NNN blood agar plate and incubated as described for the cultivation of promastigotes. After seven days of incubation, transformation of axenic amastigotes to promastigotes was confirmed visually at an inverse light microscope and the entire parasite suspension, termed P-A-P, was harvested and counted. Parasites were spun down, re-suspended in LM supplemented with 40 % FCS and 10 % DMSO at densities of $1-5*10^7$ cells/ml and transferred to freezing tubes. Parasites were, subsequently, frozen in a - 80 °C freezer using a Mr. Frosty freezing container for 24 h. Afterwards, cryo-stocks were stored in liquid nitrogen until use.

L. major promastigotes were discarded after eight passages in NNN blood agar plates and a fresh P-A-P aliquot of the respective strain was thawed. For this, the parasites were removed from the liquid nitrogen and quickly thawed in a 37 °C water bath. Parasites were transferred to a 50 ml falcon tube and 19 ml of medium were carefully added over the course of 3 min to lower the DMSO concentration without cell rupture. Parasites were spun down, re-suspended in 5 ml of fresh LM and seeded into a 96-well NNN blood agar plate. *L. major* strains expressing a fluorescent protein, a T7 RNA polymerase-Cas9 construct or with knocked out genes were cultured in LM supplemented with antibiotics as described in section 3.1.14.

3.2.2 Infection experiments and cell labeling

All infections of hMDMs or tdBLaER1 cells were performed for 3 h at 37 °C, 5 % CO_2, if not stated otherwise. All incubations were done at 37 °C, 5 % CO_2 for the indicated time period unless stated otherwise.

For the acquisition of z-stack by confocal immunofluorescence microscopy $2*10^5$ tdBLaER1 cells, GM-CSF-derived macrophages and M-CSF-derived macrophages were seeded into a 12-well chamber slide with removable gasket. Cells were incubated for 1 h at 37 °C, 5 % CO_2 to allow adhesion. Meanwhile, stationary-phase *L. major* wild type promastigotes were harvested and counted. The supernatant was discarded and cells were infected at a multiplicity of infection (MOI) of 10. Extracellular parasites were removed by washing twice with PBS. Infected cells were either stained directly or further incubated for up to 96 h at 37 °C, 5 % CO_2. For all other immunofluorescence microscopic experiments, $1.5\text{-}2*10^5$ tdBLaER1 cells per well were seeded into PDL-coated 8-well chamber slides, but otherwise treated as described above. The MOI was reduced to 5 for live cell imaging.

For the determination of infection rate and parasite burden by flow cytometry $5*10^5$ tdBLaER1 cells, GM-CSF-derived macrophages and M-CSF-derived macrophages were seeded into a 12-well plate. Cells were incubated for 1 h at 37 °C, 5 % CO_2 to allow adhesion. Meanwhile, stationary-phase *L. major* and *L. major DsRed* promastigotes were harvested and counted and labeled with AlexaFluor647-NHS ester (see 3.2.2.1). The supernatant of the tdBLaER1 cells, GM-CSF-derived macrophages and M-CSF-derived macrophages was discarded and cells were infected at a MOI of 10. Extracellular parasites were removed by washing twice with BM. Afterwards, cells were either harvested directly for analysis or further incubated at 37 °C, 5 % CO_2 for up to 96 h.

For all other flow cytometric experiments $1*10^5$ tdBLaER1 cells or hMDMs per well were seeded into PDL coated 96-well plates and incubated for 1 h to allow cell adhesion. Stationary-phase *L. major* and *L. major* DsRed*, L. major* T7/Cas9 DsRed or *L. major* T7/Cas9 DsRed LPG1$^{-/-}$ promastigotes were harvested and counted. In experiments, which included the measurement of ROS production, *L. major* parasites were additionally labeled with AlexaFluor405-NHS ester. TdBLaER1 cells were infected at a MOI of 10 and parasites were centrifuged onto the cell layer at 339 *g* for 4 min to synchronize the infection. After incubation, extracellular parasites were removed by washing twice with BM. Afterwards, cells were either harvested directly for analysis or further incubated at 37 °C, 5 % CO_2 for up to 96 h.

For the determination of the parasite burden of tdBLaER1 cells by high-throughput microscopy (HTM), *L. major* parasites were labeled with CFSE and infection time was reduced to 2 h. TdBLaER1 cells were counterstained with wheat germ agglutinin (WGA)-CF568.

For the determination of TNF-α and IL-10 secretion, $1*10^5$ tdBLaER1 cells GM-CSF-derived macrophages or M-CSF-derived macrophages were seeded into a 96-well plate. Cells were incubated at 37 °C, 5 % CO_2 to allow adhesion. Logarithmic- or stationary-phase *L. major* promastigotes were harvested and counted. The supernatant was discarded and cells were infected at a MOI of 5. Supernatants were collected at 24 h post infection and transferred to a fresh 96-well V-bottom plate. Supernatants were stored at -80 °C until analysis.

For gene expression experiments, $1*10^6$ tdBLaER1 cells, GM-CSF-derived macrophages and M-CSF-derived macrophages were seeded into a micro-reaction tube. Logarithmic- and stationary-phase *L. major* promastigotes were harvested and counted. Cells were pelleted by centrifugation of the micro-reaction tube at 500 *g* for 5 min. The supernatant was discarded and cells were taken up in fresh BM (uninfected control), parasite suspension (log. - and stat.-phase) at a MOI of 10 or BM containing 100 ng/ml LPS (positive control). Extracellular parasites were removed by washing twice. For this, cells were spun down and re-suspended in BM. After 24 h, RNA was isolated as described below.

For co-incubation experiments by high throughput microscopy, tdBLaER1 cells and tdBLaER1 *GSDMD*^{-/-} cells were transdifferentiated in PLO-coated 96-well plates and labeled with CFMDA (see 3.2.2.2) prior to infection. Afterwards, cells were infected with stationary-phase *L. major* DsRed promastigotes at an MOI of 5 or axenic *L. major* DsRed amastigotes at a MOI of 2 as described for flow cytometric experiments. Cells were washed twice with BM to remove extracellular parasites and incubated overnight. Fresh tdBLaER1 *GSDMD*^{-/-} cells were harvested from a 6-well plate, labeled with CellTracker DeepRed, and adjusted to a cell density of $1*10^6$ cells/ml. The supernatant of tdBLaER1 cells was discarded and co-incubation with tdBLaER1 *GSDMD*^{-/-} cells was started by addition of 100 µl of cell suspension to each well. After 1 h of co-incubation, pyroptosis was induced as described in 3.2.3.2. For co-incubation experiments by flow cytometry $0.25*10^6$ tdBLaER1 *eGFP*^{-/-} and tdBLaER1 *GSDMD*^{-/-} x *eGFP*^{-/-} were seeded into PDL-coated 12 well plates and infected by stationary-phase *L. major* DsRed at an MOI of 5 or by axenic *L. major* DsRed amastigotes at an MOI of 2. Extracellular parasites were washed off by an exchange of BM and addition of fresh medium. After 1 h of incubation, uninfected tdBLaER1 *GSDMD*^{-/-} were harvested from a 6-well plate and $0.25*10^6$ cells per well were added to the infected samples. After 18 h of co-incubation, pyroptosis was induced as described in 3.2.3.2.

62

The infection conditions of all experiments are summarized in **Table *3***. The table includes fluorescent labelling of parasites and cells with NHS esters, but not other stainings performed downstream of the infection but prior to analysis.

Table 3: Summary of experimental conditions of infection experiments.

Summary of infection experiments described in section 3.2.2. The table lists the different experiments performed with infected cells, the figures they appear in, and an array of the most important parameters of infection experiments with Leishmania, which were varied between experiments.

experiment	figures	seeded cells	well format	MOI	time of infection	parasite strain[††]	fluorescent labeling	wash steps
z-stacks by confocal fluorescence microscopy	10, 11	$2*10^5$	12-well chamber slide	10	3 h	wt	-	2
parasite burden by HTM	12	$1*10^5$	96-well	10	2 h	wt	CFSE	2
infection rate and parasite burden by flow cytometry (12 well)	13, 14	$5*10^5$	12-well	10	3 h	DsRed	AF647	2
gene expression	15	$1*10^6$	1.5 ml micro-reaction tube	5	3 h	wt	-	2
cytokine response	16	$1*10^5$	96-well	5	3 h	wt	-	0
infection rate and parasite burden (96 well)	17, 18, 24, 28-30, 32-36	$1*10^5$	96-well	10	3 h	DsRed, T7/Cas9, DsRed T7/Cas9 LPG1$^{-/-}$	-	2
ROS production by flow cytometry[†]	20-22, 31	$1*10^5$	96-well	10	3 h	wt	AF405	2
fluorescence microscopy	19, 39	$1.5-2.0*10^5$	8-well chamber slide	5, 10	3 h	DsRed	-	2
Co-incubation assays (HTM)	42, 43, 45	$1*10^5$	96-well	5 (PRO), 2 (AMA)	3 h	DsRed	CMFDA (cells), CellTracker DR (cells)	2
Co-incubation assays (flow cytometry)	47	$2.5*10^5$	12-well	5 (PRO), 2 (AMA)	3 h	DsRed	-	2

[†]Some experiments contained multiple readouts, thus, some figures are listed multiple times.

[††] All parasites are *L. major* strains, hence, only the genetic modification or lack thereof (wt) was specified

3.2.2.1 Labeling of parasites with succinimidyl ester dyes

Up to $1*10^8$ parasites at a time were labeled with Alexa-Fluor647/405-NHS ester of CFSE. For this, parasites were spun down at and re-suspended in 6 ml the respective dye diluted in PBS. Parasites were incubated for 10 min at 27 °C, 5 % CO_2. Afterwards, the volume was adjusted to 12 ml with PBS and the parasites were spun down. Labeled parasites were re-suspended in BM or CM and used for infection experiments.

3.2.2.2 Labeling of cells with succinimidyl ester dyes

TdBLaER1 cells were labeled with CMFDA directly in the 96-well plate. For this the supernatant was discarded and 100 µl of CMFDA diluted in PBS was added to each well. Cells were incubated for 10 min and the dye was subsequently discarded. Residual dye was quenched by addition of 100 µl of fresh BM to each well.

Labeling of tdBLaER1 cells with Cell Tracker DeepRed was performed in a 15 ml falcon tube. Cells were spun down, re-suspended in 6 ml Cell Tracker DeepRed diluted in PBS and incubated for 10 min. Afterwards, the volume was adjusted to 12 ml with PBS cells were spun down and re-suspended in fresh BM to quench residual dye.

3.2.3 Stimulation with immunomodulators, induction of pyroptosis and NO treatment

3.3.3.1 Priming of the NLRP3 inflammasome

In experiments that measured the activation of the NLRP3 inflammasome by IL-1β secretion, cells were transcriptionally primed by stimulation with 200 ng/ml LPS or 500 nM R848 for 15 h prior to infection. If the production of ROS was analyzed concomitantly with NLRP3 inflammasome activation, control cells were additionally treated with ROS inhibitors apocynin, diphenylene iodonium chloride (DPI) or NOX VII for 1 h in between of priming and infection.

3.2.3.2 Pyroptotic cell death

In all experiments that analyzed the susceptibility of tdBLaER1 cells to pyroptosis by flow cytometry, or measured the effect of pyroptotic cell death on parasite release and secondary infection rate by HTM or flow cytometry, pyroptosis was induced by transcriptional priming with 200 ng/ml LPS for 3 h

45 min followed by activation of the NLRP3 inflammasome by treatment with 4 µM nigericin for up to 8 h.

To determine the activation of the NLRP3 inflammasome by live cell fluorescence microscopy, or flow cytometry tdBLaER1 cells were stimulated with 500 ng/ml LPS followed by activation of the NLRP3 inflammasome by addition of 20 µM nigericin. Negative control samples were additionally treated with 50 µM of pan-caspase inhibitor Z-VAD for 1 h prior to NLRP3 inflammasome activation.

3.2.3.3 NO treatment

To investigate the role of NO as an effector mechanism, tdBLaER1 cells were treated with 10 µM, 20 µM, 40 µM or 80 µM of the NO-generating compounds DEA-NONOate, SNI-1 or SNAP. All stocks were prepared in DMSO since compounds release NO in watery solutions. To minimize the addition of DMSO to the cells, stocks were prepared at a concentration of 100x of the final concentration. Compounds were added up to four times to the cells, the first addition was performed immediately after the extracellular parasites were washed off (1x NO), the second addition was done 18.5 h post infection (2x NO), the third addition was performed at 42.5 h post infection (3x NO) and the final addition was done at 66.5 h post infection (4x NO).

3.2.3.4 Pro-inflammatory stimulation of human and murine cells

To investigate the effect of pro-inflammatory activation on the restriction of intracellular parasites, BLaER1 cells or GM-BLaER1 cells were treated with either a combination of LPS (200 ng/ml) and IFN-γ (50 ng/ml) or IFN-γ (50 ng/ml) alone for 24 h prior to infection.

To generate a positive control for the determination of iNOS expression by qRT-PCR, murine bone-marrow-derived macrophages were treated with combination of LPS (500 ng/ml) and IFN-γ (50 ng/ml) for 24 h prior to cell harvest and subsequent RNA isolation.

3.2.4 Analysis methods

3.2.4.1 Microscopy

3.2.4.1.1 Confocal fluorescence microscopy

To confirm the presence of intracellular parasites, infected cells in 12-well chamber slides, were fixed with 4 % PFA for 10 min at room temperature and, then, washed twice with PBS. Afterwards, cells were permeabilized with permeabilization buffer for 15 min at room temperature and washed twice with PBS. Next, unspecific protein binding sites were blocked with blocking buffer for 30 min at room temperature. The blocking buffer was discarded and cells were stained with rabbit anti-Lm serum in antibody staining buffer for 30 min at room temperature. Cells were washed twice with PBS and incubated with secondary antibody mix (antibody staining buffer containing DAPI, phalloidin-AlexaFluor488, chicken anti-rabbit-AlexaFluor647) for 30 min at room temperature. Cells were washed twice with PBS and the supernatant was discarded. The removable gasket was removed and the chamber slide left to dry in the dark at room temperature until the residual PBS was dried. Cells were mounted with 50 µl Mowiol and a coverslip was placed on top of the mounting medium. After the Mowiol had dried, the coverslip edges were sealed with nail polish. Samples were stored at 4 °C in the dark until analysis. Confocal fluorescence microscopy was performed using a Leica SP8 confocal microscope at a 63x magnification. The height of the z-dimension was manually determined by shifting the focus plane up and down until no fluorescent signal was visible anymore. The number of z-planes was subsequently calculated by dividing the height of the z-dimension by the pixel size of the image to achieve a xyz-image stack with square voxels. The z-stacks were analyzed using the ImageJ software and the "Volume Viewer" plug in. First, z-stacks were scaled and converted to a composite image. Then, a maximum projection was generated of every image-stack using the z-project command. Then, stacks were loaded into the volume viewer plugin and infected cells were examined in the yz-plane for parasites, which were surrounded by cytoskeleton staining and. Images of these yz-planes were saved in as a new image file. Maximum projections were annotated with a scale bar and saved.

3.2.4.1.2 Live cell imaging

Caspase-1 activity and the pyroptosis-dependent release of parasites from their host cell were analyzed by live-microscopy. Live-cell imaging was performed employing a Zeiss Live-7 confocal microscope using a 40x magnification.

For the determination of caspase-1 activity, cells were stained with FLICA 660 caspase-1 assay kit according to the manufacturer's instructions. In brief, FLICA working solution was added to the cells at a final dilution of 1:60 at 1 h before the experimental endpoint. Cells were washed thrice with cellular wash buffer (supplied), the supernatant was discarded, and 200 µl of fresh BM were added to each well. Cells were imaged immediately.

For the pyroptosis-dependent parasite release, samples were pre-warmed to 37 °C in the incubation chamber of the live-cell microscope, which was adjusted to 37 °C, 5 % CO_2. Then, cells were primed with LPS for 3 h 45 min. The priming step was imaged to control the maintenance of the focus plain over time and during position changes. If necessary, these settings were adjusted immediately after induction of pyroptotic cell death. After addition of nigericin, cells were imaged for up to 8 h in 2.5-minute intervals. Videos were important as xyzct-stack to Fiji and exit events manually counted and annotated.

3.2.4.1.3 High throughput microscopy

For quantitative microscopic analyses with high sample sizes, infected cells were imaged in an Operetta high-throughput microplate imager. Raw image files were imported into the CellProfiler software and analyzed with experiment-specific image analysis pipelines (explained in experiment subsection; Illustration and example images in (**Figure 41**). Afterwards, parameters of interest were extracted from the output spreadsheets and relevant indices, like infection rate or parasite burden, were calculated using R. Tidied data and calculated indices were exported as excel files and loaded into GraphPad Prism for statistical analysis.

3.2.4.1.3.1 Parasite burden

Since both parasites and host cells were fluorescently labeled with NHS esters prior to infection and fixation, no additional staining was required for this experiment. Therefore, cells were fixed for 10 min at room temperature with 4 % PFA, washed twice with PBS and finally 100 µl of PBS per well were added to the fixed cell layer for analysis. Four wells per experimental condition and 25 spots per well were imaged. The image analysis started with smoothing of WGA-CF568 signal using the "Smooth" module and a median filter, followed by identification of the individual cells by the "IdentifyPrimaryObject" module. Next, CFSE signal of the parasites was enhanced using the "EnhanceOrSuppressFeatures" module treating *Leishmania* as speckles, followed by identification of

parasites by the "IdentifyPrimaryObject" module. Intracellular parasites were identified by relating parasites and cells with "RelateObjects", creating the subset "intracellular parasites" as child object of cells. Then, infected cells were identified by filtering cells by a minimum child object count of 1, using "FilterObjects". Finally, measurements were exported as spreadsheets using the "ExportToSpreadsheet" module and RGB images overlayed with object outlines were exported using the modules "GrayToColor", "OverlayOutlines" and "SaveImages".

3.2.4.1.3.2 Number of extracellular parasites

To determine the role of pyroptosis as a mechanism of parasite release from its host cell, the number of extracellular parasites after pyroptosis induction was analyzed by fluorescent microscopy. Cells were fixed with 4 % PFA for 10 min at room temperature and, then, washed twice with PBS. Afterwards, cells were permeabilized with permeabilization buffer for 15 min at room temperature and washed twice with PBS. Next, unspecific protein binding sites were blocked with blocking buffer for 30 min at room temperature. The blocking buffer was discarded and cells were stained with mouse anti-Lm serum in antibody staining buffer for 30 min at room temperature. Cells were washed twice with PBS and incubated with secondary antibody mix (antibody staining buffer containing DAPI, anti-mouse-AlexaFluor568) for 30 min at room temperature. Cells were washed twice with PBS and the supernatant was discarded. Finally, the cell layer was overlayed with 200 µl of PBS for imaging. One well per experimental condition and 80 spots per well were imaged. For image analysis, the nuclei of cells based on the DAPI signal were identified using "IdentifyPrimaryObject" module. Next, individual cells were seeded from the nuclei using "IdentifySecondaryObject" module. Signal enhancement, parasite identification and determination of intracellular parasites and infected cells was done as described for 3.2.4.1.3.1. Then, identified parasites were masked using the "intracellular parasite" subset and the remaining parasites were considered to be extracellular and termed "extracellular parasites". Finally, measurements were exported as spreadsheets using the "ExportToSpreadsheet" module and RGB images overlayed with object outlines were exported using the modules "GrayToColor", "OverlayOutlines" and "SaveImages".

3.2.4.1.3.3 Co-incubation

To determine the role of pyroptosis as a mechanism of parasite spread to new host cells, the secondary infection rate in a co-incubation assay after pyroptosis induction was analyzed by fluorescent microscopy. Staining was performed as described for 3.2.4.1.3.2, but DAPI was not included in the secondary antibody mix. One well per experimental condition and 80 spots per well were imaged. The

images analysis was mostly performed as described for 3.2.4.1.3.2. Divergently, the primary infected cells (CMFDA-labeled) and the co-incubated cells (Cell Tracker Deep Red) were identified in two separate "IdentifyPrimaryObject" modules. Furthermore, the parasite subset from the penultimate step was not termed "extracellular parasites, but "residual parasites" and used for the identification of secondary infected cells using the "RelateObjects" and "FilterObjects" modules. Finally, overlayed RGB images and results in spreadsheet format were exported as described above.

3.2.4.2 Flow cytometry

Immunophenotype, infection rate, parasite burden, caspase-1 activity and production of ROS of hMDMs and BLaER1 cells were determined by flow cytometry. All centrifugation steps during flow cytometric sample preparation were performed at 339 g, 4 min at 4 °C and all incubation steps were done at 4 °C in the dark. For immunophenotyping and all experiments involving an extracellular antibody staining, cells were detached by pipetting up and down (tdBLaER1 cells) or by scraping of the cells after incubation on ice for 30 min (hMDMs) For all other experiments cells were detached by trypsinizing with pre-warmed trypsin-EDTA (0.025 %) for up to 10 min at 37 °C, 5 % CO_2. Trypsinizing was stopped by addition of the threefold volume of BM or CM. Irrespective of harvesting method, cells were transferred to a 96-well V-bottom plate, spun down and re-suspended in MACS buffer. If the sample volume was too large for an immediate transfer to a 96-well V-bottom plate, samples were transferred to a 1.5 ml micro-reaction tube instead, spun down, re-suspended in MACS buffer and, then, transferred to a 96-well V-bottom plate. For the assessment of infection rate and parasite burden, without additional stainings, no further sample preparation was required and cells were directly analyzed at this point. For additional extracellular antibody staining, cells were spun down and blocked for 30 min in blocking buffer. Next, cells were spun down and re-suspended in antibody staining solution with antibodies against surface protein of interest. Antibody staining solution was prepared in staining buffer for all experiments in which eGFP expression of BLaER1 cells was used as viability marker, or were prepared in PBS containing the viability dye Zombie aqua for all experiments with hMDMs or BLaER1 eGFP$^{-/-}$ strains that required a viability staining. Cells were incubated for 30 min, spun down and washed twice with MACS buffer. If cells were not analyzed immediately, they were fixed with 4 % PFA for 10 min, washed once with MACS buffer, spun down and re-suspended in MACS buffer. Cells were stored at 4 °C, dark until analysis.

3.2.4.2.2 Caspase-1 activity

Flow cytometry analysis of caspase-1 activity, cells were treated with FLICA 660 caspase-1 assay kit according to the manufacturer's instructions as described in 3.2.3.1.2. Divergently, cells were re-suspended in MACS buffer for flow cytometric analysis as a last preparation step.

3.2.4.2.3 ROS measurement

To quantify the production of ROS, tdBLaER1 cells were stained with DHE. For this, DHE working stocks were prepared in BM and added to the cells 30 min before the experimental endpoint i.e., cell harvest and sample preparation. Geometric mean fluorescence intensity values (MFIs) of viable cells were normalized between an untreated sample as negative control and a positive control treated with 1 mM menadione 1 h before the experimental endpoint. Normalization was performed for each independent experiment prior to statistical analysis.

3.2.4.3 Enzyme-linked immunosorbent assay (ELISA)

Supernatants of samples were transferred to a 96-well V-bottom plate, spun down at 2400 *g* for 8 min at room temperature to remove cell debris and residual parasites and transferred to a fresh 96-well plate. Supernatants were stored at -80 °C until analysis. For analysis, supernatants were thawed on ice and analyzed with human TNF-α, human IL-10, human IL-1β or human IL-12p70 kits according to the manufacturer's instructions. Concentrations were calculated based on a standard curve generated by performing a 4-parameter logistic regression (4PL) of the standard dilutions in Graphpad Prism (TNF-α and IL-10) or Mars (IL-1β and IL-12p70). Non-detected values were set to 0 to allow statistical testing.

3.2.4.4 Griess assay

Successful treatment with NO-generating compounds was validated by determination of NO concentrations of cell culture supernatants. Supernatants were collected, processed, and stored as described in 3.2.4.3. For analysis, samples were thawed on ice and NO concentrations were determined using the Nitric oxide (total) detection kit according to the manufacturer's instructions. Concentrations were calculated based on a standard curve generated by performing a 4PL in Mars.

3.2.5 Molecular biology methods

3.2.5.1 Generation of knockout cell lines using ribonucleotide-protein complexes

BLaER1 cells were split 1:10 two days prior to nucleofection to avoid cell stress caused by high cell densities and to improve viability throughout the knockout generation. After two days, BLaER1 cells were harvested, counted, spun down and re-suspended in freshly prepared, supplemented nucleofection solution (nucleofector solution + 18 % of supplement; from Lonza human B cell kit). Ribonucleotide-protein complexes (RNPs) were prepared in sterile, nuclease-free 200 µl micro-reaction tubes by mixing 3 µl of nuclease-free aqua bidest., 1 µl of sgRNA against target gene and 1 µl of 40 µM Cas9 NLS protein. Complexing of Cas9 NLS protein and sgRNA was achieved by incubation at 37 °C for 15 min in thermocycler. The resulting RNP solution was transferred into an electroporation cuvette (Lonza human B cell kit). Then, 100 µl of cell suspension were added to each cuvette, carefully mixed by flicking the cuvette and electroporated in a nucleofector using the program U-015 (human B cells). A mock nucleofection without RNPs, an RNP complexion control consisting of an sgRNA against eGFP and a nucleofection control consisting of 2.5 µg of CAGGS-RedStar plasmid were included in each experiment. After nucleofection, 400 µl of fresh BM were added to each cuvette and the sealed cuvettes were incubated for 10 min to allow cells to recover. Afterwards, cells were transferred to a 1.5 ml micro-reaction tube spun down at 500 g for 5 min at room temperature and re-suspended in 100 µl of fresh BM. For the cultivation of the nucleofected cell populations, 50 µl of fresh pre-warmed BM per well was added to a 96-well plate and each sample was distributed to two wells, resulting in a final volume of 100 µl per well.

After 24 hours of incubation, 20 µl of mock-nucleofected control and plasmid-nucleofected control were harvested, spun down and re-suspended in 200 µl of MACS buffer. Successful nucleofection was subsequently checked by flow cytometric analysis of RedStar expression using mock-transfected cells as a gating control. If an eGFP$^-$ BLaER1 cell line was used, eGFP was replaced as a viability marker by addition of 2 µg/ml of propidium iodide (PI) one minute before sample acquisition. After confirmation of the successful nucleofection, a limiting dilution was performed by harvesting one well per sample and transferring the cell suspension to a fresh 50 ml falcon tube. The volume was adjusted to 5 ml with BM, the cell suspension was counted and adjusted to a density of 5 cells/ml with BM. 100 µl of cell suspension per well were seeded in two to four 96-well plates per target (0.5 cells per well) and incubated for 21 days.

After six days of incubation, the successful complexion of the RNPs was validated by flow cytometric analysis of the eGFP knockout efficiency. For this, the RNP complexion control was harvested, spun down at 500 g for 5 min at room temperature and re-suspended in 200 µl of MACS buffer. Cells were analyzed by flow cytometry using BLaER1 eGFP$^{-/-}$ cells and BLaER1 cells as negative and positive gating control, respectively. To exclude dead cells, all samples were stained with 2 µg/ml PI one minute before sample acquisition. RNP complexion was deemed successful if a large share of cells from the complexion control shifted from the eGFP^{+} gate to either the eGFP^{-} gate or the eGFP^{int} i.e., the gate covering the relative fluorescence intensities in between the eGFP^{-} gate and the eGFP^{+} gate.

After 21 days of incubation, grown single clones were identified at an inverted microscope and counted by flow cytometry. Single clones were transdifferentiated in 96-well plates and, subsequently analyzed for the expression of the protein of interest by western blot.

3.2.5.2 Gibson Assembly

The LEXSY-DsRed-sat2.1 plasmid was generated by Gibson assembly from pLEXSY-sat2.1 backbone. To generate the vector fragment, pLEXSY-sat2.1 was digested with the restriction enzymes NheI and XbaI for 3 h at 37 °C followed by enzyme inactivation at 80 °C for 20 min. The digestion reaction was mixed in a 1.5 ml micro-reaction tube on ice as follows:

pLEXSY-sat2.1	15 µg
CutSmart buffer (10x)	5 µl
XbaI	1 µl (= 20 units)
NheI	1 µl (= 20 units)
H_2O	ad. 50 µl

The insert was generated by long primer PCR using primers with 40 bp 5'-overhangs homologous to the 5' and 3' regions of the vector. These primers were designed using the Gibson assembly tool of the SnapGene software. The PCR reaction was mixed on ice in 200 µl micro-reaction tubes as follows:

pSSU-DsRed	1 µl (= 15 ng)
PWO Master mix (2x)	10 µl
DsRed fwd	1 µl
DsRed rev	1 µl
H_2O	ad. 20 µl

PCR was performed in a thermocycler using the following program:

Step 1:	95 °C	3 min
Step 2:	95 °C	30 s
Step 3:	58 °C	30 s
Step 4:	72 °C	1 min 30 s

Repetition of steps 2-4 for 29 cycles

Step 5:	72 °C	10 min
Step 6:	4 °C	indefinite

Linearization of the plasmid and PCR of the insert were controlled by agarose gel electrophoresis of restriction digest and PCR reaction mix. Linearized vector and PCR product were used for Gibson assembly without purification. For this, the following reaction mix was prepared on ice and incubated for 1 h at 50 °C:

NEBuilder Hifi DNA assembly master mix (2x)	10 µl
restriction digest	1 µl (= 200 ng)
PCR reaction	2 µl
H_2O	ad. 20 µl

Gibson assembly reaction was stored at 4 °C until transformation.

3.2.5.3 Transformation

Chemically competent *E. coli* were thawed on ice for up to 20 min. Then, 50 µl of bacteria suspension were transferred to a fresh 1.5 ml micro-reaction vessel and 2 µl of Gibson assembly reaction were added. The bacteria suspension was carefully mixed by flicking the tube and incubated on ice for 20 min. Afterwards, heat shock was performed by incubation at 37 °C for 2 min followed by incubation on ice for another 2 min. Subsequently, 750 µl of pre-warmed SOC medium was added to the cells and the cells were incubated at 37 °C for 40 min. Afterwards, 10 µl, 100 µl or 300 µl of bacteria suspension were plated on a LB$_{Amp}$ agar plate under a laminar flow workbench. Plates were allowed to dry for up to 5 min, followed by incubation overnight at 37 °C.

3.2.5.4 Stable integration by homologous recombination

For stable integration of DsRed into the 18S-rRNA locus of *Leishmania* parasites, 15 µg of pLEXSY-DsRed-sat2.1 were digested with 3 µl SwaI (= 30 units) using NEB buffer 3.1 as described for Gibson assembly. Successful excision of the integrating fragment was checked by agarose gel electrophoresis and the reaction mix was subsequently sterilized in a thermocycler by incubation at 95 °C for 5 min and stored at 4 °C until use. $1*10^7$ logarithmic-phase *L. major* T7/Cas9 promastigotes were harvested, counted, spun down and re-suspended in Zimmerman buffer. Afterwards, cells were spun down and re-suspended in 200 µl of Zimmerman buffer and transferred to an electroporation cuvette. 16 µl of restriction digest (= 4.8 µg) were added to the cuvette. Afterwards, the parasite suspension was carefully mixed by flicking the cuvette and parasites were electroporated in a nucleofector using the program X-001. Parasites were transferred to a T-25 flask and 5 ml of fresh LM were added. Parasites were incubated overnight for recovery. Next, the parasite culture was supplemented with 10 % FCS and 100 µg/ml nourseothricin, seeded into a 96-well blood agar plate, and incubated for 21 days. After antibiotic selection, viable parasite populations were picked, counted, spun down and re-suspended in LM supplemented with 100 µg/ml nourseothricin at a density of $2*10^5$ parasites/ml. A limiting dilution was performed by transferring 100 µl of parasites suspension into the first column (well IDs A1-H1) of a fresh 96-well blood agar plate. One row was used for each parasite population. Next, 20 µl of parasite suspension were transferred to the second column (well IDs A2-H2) and the volume was adjusted to 100 µl with LM supplemented with 100 µg/ml nourseothricin, resulting in a fivefold dilution. This process was repeated across all remaining columns of the 96-well plate. Finally, the volume of all wells was adjusted to 100 µl with LM supplemented with 100 µg/ml nourseothricin. After another 21 days of incubation, viable parasites from wells, which mathematically contained a single or less parasites, were considered single clones and expanded.

Successful integration of the linearized plasmid fragment was confirmed by two PCRs, one with a forward primer binding the 5'UTR of the 18s-rRNA locus (SSU fwd) and a reverse primer binding the 3'-UTR of the 18s-rRNA locus (SSU rev), and another with a forward primer binding in coding sequence of the nourseothricin resistance gene SAT (SAT fwd) and a reverse primer binding the 3'-UTR of the 18s-rRNA locus (SSU rev) (**Figure 7**). Finally, expression of DsRed was confirmed on protein level by flow cytometric analysis of the parasites (**Figure 8**).
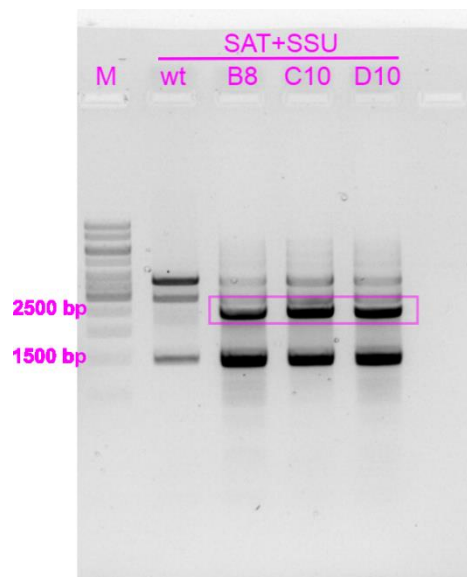
Figure 7: Confirmation of integration of DsRed into 18S-rRNA locus by PCR.
Integration of DsRed into 18S-rRNA locus was confirmed by PCR with a forward primer binding in the coding sequence of the nourseothricin resistance gene and a reverse primer binding in the 3'-UTR of the 18S-rRNA locus (SAT+SSU). A product of approximately 2.5 kbp as shown for single clones B8, C10 and D10 confirmed the integration of linearized plasmid fragment. Wild type parasites were used as negative control.
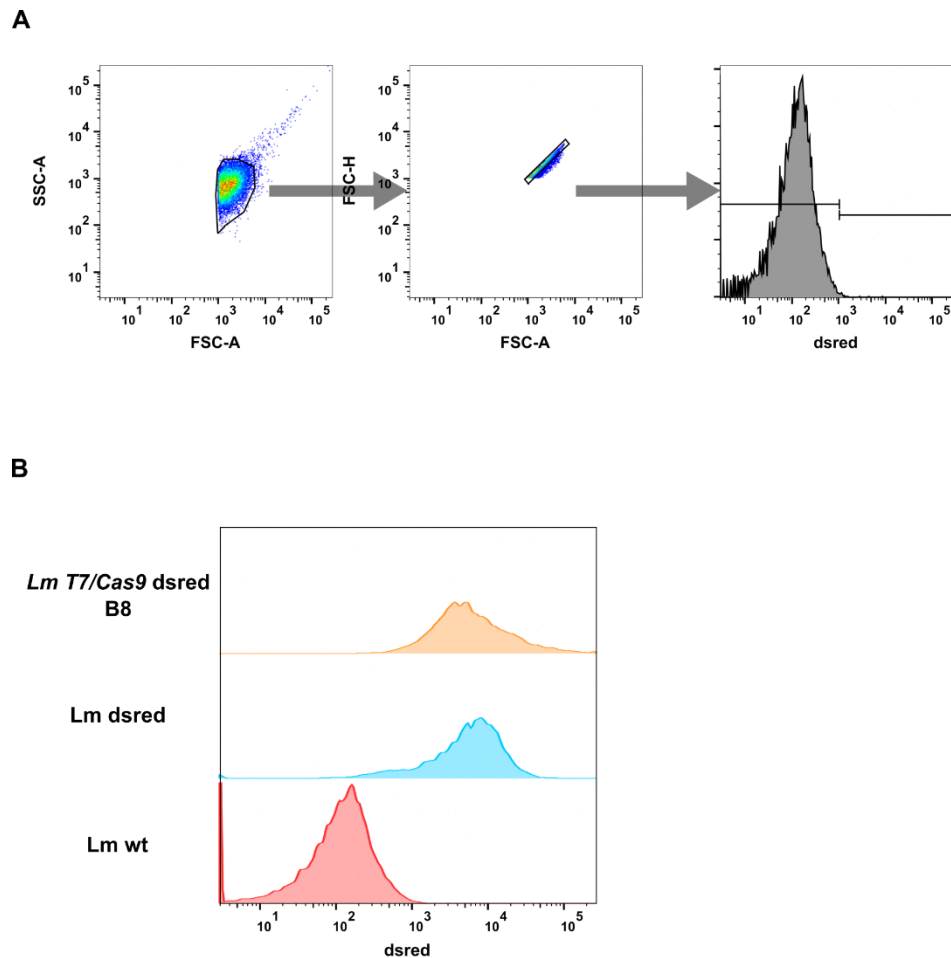
Figure 8: Confirmation of DsRed expression by flow cytometry.
(A) Gating strategy used for *L. major* promastigotes. Parasites were distinguished from cell debris and background noise in a FSC vs. SSC plot, followed by a single cell gate. Wild type parasites were used as gating control for DsRed positivity and L. major DsRed parasites are shown as positive control. (B) histogram of relative DsRed fluorescence intensities of *L. major* wildtype, *L. major* DsRed and *L. major* T7/Cas9 DsRed clone B8.

3.2.5.5 Knockouts in Leishmania

Knockouts in *Leishmania* were done using the cloning-free Cas9-based approach published by *Beneke et al.* [154]. The approach requires a T7/Cas9 expressing *Leishmania* strain, which is electroporated with PCR products encoding a T7 promoter followed by an sgRNA either targeting the 5'-UTR upstream of the gene of interest (GOI) or the 3'-UTR downstream of the gene of interest. The sgRNAs are transcribed in vivo and subsequently, complex with the Cas9 protein and excise the GOI. A repair cassette with an antibiotic resistance marker and 30 bp microhomology flanks homologous for the 5'- and 3'-UTR of the GOI is generated by long primer PCR, as described for Gibson assembly, and electroporated together with the sgRNA-encoding PCR products. The repair cassette is integrated into

the genome by homologous recombination thereby replacing the GOI. Primers for the PCRs were designed using the LeishGEdit tool (available at: http://www.leishgedit.net/Home.html).

Repair cassettes were generated by preparing the following PCR reaction mix on ice and running the following program in a thermocycler:

PCR reaction mix

pTPuro / pTBlast 15 ng/µl	2 µl
PWO Master mix (2x)	10 µl
LPG1 5'-HR (20 µM)	2 µl
LPG1 3'-HR (20 µM)	2 µl
DMSO	0.6 µl
MgCl$_2$ (10 mM)	2.76 µl
H2O	0.65 µl

PCR program:

Step 1:	94°C	5 min
Step 2:	94°C	30 s
Step 3:	65°C	30 s
Step 4:	72°C	2 min 15 s

Repetition of steps 2-4 for 39 cycles

Step 5:	72°C	7 min
Step 6:	4°C	indefinite

PCR products encoding the T7 promoter followed by an sgRNA targeting either the 5'-UTR or 3'-UTR of the GOI were generated by preparing the following PCR reaction mix on ice and running the following program in a thermocycler:

PCR reaction mix

LPG1 5'-/ 3'-sgRNA primer (20 µM)	4 µl
sgRNA scaffold (10 µM)	4 µl
PWO Master mix (2x)	10 µl
H_2O	2 µl

PCR program:

Step 1:	98°C	30 s
Step 2:	98°C	10 s
Step 3:	60°C	30 s
Step 4:	72°C	15 s

Repetition of steps 2-4 for 34 cycles

Step 5:	4°C	indefinite

All PCR products were sterilized by incubation in a thermocycler for 5 min at 95 °C and stored at 4 °C until use. Logarithmic-phase *L. major* T7/Cas9 parasites were prepared for electroporation as described in 3.2.5.4. 7.5 µl of both sgRNAs and either the puromycin- or blasticidin-encoding resistance cassette were added to the parasite suspension in the electroporation cuvette. Afterwards, electroporation, parasite recovery, antibiotic selection and limiting dilution were performed as described in 3.2.5.4. Successful knockout of the GOI was confirmed by three PCRs, (I): A PCR with a forward primer (5) and a reverse primer (6) binding inside of the coding sequence of the GOI, (II): A PCR with a forward primer (5) binding inside of the coding sequence and a reverse primer binding inside of the GOI's 3'-UTR (7), and (III): A PCR with a forward primer binding inside of the coding sequence of the blasticidin resistance gene Blast (B) and a reverse primer binding inside of the GOI's 3'-UTR (7). Lastly, continued expression of DsRed was confirmed on protein level by flow cytometry.

3.2.5.6 qRT-PCR

3.2.5.6.1 RNA isolation

To isolate RNA, $1*10^6$ BLaER1 cells or hMDMs were spun down at 500 *g* for 5 min and washed once with PBS (pH 7.4). Cells were pelleted again by centrifugation and RNA was isolated using a RNeasy plus micro kit in accordance with the manufacturer's instructions. To check the integrity of the isolated RNA, 5 µl of RNA were mixed with 2 µl of 5x RNA loading dye and run on an agarose gel containing 40 ng/ml ethidium bromide. After electrophoresis, the gel was visualized using an image station. A hallmark of intact RNA are two defined bands, representing 28S RNA and 18s RNA – the most abundant RNA species in eukaryotic organisms. Therefore, if two sharp bands were recognizable on the imaged gel, the RNA was considered intact. The concentration of all intact RNA samples was determined by measurement of 2 µl RNA solution at Nanodrop. Afterwards, 0.5 µl of Ribolock RNase inhibitor (ThermoFisher) was added to all RNA samples to prevent degradation. RNA samples were stored at -80 °C until further analysis.

Divergently, RNA was isolated from $3.5*10^6$ bone-marrow-derived macrophages, by discarding the supernatant and directly adding lysis buffer (RLT, supplied in Qiagen RNeasy plus micro kit) to the well. The rest of the RNA isolation was performed as described for BLaER1 cells and hMDMs.

3.2.5.6.2 cDNA synthesis

Synthesis of cDNA was performed using an ImProm-II reverse transcription system kit according to the manufacturer's instructions. In brief, equal amounts of isolated RNA were mixed with random primers, denatured at 70 °C for 5 min and cooled on ice for 5 min. Meanwhile, an RT-PCR reaction mix was prepared on ice and added to the RNA-primer mix. RT-PCR was, then performed in a thermocycler. All cDNA preparations were stored at -20 °C until further analysis.

3.2.5.6.3 qPCR

Quantitative PCR was performed using the MESA BLUE qPCR mastermix plus for SYBR assay kit in accordance with the manufacturer's instructions. All used primers are listed in 2.1.8.. Quantitative PCR was performed in an LC480 lightcycler (Roche). Cycle threshold (Ct) values were calculated using the LC480 software. Relative gene expression was calculated using the $2^{-\Delta\Delta Ct}$ method.

3.2.6 Biochemical methods

3.2.6.1 SDS-PAGE

To confirm successful knockouts in BLaER1 cells, the protein expression was analyzed by SDS-PAGE and subsequent Western blot. For this, $6*10^4$-$2*10^5$ transdifferentiated BLaER1 cells were spun down and re-suspended in 40 µl of Lämmli buffer and lysed by heating at 90 °C for 10 min. 20 µl of each sample were loaded onto two 10 % SDS-polyacrylamide gels (**Table 4**). A pre-stained molecular weight marker was loaded in a separate lane on each gel. Proteins were separated based on their molecular weight by electrophoresis, first at 100 V for 20 min in the stacking gel, then at 120 V for 1.5 h in the separating gel. One gel was used for Coomassie staining, the other one was used for Western blotting.

Table 4: Composition of a 10 % SDS-polyacrylamide gel with a thickness of 1.5 mm.
The table list the required volumes of all components required for a single 10 % SDS-polyacrylamide gel with a thickness of 1.5 mm, consisting of a stacking and a separating gel.

chemical	stacking gel	separating gel
H_2O	1.25 ml	1.62 ml
Tris-HCl (1.5 M, pH 8.8)	-	1 ml
Tris-HCl (0.5 M, pH 6.8)	0.5 ml	-
polyacrylamide (30 %)	250 µl	1.34 ml
SDS (10 %)	20 µl	40 µl
APS (10 %)	20 µl	40 µ
TEMED	5 µl	8.3 µl

3.2.6.2 Coomassie staining

Coomassie staining was performed to verify that a sufficient number of cells has been harvested for Western blot analysis and to rule out that the absence of protein of interest was due to successful knockout of the GOI and not caused by loading of too small amounts of protein. Loading was considered successful, if Coomassie staining revealed visible band patterns. Gels were rinsed once with H_2O, followed by fixation in Coomassie fixing solution for 1 h at room temperature with shaking. Next, fixing solution was removed and the gels were stained in Coomassie staining solution for 2 h at room temperature with shaking. Finally, the staining solution was removed and the gels were destained with Coomassie washing solution overnight. Destained gels were visualized at a Gel Doc image station.

3.2.6.3 Western blot

To analyze the expression of the protein of interest, proteins were transferred from the SDS-polyacrylamide gel to a PVDF membrane by semi-dry blotting for 1.5 h at 1.5 mA per cm^2. The membrane was blocked in blocking buffer for 1 h at room temperature with shaking. Next, the membrane was incubated with the primary unconjugated antibody diluted in blocking buffer for 1 h at room temperature with shaking or overnight at 4 °C with shaking. The membrane was washed thrice with TBS/T buffer for 10 min at room temperature with shaking and, subsequently, incubated with the HRP-conjugated secondary antibody diluted in blocking buffer for 1 h at room temperature with shaking. The membrane was washed thrice with TBS/T buffer for 10 min at room temperature with shaking, then, the membrane was incubated with HRP substrate for 1 min at room temperature and chemiluminescence was detected by analysis with an ECL imager.

3.2.7 Statistical analysis and visualization

Statistical significance was determined by Two-Way-ANOVA for all comparisons of multiple independent groups across multiple experimental conditions; by Dunnet's multiple comparison test, for all comparisons of multiple independent groups and experimental conditions with one experimental condition serving as universal control; by multiple Mann-Whitney test for all comparisons of multiple independent groups across multiple experimental conditions, if the data was not normally distributed; and by unpaired t-tests for all comparisons of two independent groups. All statistical tests were performed in GraphPad Prism as a two-sided test and $\alpha=0.05$. P-values $p<0.05$, **$p<0.01$, ***$p<0.001$, ****$p<0.0001$ were considered to be statistically significant.

All bar plots, dot plots and histograms were created using GraphPad Prism; lolliplots were created in R using the ggdotchart() function of the ggpubr package, which is dependent on ggplot2 package; Representative histograms and scatter plots of flow cytometric data were created in FlowJo; Microscopic images were created from raw image files in Fiji; Schematics and illustrations were created in Biorender. Finally, all graphical elements were compiled to the final figure in Inkscape and further annotated, if required.

4 Results

4.1 BLaER1 as infection model for *L. major* infection of hMDMs

In the beginning of this work, BLaER1 cells were compared to GM-CSF-derived and M-CSF-derived hMDMs to assess their suitability as a cell line model for the infection of hMDMs with *L. major* parasites. For this, a flow cytometric comparison of the immunophenotype of undifferentiated BLaER1 (udBLaER1), transdifferentiated BLaER1 (tdBLaER1) and hMDMs was performed. Next, the susceptibility of BLaER1 cells to *L. major* infection was analyzed, along with a morphologic comparison to hMDMs by fluorescence microscopy Finally, several characteristics of the *L. major* infection were compared by flow cytometry, qPCR, and ELISA, in order to proof that BLaER1 cells can be infected with *L. major*, allow the intracellular differentiation to the amastigote stage and amastigote replication in the phagolysosome.

4.1.1 Immunophenotyping of BLaER1 cells and hMDMs

To show that BLaER1 cells have a comparable expression of surface markers compared to hMDMs, the immunophenotype of tdBLaER1, M-CSF-derived and GM-CSF-derived hMDMs was compared using udBLaER1 as a control. Immunostained cells were analyzed by flow cytometry. CD19 was included in the antibody panel as an important marker for the undifferentiated pre-B cell form of the BLaER1 cells. In terms of transdifferentiation, it could be confirmed that tdBLaER1 cells lost the expression of CD19, while acquiring a CD11b-positive and CD14-positive phenotype with 90 % of the cells being CD11b-positive and 63 % of the cells being CD14-positive. (**Figure 9A**). Furthermore, tdBLaER1 became positive in expression for CD163. CD206, CD86, HLA-ABC, CD116, CD115, HLA-DR and CD18, to a similar extend as hMDMs. BLaER1 cells and hMDMs had a low to absent expression of CD83, CD209 and CD124. I found a significantly smaller share of CD206 positive, CD18 positive and HLA-DR positive tdBLaER1 cells compared to both GM-CSF-derived macrophages (62 % vs. 100 %, 52 % vs. 100 % and 47 % vs. 95 %, respectively) and M-CSF-derived macrophages (62 % vs. 98 %, 52 % vs. 100 % and 47 % vs. 87 %, respectively). In comparison to M-CSF-derived macrophages, a significantly smaller share of, CD163-positive, CD14-positive, and CD116-positive tdBLaER1 cells was found, with tdBLaER1 cells being 68 % positive for CD163, 63 % for CD14 and 60 % positive for CD116, compared to 95 % CD163 positivity, 97 % CD14 positivity and 90 % CD116 positivity for M-CSF-derived macrophages.

In addition to the percentage of cells positive for a certain marker, the level of expression by the positive subsets of tdBLaER1 cells, GM-CSF-derived macrophages, and M-CSF-derived macrophages

was also compared. TdBLaER1 cells showed a higher expression of CD115, CD19 and CD14 compared to both GM-CSF-derived macrophages and M-CSF-derived macrophages and a higher expression of CD163 and CD206 compared to GM-CSF-derived macrophages and M-CSF-derived macrophages, respectively (**Figure 9B**). In summary, this data shows that tdBLaER1 cells acquire an immunophenotype that corresponds well to hMDMs in both the frequency of marker-positive cells and the expression level of the respective surface marker, and is slightly more comparable to the immunophenotype of GM-CSF-derived macrophages.
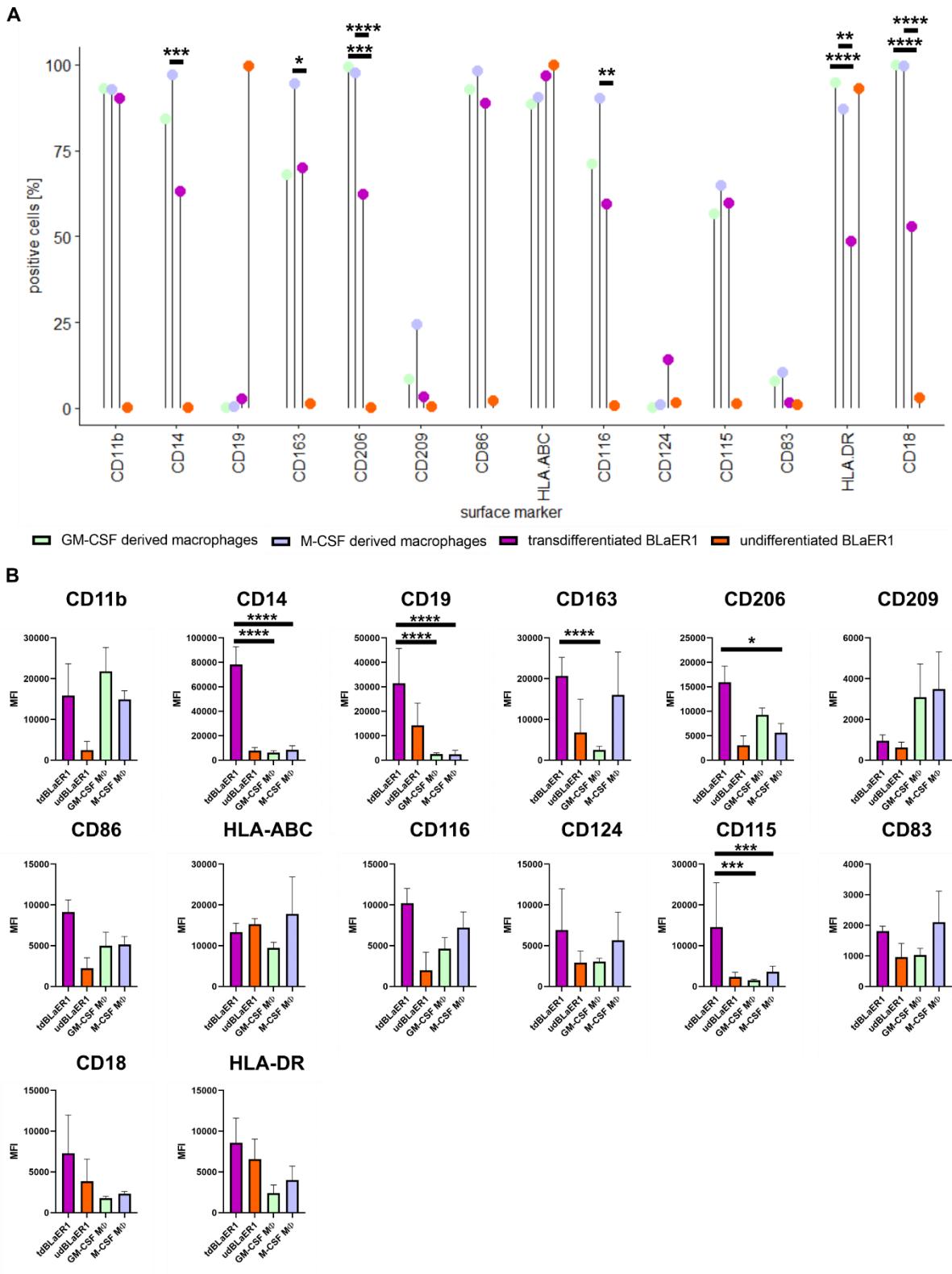
Figure 9: BLaER1 cells show a similar immunophenotype as M-CSF-derived and GM-CSF-derived macrophages.
(A and B) Immunophenotyping of undifferentiated BLaER1 cells (udBLaER1), transdifferentiated BLaER1 cells (tdBLaER1), M-CSF-derived macrophages and GM-CSF derived macrophages. All cell types were stained with fluorochrome-conjugated antibodies against surface markers of myeloid cell types and analyzed by flow cytometry. (A) Lolli-plot of the percentage of positive cells for each marker. (B) MFI values of each marker as indicator of expression level. Significant comparisons between tdBLaER1 cells and M-CSF-derived macrophages or GM-CSF-derived macrophages were annotated in the graphs. N=3-4. Graphs depict mean values (A) or mean values +SD (B). Significance was determined using Two-Way-ANOVA. * p<0.05, **p<0.01, ***p<0.001, ****p<0.0001.

4.1.2 BLaER1 cells sustain *L. major* infection despite smaller cell size and cytoplasm

Since all experiments after the initial immunophenotyping will focus on the transdifferentiated macrophage-like phenotype of BLaER1 cells, tdBLaER1 cells will be referred to as BLaER1 cells throughout the rest of the section. If udBLaER1 cells are part of an experiment, the nomenclature from 4.1.1 will be used.

After confirmation of a similar immunophenotype and concomitant validation of the transdifferentiation process, I sought to perform a morphological comparison of cell size and cytoplasm area of BLaER1 cells and hMDMs and confirm the susceptibility of BLaER1 cells to *L. major* infection. For this, BLaER1 cells hMDMs were infected with *L. major* promastigotes, stained with DAPI and phalloidin - to determine cell size and cytoplasm size, and immunostained with rabbit α-*L. major* (α-Lm) serum to visualize parasites Subsequently, infected cells were analyzed by confocal fluorescence microscopy (**Figure 10** and **Figure 11**). BLaER1 cells had a significantly smaller cell area than M-CSF derived hMDMs at 3 h (149 μm^2 vs. 479 μm^2), 24 h (376 μm^2 vs. 485 μm^2) and 96 h post infection (p.i.) (119 μm^2 vs. 627 μm^2), and a smaller cell area than GM-CSF derived hMDMs at 3 h and 96 h p.i. (149 μm^2 vs. 238 μm^2 and 119 μm^2 vs. 422 μm^2, respectively) (**Figure 10A**). Moreover, the cell area of M-CSF-derived hMDMs was significantly larger than the one of GM-CSF-derived hMDMs at 24 h and 96 h. Interestingly, after an initial increase from 3 h p.i. to 24 h p.i., the cell area of BLaER1 cells decreased again between 24 h and 96 h p.i., while the cell area of both types of hMDMs increased consistently from 3 h to 96 h p.i.. Based on the measured cell area, the cell diameter was calculated for each cell, assuming a round cell shape (**Figure 10B**). Since the cell diameter is a mathematical transformation of the cell area, all observed differences in cell area apply equally to the cell diameter. In BLaER1 cells, a significantly larger share of the cytoplasm was occupied by the nucleus compared to GM-CSF derived and M-CSF derived hMDMs at 3 h, 24 h and 96 h p.i. (32.6 % vs. 17.0 % and 26.8 %, 35.0 % vs. 11.6 % and 21.2 % and 45.7 % vs 14.8 % and 24.7 %, respectively) (**Figure 10C**).
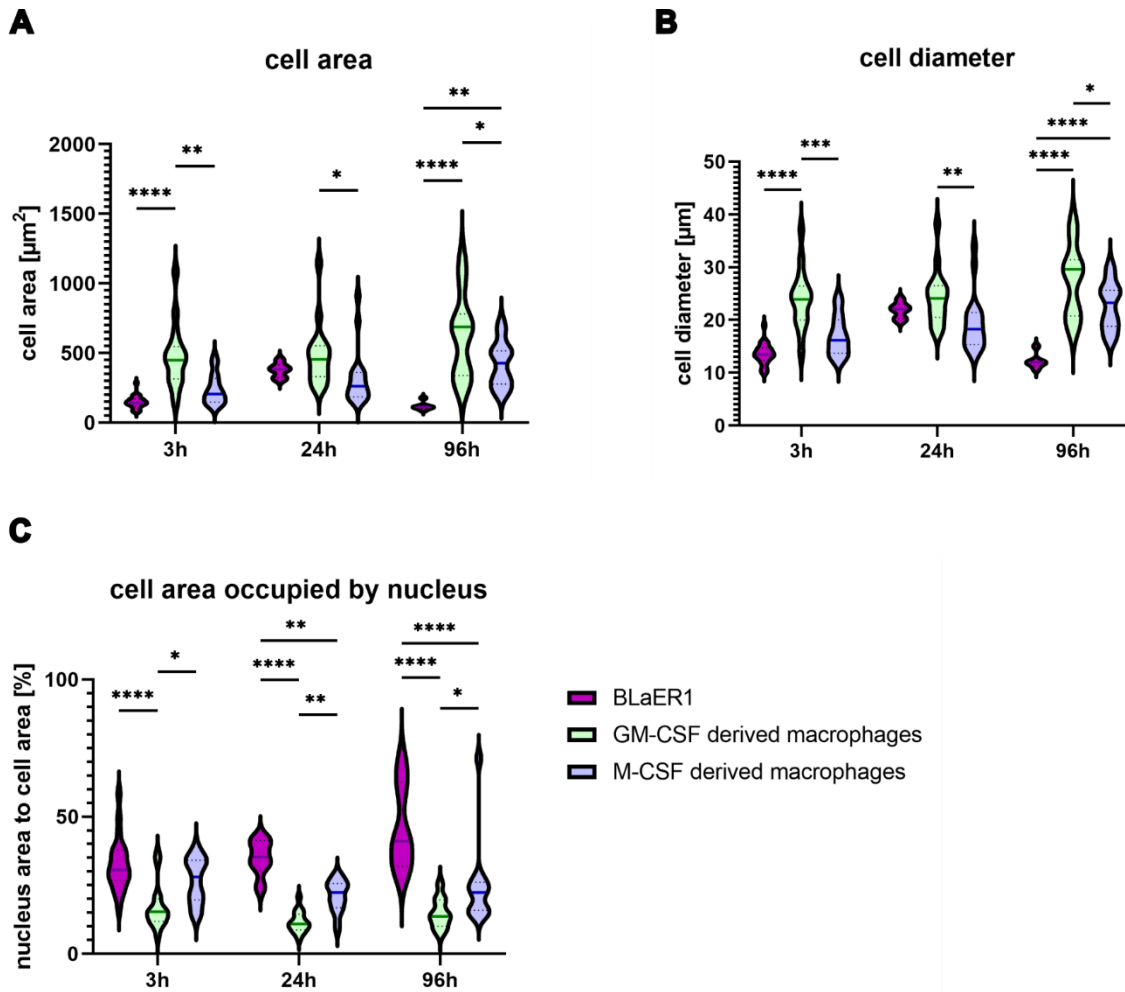
Figure 10: BLaER1 cells have a smaller cell diameter than hMDMs and a larger share of the cell is occupied by the nucleus.
(A to C) BLaER1 cells, M-CSF-derived macrophages and GM-CSF-derived macrophages were infected with stationary-phase *L. major* promastigotes at MOI 10 for up to 96 h. At indicated time points, cells were subjected to immunofluorescence staining and z-stacks were acquired by confocal microscopy. Maximum projections of the DAPI channel (DNA) and the AlexaFluor488 channel (actin) of the confocal images were analyzed using the CellProfiler software. (A and B) the area occupied by the actin staining was measured each cell to determine the mean cell area for each cell type at each time point (A). Assuming a round cell shape, the mean cell diameter was calculated (B). (C) The mean area occupied by DNA staining per cell was determined as described for the actin staining. The share of cell area occupied by the nucleus was then calculated by dividing the mean area of DNA stain per cell by the mean cell area. N=1, with 6-22 cells per cell type and time point. Graphs show data distribution as violin plots + median (line) and interquartile range (in between dotted lines). Significance was determined using Two-Way-ANOVA. * $p<0.05$, **$p<0.01$, ***$p<0.001$, ****$p<0.0001$.

To distinguish intracellular parasites from parasites that only overlap with cells or parasites that are associated to the cell membrane, we examined maximum projections of infected BLaER1 cells and both types of hMDMs (**Figure 11**, upper panels) for presumed intracellular parasites. The enclosure of parasites by the cytoskeleton of the host cell was, subsequently, confirmed by depiction of selected cells (yellow boxes) as an orthogonal view onto the yz-axis (lower row of images in each panel). We observed parasites surrounded by host cell cytoskeleton (white arrows) at all time points for BLaER1 cells (**Figure 11A**), GM-CSF-derived hMDMs (**Figure 11B**) and M-CSF-derived hMDMs (**Figure 11C**). This

finding confirms that, notwithstanding their smaller cell size and cytoplasm size, BLaER1 cells are susceptible to infection with *L. major* promastigotes and sustain the infection at every time point tested in this work.
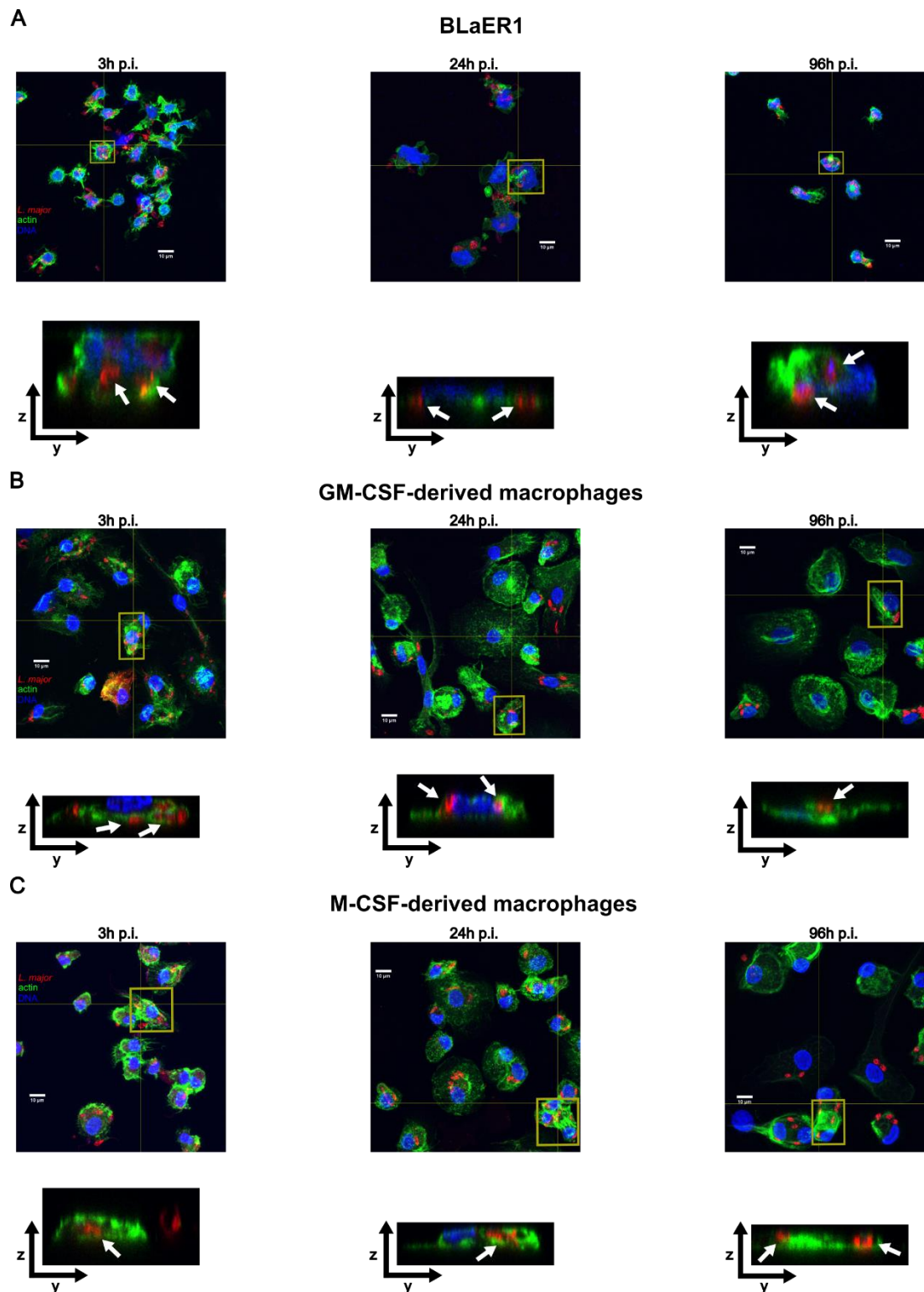
Figure 11: BLaER1 cells are susceptible to infection with *L. major* and able to sustain the infection.
(A to C) To confirm the presence of intracellular parasites, the z-stacks from figure 3 were analyzed using the ImageJ software. The upper images in each panel shows a maximum projection of the stack. The yellow lines indicate the positions on x-axis (vertical line) and y-axis (horizontal line) at which the orthogonal view was done. The yellow square highlights the cell that is seen in the orthogonal view. The lower images in each panel shows the orthogonal view onto the yz-axis at the indicated position. White arrows indicate parasites enclosed by cytoskeleton (green dye). (A), infected BLaER1 cells, (B), infected GM-CSF-derived macrophages, (C), infected M-CSF-derived macrophages.

4.1.3 Intracellular parasites cannot be identified in BLaER1 cells by histological staining, but can be determined by fluorescence microscopy

Next, I intended to determine the infection rate and parasite burden of BLaER1 cells infected with stationary-phase *L. major* by histological staining. For this, BLaER1 cells were infected with stationary-phase *L. major*, stained with Diff-Quick staining kit and analyzed by transmission light microscopy. Due to the smaller cell size and darker cytoplasm stain compared to hMDMs, parasites could not be counted using this method (data not shown). Therefore, the parasite burden of infected BLaER1 cells was analyzed using fluorescent dyes and an Operetta high-content microplate imager (Perkin-Elmer). BLaER1 cells were infected with CFSE-labeled stationary-phase *L. major*, the cell membrane stained with WGA-568 and subsequently analyzed by fluorescence microscopy. The analysis of 13,106 cells showed an infection rate of 88.43 % ± 9.32 % and an average parasite burden of 3.50 ± 1.11 parasite per cell. On average, most infected cells harbored either two intracellular parasites (755 cells) or three intracellular parasites (698) (**Figure 12**). While the abundance of cells with higher parasite burdens decreased strongly with the number of parasites, BLaER1 cells with up to 19 intracellular parasites (0.66 cells i.e., one cell in two out of three replicates) could be observed. This data shows that despite their size, BLaER1 cells can sustain high parasite burdens.
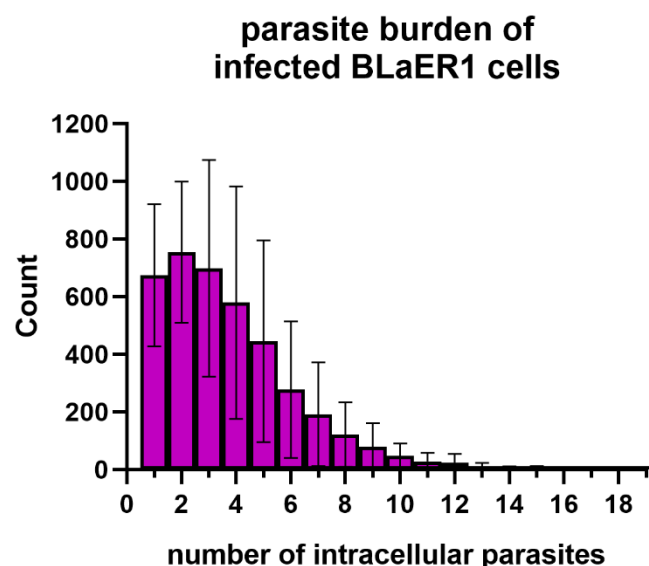
Figure 12: Determination of parasite burden of infected BLaER1 cells by high-throughput microscopy.
BLaER1 cells were infected with CFSE labeled, stationary-phase *L. major* DsRed parasites at MOI 10 for 2 h. Afterwards, the membrane of BLaER1 cells was stained with wheat germ agglutinin (WGA-568) and cells were analyzed by automated fluorescence microscopy. Infected cells and the number of intracellular parasites were determined using the CellProfiler software. Graph shows a histogram of the determined parasite burdens. N=3. Graphs show mean values +SD.

4.1.4 BLaER1 cells resemble hMDMs in both infection rate and parasite burden

After determining the parasite burden of BLaER1 cells, flow cytometry was used to investigate whether tdBLaER1 cells are infected at a similar rate as M-CSF-derived hMDMs and GM-CSF-derived hMDMs. For this, BLaER1 cells, M-CSF derived hMDMs and GM-CSF-derived hMDMs were infected with Alexa-Fluor647-conjugated stationary-phase *L. major* and analyzed by flow cytometry (**Figure 13**). No differences of infection rates were observed at 3 h p.i. and 24 h p.i.. However, at 96 h p.i., both M-CSF-derived hMDMs and GM-CSF- derived hMDMs were infected at a significantly higher rate than BLaER1 cells. (78 % and 78 % vs. 22 %). Since this strong decrease in the infection rate occurred simultaneously with an increase in cell numbers (data not shown) for BLaER1 cells, I suspected residual non-quiescent, undifferentiated BLaER1 cells in the culture supernatant as reason for the proportional decrease of infected cells.
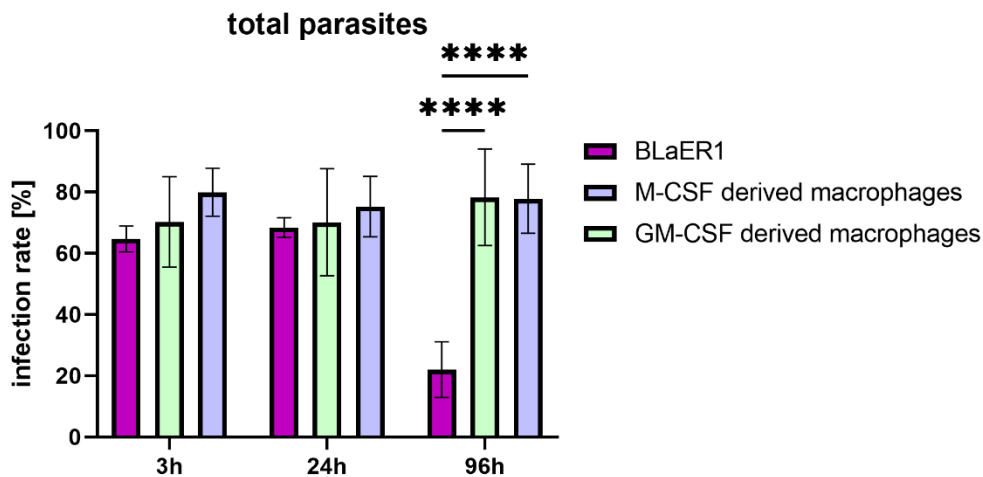
Figure 13: BLaER1 cells show a decreased infection rate at 96 h p.i.
BLaER1 cells, M-CSF-derived hMDMs and GM-CSF-derived hMDMs were infected with AlexaFluor647 labeled, stationary-phase *L. major* parasites at MOI 10 for up to 96 h. Percentage of AlexaFluor647 positive cells as indicator for the uptake of both viable and dead (total) parasites. N=3. Graphs show mean values +SD. Significance was determined by Two-Way-ANOVA. * $p<0.05$, **$p<0.01$, ***$p<0.001$, ****$p<0.0001$.

Hence, the experiment was repeated with BLaER1 cells whose supernatant, containing undifferentiated, non-adherent cells, had been discarded before harvesting and re-seeding for the infection experiment. To test whether undifferentiated BLaER1 cells were part of the culture, BLaER1 cells were also immunostained for CD14. Additionally, since it has been shown previously [155] that the apoptotic subset of parasites in their stationary-phase plays an important immunosuppressive role for the *L. major* infection, the uptake of viable and total, i.e., viable, and dead parasites, was distinguished by using Alexa-Fluor647-conujgated *L. major* DsRed-expressing parasites. As measured by the percentage of Alexa-Fluor647-positive cells, no significant differences in the total uptake of

parasites between BLaER1 cells and hMDMs was observed at 3 h and 24 h p.i., irrespective of gating on all cells or only CD14$^+$ cells. At 3 h p.i. 56 % of BLaER1 cells were infected compared to 69 % and 78 % for GM-CSF-derived hMDMs and M-CSF-derived hMDMs, respectively (**Figure 14A and B**). At 24 h p.i., 78 % of CD14$^+$ BLaER1 cells and 75 % of the total BLaER1 cells were infected compared to 72 % and 76 % for GM-CSF-derived hMDMs and M-CSF-derived hMDMs, respectively. At 96 h p.i. the infection rate of CD14$^+$ BLaER1 cells was significantly increased compared to GM-CSF-derived hMDMs (98 % vs 69 %) but not in comparison to M-CSF-derived hMDM. In contrast, the infection rate of total BLaER1 cells was significantly decreased compared to M-CSF-derived hMDMs and GM-CSF derived hMDMs (44 % vs. 74 % and 69 %, respectively). Interestingly, I did not observe any differences in the infection rate of CD14$^+$ BLaER1 cells and either type of hMDM with only viable parasites, with infection rates of 12 %, 29 % and 54 % for CD14$^+$ BLaER1 cells at 3 h, 24 h and 96 h p.i., respectively, compared to infection rates of 17 %, 32 % and 35 %, respectively, for GM-CSF-derived hMDMs and 28 %, 37 % and 34 %, respectively, for M-CSF-derived macrophages. (**Figure 14C**).
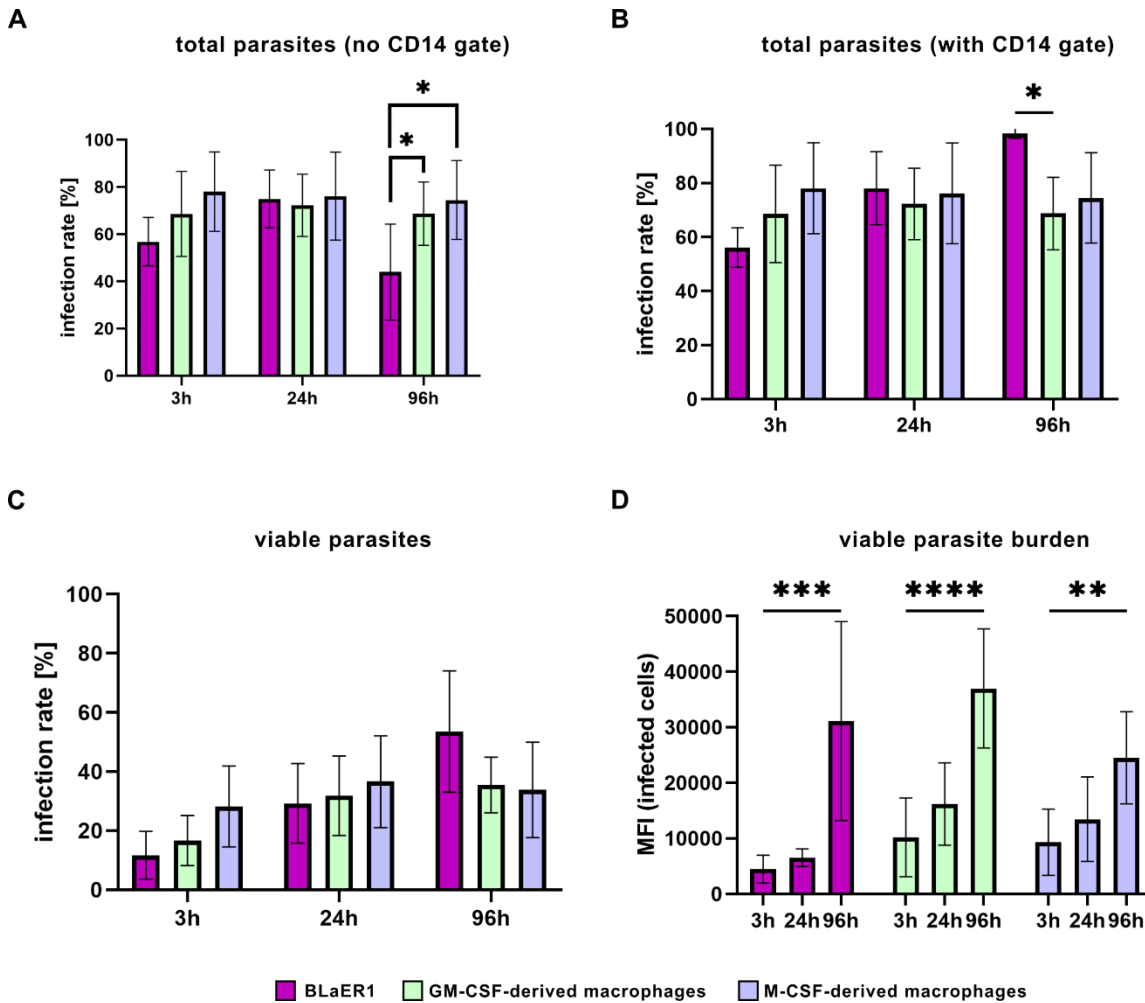
Figure 14: BLaER1 cells show similar infection rate and parasite burden for both viable and dead parasites.
BLaER1 cells, M-CSF-derived macrophages and GM-CSF-derived macrophages were infected with AlexaFluor647 labeled, stationary-phase *L. major* DsRed parasites at MOI 10 for up to 96 h. BLaER1 cells were additionally stained with CD14-PB to exclude undifferentiated cells. (A) Percentage of AlexaFluor647+ cells as indicator for the uptake of both viable and dead (total) parasites without a CD14 gate for BLaER1 cells. (B) Percentage of AlexaFluor647+ cells as indicator for the uptake of both viable and dead (total) parasites with a CD14 gate for BLaER1 cells. (C) Percentage of DsRed+ cells as indicator for the uptake of viable parasites. (D) Comparison of the DsRed MFI of infected cells over time as a measure of the parasite burden. N=3-4. Graphs show mean values +SD. Significance was determined by Two-Way-ANOVA. * $p<0.05$, **$p<0.01$, ***$p<0.001$, ****$p<0.0001$.

In order to determine whether BLaER1 cells support the transformation of *L. major* promastigotes to the amastigote stage and their subsequent intracellular proliferation, I compared the DsRed mean fluorescence intensity (MFI) of intracellular *L. major* parasites in CD14+ BLaER1 cells, GM-CSF-derived hMDMs, and M-CSF-derived hMDMs up to 96 h p.i. to the initial fluorescence intensity 3 h p.i.. A strong and significant increase in the DsRed MFI was observed for cells infected with viable *L. major* DsRed-expressing promastigotes after 96 h for CD14+ BLaER1 cells (31,110 vs. 3,389), GM-CSF derived hMDMs (36,997 vs 10,174) and M-CSF derived hMDMs (24,522 vs. 9,301) (**Figure 14D**). Taken together, these

findings show that BLaER1 cells take up both viable and dead *L. major* parasites at the same rate as hMDMs and support the intracellular proliferation of the parasite.

4.1.5 *L. major* promastigotes transform to amastigote form inside of BLaER1 cells

To further corroborate the intracellular transformation of *L. major* promastigotes to the amastigote stage, I analyzed the expression of two proteins that are differentially expressed based on the life cycle stage of the parasite: SHERP, which is expressed higher in promastigotes, and ABC transporter homologue, which is expressed higher in amastigotes, by qPCR. The promastigote marker SHERP was significantly downregulated for BLaER1 cells and M-CSF-derived hMDMs at 96 h p.i. (**Figure 15A**). While a similar trend was clearly recognizable for GM-CSF-derived hMDMs, too, it did not reach the level of significance. In BLaER1 cells, we found the amastigote marker ABC transporter homologue to be significantly upregulated at 24 h and 96 h post infection, with the strongest expression at 24 h p.i. (**Figure 15B**). For both M-CSF-derived hMDMs and GM-CSF-derived hMDMs, no significant upregulation of ABC transporter homologue could be observed. Together with the flow cytometry data from **Figure 14C**, the qPCR results provide strong evidence for a similar intracellular transformation of *L. major* promastigotes to the amastigote stage and a subsequent intracellular proliferation in all three tested cell types.
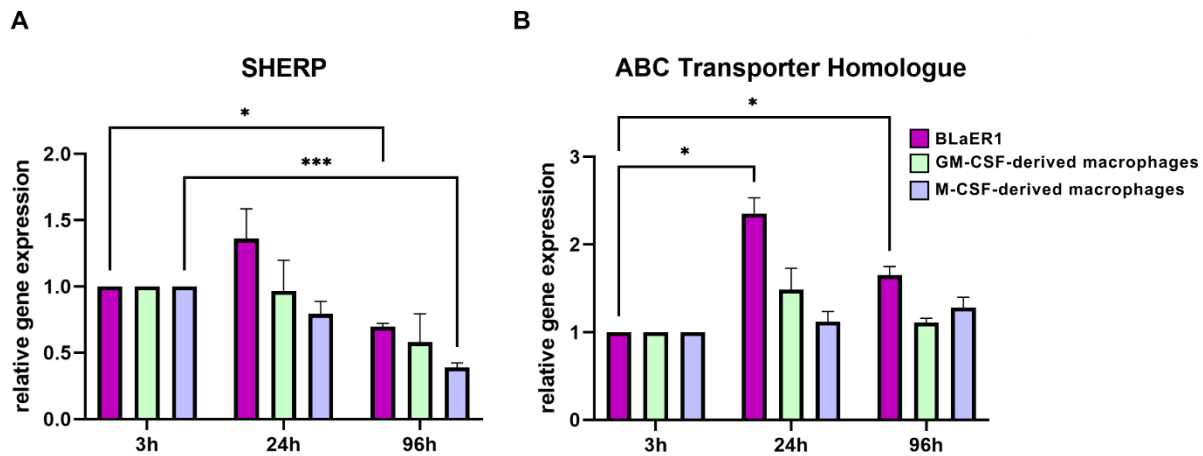
Figure 15: BLaER1 cells support the transformation to the amastigote stage.
(A and B), BLaER1 cells, M-CSF-derived and GM-CSF-derived macrophages were infected with stationary-phase *L. major* promastigotes at MOI 10 and incubated for up to 96 h. RNA was isolated at the indicated time points and reverse transcribed. The resulting cDNA was used for qPCR to determine the expression of the life cycle specific proteins SHERP and ABC transporter homologue. (A), expression level of the promastigote specific protein SHERP. (B), expression level of the amastigote specific protein ABC transporter homologue. N=3. Graphs show mean values +SEM. Significance was determined by Two-Way-ANOVA. * p<0.05, **p<0.01, ***p<0.001, ****p<0.0001.

4.1.6 BLaER1 cells show a comparable cytokine response as hMDMs

Finally, I compared the secretion of TNF-α and IL-10 by BLaER1 or macrophages in response to an infection with either logarithmic-phase *L. major* promastigotes or stationary-phase *L. major,* and used LPS stimulation of uninfected host cells as a positive control. For TNF-α, a significantly increased secretion was found in response to an infection with logarithmic-phase promastigotes, but not stationary-phase promastigotes for M-CSF-derived hMDMs (1,467 pg/ml vs. 436 pg/ml in untreated control) and GM-CSF-derived hMDMs (725 pg/ml vs. 170 pg/ml in untreated control) but not for BLaER1 cells (**Figure 16A**). All three cell types responded to LPS stimulation with a strong and highly significant increase in TNF- α secretion of 631 pg/ml for BLaER1 cells, 9106 pg/ml for GM-CSF-derived hMDMs and 4735 pg/ml for M-CSF-derived hMDMs. Interestingly, the TNF-α secretion of BLaER1 cells was about one order of magnitude lower than the secretion by hMDMs. For IL-10, a significantly increased secretion in response to the infection with logarithmic- and stationary-phase promastigotes was observed for M-CSF derived hMDMs (1,379 pg/ml and 483 pg/ml, respectively, vs. 48 pg/ml in untreated control), but I did not observe any significant increase for BLaER1 cells of GM-CSF-derived hMDM in response to either infection (**Figure 16B**). Similar to the TNF-α secretion, a strong and highly significant increase in IL-10 secretion was found in response to LPS stimulation of 1188 pg/ml for BLaER1 cells, 1,487 pg/ml for GM-CSF derived hMDMs and 5,754 pg/ml in M-CSF derived hMDMs. In

summary, BLaER1 cells display a comparable but overall lower cytokine secretion than both types of hMDMs, with a stronger similarity to GM-CSF-derived hMDMs than to M-CSF-derived hMDMs.
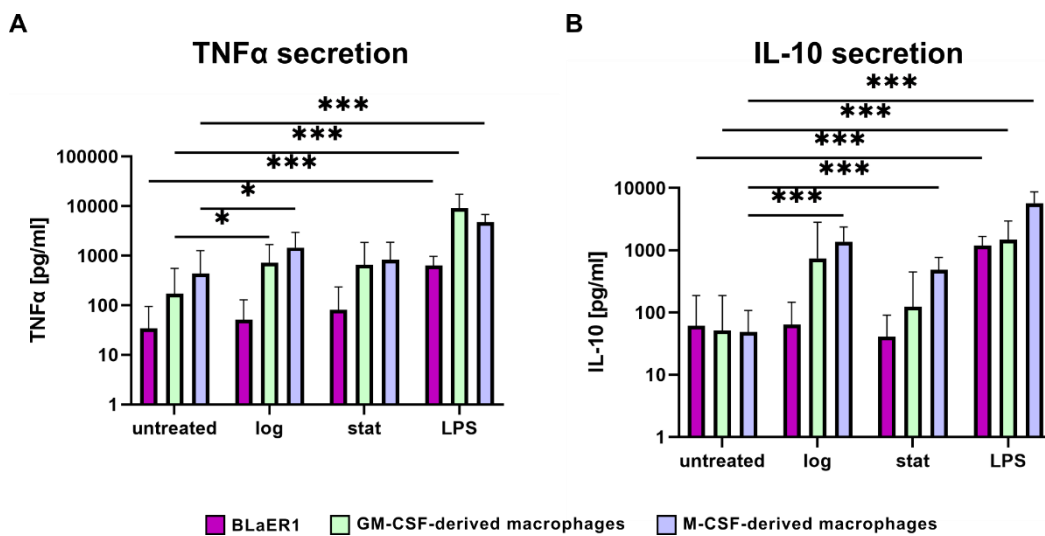

Figure 16: BLaER1 cells show a lower overall cytokine response.
(A and B), BLaER1 cells, M-CSF-derived and GM-CSF-derived macrophages were infected with either logarithm-phase *L. major* promastigotes or stationary-phase *L. major* promastigotes at MOI 5, or stimulated with 100 ng/ml LPS. After 24 h, supernatant was collected and the concentration of TNF-α (A) and IL-10 (B) were determined by Sandwich-ELISA. N=7. Graphs show mean values +SD. Dunnet's multiple comparisons test. * p<0.05, **p<0.01, ***p<0.001, ****p<0.0001.

4.2 Characterization of the human NLRP3 inflammasome activation in response to *L. major* infection

The NLRP3 inflammasome plays an important role in the innate immunity against *Leishmania ssp.* in murine macrophages, but the role in the human infection remains elusive due to species-specific differences pertaining the NLRP3 inflammasome itself as well as downstream effector mechanisms. Furthermore, mechanistic insights into the pathways, which lead to *Leishmania*-mediated NLRP3 inflammasome activation are lacking due to the limited possibilities of reverse genetic methods in human macrophages. After establishing BLaER1 cells as a suitable model for the infection of human hMDMs with *L. major* parasites, I used them to characterize the activation of the human NLRP3 inflammasome upon *L. major* infection. For this, I investigated whether *L. major* infection activates the human NLRP3 inflammasome. Next, the dependence of inflammasome activation on phagocytosis-mediated phagolysosomal ROS production and the presence of lipophosphoglycan (LPG) on the parasite surface was investigated. Finally, the influence of inflammasome activation on parasite restriction was analyzed.

4.2.1 Infection with *L. major* promastigotes activates human NLRP3 inflammasome

First, I sought to investigate whether infection with *L. major* promastigotes leads to an activation of the human NLRP3 inflammasome. To this end, I compared the inflammasome activation in BLaER1 cells, the inflammasome-incompetent BLaER1 *Casp1*$^{-/-}$ cells as well as the inflammasome-deficient BLaER1 *NLRP3*$^{-/-}$ cells. All cells were stimulated with LPS or R848 to ensure a detectable IL-1β secretion and to distinguish the compounded effects of alternative inflammasome activation and *Leishmania* infection expected for LPS stimulated from the effect of *Leishmania* infection alone expected for R848 stimulated cells. Stimulated cells were subsequently infected with stationary-phase *L. major* DsRed. Infection rate and parasite burden were analyzed by flow cytometric analysis, while NLRP3 inflammasome activation was assessed by IL-1β ELISA. At 3 h p.i., *L. major* infection led to a strong increase in both LPS- and R848-stimulated BLaER1 cells (440 pg/ml and 190 pg/ml, respectively) (**Figure 17A**). This increase was NLRP3 inflammasome-specific, as it was not observed for BLaER1 *Casp1*$^{-/-}$ or BLaER1 *NLRP3*$^{-/-}$ cells. BLaER1, BLaER1 *Casp1*$^{-/-}$ or BLaER1 *NLRP3*$^{-/-}$ cells did not differ in infection rate and parasite burden at 3 h p.i. (**Figure 17C** and **Figure 17D**). As expected, LPS stimulation of uninfected BLaER1 cells led to an increase of the IL-1β secretion (229 pg/ml), which was not observed for R848-stimulated cells (74 pg/ml). At 24 h p.i., a significantly increased IL-1β secretion was only observed for LPS-stimulated uninfected BLaER1 and BLaER1 *Casp1*$^{-/-}$ cells and for R848-stimulated uninfected BLaER1 *NLRP3*$^{-/-}$ cells (**Figure 17B**).
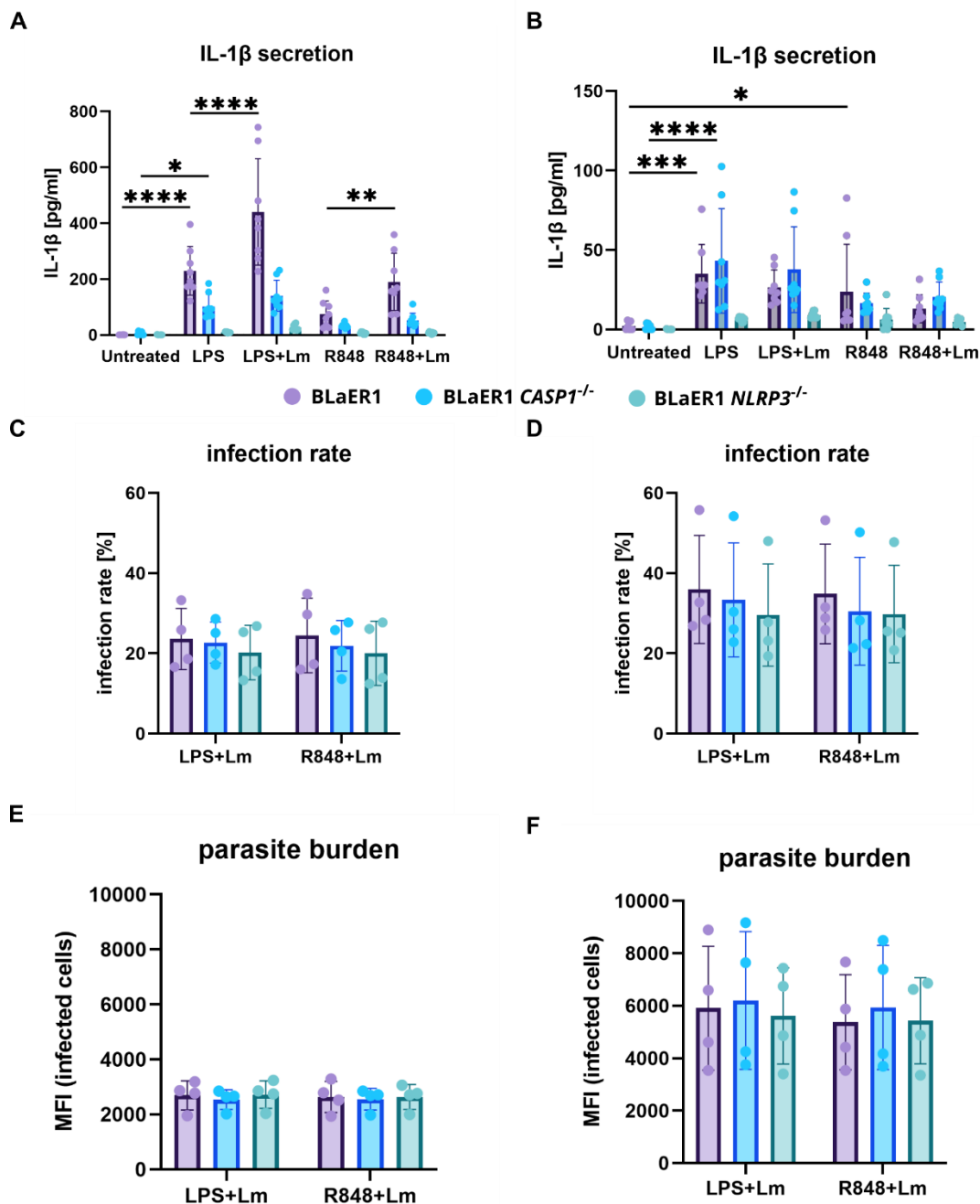
Figure 17: The human NLRP3 inflammasome is activated in response to *L. major* infection.
BLaER1, BLaER1 *Casp1*^{-/-} and BLaER1 *NLRP3*^{-/-} cells were primed with 200 ng/ml LPS or 500 nM R848 for 15 h and subsequently infected with stationary-phase *L. major* DsRed parasites at MOI 10 for 3h (A, C and D) or 24 h (B, D and F). (A and B) IL-1β concentrations of supernatants collected 3 h (A) or 24 h (B) post infection determined by ELISA. (C-F) cells were harvested and analysed by flow cytometry. (C and D) Share of DsRed+ BLaER1, BLaER1 *Casp1*^{-/-} and BLaER1 *NLRP3*^{-/-} cells at 3 h (C) and 24 h (D) post infection. (E and F) MFI of DsRed+ BLaER1, BLaER1 Casp1^{-/-} and BLaER1 NLRP3^{-/-} cells at 3 h (E) and 24 h (F) post infection. N=4. Graphs show mean values + SD. Significance was determined by Two-Way-ANOVA. * p<0.05, **p<0.01, ***p<0.001, ****p<0.0001.

To further corroborate the NLRP3 inflammasome activation by *L. major* infection, I sought to measure the activity of caspase-1 using the caspase-1 probe 660-YVAD-FMK. BLaER1 cells were stimulated with

LPS for 3 h, followed by infection with stationary-phase *L. major* DsRed for 3h, or treatment with the NLRP3 inflammasome-activating potassium ionophore nigericin for 30 min. Simultaneous with the addition of nigericin, cells destined as negative control were treated with the pan-caspase-inhibitor ZVAD to inhibit the inflammasome activation. Cells were analyzed by either flow cytometry of fluorescence microscopy. The flow cytometric analysis showed that the relative fluorescence intensity of 660-YVAD did not shift very strongly between the different treatments (**Figure 18A**). Notably, for nigericin-treated BLaER1 cells the entire population shifted towards a higher fluorescence intensity, while in infected BLaER1 cells the population only skewed towards a higher fluorescence intensity. ZVAD treatment ablated the shift observed in nigericin treated BLaER1 cells, but did not affect the skewing of infected BLaER1. The measured 660-YVAD MFI values of infected and nigericin treated BLaER1 cells (2526 and 3015, respectively) increased compared to the unstimulated and ZVAD-inhibited BLaER1 control condition (1660 and 1680, respectively). Interestingly, treatment with ZVAD had no effect on the MFI value of infected BLaER1 cells, while it completely ablated caspase-1 activity in nigericin-stimulated cells (**Figure 18D**). No pronounced differences were observed between infection rates and parasite burdens, irrespective of treatment or cell type (**Figure 18B** and **Figure 18C**).

Figure 18: *L. major* **infection leads to increased caspase-1 activity in BLaER1 cells**
BLaER1, BLaER1 *Casp1*^{-/-} and BLaER1 *NLRP3*^{-/-} cells were primed with 200 ng/ml LPS for 3 h, followed by treatment with nigericin for 30 min or infection with stationary-phase *L. major* DsRed at MOI 10 for 3 h. After 2.5 h of infection and simultaneously with nigericin treatment 50 µM of pan-caspase-inhibitor ZVAD was added to all inhibited conditions. After 3 h of infection, cells were harvested, stained with 660-YVAD, and analyzed by flow cytometry. (A) overlaid histograms of relative 660-YVAD fluorescence intensity for BLaER1, BLaER1 *Casp1*^{-/-} and BLaER1 *NLRP3*^{-/-} cells. (B) Share of infected BLaER1, BLaER1 *Casp1*^{-/-} and BLaER1 *NLRP3*^{-/-} cells, ZVAD treated and unstained controls. (C) MFI of DsRed+ BLaER1, BLaER1 *Casp1*^{-/-} and BLaER1 *NLRP3*^{-/-} cells. (D) Caspase-1 activity BLaER1, BLaER1 *Casp1*^{-/-} and BLaER1 *NLRP3*^{-/-} cells.

Microscopic analysis showed that caspase-1 activity was considerably weaker in infected BLaER1 cells (**Figure 19A**) than in nigericin treated cells (**Figure 19B**). Notably, the caspase-1 activity was strongest in eGFP-negative/dead cells, indicating pyroptotic cell death (**Figure 19B**, upper panel, merge).

Caspase-1 activity could be completely ablated by ZVAD treatment in nigericin treated cells (**Figure 19B**, lower panel). For infected cells, the observed caspase-1 activity was much lower than for nigericin treated cells. Interestingly, caspase-1 activity in infected cells was observed in close proximity to the intracellular parasites. In contrast to the flow cytometric analysis, ZVAD treatment seemed to ablate the caspase-1 activity in infected BLaER1 cells **Figure 19A**, lower panel). Taken together this data showed that *L. major* infection activates the human NLRP3 inflammasome. Since the analysis of inflammasome activation with a caspase-1 probe was more effortful and less compatible with other analyses, due to the occupation of fluorescence channels in both flow cytometric and microscopic analyses, than the determination of the IL-1β concentrations of supernatants, the latter method was chosen in all further experiments.

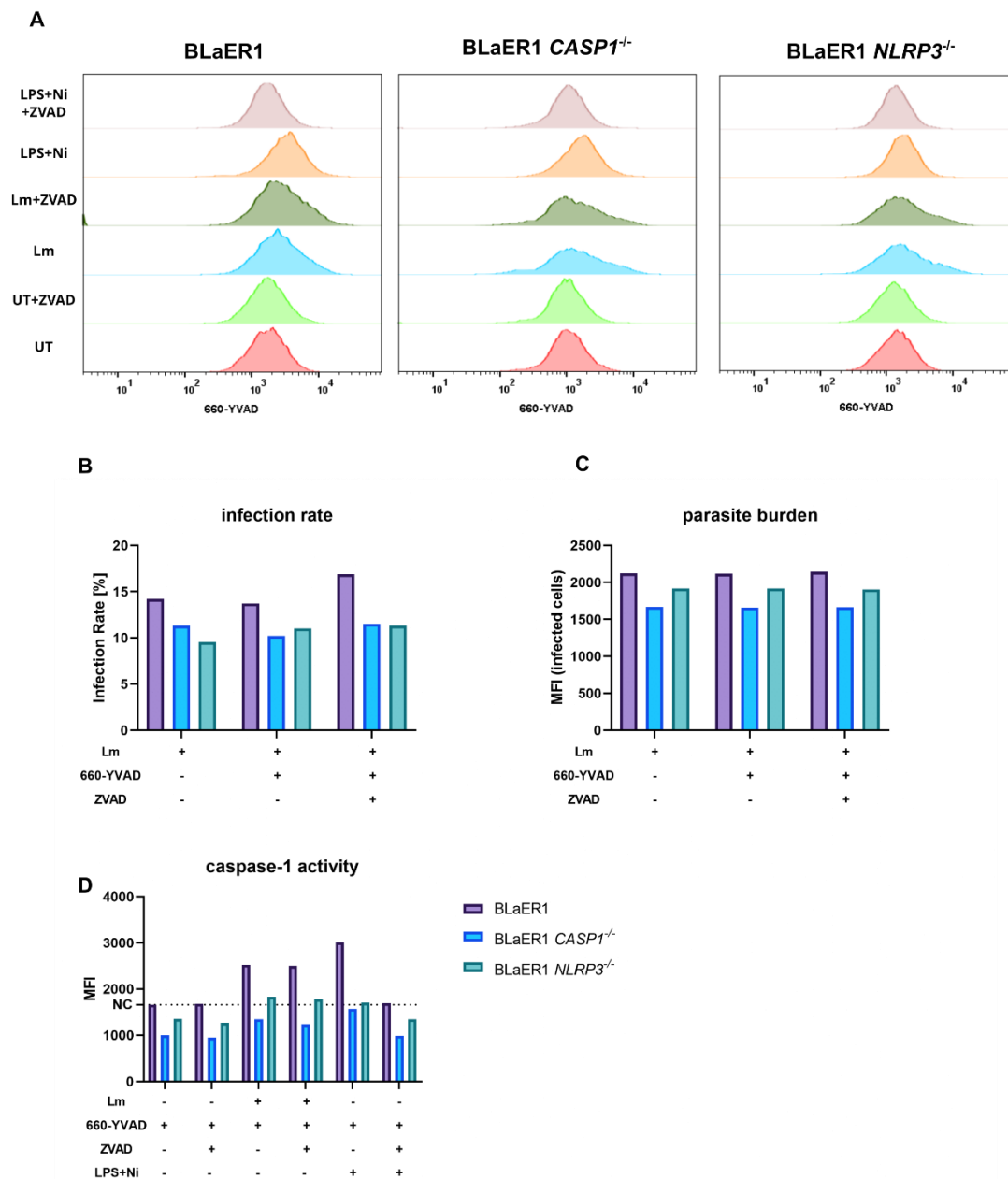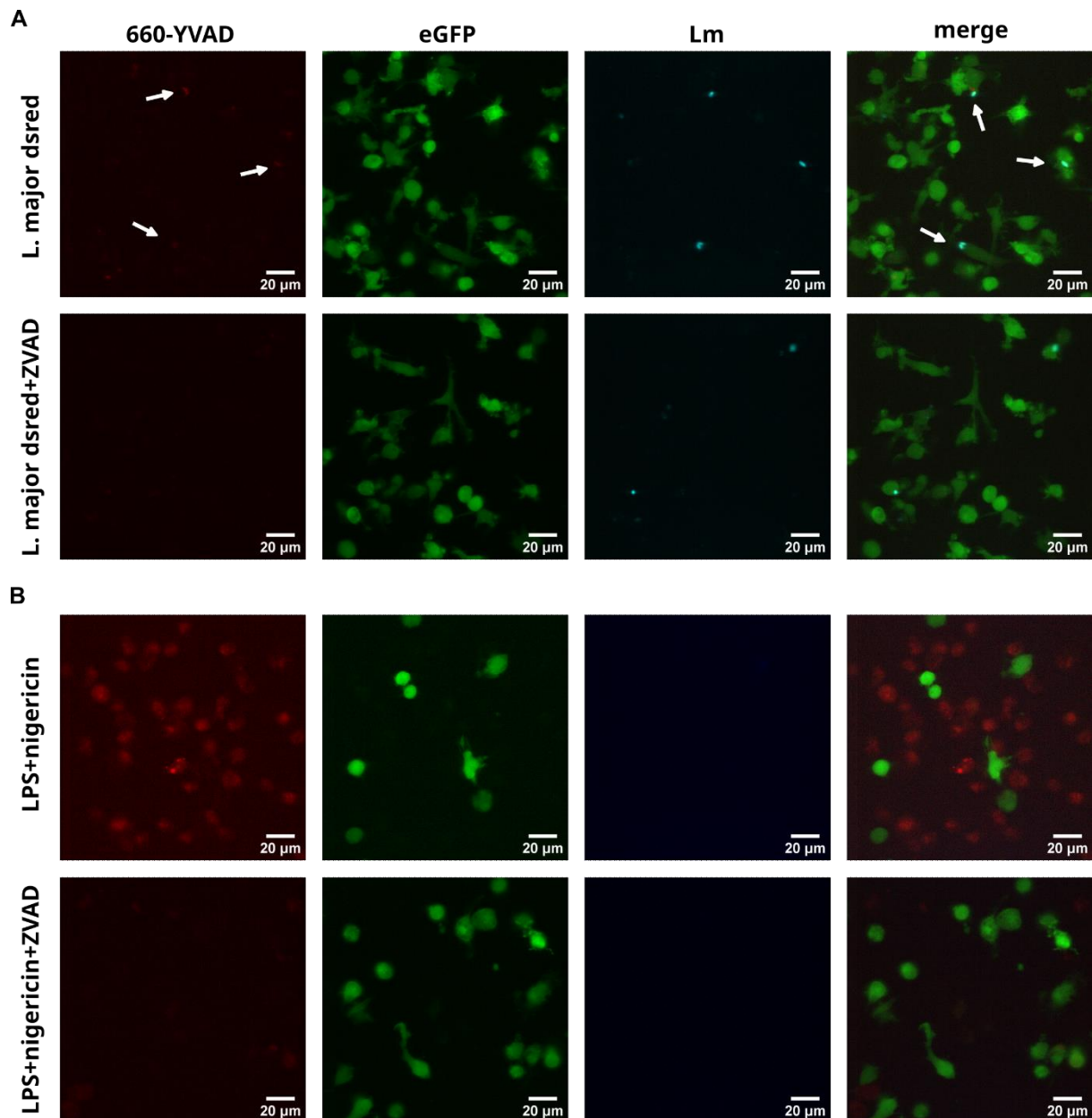**Figure 19: *L. major* infection leads to caspase-1 activity in BLaER1 cells**

BLaER1, BLaER1 *Casp1*^{-/-} and BLaER1 *NLRP3*^{-/-} cells were seeded into a chamber slide, primed with 200 ng/ml LPS for 3 h, followed by treatment with nigericin for 30 min or infection with stationary-phase *L. major* DsRed at MOI 10 for 3 h. After 2.5 h of infection and simultaneously with nigericin treatment 50 µM of pan-caspase-inhibitor ZVAD was added to all inhibited conditions. After 3 h of infection, cells were harvested, stained with 660-YVAD, and analyzed by fluorescence microscopy. Images show the 660-YVAD staining, eGFP signal, DsRed signal and a merge of all channels (from left to right) of cells infected with *L. major* DsRed (A, upper panel), cells infected with *L. major* DsRed and inhibited with ZVAD (A, lower panel), cells treated with LPS and nigericin (B, upper panel) or cells treated with LPS and nigericin and inhibited with ZVAD (B, lower panel). The intensity values of the 660-YVAD channel were multiplied by two for better visualization. Caspase-1 activity in proximity to intracellular *L. major* DsRed is indicated by white arrows.

4.2.2 Activation of NLRP3 inflammasome is dependent on phagocytosis-mediated production of ROS

To determine whether the activation of the human NLRP3 inflammasome by *L. major* infection was dependent on the NADPH oxidase-mediated production of phagolysosomal ROS by the host cell upon uptake of the parasite, one of the main NLRP3 activating pathways in the murine system, BLaER1 cells were stimulated with LPS or R848, treated with the NADPH oxidase inhibitor DPI or left untreated and were, subsequently, infected with Alexa-Fluor405-labeled stationary-phase *L. major* for 3 h. 30 min before the end of the infection, cells were stained with fluorescent ROS probe DHE, which is specific for superoxide and hydrogen peroxide. For LPS-stimulated cells, a significantly higher level of ROS was detected in the infected BLaER1 cells (33 % of positive control) compared to the uninfected, stimulated control (**Figure 20A**). This effect was specific to *L. major* infection, as it could also be observed in an unstimulated, infected control (18 % of positive control) (**Figure 20A**) and in R848 stimulated cells (26 % of positive control) (**Figure 20C**). Unexpectedly, treatment of cells with DPI lead to a high level of ROS in uninfected LPS- (76 % of positive control) and R848-stimulated (72 % of positive control) cells (**Figure 20A** and **Figure 20C**). Infection of DPI-treated, infected BLaER1 cells did not lead to an additional increase in ROS level in either LPS stimulated (76 % of positive control) or R848-stimulated (82 % of positive control) cells above the high background caused by DPI treatment alone. *L. major* infection of LPS-stimulated cells lead to a strong and significant increase in IL-1β secretion compared to the uninfected control (366 pg/ml vs. 223 pg/ml), but not in cells additionally treated with DPI (147 pg/ml vs. 135 pg/ml) (**Figure 20B**). The same trend was observed for R848-stimulated BLaER1 cells (273 pg/ml vs. 112 pg/ml for cells without DPI and 81 pg/ml vs. 58 pg/ml for DPI treated cells), even though the level of significance was not reached (**Figure 20D**). Notably, DPI-treated cells showed a significantly reduced infection rate for both LPS stimulated and R848 stimulated BLaER1 cells, when compared with an infected non-DPI treated control (**Figure 20E**). Taken together, the inhibition of infection-specific ROS in DPI-treated BLaER1 cells and the associated ablation of IL-1β secretion showed a dependence of NLRP3 inflammasome activation on the production of ROS mediated by parasite uptake, while the high ROS background caused by DPI treatment did not activate NLRP3 inflammasome.
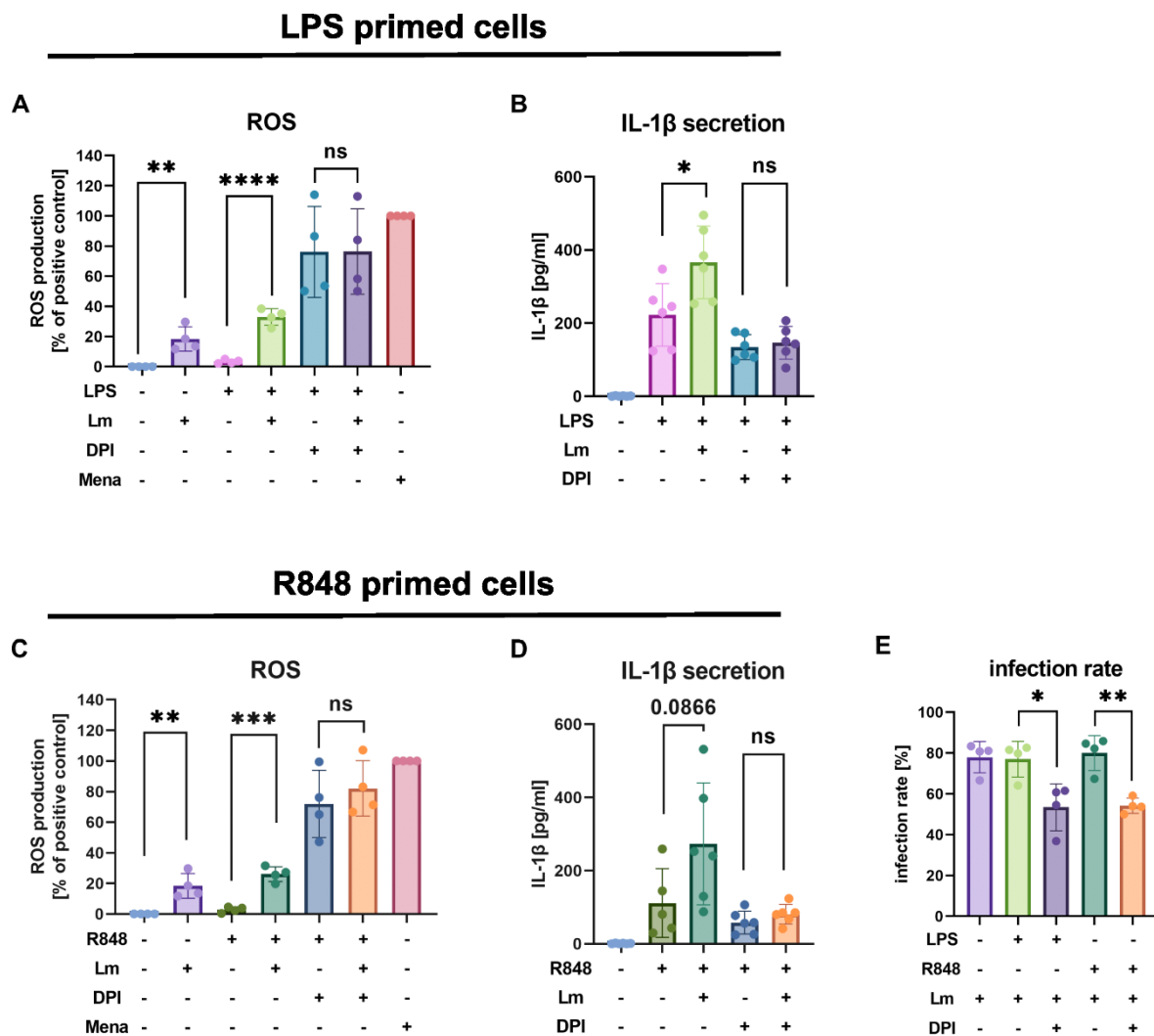
Figure 20: Phagocytosis-mediated ROS production is crucial for NLRP3 inflammasome activation by *L. major*
BLaER1 cells were primed with 200 ng/ml LPS (A and B) or 500 nM R848 (C and D) for 15 h, treated for 1 h with 50 µM DPI and subsequently infected with Alexa-Fluor405 stationary-phase *L. major* parasites at MOI 10 for 3 h. After 2.5 h cells were stained with 5 µM DHE. (B and D) IL-1β concentrations of supernatants of LPS primed (B) and R848 primed (D) cells were collected at 3 h post infection. (A, C and E) cells were harvested and analyzed by flow cytometry. (A and C) MFI of DHE stained cells primed with LPS (A) or R848 (C) normalized between an untreated negative control and a positive control of cells stimulated with 1 mM menadione for 1 h. (E) Share of Alexa-Fluor405+ BLaER1 cells. N=3-4. Graphs show mean values + SD. Significance was determined by unpaired t-test. * p<0.05, **p<0.01, ***p<0.001, ****p<0.0001.

To elucidate the high level of ROS observed for DPI-treated cells, the experiment was repeated with two alternative NADPH oxidase inhibitors, apocynin and NOX VII. As observed for DPI in the previous experiment, the treatment with apocynin and NOX VII led to a higher level of ROS that was significant compared to cells stimulated with LPS or R848 (**Figure 21A**). Because fewer controls were used in the flow cytometric analysis of this experiment, it could not be determined whether apocynin and NOX VII ablated the infection-specific increase of ROS levels previously observed for DPI-treatment. Regarding IL-1β, no significant differences in secretion could be observed irrespective of stimulus, infection, and inhibitor. Notably, cells treated with apocynin or NOX VII alone showed a trend towards a higher IL-1β

secretion compared to infected cells treated with apocynin or NOX VII (**Figure 21B**). This observation was made irrespective of the used priming stimulus. To ensure comparability of the samples infected with *Leishmania*, no differences in the infection rate could be observed (**Figure 21C**). This experiment suggested that the high background level of ROS was not specific to a particular NADPH oxidase inhibitor.
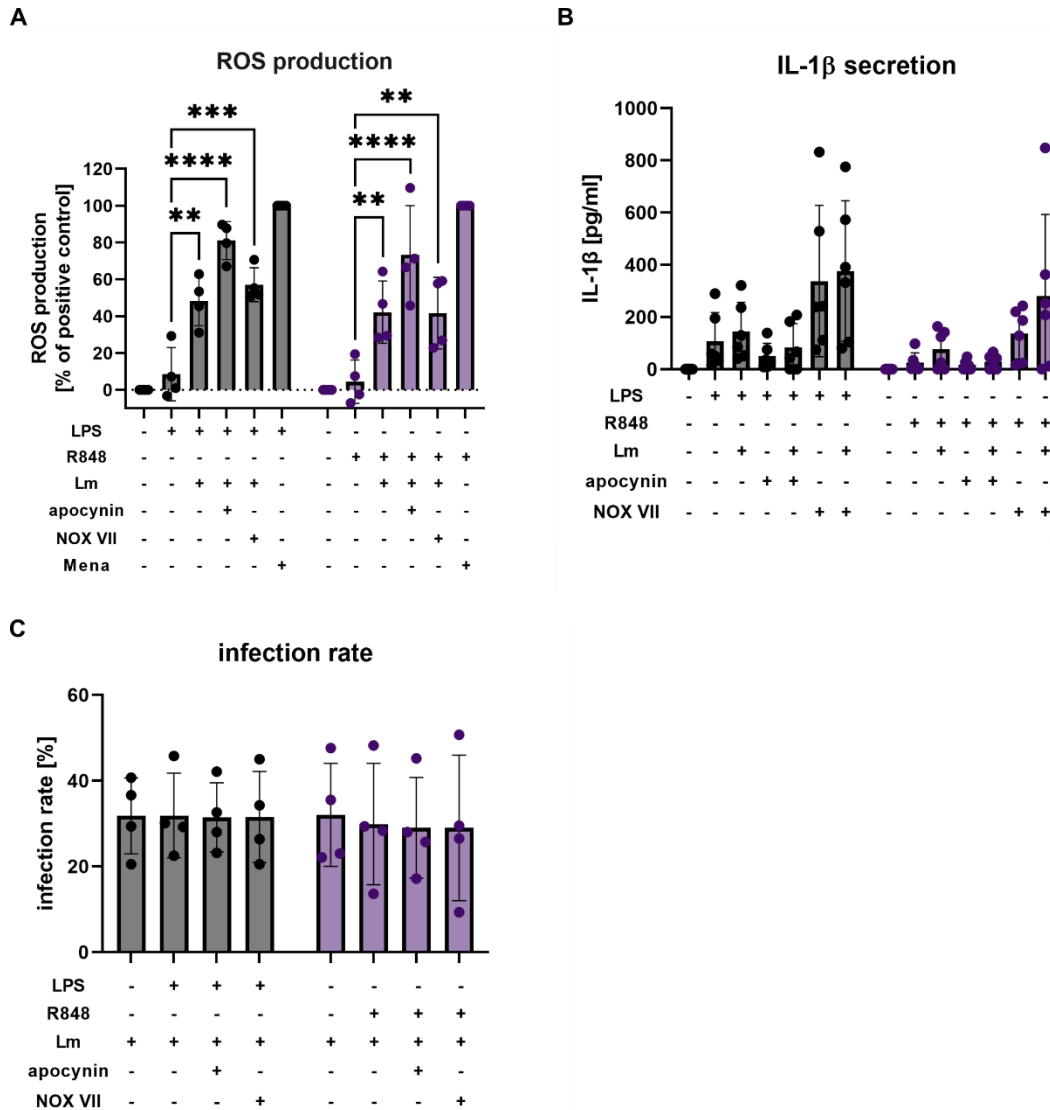
Figure 21: High ROS signal is also observed for alternative NADPH oxidase inhibitors apocynin and NOX VII
BLaER1 cells were primed with 200 ng/ml LPS or 500 nM R848 for 15 h, treated for 1 h with 1 µM of apocynin or 50 ng/ml NOX VII and subsequently infected with Alexa-Fluor405 stationary-phase *L. major* parasites at MOI 10 for 3 h. After 2.5 h cells were stained with 5 µM DHE. (B) IL-1β concentrations of supernatants were collected at 3 h post infection. (A, C and D) cells were harvested and analyzed by flow cytometry. (A) MFI of DHE stained cells normalized between an untreated negative control and a positive control of cells stimulated with 1 mM menadione for 1 h. (C) Share of Alexa-Fluor405+ BLaER1 cells. N=4. Graphs show mean values + SD. Significance was determined by Two-Way-ANOVA. * $p<0.05$, **$p<0.01$, ***$p<0.001$, ****$p<0.0001$.

Next, to determine whether the high ROS background was caused by DMSO used to dissolve the inhibitors, R848 stimulated cells were treated with different concentrations of DPI and NOX VII, thereby, introducing different amounts of DMSO into the culture. R848 stimulated and NADPH oxidase inhibitor-treated cells were subsequently infected with Alexa-Fluor405 labeled stationary-phase *L. major* for 3 h. Treatment with high concentrations of DMSO alone (5 % and 10 %) served as a positive control. Flow cytometric analysis of the ROS production showed that the concentration of the NADPH oxidase inhibitors had a small and inconsistent effect on the observed ROS level (**Figure 22A**). While reduction of the concentration lead to a decrease of ROS in NOX VII treated cells, it led to an increase in DPI treated cells. Moreover, the treatment with DMSO alone did not only not increase the level of ROS, but decreased ROS levels to -27 % for cells treated with 5 % of DMSO and -28 % for cells treated with 10 % of DMSO, meaning that ROS levels of DMSO-treated BLaER1 cells were lower than the ROS levels of untreated BLaER1 cells used for normalization. IL-1β secretion of NOX VII treated cells, decreased with decreasing concentrations, while it remained constant for cells treated with different concentrations of DPI (**Figure 22B**). Summing it up, while the first experiment provided strong evidence that inhibition of phagocytosis-mediated ROS production leads to a reduction of NLRP3 inflammasome activation despite the high background ROS level caused by DPI treatment, the follow-up experiments with apocynin, NOX VII and DMSO controls failed to elucidate the high background signal caused by NADPH oxidase inhibition.
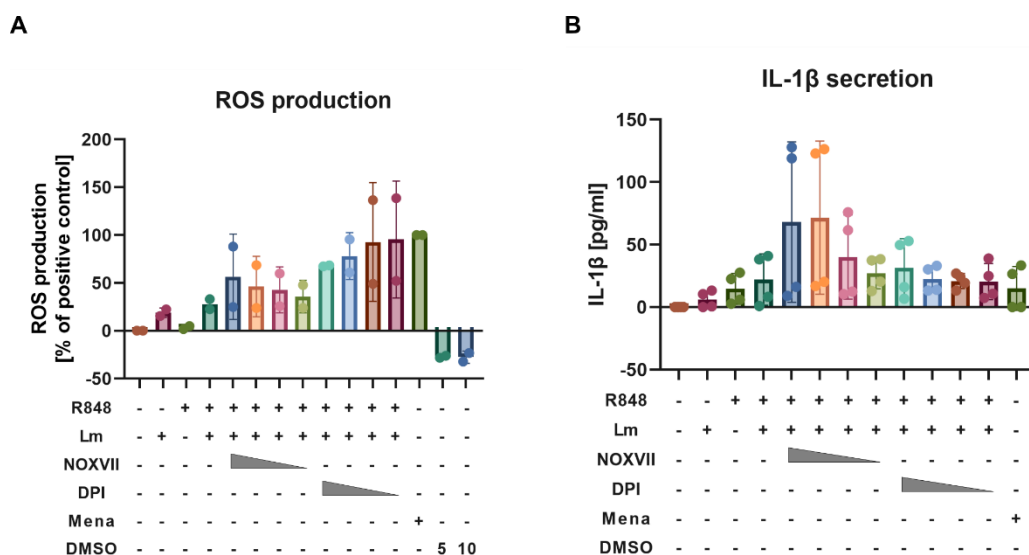
Figure 22: High ROS signal of NADPH oxidase inhibitors is independent of concentration, inhibitor or DMSO.
BLaER1 cells were primed with 500 nM R848 for 15 h, treated for 1 h with 125 ng/ml, 50 ng/ml, 25 ng/ml, or 12.5 ng/ml NOX VII, or 2.5 µM, 1.25 µM, 612 nM or 25 nM of DPI (high to low indicated by grey gradient) or with high concentrations of DMSO (5% or 10 %) and subsequently infected with Alexa-Fluor405 stationary-phase *L. major* parasites at MOI 10 for 3 h. After 2.5 h cells were stained with 5 µM DHE. (B) IL-1β concentrations of supernatants were collected at 3 h post infection. (A) cells were harvested and analyzed by flow cytometry. MFI of DHE stained cells normalized between an untreated negative control and a positive control of cells stimulated with 1 mM menadione for 1 h. N=2. Graphs show mean values + SD.

4.2.3 Generation of DsRed expressing *L. major* T7/Cas9 and *L. major* T7/Cas9 *LPG1*^{-/-}

After demonstrating the dependence of NLRP3 inflammasome activation on *L. major*-mediated ROS production, I sought to investigate the second major NLRP3-activating pathway in the murine system, the presence of LPG on the parasite surface. For this, a DsRed-expressing *L. major* strain with a knocked out *LPG1* gene, which has been previously reported to not express LPG on the cell surface [156], had to be created.

4.2.3.4 Generation of L. major T7/Cas9 DsRed

In a first step, *L. major* T7/Cas9 DsRed was created, by integration of pLEXSY-DsRed-sat2.1 into the 18S-rRNA locus of *L. major* T7/Cas9. The plasmid was generated by Gibson assembly of a 6.3 kbp fragment of the pLEXSY-sat2.1 vector and a DsRed sequence amplified from pSSU-DsRed-hyg. The resulting pLEXSY-DsRed-sat2.1 plasmid was digested with SwaI and the resulting 6.3 kbp fragment, was introduced into logarithmic-phase *L. major* T7/Cas9 by electroporation. After subsequent limiting dilution, DsRed expressing clones were identified by flow cytometry. Successful integration of DsRed into the genome was confirmed by PCR with primers for the sat resistance cassette and the 3'-UTR of the 18s-rRNA locus (SAT+SSU). Subsequent electrophoresis showed a band with a size of approximately 2.5 kbp for all tested clones but not the wild type control, indicating that the DsRed cassette integrated into the genome at the designated site. PCR with primers for 18s-rRNA locus (SSU+SSU) showed a band with a size of approximately 1.5 kbp for all tested clones, indicating the presence of intact 18s-rRNA loci in these strains. Unexpectedly, no 1.5 kbp band was visible for the wild type control. All clones retained DsRed expression as determined by flow cytometry using non-fluorescent *L. major* wild type parasites as control.

4.2.3.5 Generation of L. major T7/Cas9 DsRed LPG1^{-/-}

After generation of *L. major* T7/Cas9 DsRed, a *L. major* T7/Cas9 DsRed *LPG1*^{-/-} strain was generated by electroporation of logarithmic-phase *L. major* T7/Cas9 DsRed with two sgRNAs targeting the 5' and 3' end of the *LPG1* gene and a blasticidin resistance cassette with homology flanks added by long primer PCR. After antibiotic selection and two rounds of limiting dilution, *L. major* T7/Cas9 DsRed *LPG1*^{-/-} single clones were tested for the presence of the *LPG1* gene and genomic integration of the blasticidin resistance cassette by PCR with *L. major* T7/Cas9 DsRed parasites serving as negative control.

PCR with primer pairs binding the *LPG1* gene (5+6) or the *LPG1* gene and its 3'-UTR showed band with sizes of 1 kbp and 1.5 kbp, respectively, for the *L. major* T7/Cas9 DsRed (wt) but not for the clones A9 and F1 (**Figure 23A**), indicating the absence of the *LPG1* gene in these clones. Additionally, a 1.5 kbp sized band was observed for the primer pair binding the blasticidin resistance cassette and the 3'UTR of the *LPG1* gene (B+7) for both clones, confirming the integration of the resistance cassette into the *LPG1* locus. Both clones retained DsRed expression as determined by flow cytometry using non-fluorescent *L. major* wild type parasites as control (**Figure 23B**).
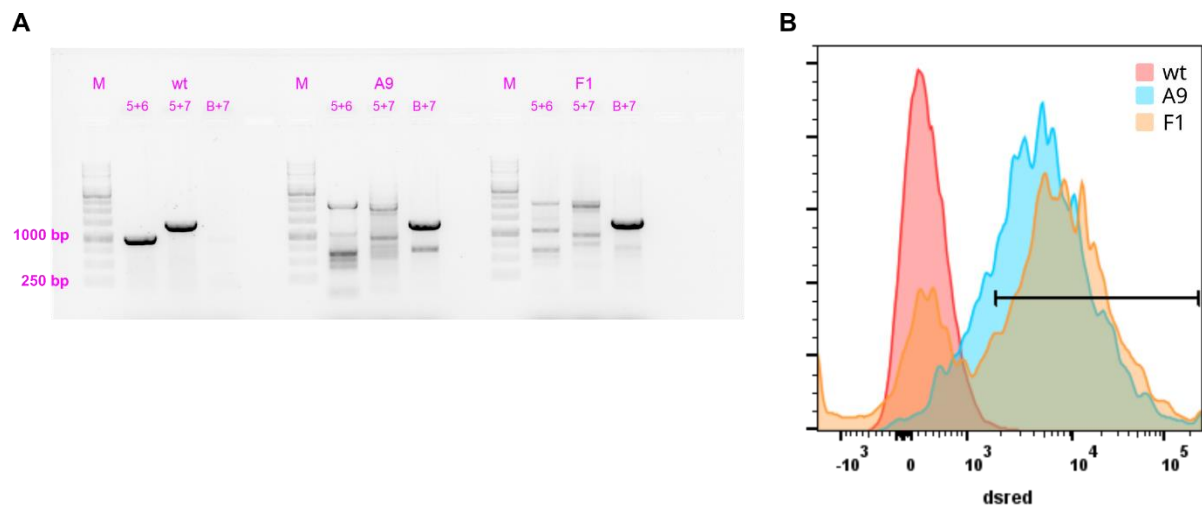
Figure 23: Generation of *L. major* T7/Cas9 DsRed LPG1$^{-/-}$.
L. major T7/Cas9 DsRed were electroporated with a 5'-sgRNA targeting the LPG1 gene, a 3'-sgRNA targeting the LPG1 gene and a linearized blasticidin or puromycin resistance cassette amplified from the pPT plasmids by long primer PCR to create homology flanks. After recovery and two rounds of limiting dilution clones were tested for integration of the resistance cassette by PCR and for retained DsRed expression by flow cytometry. (A) Colony PCR of selected clones from with primer pair binding inside of the LPG1 gene (5+6), inside the LPG1 gene and downstream of the LPG1 gene (5+7), or inside of the blasticidin resistance gene and downstream of the LPG1 gene (B+7). (B) Relative DsRed fluorescence of confirmed knockouts from C.

4.2.4 Activation of the NLRP3 inflammasome is dependent on presence of LPG on the parasite surface

After successful generation of *L. major* T7/Cas9 DsRed and *L. major* T7/Cas9 DsRed *LPG1$^{-/-}$*, the role of parasite LPG on NLRP3 inflammasome activation was investigated. For this, BLaER1 cells, BLaER1 *Casp1$^{-/-}$* cells and BLaER1 *NLRP3$^{-/-}$* cells were stimulated with LPS (**Figure 24A**, **C** and **E**) or R848 (**Figure 24B**, **D** and **F**) and subsequently infected with stationary-phase *L. major* T7/Cas9 DsRed or *L. major* T7/Cas9 DsRed *LPG1$^{-/-}$*. Infection rate and parasite burden were analyzed by flow cytometric analysis, while NLRP3 inflammasome activation was assessed by IL-1β ELISA. For LPS stimulated cells, infection with *L. major* T7/Cas9 DsRed resulted in a strong and significant increase in IL-1β secretion compared

to the uninfected control (702 pg/ml vs. 217 pg/ml) (**Figure 24A**). In contrast, IL-1β secretion did not increase significantly in response to infection with *L. major* T7/Cas9 DsRed *LPG1*^{-/-} (333 pg/ml). The same observations were made for R848 stimulated cells, in which infection with *L. major* T7/Cas9 DsRed resulted in a significantly increased IL-1β secretion of 286 pg/ml compared to the uninfected control (57 pg/ml) while to infection with *L. major* T7/Cas9 DsRed *LPG1*^{-/-} did not increase IL-1β secretion (102 pg/ml) (**Figure 24B**). NLRP3 inflammasome specificity was confirmed by the absence of IL-1β secretion in BLaER1 *Casp1*^{-/-} and BLaER1 *NLRP3*^{-/-} cells irrespective of stimulus and parasite strain (**Figure 24A** and **B**). Notably, an increased infection rate was observed for *L. major* T7/Cas9 DsRed *LPG1*^{-/-} infected BLaER1 and BLaER1 *NLRP3*^{-/-} cells compared to BLaER1 and BLaER1 *NLRP3*^{-/-} cells infected with *L. major* T7/Cas9 DsRed. Thus, the impaired NLRP3 inflammasome activation caused by absence of LPG was not only independent of the infection rate, but also could not be rescued by the higher infectivity of the knockout parasites. This was the case for both LPS stimulated (**Figure 24C**) and R848 stimulated (**Figure 24D**) cells. No differences in parasite burden were observed between *L. major* T7/Cas9 DsRed and *L. major* T7/Cas9 DsRed *LPG1*^{-/-} for any tested cell type and stimulus (**Figure 24E** and **F**). Summing it up, the drastic reduction of NLRP3-dependent IL-1β secretion in absence of LPG on the parasite surface demonstrated the dependency of inflammasome activation on parasite LPG.
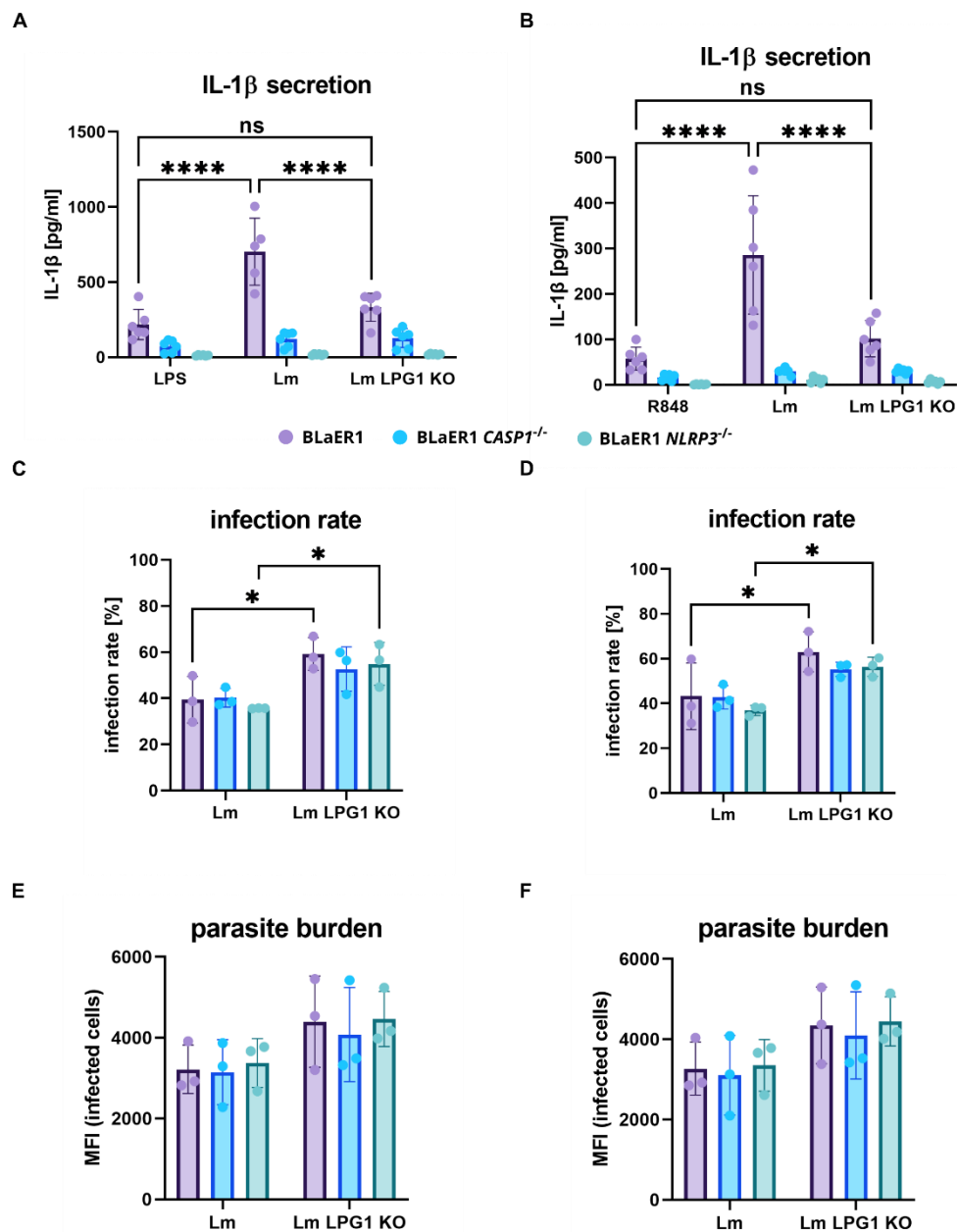
Figure 24: *Leishmania*-mediated NLRP3 inflammasome activation is dependent on the presence of LPG on the surface of the parasite.
BLaER1, BLaER1 *Casp1*^{-/-} and BLaER1 *NLRP3*^{-/-} cells were primed with 200 ng/ml LPS (A, C and E) or 500 nM R848 (B, D and F) for 15 h and subsequently infected with stationary-phase *L. major* T7/Cas9 DsRed parasites or *L. major* T7/Cas9 DsRed LPG1^{-/-} parasites at MOI 10 for 3 h. (A and B) IL-1β concentrations of supernatants of LPS primed (A) and R848 primed (B) cells determined by ELISA. (C-F) cells were harvested and analyzed by flow cytometry. (C and D) Share of LPS primed (C) and R848 primed (D) DsRed+ BLaER1, BLaER1 *Casp1*^{-/-} and BLaER1 *NLRP3*^{-/-}. (E and F) MFI of LPS primed (E) and R848 primed (F) DsRed+ BLaER1, BLaER1 *Casp1*^{-/-} and BLaER1 *NLRP3*^{-/-} cells. N=3. Graphs show mean values + SD. Significance was determined by Two-Way-ANOVA. * p<0.05, **p<0.01, ***p<0.001, ****p<0.0001.

4.2.5 Generation of caspase-4 and caspase-5 knockouts in BLaER1 cells

After demonstrating that the presence of LPG on the parasite surface is crucial for *Leishmania*-mediated NLRP3 inflammasome activation, I wondered whether this activation is facilitated by the human orthologs of murine caspase-11, namely caspase-4 and caspase-5. To allow the investigation of this hypothesis, BLaER1 *CASP4$^{-/-}$* and BLaER1 *CASP5$^{-/-}$* cell lines were created by nucleofection of udBLaER1 cells with ribonucleotide protein complexes (RNPs) consisting of a sgRNA targeting either the *CASP4* or the *CASP5* gene and recombinant Cas9 protein. At 24 h post nucleofection (p.n.), udBLaER1 cells nucleofected with pCAGGS-Redstar (plasmid) and or water (mock) were harvested and analyzed by flow cytometry (**Figure 25A-C**). The gating strategy consisted of an FSC-A vs. SSC-A gate to identify udBLaER1 cells, followed by a single cell gate and a viability gate based on eGFP expression (**Figure 25A**). The overlayed histogram of the relative RedStar fluorescence of viable mock and plasmid nucleofected cells (**Figure 25B**) showed high share of RedStar expressing cells (56 %), thus confirming the successful nucleofection of udBLaER1 cells (**Figure 25C**). Seven days p.n. the nuclease activity of the used RNPs was controlled by flow cytometric analysis of udBLaER1 cells nucleofected with an RNP targeting eGFP, thereby confirming the successful complexion of the RNPs and activity of the Cas9 protein. The gating strategy was similar to the one used for to control the nucleofection efficiency, but viability was determined by PI exclusion to be independent of eGFP expression (**Figure 25D**). For the nucleofected udBLaER1 eGFP$^{-/-}$ population (BLaER1 eGFP$^{-/-}$ pop) a strong decrease in eGFP$^+$ was observed compared to the non-nucleofected udBLaER1 cells (13 % vs. 100 %), while the share of eGFP$^-$ cells increased (30 %) compared to the clonal udBLaER1 eGFP$^{-/-}$ cells (BLaER1 eGFP$^{-/-}$). Most of the cells retained an intermediate expression of eGFP (**Figure 25E**).
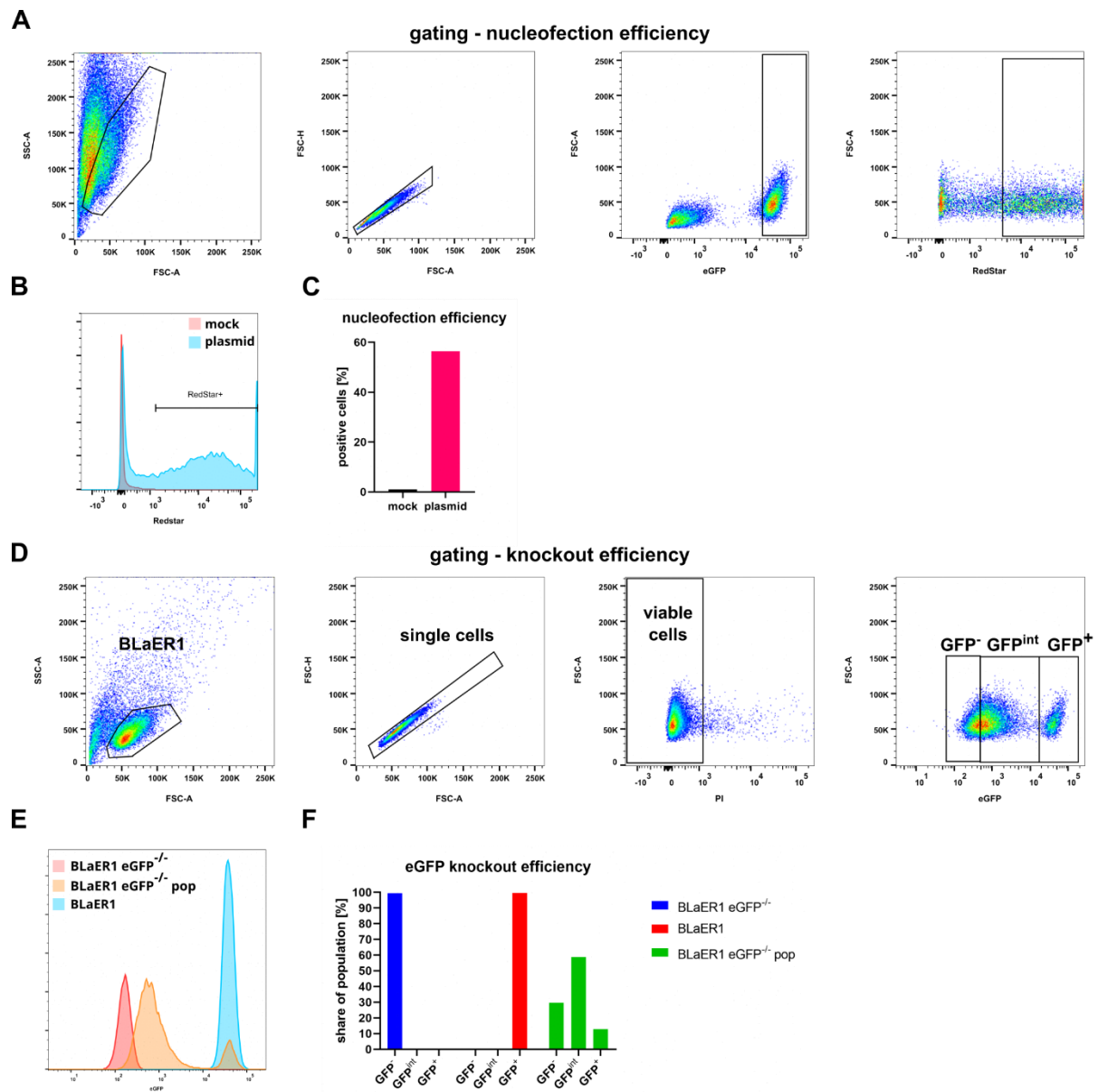
Figure 25: Flow cytometric analysis of nucleofection efficiency and functionality of RNPs.
BLaER1 cells were nucleofected with ribonucleoprotein complexes (RNPs) consisting of recombinant Cas9 protein and sgRNAs targeting the CASP4 gene, CASP5 gene or the eGFP gene. Additionally, BLaER1 cells were nucleofected with a CAGGS-RedStar plasmid to control the nucleofection process. After 24 h of recovery, plasmid-nucleofected BLaER1 cells were harvested and analyzed by flow cytometry. At seven days post nucleofection, the functionality of the used RNPs was assessed by flow cytometric analysis of the eGFP knockout efficiency. BLaER1 cells nucleofected with eGFP targeted RNPs were harvested, stained with 500 ng/ml PI and analyzed by flow cytometry. (A) BLaER1 population was identified in FSC-A vs. SSC-A plot, followed by quality control gates for single cells and viability. Finally, RedStar positivity was determined by gating against mock nucleofected cells. (B) Overlay of relative fluorescence histograms of mock and plasmid nucleofected cells. (C) Share of RedStar⁺ cells. (D) Gating strategy used to determine eGFP knockout efficiency. Population and single cells were gated as described in A and viability was determined by PI exclusion. GFP positivity and negativity were gated against BLaER1 and BLaER1 eGFP$^{-/-}$ cells, respectively. The relative fluorescence values in between these controls were termed intermediate. (E) Overlay of relative fluorescence histograms of BLaER1, BLaER1 eGFP$^{-/-}$ and the BLaER1 eGPF$^{-/-}$ population. (F) Share of eGFP positive, eGFP negative and eGFP intermediate cells.

After complexion and activity of the used RNPs had been validated, putative udBLaER1 *Casp4*^{-/-} and udBLaER1 *Casp5*^{-/-} single clones were generated by limiting dilution, transdifferentiated, and tested by Western blot for successful knockout of caspase-4 or caspase-5, respectively. Putative BLaER1 *Casp4*^{-/-}, clones (**Figure 26A** and **B**), were analyzed by SDS-PAGE. Loading of a sufficient amount of protein was controlled by Coomassie staining (**Figure 26A**). On the western blot, a band of approximately 45 kDa could be observed for 10 of the 12 clones (**Figure 26B**). This corresponds well to the molecular weight of caspase-4 of 43 kDa (gene ID: ENSG00000196954.14; [157]). Therefore, knockout of caspase-4 was considered to be successful for all clones that did not display a band with a size of approximately 45 kDa, despite sufficient protein loading. After confirmation of the *Casp4* knockout, the efficiency of two clones (C9 and C3) to be transdifferentiated into the macrophage-like phenotype was analyzed flow cytometry. After transdifferentiation, both clones displayed a high expression of CD14 and CD11b while losing CD19 expression almost entirely (**Figure 26C**).
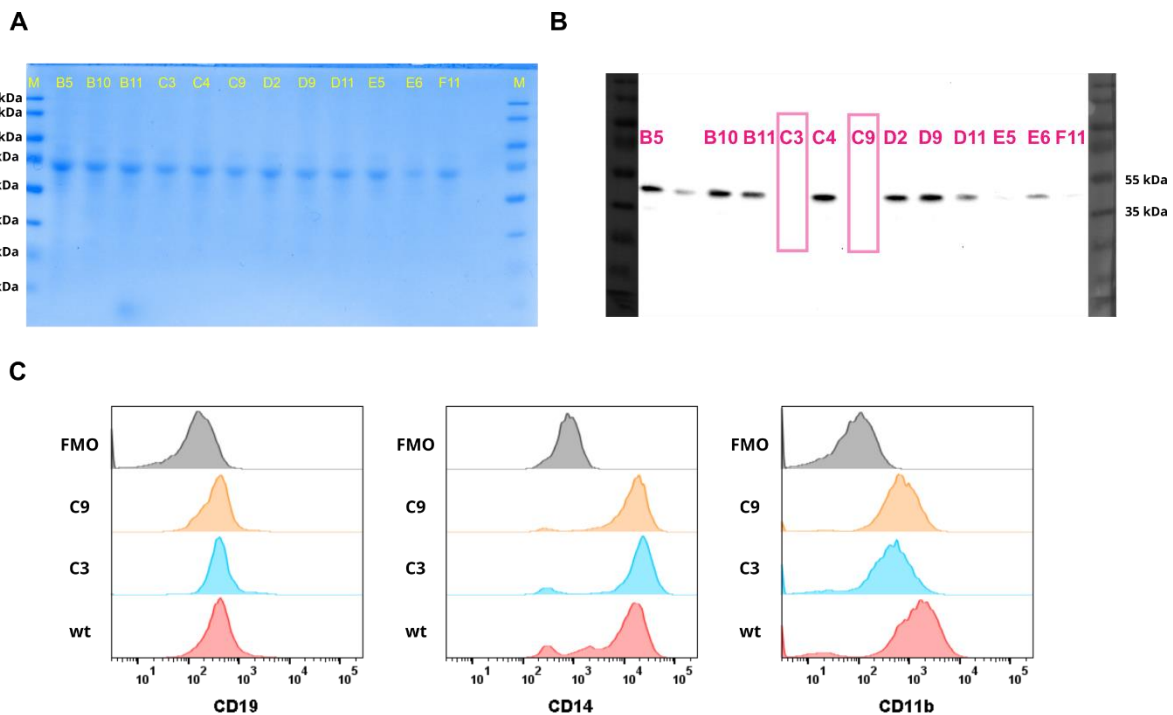
Figure 26: Confirmation of successful caspase-4 knockout in BLaER1 by western blot.
Single clones of BLaER1 cells nucleofected with CASP4 targeted RNPs were generated by limiting dilution, transdifferentiated and the expression of caspase-4 analyzed by western blot and Coomassie staining as loading control. (A) Coomassie stained gels of selected clones. (B) Western blots of selected clones (caspase-4 negative clones are highlighted by pink box). (C) Flow cytometric analysis of two confirmed caspase-4 knockout.

As for *Casp4* knockouts, putative BLaER1 *Casp5*^{-/-} clones), were analyzed by SDS-PAGE and Western blotting. However, on the initial Western blots intense protein bands at the size of 45 kDa and 70 kDa and several less intense ones were detected (data not shown). While the bands at approximately 45 kDa corresponds well to the predicted molecular weight of caspase-5 of 49 kDa (gene ID:

112

ENSG00000196954.14 [157]), the observation of multiple bands without consistent differences in intensity did not allow the unambiguous identification of BLaER1 *Casp5-/-* clones. Therefore, all putative BLaER1 *Casp5-/-* clones with no observed band at 45 kDa were analyzed again by western blot along with BLaER1 wild type cells as positive control. Sufficient loading of protein was confirmed by Coomassie staining (**Figure 27A**), while the western blot showed a very intense band at approximately 45 kDa for BLaER1 wild type cells, but not for any of the putative BLaER1 *Casp5-/-* (**Figure 27B**). As for *Casp4* knockouts, the knockout of *Casp5* was considered to be successful for all clones without a visible band with a size of approximately 45 kDa.
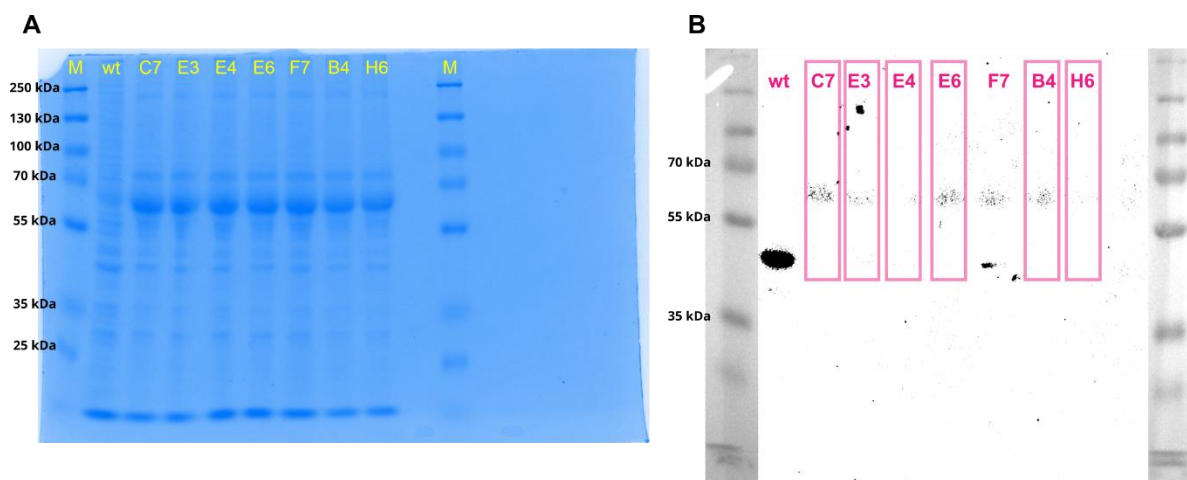
Figure 27: Confirmation of successful caspase-5 knockout in BLaER1 by western blot.
BLaER1 cells and BLaER1 *CASP5-/-* clones were transdifferentiated and analyzed for caspase-5 expression by western blot and Coomassie staining. (A) Coomassie stained gel. (B) western blot (caspase-5 negative clones are highlighted by pink box)

4.2.6 Infection of BLaER1 *Casp4-/-* and BLaER1 *Casp5-/-* cells with *L. major*

After successful generation of BLaER1 *Casp4-/-* and BLaER1 *Casp5-/-* cell lines, the role of these cytosolic sensor caspases on *L. major*-mediated NLRP3 inflammasome activation was investigated. For this, BLaER1 cells, BLaER1 *Casp4-/-* cells and BLaER1 *Casp5-/-* cells were stimulated with LPS, followed by aspiration of the supernatant and subsequent infection with stationary-phase *L. major* T7/Cas9 DsRed or *L. major* T7/Cas9 DsRed *LPG1-/-* (**Figure 28**). The infection rate was analyzed by flow cytometric analysis, while NLRP3 inflammasome activation was assessed by IL-1β ELISA. For LPS stimulated BLaER1 cells, BLaER1 *Casp4-/-* cells and BLaER1 *Casp5-/-* cells a significantly increased secretion of IL-1β was observed (**Figure 28A**). Upon infection with *L. major* T7/Cas9 DsRed or *L. major* T7/Cas9 DsRed *LPG1-/-* no cell type showed a significant increase of IL-1β secretion. However, for BLaER1 cells a clear trend towards an increase upon infection with *L. major* T7/Cas9 DsRed compared to LPS stimulated

uninfected cells could be observed (103 pg/ml vs 66 pg/ml), while the IL-1β secretion upon infection with *L. major* T7/Cas9 DsRed *LPG1*^{-/-} was less pronounced (74 pg/ml vs 66 pg/ml). Interestingly, the same trend could be observed for BLaER1 *Casp4*^{-/-} cells (114 pg/ml vs 76 pg/ml and 84 pg/ml) and BLaER1 *Cas5*^{-/-} cells (132 pg/ml vs 93 pg/ml and 104 pg/ml vs 93 pg/ml). Notably, neither the knockout of caspase-4 nor the knockout of caspase-5 reduced the IL-1β secretion upon *L. major* T7/Cas9 DsRed infection to the levels of *L. major* T7/Cas9 DsRed *LPG1*^{-/-} infected cells. This suggests a functional redundancy of these caspases in human cell. Noteworthy, that discarding of the supernatant prior to infection, led to an overall strongly decreased IL-1β secretion, when the findings from this experiment are compared to the results from **Figure 24**. Comparable to the previous experiments (**Figure 24**), the infection rate of BLaER1 cells, BLaER1 *Casp4*^{-/-} cells and BLaER1 *Casp5*^{-/-} cells with *L. major* T7/Cas9 DsRed *LPG1*^{-/-} parasites was significantly higher than the infection rate of *L. major* T7/Cas9 DsRed infected cells (57 % vs. 41 % for BLaER1, 48 % vs. 33 % for BLaER1 *Casp4*^{-/-} and 54 % vs. 36 % for BLaER1 *Casp5*^{-/-}) (**Figure 28B**).
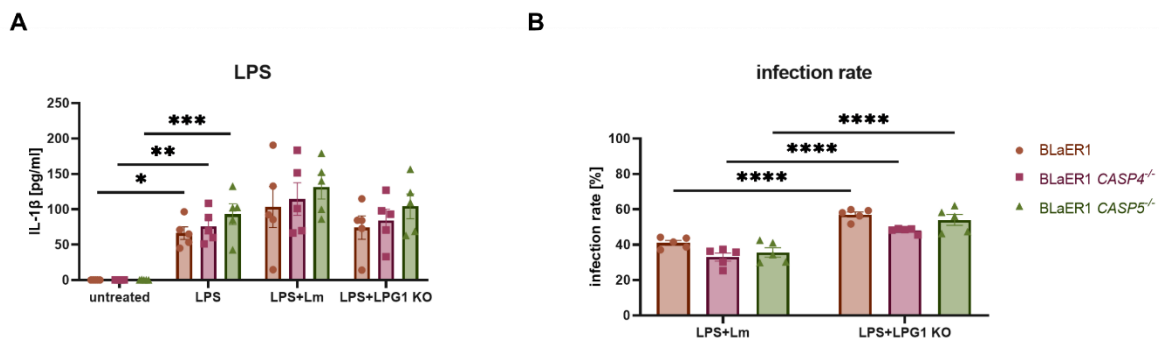
Figure 28 Caspase-4 and caspase-5 have a redundant function of sensing *L. major* LPG.
BLaER1, BLaER1 *CASP4*^{-/-} and BLaER1 *CASP5*^{-/-} cells were primed with 200 ng/ml LPS for 15 h and subsequently infected with stationary-phase *L. major* T7/Cas9 DsRed parasites or *L. major* T7/Cas9 DsRed LPG1^{-/-} parasites at MOI 10 for 3 h. (A) IL-1β concentrations of supernatants of LPS primed cells determined by ELISA. (B) Cells were harvested and analyzed by flow cytometry. (B) Share of DsRed+ BLaER1, BLaER1 *CASP4*^{-/-} and BLaER1 *CASP5*^{-/-}. N=5. Graphs show mean values + SD. Significance was determined by Two-Way-ANOVA. * p<0.05, **p<0.01, ***p<0.001, ****p<0.0001.

4.2.7 The NLRP3 inflammasome is functional, but subject to high donor variation in hMDMs.

Next, I sought to determine whether experiments conducted with BLaER1 cells could be performed in primary human cells using an inflammasome inhibitor instead of cell lines with knocked out components of the NLRP3 inflammasome. For this GM-CSF and M-CSF derived hMDMs were stimulated with LPS or R848, followed by treatment with the NLRP3 inflammasome inhibitor MCC950 and subsequent infection with stationary-phase *L. major* DsRed or treatment with nigericin. The infection rate was analyzed by flow cytometry, while NLRP3 inflammasome activation was assessed by

IL1-β secretion. No significant increase in IL1-β secretion was observed except for nigericin treated GM-CSF derived and M-CSF derived hMDMs, that were previously stimulated with LPS (3845 pg/ml and 3684 pg/ml, respectively) (**Figure 29A**) or R848 (3354 pg/ml and 4712 pg/ml, respectively) (**Figure 29B**). It is particularly noteworthy that the range of this positive control was very large and ranged from 145 pg/ml to 14,110 pg/ml for LPS stimulated GM-CSF hMDMs, 122 pg/ml to 8,721 pg/ml for LPS stimulated M-CSF derived hMDMs, 269 pg/ml to 10,918 pg/ml for R848 stimulated GM-CSF-derived hMDMs and 264 pg/ml to 13,589 pg/ml for R848 stimulated M-CSF-derived hMDMs. There was a clear trend towards an increase of IL1-β secretion for infected LPS stimulated GM-CSF derived hMDMs and R848 stimulated GM-CSF derived and M-CSF derived hMDMs. Furthermore, treatment with either concentration of MCC950 resulted in a trend towards a lower IL1-β secretion, irrespective of cell type and stimulus. MCC950 treatment did not result in any differences of the infection rate, but a significantly higher infection rate was observed for M-CSF derived hMDMs compared to GM-CSF derived hMDMs irrespective of stimulus (**Figure 29C** and **D**). Taken together, this data showed that even though primary hMDMs are inflammasome competent, the NLRP3 activation is donor-dependent and fluctuates strongly.
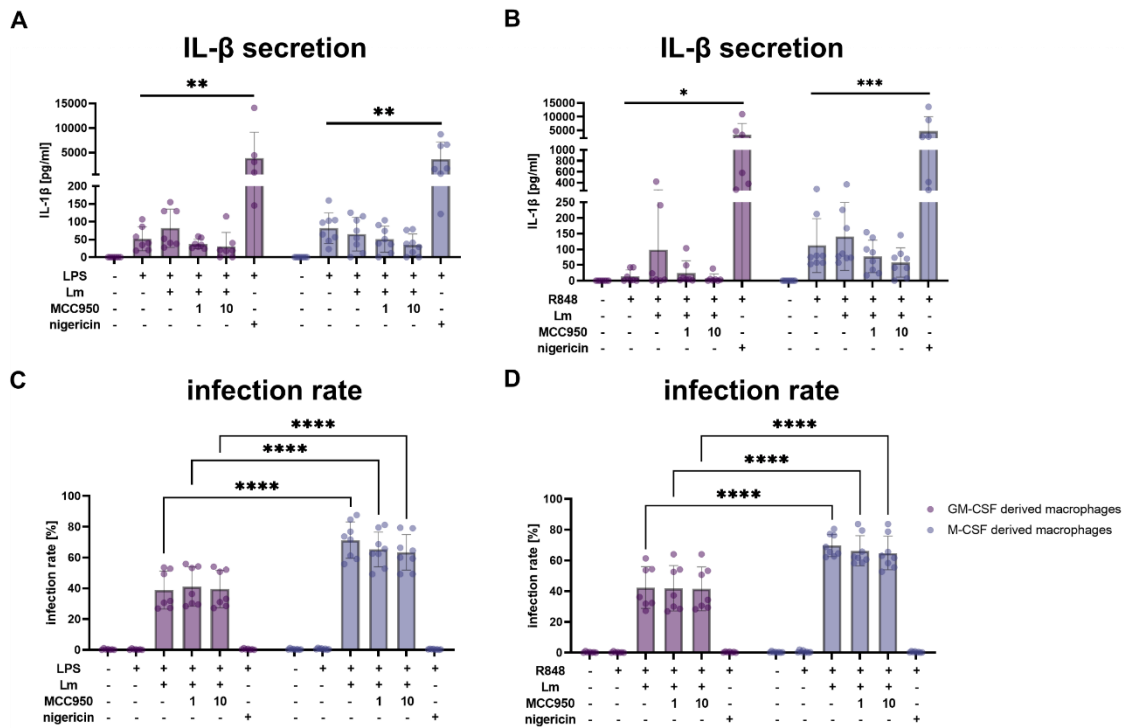
Figure 29: The NLRP3 inflammasome is functional in hMDMs, but subject to high donor variation.
GM-CSF derived and M-CSF derived hMDMs were stimulated with 500 ng/ml LPS (A and C) or 1 µM R848 (B and D) for 4 h, followed by infection with stationary-phase *L. major* DsRed at MOI 10 for 3 h. IL-1β concentrations of supernatants were determined by ELISA (A and B). Cells were harvested and analyzed by flow cytometry (C and D). (A and B) IL-1β concentrations of supernatants from LPS stimulated (A) or R848 stimulated (B) GM-CSF derived and M-CSF derived hMDMs. (C and D) Share of DsRed+ LPS stimulated (C) or R848 stimulated (D) GM-CSF derived and M-CSF derived hMDMs. N=3. Graphs show mean values + SD. Significance was determined by Two-Way-ANOVA. * p<0.05, **p<0.01, ***p<0.001, ****p<0.0001.

4.2.8 NLRP3 inflammasome activation does not lead to parasite restriction in human host cells

After characterization of the signals which lead to *Leishmania*-mediated NLRP3 inflammasome activation in human host cells, I investigated whether activation of the NLRP3 inflammasome leads to parasite restriction as it has been reported for the murine system [128]. For this, BLaER1 cells, BLaER1 *Casp1*-/- cells and BLaER1 *NLRP3*-/- cells were stimulated with LPS (**Figure 30B**, **E** and **H**), R848 (**Figure 30C**, **F** and **I**) or were left unstimulated (**Figure 30A**, **D** and **G**) and were, subsequently infected with stationary-phase *L. major* DsRed for up to 72 h. As in previous experiments, infection rate and parasite burden were analyzed by flow cytometry, while NLRP3 inflammasome activation was assessed by IL-1β ELISA. At 3 h p.i. *L. major* DsRed infection led to a strong increase of IL-1β in both LPS and R848 stimulated BLaER1 cells (459 pg/ml and 85 pg/ml, respectively) **(Figure 30B** and **C)** and to a small but significant increase in unstimulated BLaER1 cells (21 pg/ml) (**Figure 30A**). At 24 h p.i. IL-1β secretion was still significantly increased for unstimulated BLaER1 cells compared to BLaER1 *Casp1*-/- cells but not compared to BLaER1 *NLRP3*-/- cells. All observed increases in IL-1β were NLRP3 inflammasome

specific, as they were not observed for BLaER1 *Casp1*^{-/-} or BLaER1 *NLRP3*^{-/-} cells irrespective of infection or stimulus.
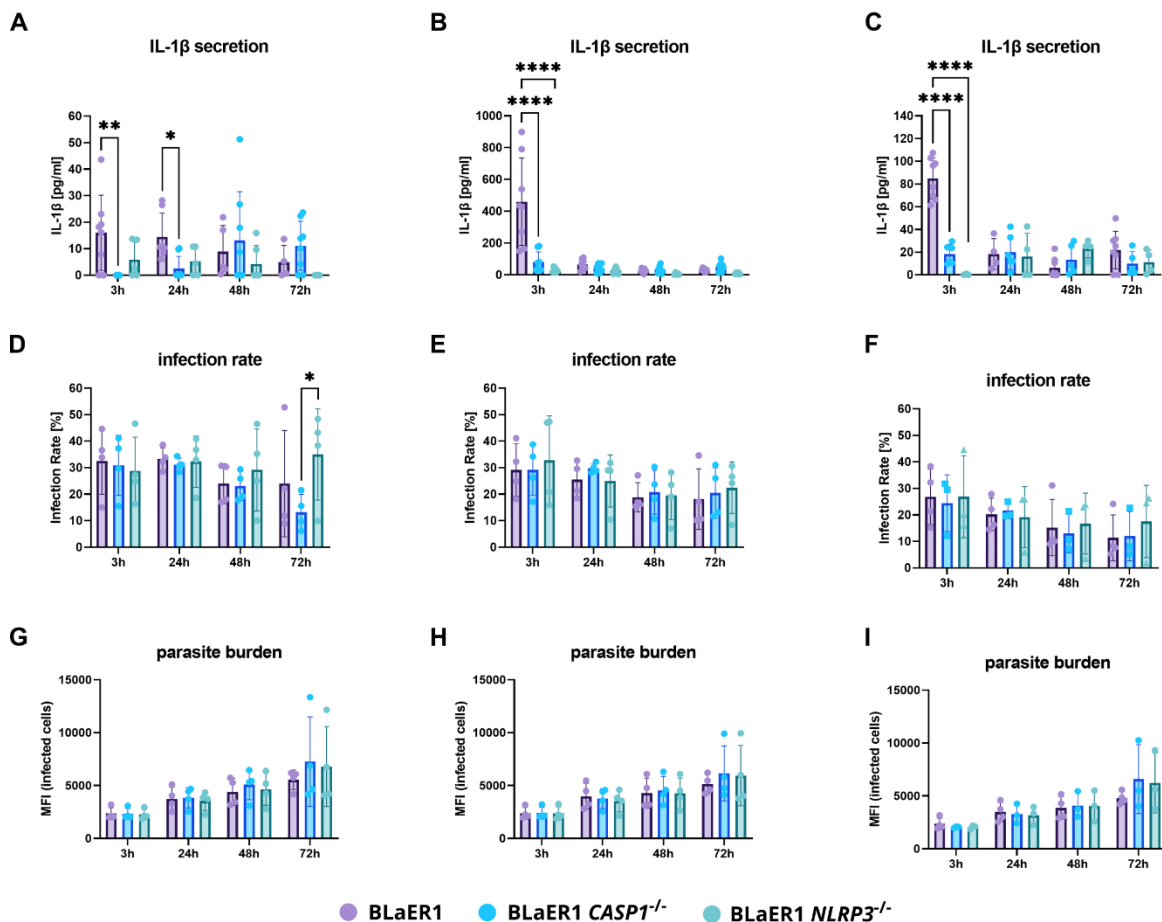
Figure 30: Activation of the NLRP3 inflammasome does not lead to parasite restriction.
BLaER1, BLaER1 *Casp1*^{-/-} and BLaER1 *NLRP3*^{-/-} cells were stimulated with 200 ng/ml LPS (B, E and H), 500 nM R848 (C, F and I) or left untreated (A, D and G) for 15 h and subsequently infected with stationary-phase *L. major* DsRed parasites at MOI 10 for up to 96 h. (A-C) IL-1β concentrations of supernatants collected between 3 h and 72 h post infection determined by ELISA. (D-I) cells were harvested and analyzed by flow cytometry. (D-F) Share of DsRed⁺ BLaER1, BLaER1 *Casp1*^{-/-} and BLaER1 *NLRP3*^{-/-} cells between 3 h and 72 h post infection. (G-I) MFI of DsRed⁺ BLaER1, BLaER1 *Casp1*^{-/-} and BLaER1 *NLRP3*^{-/-} cells between 3 h and 72 h post infection. N=4. Graphs show mean values + SD. Significance was determined by Two-Way-ANOVA. * $p < 0.05$, **$p < 0.01$, ***$p < 0.001$, ****$p < 0.0001$.

Neither LPS stimulated nor R848 stimulated infected BLaER1 cells showed a reduction of the infection rate (**Figure 30D**, **E** and **F**) or the parasite burden (**Figure 30G**, **H** and **I**) compared to either BLaER1 *Casp1*^{-/-} or BLaER1 *NLRP3*^{-/-} cells. The infection rate decreased over time for all used stimuli. For LPS-stimulated cells, the infection rate decreased from 29% at 3 h p.i. to 18 % at 72 h p.i. for BLaER1 cells, from 29 % at 3 h p.i. to 20 % at 72 h p.i. for BLaER1 *Casp1*^{-/-} and from 33% at 3 h p.i. to 22 % at 72 h p.i. for BLaER1 *NLRP3*^{-/-} (**Figure 30E**). For R848 stimulated cells the infection rate decreased from 27 % at 3 h p.i. to 11 % at 72 h p.i. for BLaER1 cells, from 24 % at 3 h p.i. to 12 % at 72 h p.i. for BLaER1 *Casp1*^{-/-}

and from 27% at 3 h p.i. to 18 % at 72 h p.i. for BLaER1 $NLRP3^{-/-}$ (**Figure 30F**). Finally, for unstimulated cells the infection rate decreased from 33% at 3 h p.i. to 24 % at 72 h p.i. for BLaER1 cells and from 31 % at 3 h p.i. to 13 % at 72 h p.i. for BLaER1 $Casp1^{-/-}$. Interestingly, the infection rate of BLaER1 $NLRP3^{-/-}$ increased from 29% at 3 h p.i. to 35 % at 72 h p.i. and reached the level of significance in comparison to BLaER1 $Casp1^{-/-}$ but not compared to BLaER1 (**Figure 30D**). In contrast to the infection rate the parasite burden increased over time for all tested stimuli. In LPS stimulated cells mean DsRed MFI increased from 2,381 at 3 h p.i. to 5,134 at 72 h p.i. for BLaER1, from 2,388 to 6,151 in BLaER1 $Casp1^{-/-}$ and from 2,370 to 5,937 in BLaER1 $NLRP3^{-/-}$ (**Figure 30H**). In R848 stimulated cells mean DsRed MFI increased from 2,351 at 3 h p.i. to 4,799 at 72 h p.i. for BLaER1, from 2,048 to 6,592 in BLaER1 $Casp1^{-/-}$ and from 2,047 to 6,227 in BLaER1 $NLRP3^{-/-}$ (**Figure 30I**). Lastly, for unstimulated cells mean DsRed MFI increased from 2,350 at 3 h p.i. to 5,544 at 72 h p.i. for BLaER1, from 2,321 to 7,262 in BLaER1 $Casp1^{-/-}$ and from 2,258 to 6,800 in BLaER1 $NLRP3^{-/-}$ (**Figure 30G**). Taken together, this data demonstrates that neither prolonged low-level secretion of IL-1β observed for unstimulated, infected BLaER1 cells of the NLRP3 inflammasome nor strong high-level secretion of IL-1β observed for primed, infected BLaER1 cells resulted in any reduction of parasite burden or infection rate of human host cells.

4.2.9 Pro-inflammatory polarization of BLaER1 cells does not enhance leishmanicidal activity

After showing that, unlike in the murine system, IL-1β does not cause enhanced leishmanicidal activity in an autocrine manner in human host cells, I investigated whether BLaER1 cells could be pro-inflammatorily polarized by alternative stimuli. For this, BLaER1 cells were treated with LPS+IFN-γ, IFN-γ alone or were left unstimulated and were subsequently infected with either Alexa-Fluor405-conjugated stationary-phase *L. major* to measure ROS production - due to the spectral overlap of DsRed and DHE, or stationary-phase *L. major* DsRed to analyze infection rate and parasite burden. Additionally, CD86 expression and IL-12 secretion were analyzed by flow cytometry and ELISA, respectively, to explore their suitability as markers of pro-inflammatory polarization. ROS production, determined by DHE staining, in *Leishmania*-infected BLaER1 cells was significantly increased in IFN-γ-polarized cells (78 % of positive menadione-treated control) compared to the unactivated control (60 % of positive menadione-treated control) (**Figure 31A**). The ROS production upon *Leishmania* infection of LPS+IFN-γ polarized cells was not significantly increased compared to the unactivated control, although a trend could be recognized. Increased ROS production did not result in lower infection rate (**Figure 31B**) or parasite burden (**Figure 31C**), regardless of the stimulus chosen for polarization. While almost all BLaER1 cells, irrespective of activation state, were positive for CD86 (data not shown), no significant increase in the expression level could be observed for either LPS+IFN-γ

polarized BLaER1 cells or IFN-γ polarized BLaER1 compared to the unactivated control (**Figure 31D**). IL-12 could not be detected in the supernatant of uninfected or infected cells at 3 h p.i. nor at 24 h pi.i., irrespective of the activation state of the BLaER1 cells (**Figure 31F**). In summary, pro-inflammatory polarization of BLaER1 cells did increase the activation of the antimicrobial effector mechanism ROS. This led to a clear trend towards reduced infection rates and parasite burdens, although the level of significance was not reached at 24 h p.i.. Expression of the co-stimulatory protein B7.2 (CD86) and IL-12 secretion were ruled out as indicators of pro-inflammatory activation, because increases in CD86 expression remained insignificant and no secretion of IL-12 could be detected, irrespective of infection and activation state.
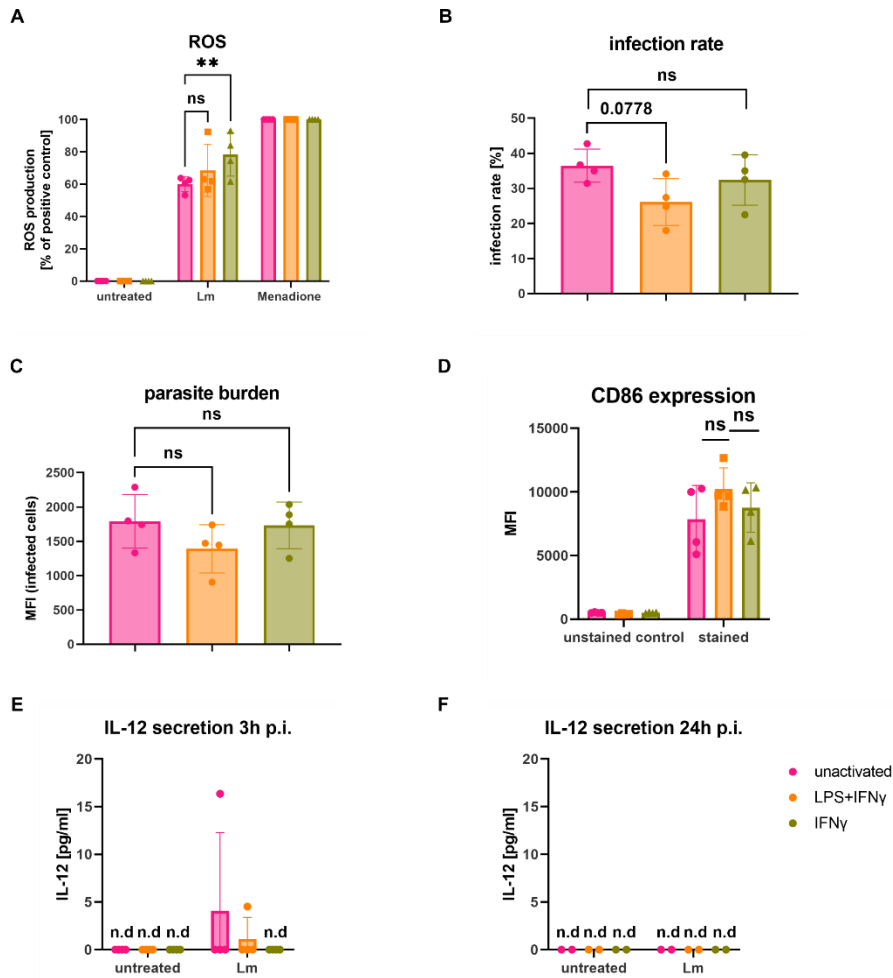
Figure 31: Pro-inflammatory polarization of BLaER1 cells does not lead to leishmanicidal activity
(A) BLaER1 cells were polarized by stimulation with a combination of 10 ng/ml LPS and 50 ng/ml IFN-γ, 50 ng/ml IFN-γ alone or left untreated for 24 h and subsequently infected with Alexa-Fluor405 labeled stationary-phase *L. major* at MOI 10. At 23.5 h post infection cells were stained with 5 µM DHE for 30 min, harvested and analyzed by flow cytometry. MFI of DHE stained cells normalized between an untreated negative control and a positive control of cells stimulated with 1 mM menadione for 1 h. (B and C) unstimulated and polarized BLaER1 cells were infected with stationary-phase *L. major* DsRed at MOI 10 for 24 h. Cells were then harvested and analyzed by flow cytometry. (B) Share of DsRed+ BLaER1 cells. (C) MFI of DsRed+ BLaER1 cells. (D) Unstimulated and polarized BLaER1 cells were incubated for 24 h, stained with CD86-APC antibody and analyzed by flow cytometry. MFI values of CD86+ BLaER1 cells compared to an unstained control. (E and F) Supernatants of unstimulated and polarized BLaER1 cells were collected for ELISA at 3 h (E) and 24 h (F) post infection and the IL-12 concentration determined by ELISA. N=4 (A-D), N=2 (E) or N=1 (F). Graphs show mean values + SD. Significance was determined by unpaired t-test. * $p<0.05$, ** $p<0.01$, *** $p<0.001$, **** $p<0.0001$.

To investigate whether the absence of IL-12 secretion in BLaER1 cells was due to their stimulation with M-CSF during the transdifferentiation procedure, BLaER1 cells were transdifferentiated with GM-CSF instead of M-CSF. The resulting cells were termed GM-BLaER1. GM-BLaER1 cells were polarized with IFN-γ or left untreated and subsequently infected with stationary-phase *L. major* DsRed for 24 h. The infection rate of GM-BLaER1 cells did not differ from the infection rate observed for BLaER1 cells transdifferentiated with M-CSF determined in the previous experiment, with an infection rate of 32 % for unactivated GM-BlaER1s and 34 % for IFN-γ-treated GM-BLaER1 cells (**Figure 32A**). These values

closely resemble the infection rates observed for M-CSF-differentiated BLaER1 of 36 % for unactivated BLaER1 cells and 32 % for IFN-γ-stimulated BLaER1 cells, determined in the previous experiment (**Figure 31A**). The same was observed for the parasite burden, with a relative fluorescence intensity of 1,310 for unactivated infected GM-BlaER1 cells and 1,512 for IFN-γ stimulated GM-BLaER1 cells (**Figure 32B**). These values corresponded well to the relative fluorescence intensities observed for M-CSF-differentiated BLaER1 cells from the previous experiment of 1,791 for unactivated BLaER1 cells and compared to 1,731 for IFN-γ stimulated BLaER1 cells (**Figure 31B**). However, transdifferentiation with GM-CSF did not lead to any detectable secretion of IL-12, demonstrating that treatment with M-CSF during the transdifferentiation process is not the cause of absent IL-12 secretion after pro-inflammatory polarization of BLaER1 cells.
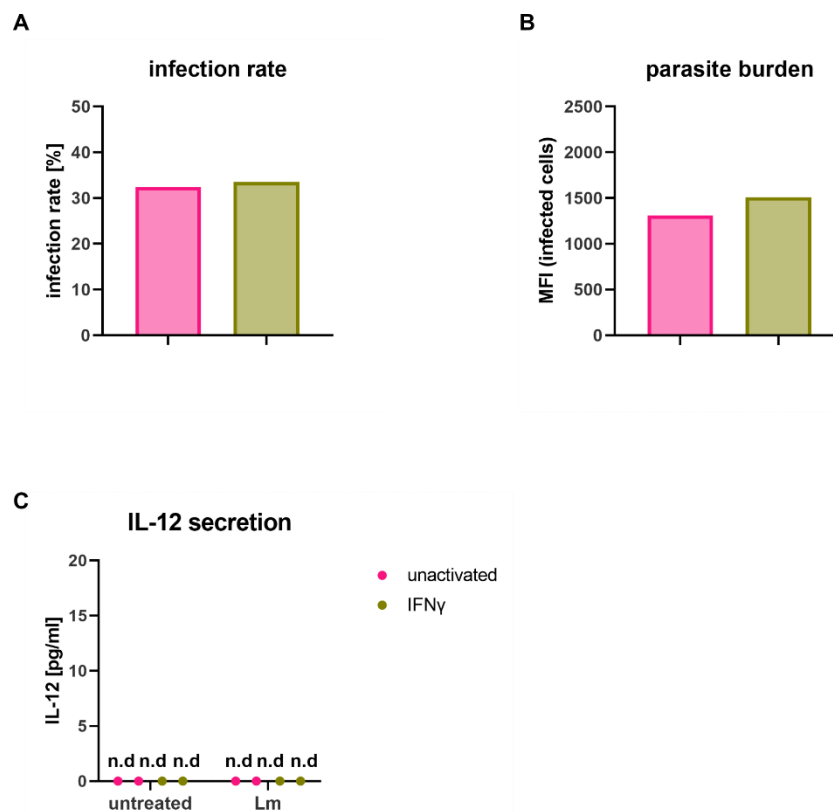
Figure 32: Transdifferentiation of BLaER1 with GM-CSF does not lead to IL-12 secretion.
BLaER1 cells were transdifferentiated with a combination of 10 ng/ml IL-3, 200 nM β-estradiol and 20 ng/ml of GM-CSF instead of 10 ng/ml M-CSF for seven days. Afterwards, cells were polarized with 50 ng/ml IFN-γ for 24h or left untreated. Cells were subsequently infected with stationary-phase *L. major* DsRed at MOI 10 for 3h. Supernatants were collected for ELISA and the cells harvested and analyzed by flow cytometry. (A) Share of DsRed+ BLaER1 cells. (B) MFI of DsRed+ BLaER1 cells. (C) IL-12 concentrations of supernatants from unstimulated and polarized BlaER1 cells determined by ELISA. N=1

4.2.10 *L. major* infection does not lead to upregulation of iNOS in BLaER1 cells or hMDMs

In murine infection models of cutaneous leishmaniasis, NO production mediated by iNOS upon infection is associated with strong parasite restriction and fast resolution of the disease [19,59,61,68,69]. To confirm that neither BLaER1 cells nor hMDMs responded to *L. major* infection with an upregulation of iNOS, the relative iNOS expression of BLaER1 cells, GM-CSF-derived hMDMs and M-CSF-derived hMDMs infected with stationary-phase *L. major* parasites was analyzed by qPCR at 3 h and 24 h p.i.. Uninfected cells were used as a negative control (**Figure 33**). Since to this date no experimental treatment has been described that leads to a pronounced upregulation of iNOS in human cells, qPCR primers were designed to bind both the murine and human iNOS mRNA sequence and tested with cDNA murine bone-marrow-derived macrophages treated with a combination of LPS (500 ng/ml) and IFN-γ (50 ng/ml) (Appendix A). No significant differences in the expression of iNOS were observed irrespective of cell type and time point (**Figure 33**). A slight trend towards a small reduction in the iNOS expression was observed for GM-CSF-derived hMDMs at 3 h p.i.. In summary, qPCR analysis confirmed that neither BLaER1 cells nor either type of hMDM upregulated iNOS upon *L. major* infection.
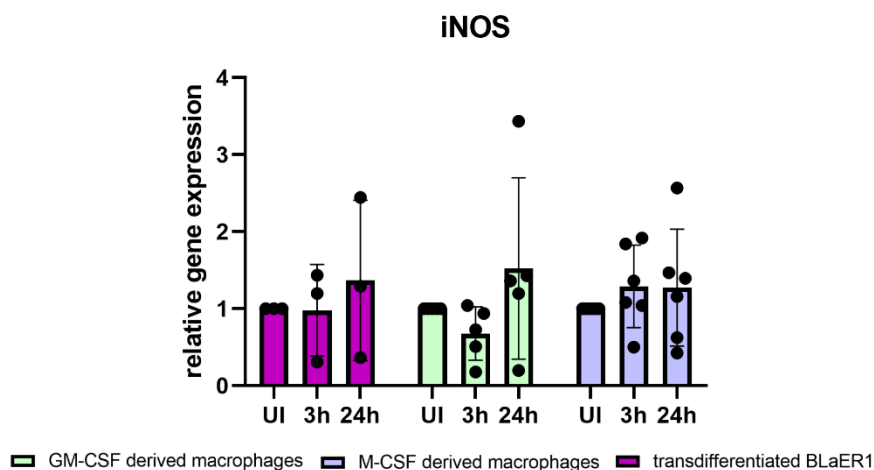
Figure 33: *L. major* infection does not induce upregulation of iNOS in BLaER1, GM-CSF-derived or M-CSF-derived macrophages.
BLaER1 cells, M-CSF-derived and GM-CSF-derived macrophages were infected with stationary-phase *L. major* promastigotes at MOI 10 for 3 h (3h), 24 h (24h) or left untreated (UI). RNA was isolated at the indicated time points and reverse transcribed. The resulting cDNA was used for qPCR to determine the expression of the phagolysosomal NO-producing enzyme iNOS. N=3. Graphs show mean values +SEM. Significance was determined by Two-Way-ANOVA. * p<0.05, **p<0.01, ***p<0.001, ****p<0.0001.

4.2.11 Nitric oxide treatment of infected BLaER1 cells leads to parasite restriction.

After neither NLRP3 inflammasome activation nor pro-inflammatory activation of BLaER1 cells resulted in significant leishmanicidal activity, I investigated whether treatment of infected BLaER1 cells with NO, a hallmark of the innate immunity of mice, could exert a restrictive effect on intracellular parasites. In a first step, the effect of several NO-generating compounds on the parasite burden of infected BLaER1 cells was determined by flow cytometric analysis. For this, BLaER1 cells were infected with stationary-phase *L. major* DsRed for up to 24 h and treated with different concentrations of DEA-NONOate (**Figure 34A** and **D**), SNAP (**Figure 34B** and **E)** or SNI-1 (**Figure 34C** and **F)** either 18.5 h (**Figure 34D-F**) or 4.5 h before analysis **(Figure 34A-C**). A reduction of the parasite burden was observed for all compounds, time points and concentrations, except for the treatment of BLaER1 cells with 10 µM of SNAP at 4.5 h before analysis and treatment with 10 µM of DEA-NONOate at 4.5 h before analysis. The strongest reduction of parasite burden was observed for SNI-1 at 80 µM after 4.5 h. Furthermore, reductions of parasite burden were more pronounced when the compound was added 4.5 h before analysis compared to 18.5 h before analysis. This finding underlined the short half-life of NO of approximately 30 min, as stated by the manufacturer, and it pointed towards a recovery of treated parasites few hours after treatment. Therefore, NO generating compounds were repeatedly added over time in all further experiments. Since 80 µM of SNI-1 showed the strongest reduction of parasite burden in this preliminary experiment, this compound and concentration were chosen for all further experiments protocols.
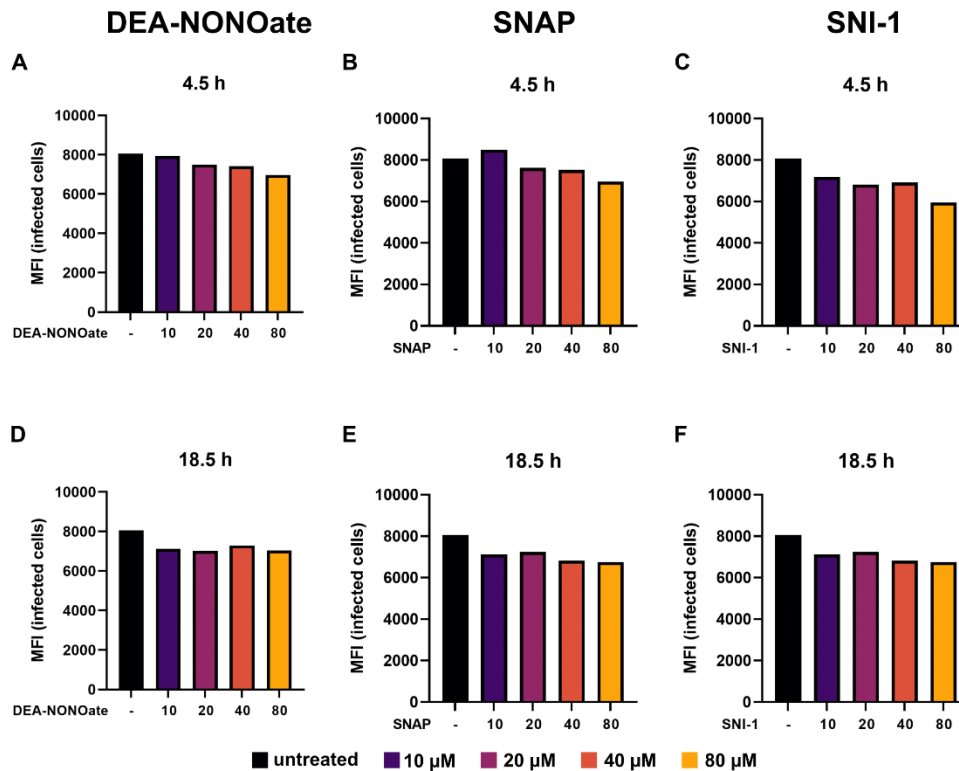
Figure 34: The nitric oxide generating compound SNI-1 causes a strong reduction in parasite burden at concentration of 80 μM.
BLaER1 cells were infected with stationary-phase *L. major* DsRed at MOI of 10 for 24 h and treated with nitric oxide generating compounds SNI-1 (C and F), DEA-NONOate (A and D) or SNAP (B and E) at concentrations of 10 μM, 20 μM, 40 μM or 80 μM at 5.5 h p.i. (18.5 h incubation with compound) (D, E and F) or at 19.5 h p.i. (4.5 h incubation with compound) (A, B and C). Cells were harvested and the parasite burden measured by DsRed MFI was analyzed by flow cytometry. N=1.

Next, the successful generation of NO from compounds was validated by measurement of the final reaction products of NO, NO_2^- and NO_3^- by Griess reaction. Because the RPMI-based BM used to cultivate BLaER1 cells contained high levels of NO_3^- (**Figure 35A**) a transdifferentiation protocol, which allowed generation of tdBLaER1 cells cultured in DMEM-based BM (BM-DMEM) with low NO_3^- concentrations (**Figure 35A**). For this, three different transdifferentiation protocols for the change from BM to BM-DMEM were tested. (I): The transdifferentiation in BM-DMEM, (II): The substitution of BM with BM-DMEM from the second medium change onward and (III): The transdifferentiation in BM followed by cell harvest in BM-DMEM. BLaER1 cells transdifferentiated with either of these protocols were infected with stationary-phase *L. major* DsRed for up to 24 h and treated at 3 h p.i. and 18.5 h p.i. with 80 μM of SNI-1. All transdifferentiation protocols successfully generated tdBLaER1 cells, which did not differ in infection rate and parasite burden (**Figure 35B-G**). Baseline-corrected NO_2^- concentrations showed little to no NO_2^- for untreated or *L. major* infected cells, but increased by approximately 50 μM for each addition of 80 μM of SNI-1 (**Figure 35H** and **I**). Measured NO_2^- concentrations did not differ between samples that were filtered through a 10 kDa MWCO filter (**Figure**

35H) as recommended by the manufacturer of the Griess assay, and those used unfiltered (**Figure 35I**). Therefore, this step was omitted in all further Griess reactions. Since no differences in infection rate, parasite burden or NO_2^- concentration were observed between the different transdifferentiation, the least effortful protocol, which is medium change to BM-DMEM upon cell harvest, was chosen for all further experiments.
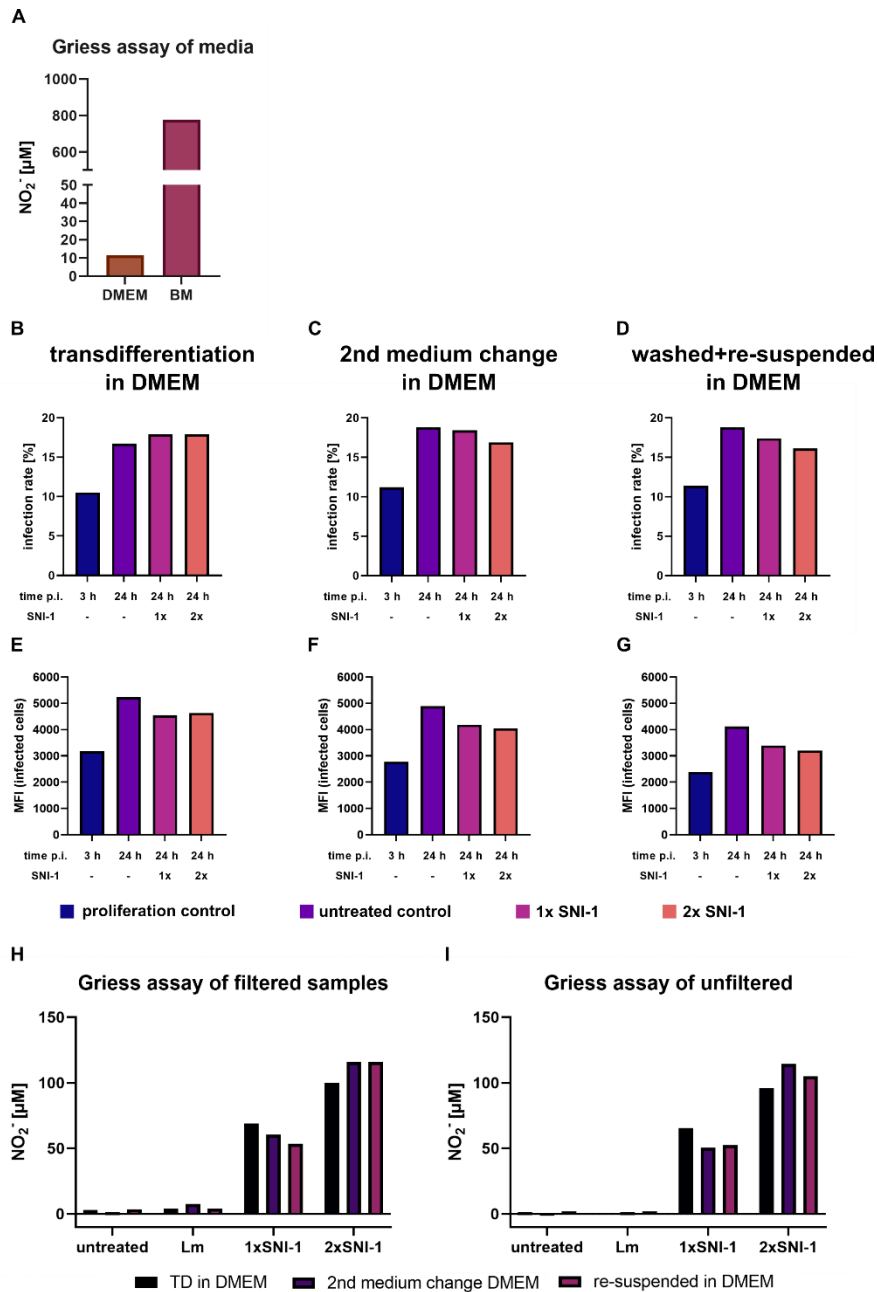
Figure 35: Functionality of SNI-1 was confirmed by successful measurement of NO reaction products in cell culture supernatants.

BLaER1 cells were transdifferentiated either in BM-DMEM (A and D), in BM and cultured in BM-DMEM from the second medium change onward (B and E), or transdifferentiated in BM and harvested in BM-DMEM (C and F). Cells were infected with stationary-phase *L. major* DsRed at MOI of 10 for 24 h and treated with 80 µM of SNI-1 at 3 h p.i. and 18.5 h p.i.. Supernatants were collected, filtered with a 10 kDA MWCO filter (G) or not filtered (H) and used for determination of NO_2^- and NO_3^- by Griess reaction (G and H). Medium controls of BM and BM-DMEM were analyzed by Griess reaction (I). Cells were harvested and analyzed by flow cytometry (A-F). (A-C) Infection rates of BLaER1 cells transdifferentiated in BM-DMEM (A), with added BM-DMEM from second medium change onward (B) or harvested in BM-DMEM (C). MFI of DsRed⁺ BLaER1 cells transdifferentiated in BM-DMEM (D), with added BM-DMEM from second medium change onward (E) or harvested in BM-DMEM (F).

To investigate the effect of NO treatment on intracellular parasites over a longer period, BLaER1 cells were infected with stationary-phase *L. major* DsRed for up to 72 h and treated with the NO generating compound SNI-1 for up to four times. Flow cytometric analysis of infected cells revealed a significant reduction of the parasite burden, determined by DsRed MFI of infected cells, as early as 24 h p.i. (3,583 vs. 4,690) (**Figure 36A**). This reduction was also observed at 48 h (4,915 vs. 7,435) and 72 h p.i. (5619 vs. 10,275), even though no fresh SNI-1 was added to the 2xNO condition after the second addition at 18.5 h post infection. The parasite burden of cells treated thrice with SNI-1 (3xNO) was significantly reduced at 48 h p.i. (4,808 vs. 7,435). This reduction was also observed at 72 h p.i. (5726 vs. 10,275) without the addition of fresh SNI-1. Finally, the parasite burden of cells treated quadruply with SNI-1 was significantly reduced at 72 h p.i. (5,073 vs 10,275). In contrast to the parasite burden, flow cytometric analysis did not show any reduction of the infection rate, regardless of time point and number of SNI-1 treatments (**Figure 36B**). To validate the successful generation of NO from SNI-1, supernatants of infected cells were collected and analyzed by Griess reaction. Little to no NO_2^- was detected in the supernatants of uninfected and infected but untreated BLaER1 cells (**Figure 36C**). Similarly, to the preliminary experiment, each addition of SNI-1 increased the nitrite concentration of the supernatant by approximately 50 µM, which remained constant over time unless further SNI-1 was added. In summary, this data shows that treatment of cells with NO strongly reduces the parasite burden in human host cells.
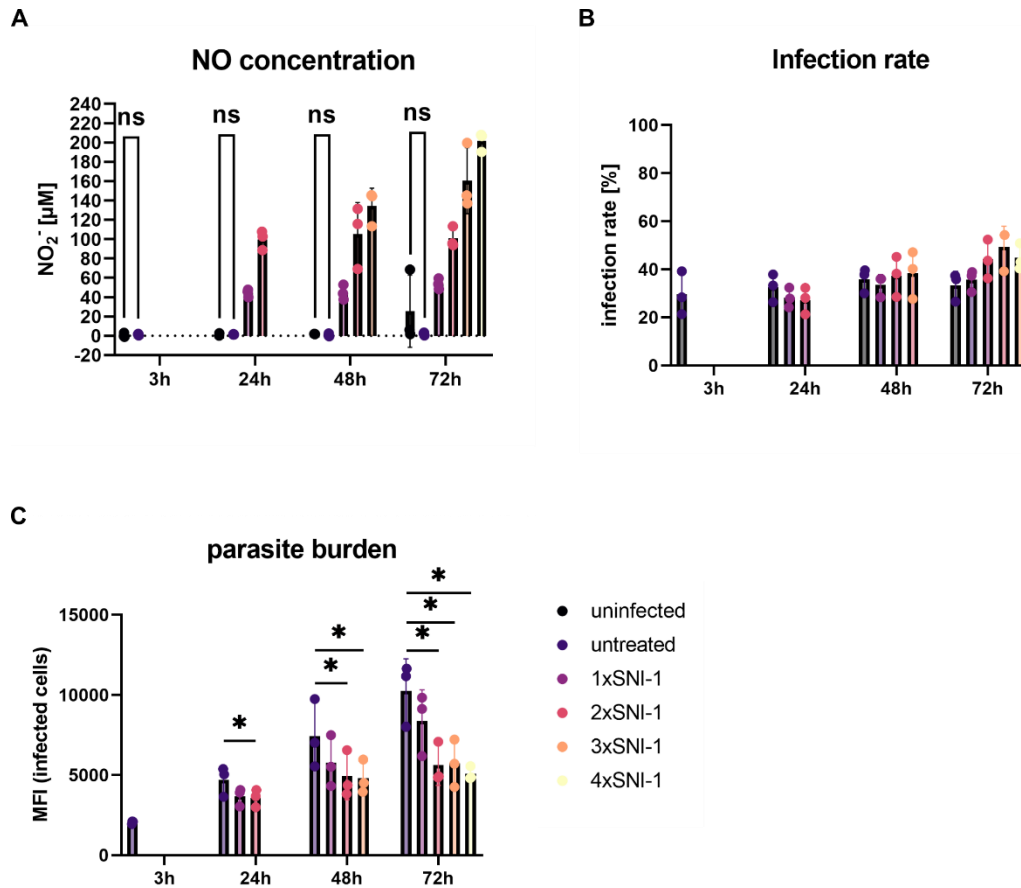
Figure 36: Nitric oxide treatment of infected BLaER1 cells reduces the parasite burden.
BLaER1 cells were infected with stationary-phase *L. major* DsRed at MOI of 10 for up to 72 h. Cells were either left untreated or treated with 80 μM of NO generating compound SNI-1 for up to four times over the course of the infection. SNI-1 was added at 3 h post infection (1x SNI-1), at 3 h and 18.5 h post infection (2x SNI-1), at 3 h, 18.5 h and 42.5 h post infection (3x SNI-1) or at 3 h, 18.5 h, 42.5 h and 66.5 h post infection (4x SNI-1). At the indicated time points cells were harvested and analyzed by flow cytometry (B and C) and the supernatants were collected for Griess assay (A). (A) Nitrite concentration of supernatants determined by Griess assay. (B) MFI of DsRed⁺ BLaER1 cells. (C) Share of DsRed⁺ BLaER1 cells. N=3. Graphs show mean values + SD. Significance was determined by Two-Way-ANOVA. * $p<0.05$, **$p<0.01$, ***$p<0.001$, ****$p<0.0001$.

To confirm that NO also reduces the parasite burden in primary human host cells, I repeated the previous experiment in hMDMs. GM-CSF-derived and M-CSF-derived hMDMs were infected with stationary-phase *L. major* DsRed for up to 48 h and treated with SNI-1 for up to three times. For GM-CSF derived hMDMs (**Figure 37A-C**), a significant reduction of the parasite burden, determined by DsRed MFI of infected cells, was observed after 24 h p.i. for cells treated twice with SNI-1 compared to the untreated control (3,561 vs. 4,651). While there was a strong trend towards a prolonged reduction at 48 h p.i. (9,459 vs. 13,071), it did not reach the level of significance at this time point. Similar to the BLaER1 cells, no differences of the infection rate, regardless of time point and number of SNI-1 treatments, were observed for GM-CSF derived hMDMs, although a trend towards an increase

of the infection rate over time can be noticed (**Figure 37B**). Finally, just like for BLaER1 cells, no nitrite was detected in the supernatants of uninfected, or infected, GM-CSF-derived hMDMs, while each addition of SNI-1 increased the concentration by approximately 50 µM (**Figure 37C**). For M-CSF-derived hMDMs, no reduction of parasite burden was observed, irrespective of time point and number of SNI-1 treatments (**Figure 37D**). Notably, the parasite burden at 48 h p.i. was considerably lower for untreated M-CSF derived hMDMs (6,440) compared to GM-CSF derived hMDMs (13,070). In contrast to GM-CSF derived hMDMs, the infection rate of M-CSF derived hMDMs increased significantly at 48 h p.i. after two and three treatments with SNI-1 (54 % and 53 %, respectively, compared to 37 % in the untreated control) (**Figure 37E**). In accordance with GM-CSF derived hMDMs and BLaER1 cells, no nitrite was detected in the supernatants of uninfected and infected but untreated M-CSF derived hMDMs, while each addition of SNI-1 increased the concentration by approximately 50 µM (**Figure 37F**). Taken together, these experiments show that while neither BLaER1 cells nor hMDMs produce NO in response to *Leishmania* infection, introduction of NO into the supernatant by SNI-1 treatment of infected cells has a restrictive effect on intracellular parasites in BLaER1 cells and GM-CSF derived hMDMs but not M-CSF derived hMDMs.
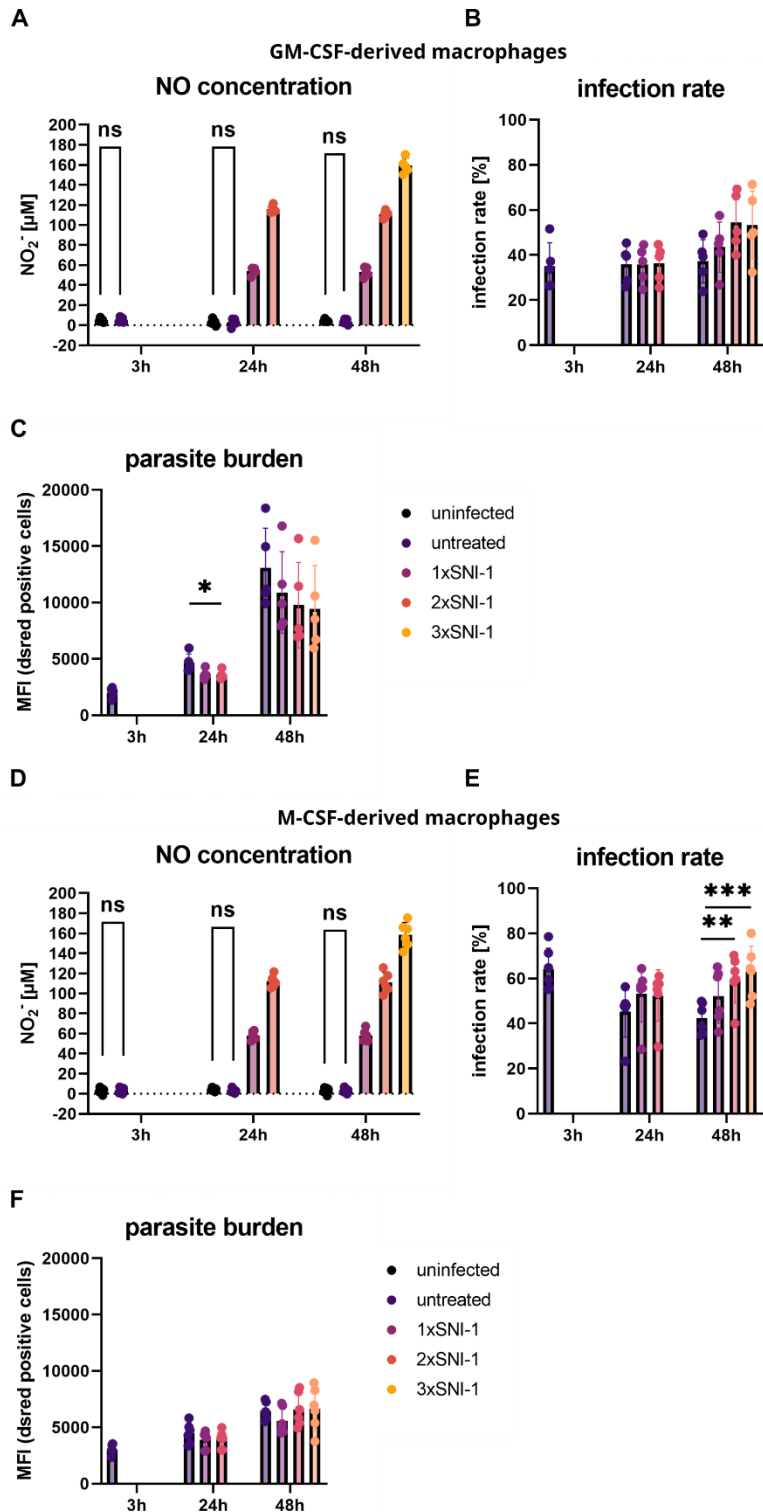
Figure 37: Nitric oxide treatment reduces the parasite burden in GM-CSF derived hMDMs but not M-CSF derived hMDMs.
GM-CSF derived hMDMs (A-C) or M-CSF derived hMDMs (D-F) were infected with stationary-phase *L. major* DsRed at MOI of 10 for up to 48 h. Cells were either left untreated or treated with 80 µM of NO generating compound SNI-1 for up to three times over the course of the infection. SNI-1 was added at 3 h post infection (1x SNI-1), at 3 h and 18.5 h post infection (2x SNI-1) or at 3 h, 18.5 h and 42.5 h post infection (3x SNI-1). At the indicated time points cells were harvested and analyzed by flow cytometry (A, B, D, E) and the supernatants were collected for Griess assay (A and D). (A and D) Nitrite concentration of supernatants of GM-CSF derived hMDMs (A) or M-CSF derived hMDMs (D) determined by Griess assay. (B and E) Share of DsRed[+] GM-CSF derived hMDMs (B) or M-CSF derived hMDMs (E). (C and F) MFI of DsRed[+] GM-CSF derived hMDMs (C) or M-CSF derived hMDMs (F). N=3. Graphs show mean values + SD. Significance was determined by unpaired t-test. * $p<0.05$, **$p<0.01$, ***$p<0.001$, ****$p<0.0001$.

4.3 Pyroptosis as a mechanism of parasite spread to new host cells.

So far, I could demonstrate that *L. major* activates the human NLRP3 inflammasome through both described main activating pathways, NADPH mediated ROS production induced by parasite uptake and LPG independent activation by cytosolic caspases. However, there was no leishmanicidal effect detected upon inflammasome activation in infected cells. As NLRP3 inflammasome activation is known to promote the pyroptosis, I wanted to elucidate whether this form of programmed cell death can function as a mechanism to induce and allow parasite spread to new host cells. In order to address this question, a BLaER1 cell line with a knockout of the pore-forming gasdermin D protein was tested for resistance to pyroptosis in comparison with BLaER1 wild type cells. Next, the time of pyroptosis-mediated parasite release was determined by live-cell imaging for BLaER1 and BlaER1 *GSDMD*$^{-/-}$. Finally, parasite spread was analyzed regarding the number of extracellular parasites and the rate of secondary infections.

4.3.1 BLaER1 *GSDMD*$^{-/-}$ cells are more resistant to pyroptosis than BLaER1 wild type cells.

To elucidate the role of pyroptosis in the cell-to-cell spread of *L. major* parasites, first, a BLaER1 knockout, which is highly refractory to pyroptosis had to be found. I hypothesized that a knockout of the pore-forming protein gasdermin D would have this property. To test this hypothesis, BLaER1 and BLaER1 *GSDMD*$^{-/-}$ cells were stimulated with LPS, followed by induction of pyroptosis by nigericin treatment. Pyroptotic cell death was determined by flow cytometric analysis of cell viability by eGFP expression and of phosphatidylserine (PS) accessibility measured by annexin V binding. The level of pyroptotic cell death was assessed by quantifying the secreted IL-1β by ELISA. For BLaER1 cells, a strong and significant reduction of eGFP expression compared to BLaER1 *GSDMD*$^{-/-}$ cells was observed for all nigericin treated samples, but not for untreated and only LPS treated samples (**Figure 38A**). Additionally, BLaER1 cells showed a significantly larger share of annexin V$^+$ BLaER1 cells after 10 min, 30 min and 120 min of nigericin treatment (**Figure 38B**). Interestingly, there was a higher level of annexin V positivity for BLaER1 *GSDMD*$^{-/-}$ cells compared to BLaER1 cells after 240 min of nigericin treatment (**Figure 38C**), indicating a higher accessibility of PS. The secretion of IL-1β was significantly increased for BLaER1 cells compared to BLaER1 *GSDMD*$^{-/-}$ cells in LPS stimulated samples (1019 pg/ml vs. 91 pg/ml) and samples treated with nigericin for 10 min, 30 min and 120 min (2280 pg/ml vs. 159 pg/ml, 7271 pg/ml vs. 189 pg/ml and 7949 pg/ml vs. 694 pg/ml, respectively). In summary, this data demonstrates a higher resistance of BLaER1 *GSDMD*$^{-/-}$ cells to pyroptotic cell death compared to BLaER1 cells (**Figure 38D**).
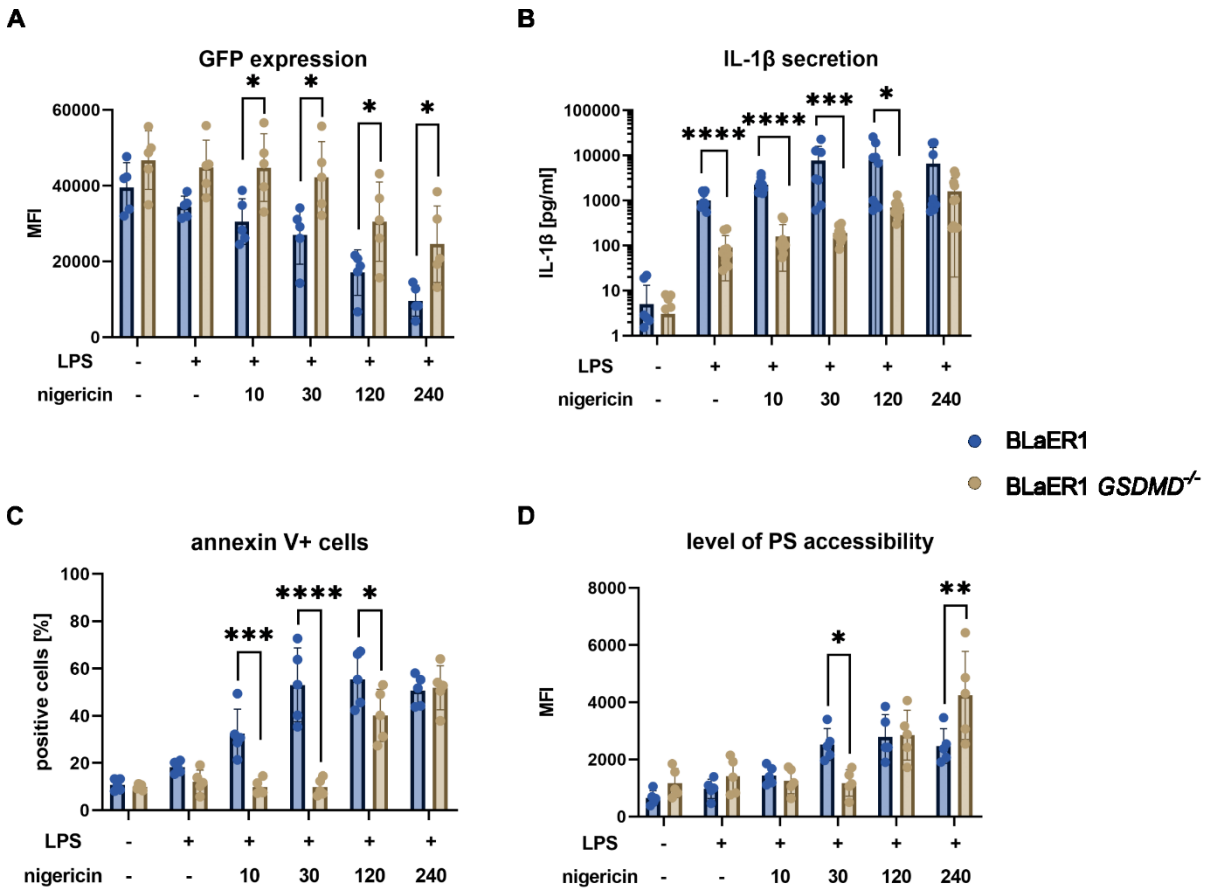
Figure 38: BLaER1 GSDMD-/- cells are more resistant to pyroptosis than BLaER1 wild type cells
BLaER1 and BLaER1 *GSDMD*^{-/-} cells were stimulated with 200 ng/ml LPS for 3.75 h before pyroptosis was induced by treatment with 4 µM nigericin for up to 4 h (time of nigericin treatment in minutes is indicated below graphs). Cells were harvested, stained with Sytox blue viability stain and Alexa-Fluor647 conjugated annexin V and analyzed by flow cytometry. Supernatants were collected and analyzed by ELISA. (A) MFI of eGFP expressed by BLaER1 and BLaER1 *GSDMD*^{-/-} cells. (B) IL-1β concentration of supernatants as determined by ELISA. (C) Share of annexin V^{+} cells. (D) MFI of annexin V[+] stained BLaER1 and BLaER1 *GSDMD*^{-/-} cells. N=5. Graphs show mean values + SD. Significance was determined by multiple Mann-Whitney tests (B) or Two-Way-ANOVA (A, C and D). * p<0.05, **p<0.01, ***p<0.001, ****p<0.0001.

4.3.2 Resistance to pyroptosis leads to delayed release of intracellular parasites

After confirming that BLaER1 *GSDMD*^{-/-} cells were refractory to pyroptosis, I sought to determine if this would be associated with a delayed release of intracellular parasites from infected cells. Therefore, BLaER1 and BLaER1 *GSDMD*^{-/-} were infected with stationary-phase *L. major* DsRed. At 24h p.i. cells were stimulated with LPS, followed by induction of pyroptosis by nigericin treatment. Immediately after addition of nigericin, cells were imaged in a confocal laser scanning live-cell microscope. Almost all infected BLaER1 cells released their intracellular parasites (73 % of infected cells) within the first eight hours after induction (**Figure 39B**). In contrast, only a small fraction of BLaER1 *GSDMD*^{-/-} cells released intracellular parasites in the same time frame (10 % of infected cells). Furthermore, parasite release from BLaER1 *GSDMD*^{-/-} cells occurred at significantly later time points compared to BLaER1 wild

type cells (409 min vs. 190 min) (**Figure 39C**). Interestingly, BLaER1 *GSDMD*^{-/-} cells showed membrane blebbing, a sign of apoptosis, prior to the release. This observation is in sharp contrast to wild type BLaER1 cells, which omitted this characteristic and released parasites much more rapidly and in concert with cellular contents indicated by the disappearance of cytosolic eGFP fluorescent signal (**Figure 39A**). This showed that a knockout of gasdermin D results in significantly less and delayed release of intracellular parasites.
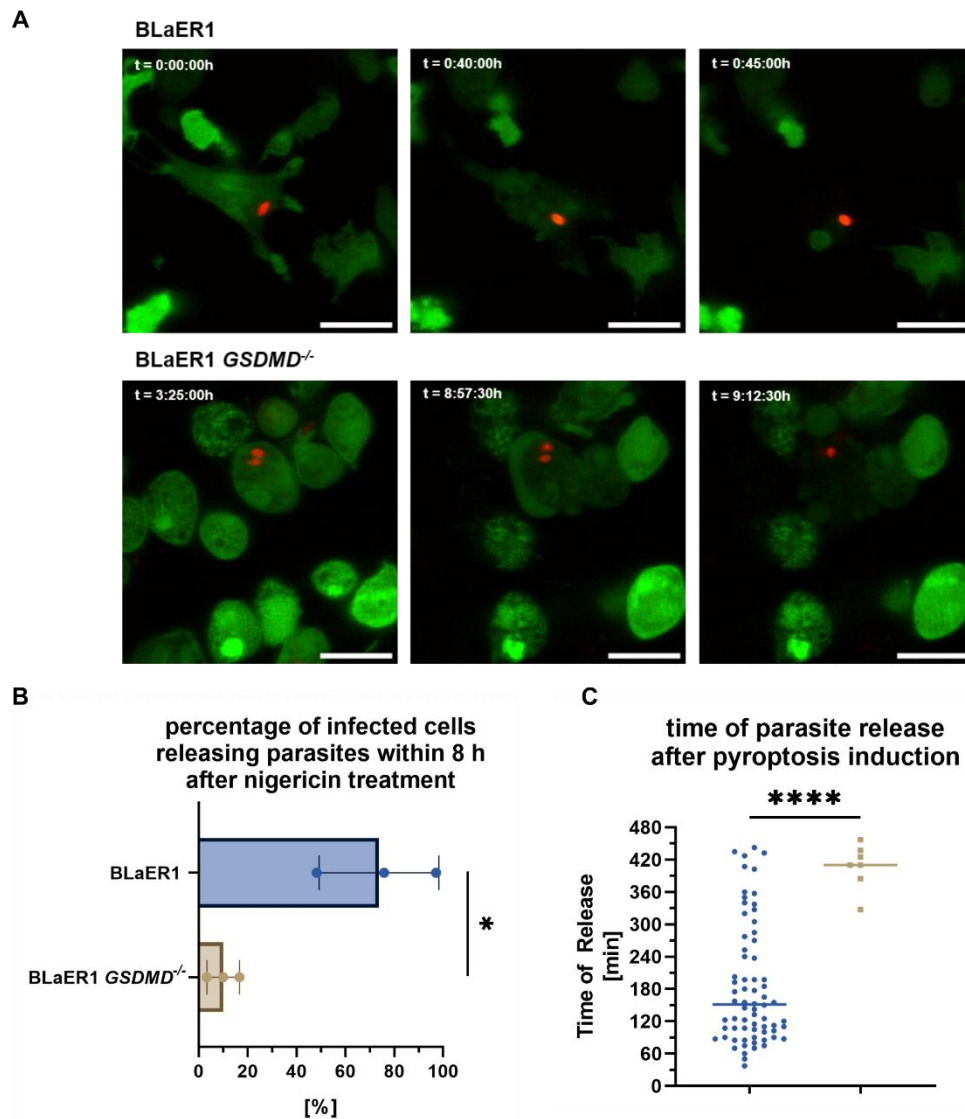
Figure 39: Pyroptosis resistance leads to delayed parasite release from BLaER1 *GSDMD*^{-/-} compared to wild type BLaER1. BLaER1 cells and BLaER1 *GSDMD*^{-/-} cells were infected with stationary-phase *L. major* DsRed at MOI 5 for 3 h. Cells were washed and incubated for overnight. Next, cells were stimulated with 200 ng/ml LPS for 3.75 h and pyroptosis was induced by treatment with 4 µM nigericin for 8 h. Simultaneously with LPS stimulation, cells were imaged by live-cell microscopy at 2.5 min intervals. (A) Time series of parasite release from an infected BLaER1 (top row) or infected BLaER1 *GSDMD*^{-/-} (bottom row) cell. Images show the intact, infected cell (left), first morphological signs of cell death (center) and released parasite (right). (B) Share of infected cells releasing their intracellular parasite during the observed time period. (C) Time of parasite release after nigericin treatment. N=3. Graphs show mean values + SD (B) or individual values + median (C). Significance was determined by unpaired t-test. * p<0.05, **p<0.01, ***p<0.001, ****p<0.0001. Live cell imaging was performed by Moritz Jaedtka.

4.3.3 Pyroptosis induction does not lead to an increase in the number of extracellular parasites

In a next step, the pyroptosis-mediated parasite exit from host cells was quantified by high-throughput automated microscopy. To quantify pyroptosis-mediated parasite egress more robustly using a larger sample size. For this, BLaER1 BLaER1 $GSDMD^{-/-}$ cells were labeled with CMFDA and infected with either stationary-phase *L. major* DsRed or axenic *L. major* DsRed amastigotes for 24 h. At 24 h p.i., cells were stimulated with LPS, followed by pyroptosis induction by nigericin treatment for up to 60 min. Afterwards, DNA was stained with DAPI and parasites were immunostained with α-Lm serum. Cells were subsequently imaged in a high-throughput microplate imager. Acquired images were analyzed in the CellProfiler software using a self-designed image analysis pipeline for the quantification of extracellular parasites. The pipeline is shown as schematic in **Figure 40** and in **Figure 41** an exemplary image of each step is shown. Nuclei were identified based on DNA staining and nuclei were used as a seed to identify the cell membrane based on the CMFDA staining (**Figure 41**, first row). Signal from immunostained parasites was first, enhanced and second, thresholded to identify parasites (**Figure 41**, second row). In a series of object-based operations, cells were first related to parasites, creating the "intracellular parasite" subset. Then, cells were filtered by the number of intracellular parasites to create the "infected cells" subset. Finally, parasites were masked using intracellular parasites. The remaining parasites were considered to be extracellular (**Figure 41**, rows 3-5).
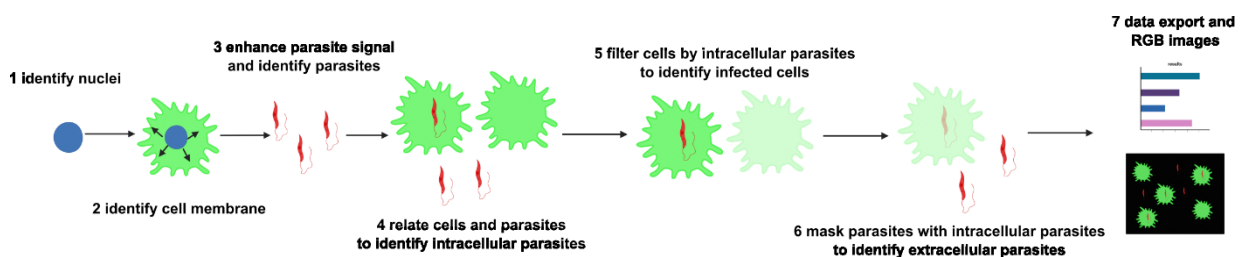
Figure 40: Schematic of image analysis pipeline for quantifying extracellular parasites.
Schematic of the CellProfiler image analysis pipeline used to analyze data from automatic microscopy experiments described in the **Figure 42** and **Figure 43**. First, the nucleus of each cell is identified. Second, the nucleus is used as a seed to identify the cell outlines using the image from the CMFDA channel. Third, the signal from stained parasites is enhanced and the parasites are identified. Forth, parasites are related to cells to identify parasites that reside inside of a cell. This subset of parasites is labeled "intracellular parasites". Fifth, cells are filtered for intracellular parasites. Cells that have at least one intracellular parasite are labeled "infected cells". Sixth, the parasites are masked with the "intracellular parasites" object i.e., parasites that are part of the "intracellular parasite" subset are removed. Finally, RGB images and numerical results are exported.
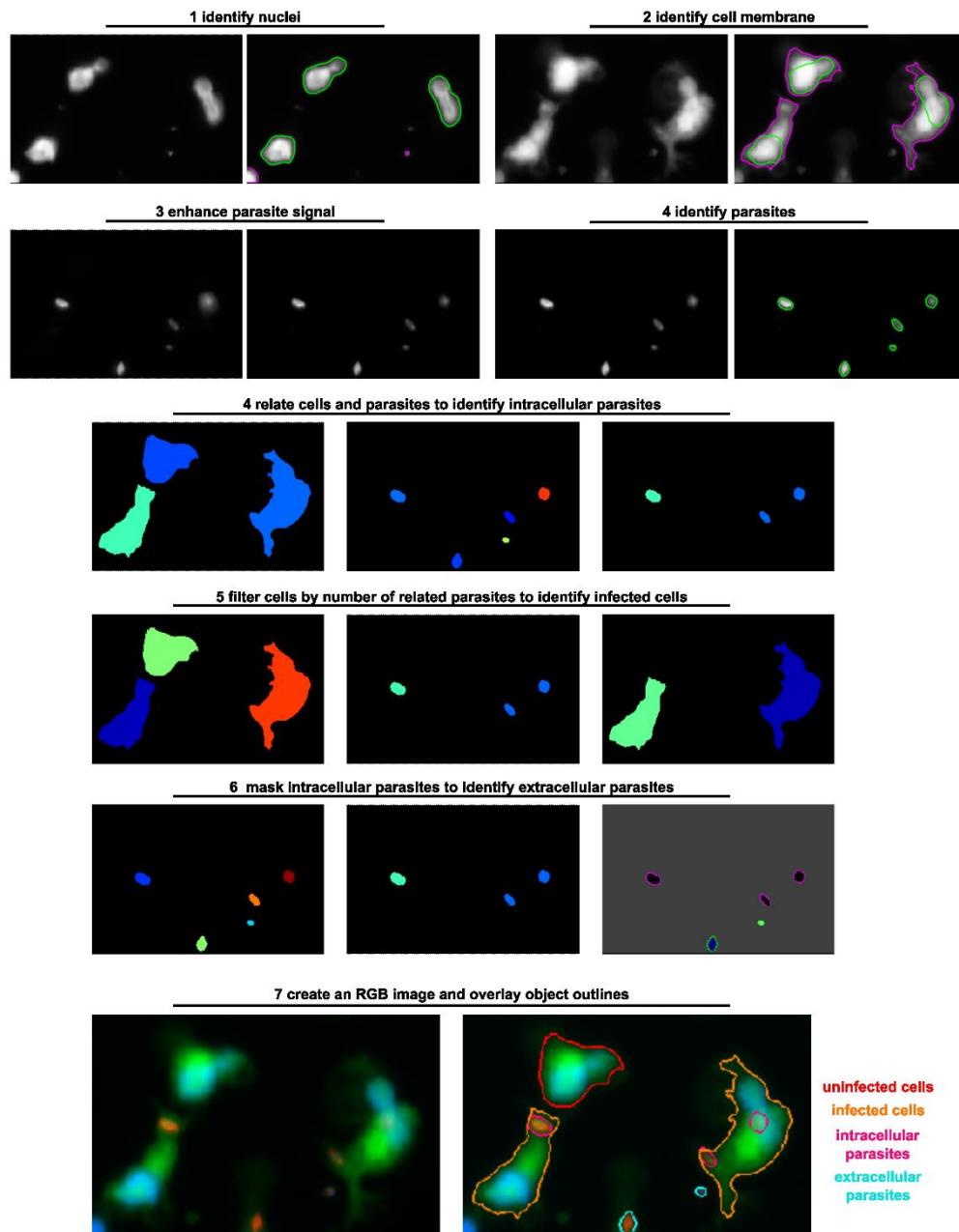
Figure 41: Exemplary images of the image analysis pipeline.
Exemplary images of the CellProfiler image analysis pipeline used to analyze data from automatic microscopy experiments described in the **Figure 42** and **Figure 43**. Each microscopy image shows a small section of an image set of three channels. Green outlines indicate a primary object. Purple outlines indicate a either a secondary object (first row, right image) or a masked object (firth row, right image). A colored fill indicates an object. The colors are assigned randomly (rows three to five, left and center images), but are matched when objects are related by an operation (rows three to five, right images). Row six shows the RGB overlay image alone (left) or overlayed with object outlines (right).

For promastigote-infected cells, no differences in the infection rate and parasite burden were observed between BLaER1 and BLaER1 *GSDMD*^-/- cells, irrespective of the used stimulus. The infection rates were 29 % vs. 18 % for unstimulated cells, 27 % vs 19 % for LPS stimulated cells, 26 %vs. 19 % after 10 min

of nigericin treatment, 14 % vs 19 % after 30 min of nigericin treatment and 27 % vs. 19 % after 60 min of nigericin treatment for BLaER1 and BLaER1 *GSDMD*$^{-/-}$ cells, respectively. Thus, infection rates were constant across all used stimuli (**Figure 42A**). The parasite burden was also constant across all used stimuli and analyzed cell types, and varied between 1.3-1.5 parasites per cell **(Figure 42B)**. The number of extracellular parasites was overall higher for BLaER1 cells than for BLaER1 *GSDMD*$^{-/-}$ cells in all tested conditions, but did not reach the level of significance (**Figure 42C**). To allow a better comparison of the individual replicates and address the variance caused by the different numbers of total parasites imaged in each replicate, a ratio of extracellular parasites to total parasites was calculated (**Figure 42D**). Here, a trend towards a higher parasite release was observed for BLaER1 cells compared to BLaER1 *GSDMD*$^{-/-}$ cells, with a larger share of extracellular parasites for LPS treated cells (7.3 % vs. 4.4 %), 10 min of nigericin treatment (5.1 % vs. 3.2 %), 30 min of nigericin treatment (12.2 % vs. 2.0 %) and 60 min of nigericin treatment (6.9 % vs 4.6 %). However, this trend did not reach the level of significance.

Figure 42: Induction of pyroptosis in promastigote infected BLaER1 cells does not lead to an increase of extracellular parasites compared to promastigote infected BLaER1 *GSDMD*-/- cells.
BLaER1 cells and BLaER1 *GSDMD*-/- cells were stained with 0.5 µg/ml CMFDA and subsequently infected with stationary-phase *L. major* DsRed at MOI 5 for 3 h. Cells were washed and incubated for overnight. Next, cells were stimulated with 200 ng/ml LPS for 3.75 h and pyroptosis was induced by treatment with 4 µM nigericin for up to 60 minutes (time of treatment indicated below graph in minutes). Afterwards, cells were fixed, permeabilized and stained with α-Lm serum and anti-mouse Alexa-Fluor568 antibody. Images were acquired using an Operetta automated microscope and analyzed with CellProfiler. (A) Share of infected cells. (B) number of parasites per infected cell. (C) number of extracellular parasites. (D) Number of extracellular parasites expressed as percent of all detected parasites. N=4. Graphs show mean values + SD. Significance was determined by Two-Way-ANOVA. * $p<0.05$, **$p<0.01$, ***$p<0.001$, ****$p<0.0001$.

For amastigote-infected cells, the observed infection rates were not significantly different and overall constant across all tested stimuli, ranging from 52 % for LPS stimulated BLaER1 cells to 62 % for BLaER1 cells treated with nigericin for 30 min in cells and ranging from 41 % for unstimulated BLaER1 *GSDMD*-/- cells to 55 % for knockout cells treated with nigericin for 10 min (**Figure 43A**). The parasite burden of BLaER1 cells was overall, but not significantly, higher than the one observed for BLaER1 *GSDMD*-/- cells and remained constant across all tested conditions. Parasite burdens ranged from 2.0- 2.4 parasites per cell in BLaER1 cells and from 1.7 to 2.0 parasites per cell in BLaER1 *GSDMD*-/- cells **(Figure 43B)**. The number of extracellular amastigotes was overall approximately two times as high as for promastigote-infected cells (**Figure 43C**). Furthermore, there was a strong trend towards a higher number of extracellular parasites for BLaER1 cells compared to BLaER1 *GSDMD*-/- cells, that increased with longer nigericin treatment times. However, this trend did not reach the level of significance. The

ratio of extracellular parasites to the total number of detected parasites was overall smaller than the one observed for promastigote infected cells (**Figure 43D**). While the ratio was higher for BLaER1 cells compared to BLaER1 *GSDMD⁻/⁻* cells in every tested condition (2.8 % vs, 2.7 % for untreated cells, 3.3 % vs. 2.9 % for LPS stimulated cells, 2.8 % vs. 2.2 % for 10 min nigericin treatment, 2.9 % vs. 2.2 % for 30 min of nigericin treatment and 6.3 % vs 4.0 % for 60 min of nigericin treatment), this trend was less pronounced than for promastigote infected cells and, also, did not reach the level of significance. In summary, the experiment showed that the parasite egress observed by life cell microscopy could not be quantified by high-throughput microscopy using extracellular parasites as a readout.
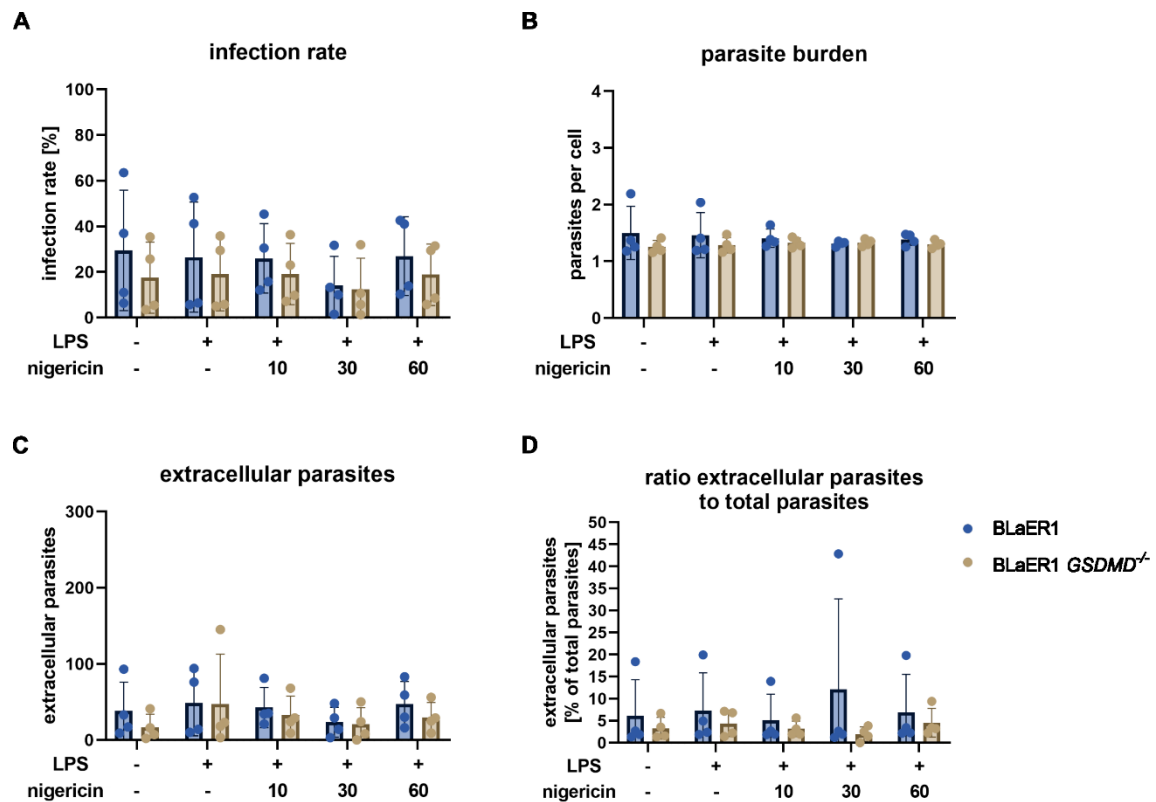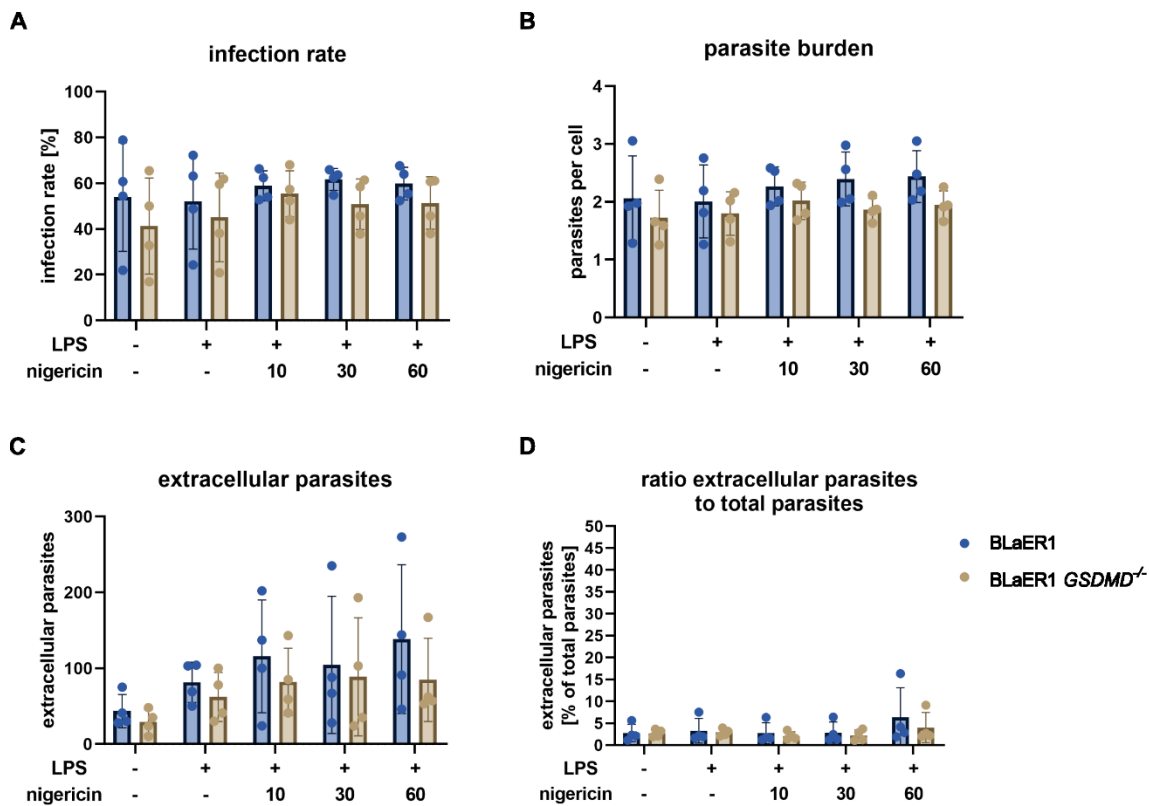

Figure 43: Induction of pyroptosis in amastigote infected BLaER1 cells does not lead to an increase of extracellular parasites compared to amastigote infected BLaER1 *GSMD⁻/⁻* cells.
BLaER1 cells and BLaER1 *GSDMD⁻/⁻* cells were stained with 0.5 µg/ml CMFDA and subsequently infected with axenic *L. major* DsRed amastigotes at MOI 2 for 3 h. Cells were washed and incubated for overnight. Next, cells were stimulated with 200 ng/ml LPS for 3.75 h and pyroptosis was induced by treatment with 4 µM nigericin for up to 60 minutes (time of treatment indicated below graph in minutes). Afterwards, cells were fixed, permeabilized and stained with α-Lm serum and anti-mouse Alexa-Fluor568 antibody. Images were acquired using an Operetta automated microscope and analyzed with CellProfiler. (A) Share of infected cells. (B) number of parasites per infected cell. (C) number of extracellular parasites. (D) Number of extracellular parasites expressed as percent of all detected parasites. N=4. Graphs show mean values + SD. Significance was determined by Two-Way-ANOVA. * $p<0.05$, **$p<0.01$, ***$p<0.001$, ****$p<0.0001$.

4.3.4 Pyroptosis induction increases the rate of secondary infections in a co-incubation assay

Due to high differences in the number of extracellular parasites between the individual replicates of the previous experiment, I suspected that released parasites could have been washed off the microplates during the staining procedure after nigericin treatment. Furthermore, the mean time of parasite release from BLaER1 cells of 190 min determined by live-cell imaging and the significantly higher cell viability of BLaER1 *GSDMD*$^{-/-}$ compared to BLaER1 cells for up to 4 h were considered, and the time of nigericin treatment increased to 4 h accordingly. To circumvent this problem, the cell-to-cell spread was analyzed in a co-incubation assay and the secondary infection rate was used as a metric for parasite exit instead of the number of extracellular parasites. For the co-incubation assay, BLaER1 BLaER1 *GSDMD*$^{-/-}$ cells were labeled with CMFDA and infected with either stationary-phase *L. major* DsRed or axenic *L. major* DsRed amastigotes for 24 h. At 24 h p.i. CellTracker DeepRed-labeled BLaER1 *GSDMD*$^{-/-}$ cells were added to both cell types, because only this pyroptosis-resistant cell type would be viable, thus, capable to take up parasites under pyroptosis-inducing conditions. Afterwards, cells were stimulated with LPS, followed by pyroptosis induction by nigericin treatment for up to 240 min. Then, DNA was stained with DAPI and parasites were immunostained with α-Lm serum. Cells were subsequently imaged in a high-throughput microplate imager. Acquired images were analyzed in the CellProfiler software using a self-designed image analysis pipeline for the quantification of the secondary infection rate. The pipeline is shown as schematic in **Figure 44**. The pipeline closely resembled the one used for the quantification of extracellular parasites (**Figure 40** and **Figure 41**). The main differences were that (I): Two different cell populations (primary cells and co-incubated cells) were identified based on the different cell surface stainings (CMFDA and CellTracker DeepRed), (II): Cells were no longer identified as a secondary object using the nucleus as a seed, but directly identified as a primary object like the parasites and (III): The "extracellular parasites" subset was termed "residual parasites" and was used for a second round of object-based relating and filtering to identify secondary infected cells, i.e. infected co-incubated cells, and secondary intracellular parasites. While this pipeline was more sophisticated than the pipeline used for detection of extracellular parasites, it was built with the same set of modules and therefore, no exemplary images are shown for it.
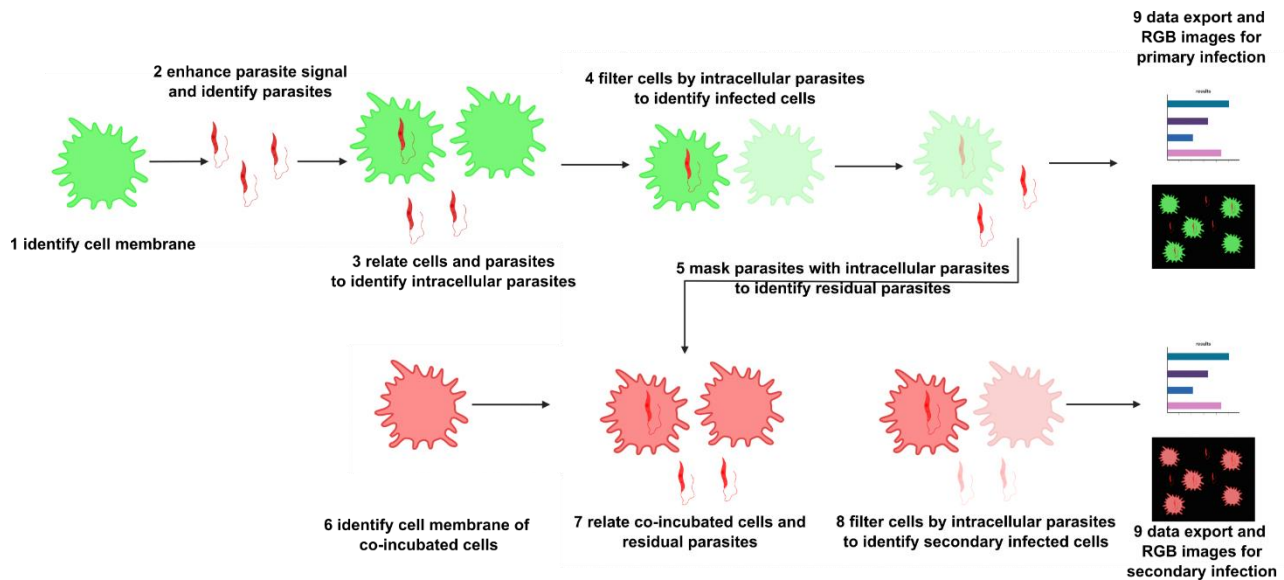
Figure 44: Schematic of image analysis pipeline for quantifying secondary infections.
Schematic of the CellProfiler image analysis pipeline used to analyze data from automatic microscopy experiments described in **Figure 45**. First, the cell membrane of each CMFDA stained cell is identified. Second, the signal from stained parasites is enhanced and the parasites are identified. Third, parasites are related to cells to identify parasites that reside inside of a cell. This subset of parasites is labeled "intracellular parasites". Forth, cells are filtered for intracellular parasites. Cells that have at least one intracellular parasite are labeled "infected cells". Fifth, the parasites are masked with the "intracellular parasites" object i.e., parasites that are part of the "intracellular parasite" subset are removed and the resulting parasites are labeled "residual parasites". Sixth, the cell membrane of co-incubated cells is identified in the Alexa-Fluor647 channel. Seventh, co-incubated cells and residual parasites are related and filtered as described in step three and four to identify secondary infected cells and secondary intracellular parasites. Finally, RGB images and numerical results are exported.

For promastigote infected cells, the observed primary infection rates were not significantly different and overall constant across all tested stimuli, ranging from 35 % for cells treated with nigericin for 240 min to 53 % for LPS stimulated cells in BLaER1 cells and ranging from 39 % for cells treated with nigericin for 120 min to 55 % for LPS-stimulated cells in BLaER1 *GSDMD*$^{-/-}$ cells (**Figure 45A**). The parasite burden did not differ between the primary infected BLaER1 and BLaER1 *GSDMD*$^{-/-}$ cells and remained constant across all tested conditions. Parasite burdens ranged from 1.5 – 2.2 parasites per cell in BLaER1 cells and from 1.5 to 2.1 parasites per cell in BLaER1 *GSDMD*$^{-/-}$ cells (**Figure 45C**). The secondary infection rate was overall slightly higher for BLaER1 *GSDMD*$^{-/-}$ cells co-incubated with BLaER1 cells than for BLaER1 *GSDMD*$^{-/-}$ cells co-incubated with BLaER1 *GSDMD*$^{-/-}$ cells in all conditions but for nigericin treatment for 180 min (**Figure 45E**). The secondary parasite burden did not differ between BLaER1 and BLaER1 *GSDMD*$^{-/-}$ cells and remained constant across all tested conditions (**Figure 45G**). The same was observed for the number of extracellular parasites (**Figure 45I**).

For amastigote infected cells, the observed primary infection rates were not significantly different and overall constant across all tested stimuli, ranging from 58 % for unstimulated cells to 72 % for cells

treated with nigericin for 180 min in BLaER1 cells and ranging from 54 % for unstimulated cells to 75 % for cells treated with nigericin for 180 min in BLaER1 *GSDMD*^{-/-} cells (**Figure 45B**). The parasite burden was overall, but not significantly higher for BLaER1 *GSDMD*^{-/-} cells than for BLaER1 and cells and remained constant across all tested conditions. Parasite burdens ranged from 2.2 – 2.7 parasites per cell in BLaER1 cells and from 2.1 to 3.1 parasites per cell in BLaER1 *GSDMD*^{-/-} cells (**Figure 45D**). The secondary infection rate was overall higher for BLaER1 *GSDMD*^{-/-} cells co-incubated with BLaER1 cells than for BLaER1 *GSDMD*^{-/-} cells co-incubated with BLaER1 *GSDMD*^{-/-} cells in all conditions. While the observed differences were small for unstimulated cells, stimulated cells and cells briefly treated with nigericin, the differences increased with prolonged time of nigericin treatment (**Figure 45F**). However, these findings did not reach the level of significance. The secondary parasite burden did not differ between BLaER1 *GSDMD*^{-/-} cells co-incubated with BLaER1 cells and BLaER1 *GSDMD*^{-/-} cells co-incubated with BLaER1 *GSDMD*^{-/-} cells and remained constant across all tested conditions (**Figure 45H**). The number of extracellular parasites fluctuated strongly and did not show any clear differences between cell types and tested conditions (**Figure 45J**). In summary, the results of the of the co-incubation experiments showed strong trends to an increased secondary infection rate of BLaER1 *GSDMD*^{-/-} cells co-incubated with BLaER1 cells compared to BLaER1 *GSDMD*^{-/-} cells co-incubated with BLaER1 *GSDMD*^{-/-} cells. This suggests a role of pyroptosis in the parasite spread of amastigotes, even though results did not reach the level of significance.

Figure 45: Induction of pyroptosis in infected BLaER1 cells does not lead to an increase of secondary infections compared to infected BLaER1 *GSMD*^-/- cells.

BLaER1 cells and BLaER1 *GSDMD*^-/- cells were stained with 0.5 µg/ml CMFDA and subsequently infected with stationary-phase *L. major* DsRed at MOI 5 (A, C, E, G, and I) or axenic *L. major* DsRed amastigotes (B, D, F, H and J) at MOI 2 for 3 h. Cells were washed and incubated for overnight. Next, fresh BLaER1 *GSDMD*^-/- cells were stained with 0.5 µM CellTracker Deep Red and added to the infected BLaER1 or infected BLaER1 *GSDMD*^-/- cells. After 1 h of co-incubation, cells were stimulated with 200 ng/ml LPS for 3.75 h and pyroptosis was induced by treatment with 4 µM nigericin for up to 4 h (time of treatment indicated below graph in minutes). Afterwards, cells were fixed, permeabilized and stained with α-Lm serum and anti-mouse Alexa-Fluor568 antibody. Images were acquired using an Operetta automated microscope and analyzed with CellProfiler. (A and B) Share of promastigote (A) or amastigote (B) infected cells. (C and D) number of intracellular promastigotes (C) or amastigotes (D) per infected cell. (E and F) Share of CellTracker Deep Red stained BLaER1 *GSDMD*^-/- cells that were secondarily infected by promastigotes (E) or amastigotes (F). (G and H) Number of intracellular promastigotes (G) or amastigotes (H) per infected CellTracker Deep Red stained BLaER1 *GSDMD*^-/- cells. (I and J) Number of extracellular promastigotes (I) or amastigotes (J) expressed as percent of all detected parasites. N=3. Graphs show mean values + SD. Significance was determined by Two-Way-ANOVA. * p<0.05, **p<0.01, ***p<0.001, ****p<0.0001.

4.3.5 Generation of BLaER1 *GSDMD*$^{-/-}$ x eGFP$^{-/-}$

To further investigate the potential role of pyroptosis in the cell-to-cell spread of *L. major,* the co-incubation assay was modified to enable analysis by flow cytometry instead of microscopy. This allowed an increase of sample size and minimized the loss of cells caused by washing steps. Furthermore, to supersede the need for cell staining, a BLaER1 *GSDMD*$^{-/-}$ with knocked out eGFP was created by nucleofection with RNPs targeting the eGFP gene. This allowed the identification of co-incubated secondary infected BLaER1 *GSDMD*$^{-/-}$ cells based on eGFP expression. Nucleofection efficiency and knockout efficiency were controlled as previously described (see **Figure 25**) and therefore, the data is not shown here. After limiting dilution, putative BLaER1 *GSDMD*$^{-/-}$ x eGFP$^{-/-}$ clones were analyzed for eGFP expression by flow cytometry **Figure 46A** and six clones, which were negative for eGFP expression were transdifferentiated, followed by analysis of their transdifferentiation efficiency by flow cytometry (**Figure 46B**). The share of positive cells for each analyzed marker are shown in Tab. 5 for all tested clones along with BLaER1 as positive control (**Table 5**). BLaER1 *GSDMD*$^{-/-}$ x eGFP$^{-/-}$ clones G2 and D2 were selected for further experimentation based on their high CD14 and CD11b positivity, low CD19 positivity and absence of eGFP expression.
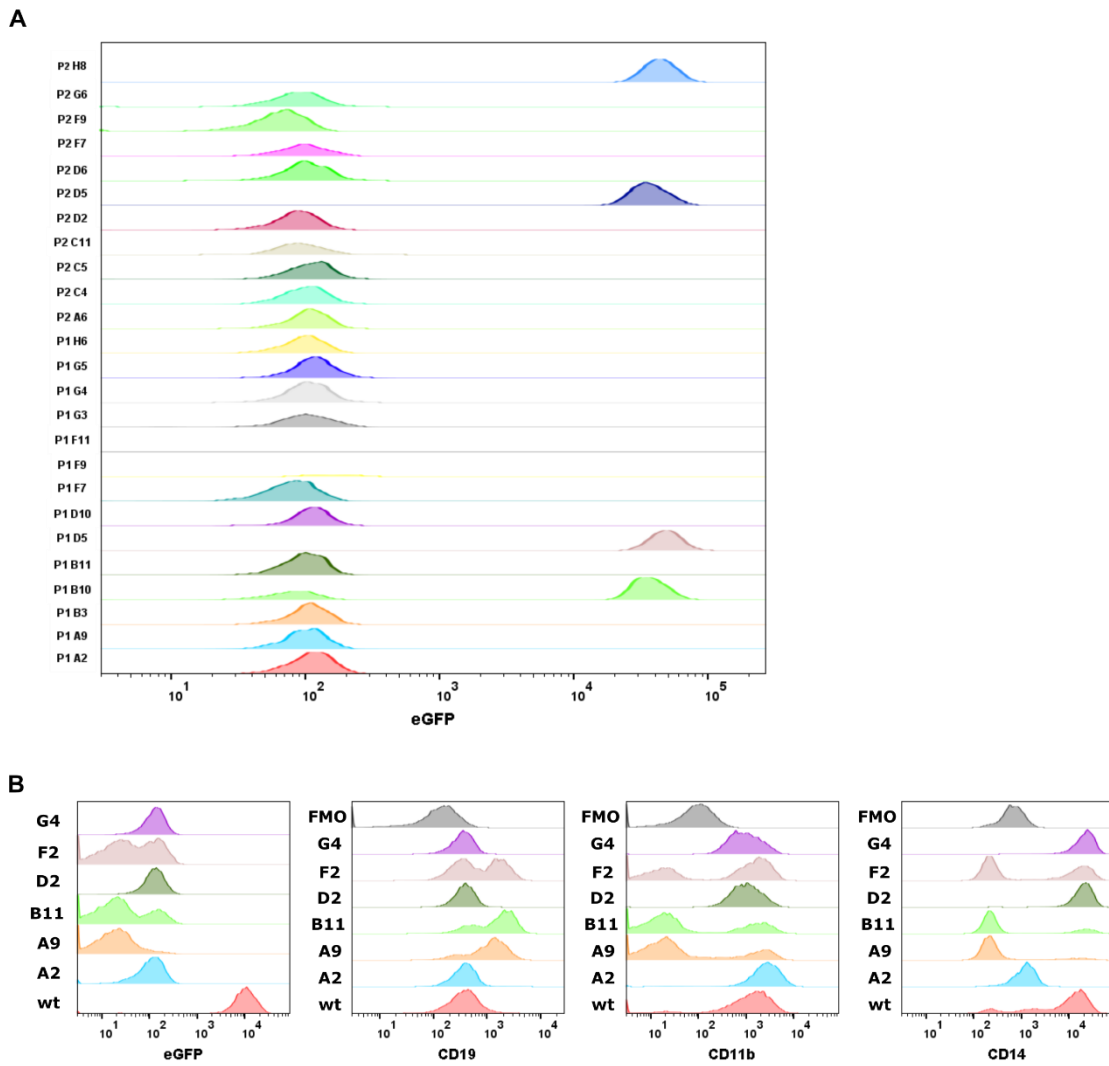
Figure 46: Generation of BLaER1 *GSDMD*$^{-/-}$ x eGFP$^{-/-}$ cell line.

BLaER1 *GSDMD*$^{-/-}$ cells were nucleofected with RNPs comprised of an sgRNA targeting eGFP and recombinant Cas9 protein. After subsequent limiting dilution, single clones were analyzed for eGFP expression by flow cytometry. Afterwards, the transdifferentiation efficiency of selected eGFP$^-$ clones were checked by staining with CD14-PB, CD19-PerCP-Cy5.5 and CD11b-PE antibodies and subsequent flow cytometric analysis. (A) Histograms of relative eGFP fluorescence of all screened BLaER1 *GSDMD*$^{-/-}$ x eGFP$^{-/-}$ clones. (B) Histograms of relative fluorescence values for eGFP and transdifferentiation markers CD11b, CD14 and CD19.

Table 5: Transdifferentiation efficiency of BLaER1 *GSDMD*-/- x eGFP-/- clones.
Table shows the share of positive cells for the marker eGFP, CD11b, CD14 and CD19 for BLaER1 wild type cells and selected BLaER1 *GSDMD*-/- x eGFP-/- clones as determined by flow cytometric analysis in **Figure 46B**.

clone	percent positivity			
	CD19	CD11b	CD14	eGFP
wt	12.6 %	78.6 %	79.4 %	94.8 %
A2	7.29 %	95.6 %	6.95 %	0 %
A9	72.7 %	19.2 %	13.9 %	0 %
B11	75.7 %	24.0 %	23.9 %	0 %
F2	49.3 %	48.0 %	46.3 %	0 %
G4	3.65 %	78.9 %	98.7 %	0 %
D2	5.17 %	83.4 %	98.9 %	0 %

4.3.6 Parasites can spread to new host cells in the same pro-inflammatory microenvironment

Using the newly generated BLaER1 *GSDMD*-/- x eGFP-/- cell line the pyroptosis-mediated cell-to-cell spread of *L. major* parasites was investigated in a modified co-incubation assay and analyzed by flow cytometry. A schematic of the flow cytometric co-incubation assay is shown in **Figure 47A**. In brief, BLaER1 eGFP-/- and BLaER1 *GSDMD*-/- x eGFP-/- cells were infected with either stationary-phase *L. major* DsRed or axenic *L. major* DsRed amastigotes for 3 h. Then, cells were washed and co-incubated with fresh BLaER1 *GSDMD*-/- cells for 18 h. Afterwards, pyroptosis was induced as previously described and followed by flow cytometric analysis. Infected cells were identified based on relative DsRed fluorescence intensity and autofluorescence and, subsequently secondary infected cells were distinguished from primary infected cells based on GFP expression (**Figure 47B**). For promastigote-infected B→G-BLaER1 *GSDMD*-/- cells, we observed a strong and significant increase in the rate of secondary infections for 120 min, 180 min and 240 min of nigericin treatment compared to G→G-BLaER1 *GSDMD*-/- cells, for which no secondary infection above background level could be observed (**Figure 47C**). For amastigote-infected B→G-BLaER1 *GSDMD*-/- cells the secondary infection rate increased strongly and significantly for LPS-stimulated cells and all time points of nigericin treatment (**Figure 47D**). For amastigote-infected G→G-BLaER1 *GSDMD*-/- cells no secondary infection above background level could be observed. Notably, amastigote-infected B→G-BLaER1 *GSDMD*-/- cells did not only show a significantly increased secondary infection rate (7.0 % vs. 0.2 %), but also an overall higher level of parasite spread for nigericin-treated conditions (6.6 % vs. 4.5 %, 9.2 % vs. 5.0 % and 11.7 % vs. 7.8 % for 120 min, 180 min and 240 min of nigericin treatment, respectively) compared to BLaER1 *GSDMD*-/- cells co-incubated with promastigote-infected B→G-BLaER1 *GSDMD*-/- cells. In summary, the modified co-incubation assay demonstrated that pyroptosis lead to parasite spread to new previously uninfected host cells. Notably, the cell-to-cell spread was not impaired by the pro-

inflammatory activation of the primary host cell by pyroptosis induction nor by the pro-inflammatory activation of the secondary host cell by IL-1β secretion.
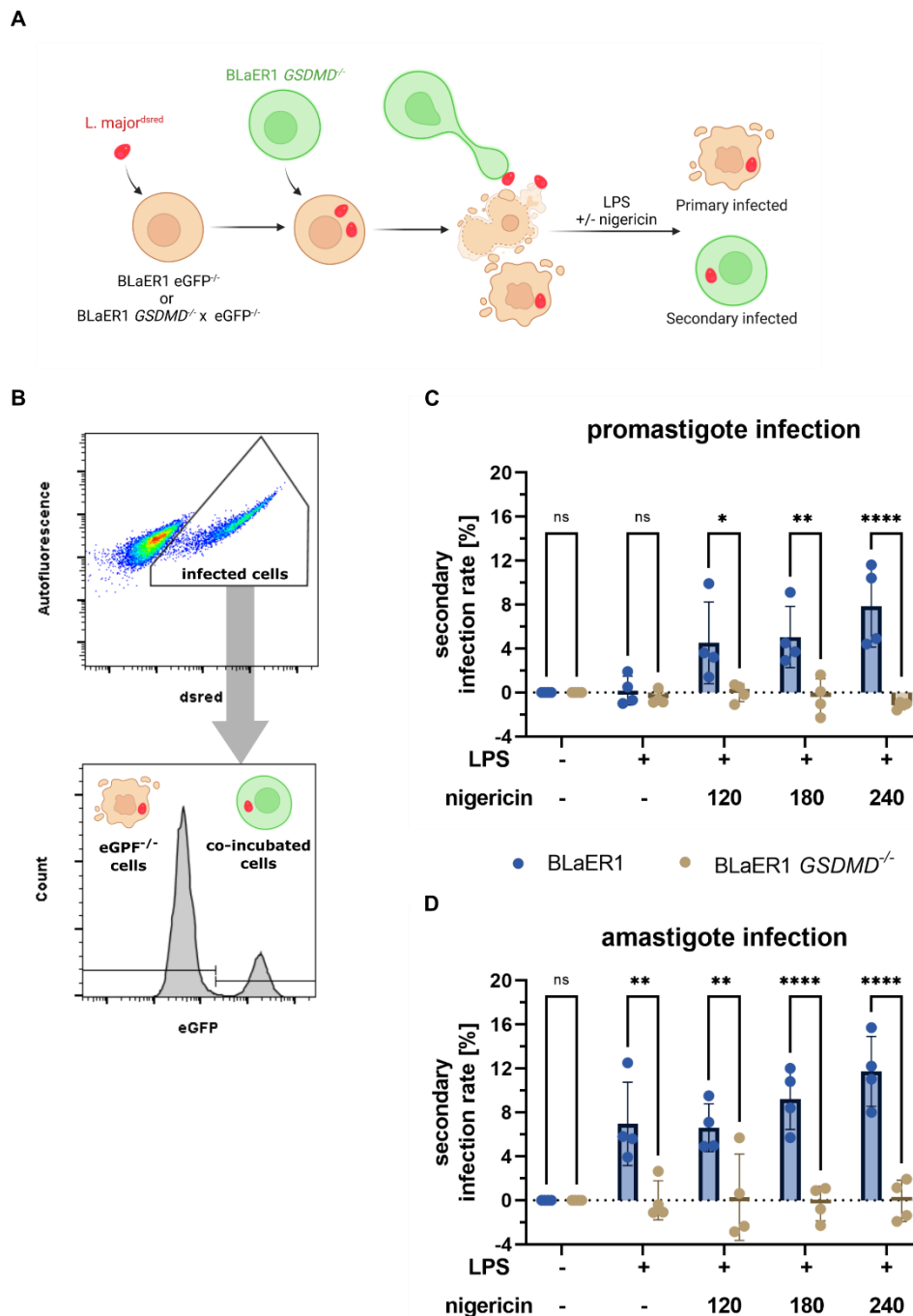
Figure 47: Parasite release and re-infection of host-cells in pro-inflammatory microenvironment.
(A) Schematic of the co-incubation assay. BLaER1 eGFP^{-/-} cells and BLaER1 *GSDMD*^{-/-} x eGFP^{-/-} cells were infected with stationary-phase *L. major* DsRed promastigotes or axenic *L. major* DsRed amastigotes before co-incubation with BLaER1 *GSDMD*^{-/-} cells. Primary and secondary infected cells were, then distinguished by eGFP positivity of infected cells. (B) Gating strategy of co-incubation assay. Infected cells were identified based on their relative DsRed fluorescence identity compared to a control infected with non-fluorescent *L. major* parasites (left plot). Infected cells were distinguished based on eGFP relative fluorescence intensity into eGFP negative (primary infected) and eGFP positive (secondary infected). (C and D) BLaER1 eGFP^{-/-} cells and BLaER1 *GSDMD*^{-/-} x eGFP^{-/-} cells were with stationary-phase *L. major* DsRed at MOI 5 (C) or axenic *L. major* DsRed amastigotes (D) for 3 h. Cells were washed and, subsequently, fresh BLaER1 *GSDMD*^{-/-} cells were added to the infected BLaER1 eGFP^{-/-} cells and BLaER1 *GSDMD*^{-/-} x eGFP^{-/-} cells. After 18 h of co-incubation, cells were stimulated with 200 ng/ml LPS for 3:45 h and pyroptosis was induced by treatment with 4 µM nigericin for up to 4 h (time of treatment indicated below graph in minutes). Afterwards, cells were harvested and analyzed directly by flow cytometry. Secondary infection rates of individual replicates were corrected for the background transfer observed in the unstimulated control before statistical analysis. N=4. Graphs show mean values + SD. Significance was determined by Two-Way-ANOVA. * $p < 0.05$, **$p < 0.01$, ***$p < 0.001$, ****$p < 0.0001$. Flow cytometry and data analysis were performed by Moritz Jaedtka.

147

5 Discussion

The goal of this thesis was to elucidate the role of the NLRP3 inflammasome during the infection of human host cells with *L. major*. This consisted of testing whether *L. major* infection leads to NLRP3 inflammasome activation in human macrophages as it has been shown for murine macrophages. Furthermore, it was analyzed if the NLRP3 inflammasome activation would lead to parasite restriction in infected host cells. Finally, it was determined whether NLRP3 inflammasome activation and subsequent pyroptosis could facilitate the spread of *L. major* parasites to new host cells. Testing of these parameters was only possible in a human macrophage cell line model. Therefore, the transdifferentiating cell line BLaER1 was analyzed for its potential as an infection model for the infection of hMDMs with *L. major* parasites. BLaER1 cells were compared to the most commonly used M-CSF- and GM-CSF-derived macrophages in regard to susceptibility for infection, infection rate, parasite burden, support of intracellular transformation to amastigote stage of *L. major* parasites and cytokine response. BLaER1 cells compared well to M-CSF-derived and GM-CSF-derived macrophages in every tested parameter, but overall resembled GM-CSF-derived macrophages more closely. By comparing the NLRP3 inflammasome activation of BLaER1 cells with BLaER1 cell lines with knocked out key components of the NLRP3 inflammasome, caspase-1 and NLRP3, I could show that the two main stimuli leading to NLRP3 inflammasome activation, phagolysosomal NADPH oxidase-mediated ROS and cytosolic LPG, also activate the human NLRP3 inflammasome. Interestingly, this NLRP3 inflammasome activation did not lead to significant parasite restriction in comparison to inflammasome-deficient knockout cell lines. While pro-inflammatory polarization of BLaER1 cells did increase the production of ROS, this did not lead to parasite restriction. However, restriction could be achieved by treatment with NO producing compounds. Finally, by using pyroptosis-refractory BLaER1 *GSDMD*$^{-/-}$ and BLaER1 *GSDMD*$^{-/-}$ x eGFP$^{-/-}$ cell lines, it could be demonstrated by live cell imaging and flow cytometry that pyroptosis can facilitate the egress of intracellular parasites. By the subsequent use of co-incubation assays followed by flow cytometric or fluorescence microscopy analysis, it could be shown that this egress allows the spread to new uninfected host cells in a highly pro-inflammatory, pyroptosis-inducing microenvironment. In the following sections all findings will be discussed in detail.
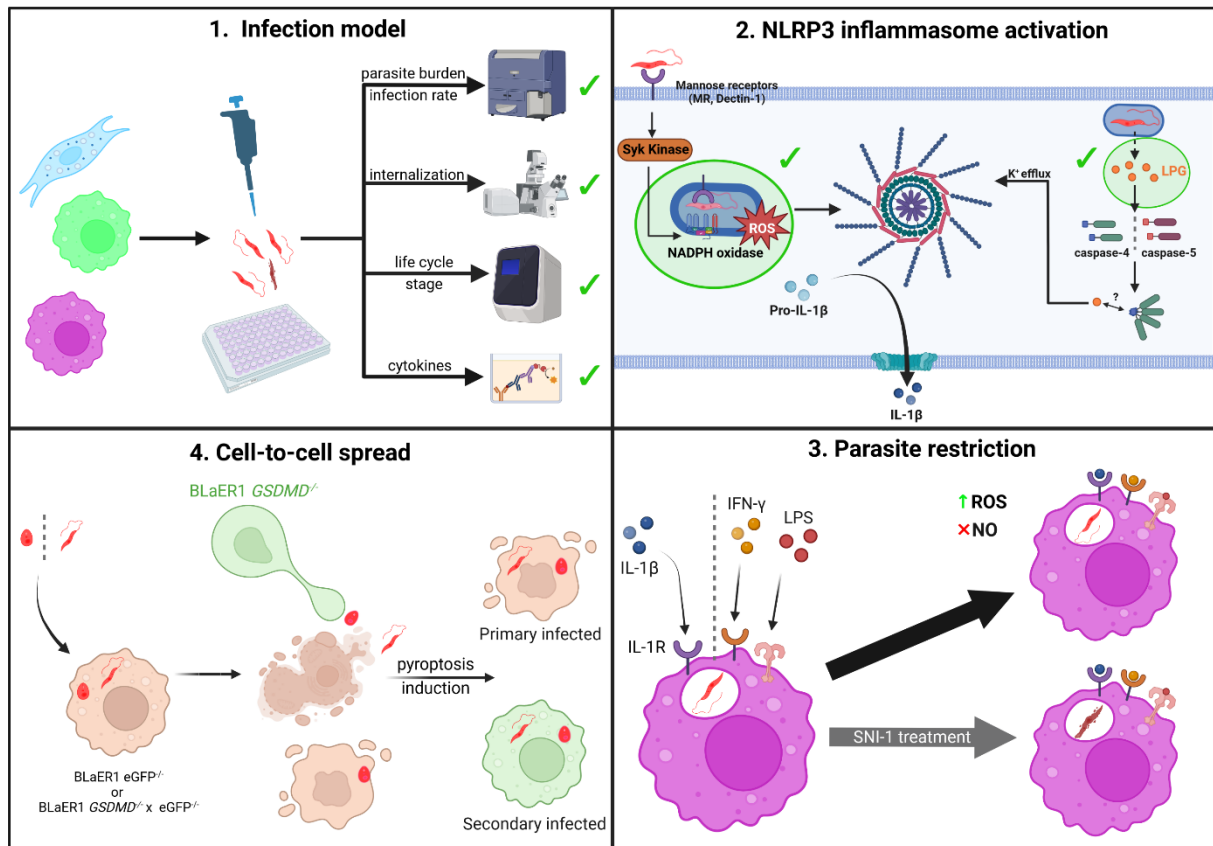
Figure 48: Schematic summary of the research results.
(1. Infection model) BLaER1 cells corresponded well to either type of hMDMs across all tested parameters. (2. NLRP3 inflammasome activation) Experiments with LPG deficient *L. major* parasites and NADPH oxidase inhibitors confirmed the role of both pathways in *L. major*-mediated inflammasome activation. (3. Parasite restriction) Neither NLRP3 inflammasome activation nor pro-inflammatory polarization led to parasite restriction in human phagocytes. Parasite restriction could be rescued by treatment with the NO-generating compound SNI-1. (4. Cell-to-cell spread) Induction of pyroptosis lead to a strong increase in the rate of secondary infections, showing that pyroptosis is a possible mechanism of parasite spread.

5.1 BLaER1 as an infection model for *L. major* infection of hMDMs

It is widely recognized that cell lines derived from transformed cells react differently than primary human cells [94,95,158]. However, when it comes to cell line models of primary human cells this fact often goes unacknowledged. An example for this are the low CD14 expression and deficient alternative NLRP3 inflammasome activation of THP-1 cells [96] that does not resemble primary hMDMs. To address this problem, the BLaER1 cell line was systematically compared to the most frequently used M-CSF-derived and GM-CSF-derived macrophages to establish the cell line as an infection model for the infection of primary human macrophages with *L. major*, prior to the analysis of the NLRP3 inflammasome response to *L. major* infection of these cells.

5.1.1 Immunophenotype of tdBLaER1 cells corresponds to well to hMDMs

Immunophenotyping of tdBLaER1 cells, udBLaER1 cells, M-CSF-derived hMDMs and GM-CSF-derived hMDMs revealed that tdBLaER1 cells resembled GM-CSF-derived hMDMs more closely with only three different markers (CD206, HLA-DR, CD18), which were expressed by a smaller percentage of cells. In comparison to M-CSF-derived hMDMs, six markers (CD206, HLA-DR, CD18, CD14, CD163, CD116) that were expressed by a smaller share of cells. The most notable of these markers were CD14, CD206 and CD18. CD14 is a co-receptor of TLR4 and important for the recognition of LPS [29], while the mannose receptor (CD206) recognizes LPG on the parasite surface and plays a role in parasite uptake [13,137,159,160,14]. Finally, integrin β-chan2 (CD18) is involved in cell adhesion [29], which might explain the weaker adherence of tdBLaER1 cells compared to macrophages, observed throughout this thesis, and reported by others [100]. This speculation is also supported by the fact that deficiencies in CD18 expression are the underlying cause of leukocyte adhesion deficiencies, which impair the extravasation of leukocytes into inflamed tissues [29]. However, it should be noted that CD18-mediated adhesion to endothelial cells is facilitated by specific interactions with endothelial intercellular adhesion molecules, thus, it is unclear whether this finding really applies to cell culture-treated surfaces. However, while the percentage of positive cells was lower for tdBLaER1 cells for the aforementioned markers (CD14, CD206, CD18), the expression level of the positive subset measured by the mean relative fluorescence intensity values (MFI) was significantly higher. Accordingly, tdBLaER1 cells showed a comparable sensitivity to LPS as hMDMs as determined by secretion of TNF-α and IL10. This result is well in line with reports by *Gaidt et al.*, who reported a highly similar LPS sensitivity of tdBLaER1 cells compared to hMDMs [77]. The different share of CD206 positive cells did also not result in different rates of parasite uptake. Likely because the functions exerted by CD18 and CD206 i.e., cell adhesion and phagocytosis of *Leishmania* are highly redundant processes [13,15,16,29,14], thus, subsets lacking these surface markers could compensate their functions with other proteins beyond the scope of this phenotyping. Overall, tdBLaER1 cells resembled GM-CSF-derived hMDMs more closely than M-CSF-derived macrophages in terms of their immunophenotype, but were very similar to both types of hMDMs. This was not surprising, because GM-CSF and M-CSF are recognized as survival cytokines for monocytes and macrophages and, while they can facilitate the differentiation from monocytes to macrophages, they do not promote a pronounced polarization of the macrophages unlike stimulation with LPS+IFN-γ or IFN-γ (pro-inflammatory; M1) or IL-4 (anti-inflammatory; M2) [40]. Accordingly, only 17 % of genes are differentially regulated between GM-CSF-derived and M-CSF-derived hMDMs [161].

5.1.2 Smaller size of BLaER1 cells does not affect their susceptibility to *L. major* infection

A notable difference between BLaER1 cells and primary human macrophages is the smaller size and the smaller cytoplasm area of BLaER1. This characteristic can be observed by any fluorescence microscopy staining that labels DNA and a cytosolic or plasma membrane-bound structure and can be inferred from the results of several groups using this cell line[99,101]. This raised the question whether BLaER1 cells would be susceptible to infection with *L. major* parasites, because *Leishmania ssp.* are relatively large intracellular pathogens (approx. 8 µm of cell body in promastigote form) and also highly motile [8,9,162]. Accordingly, promastigotes have been reported to cause cell membrane rupture of macrophages during phagocytosis [162]. The analysis of cell size, cytoplasm area and presence of intracellular parasites showed that BLaER1 cells, like hMDMs are susceptible to *L. major* infection and increase their cytoplasm area in response to the uptake of pathogens. Unsurprisingly, a larger area of the cell was occupied by the nucleus in BLaER1 cells than in either type of hMDMs at any timepoint. As enlarged and irregular nuclei are typical for transformed cells and usually do not occur in primary human cells [163–165] an influence of *L. major* infection on this morphologic characteristic was not expected.

5.1.3 BLaER1 are infected at similar rates as hMDMs and support intracellular parasite growth

In contrast to hMDMs, the parasite burden of BLaER1 cells could not be determined by Diff-Quick staining. Hence, the parasite burden was determined by automated fluorescence microscopy as an alternative. Using this method an average parasite burden of 3.50 could be determined, which corresponded extremely well with the parasite burden of 3.2 reported by *Wenzel et al.* for promastigote-infected M-CSF-derived hMDMs [166]. Thus, their smaller size does not affect the susceptibility of BLaER1 cells to *L. major* infection.

It has previously been reported that an apoptotic subset of metacyclic promastigote cultures is crucial for the establishment of a productive infection. This immunosuppressive effect is mediated by the expression of PS on the surface of the apoptotic, which induces the secretion of the anti-inflammatory cytokine TGF-β [155]. While the exact mechanism has not been demonstrated, it is assumed that the apoptotic, PS-expressing parasites hijack the host cell's efferocytosis pathway, which mediates the uptake of apoptotic cells by phagocytic cells without inflammation and is an important mechanism for tissue homeostasis [167]. This is further corroborated by findings of *Chaves et al.,* who showed that the immunosuppressive effect of parasite uptake within apoptotic neutrophils by TRMs ("Trojan horse strategy") is dependent on the expression of PS receptors Axl and mertk [25]. Since, phagocytic cells

recognize apoptotic cells and cell debris through "eat-me" signals - predominantly PS, it is likely that this is also the pathway activated by apoptotic parasites [167]. Besides its role in leishmaniasis, efferocytosis is recognized as an important anti-inflammatory feedback mechanism as the number of apoptotic neutrophils in tissues peaks concomitantly with a self-limiting inflammation and decreases through the resolution phase [168,169] In summary, the uptake of both viable and apoptotic parasites is an important characteristic of a human macrophage infection model, to correctly display the immunosuppressive effects of apoptotic parasites. The analysis of the total (viable+dead) parasite uptake of BLaER1 cells to M-CSF-derived and GM-CSF-derived macrophages showed a strong decrease of the infection rate of BLaER1 cells compared to hMDMs at 96 h p.i. (**Figure 13**). This difference decreased when the supernatant of tdBLaER1 cells was discarded prior to cell harvest and disappeared when only CD14-positive cells were compared (**Figure 14**). Hence, the observed differences in total infection rate were caused by residual udBLaER1 cells and not by a different response to *L. major* infection by BLaER1 cells compared to hMDMs. This was further corroborated by the observed infection rate of CD14$^+$ BLaER1 cells with only viable parasites i.e., DsRed-expressing parasites, which did not show any significant differences in comparison to either type of hMDM at any time point. The issue of transdifferentiation efficiency is briefly discussed by *Gaidt* et al., who report difficulties to adapt the transdifferentiation procedure to larger well formats than 96-well [100]. However, it should be noted that *Gaidt et al.* determined the transdifferentiation efficiency only by morphological assessment and not by surface marker expression, as performed by *Rapino et al.* [99] and in this thesis. During the testing of transdifferentiation protocols, I observed very uncomplete transdifferentiation of BLaER1 cells in 96-well plates, when the efficiency was assessed by surface marker expression (data not shown), despite the visual absence of cells in the supernatant, suggesting that the lack of observable udBLaER1 cells in the supernatant might be an artifact of the low medium volume per well in 96-well plates. Only the increase of the β-estradiol concentration from 100 nM to 400 nM was able to achieve a similar transdifferentiation efficiency as in 6-well plates. Notably, the transdifferentiation protocol for the 6-well format adapted from *Vierbuchen et al.* [101], also required an increase of the β-estradiol concentration from 100 nM to 200 nM, for a robust and high transdifferentiation efficiency. It could be speculated that the differences in the transdifferentiation efficiency could be the result of different cell densities, which affect the available amount of β-estradiol per cell and influence the half-life of β-estradiol in the culture. In summary, the transdifferentiation protocol of BLaER1 cells should be tested and optimized prior to experimentation and a readout for the transdifferentiation efficiency (morphology or immunophenotype) should be defined.

As amastigotes replicate within the parasitophorous vacuole of macrophages, it was important to show the intracellular transformation and determine the intracellular growth of *L. major* parasites within BLaER1 cells and compare it to GM-CSF-derived and M-CSF-derived hMDMs. Taking advantage of the work of *Stenger and van Zandbergen*, which showed that the MFI of cells infected with fluorescent parasites can be used as a proxy for the parasite burden [170], intracellular parasite growth was confirmed by flow cytometric analysis of the DsRed MFI of infected BLaER1 cells, GM-CSF-derived hMDMs and M-CSF-derived hMDMs, which increased over time. This result showed that *L. major* parasites can replicate within each tested cell type.

While the increase of fluorescence intensity in the previous experiments already provided strong evidence for the intracellular transformation of *L. major* to the amastigote stage, flow cytometric analysis, unlike a histological staining, did not allow a morphological confirmation. Therefore, the successful transformation was confirmed by qPCR of promastigote marker SHERP and amastigote Marker ABC transporter homologue, as reported by [166]. Interestingly, the expected reduction in SHERP expression was only significant in BLaER1 cells and M-CSF-derived hMDMs, and the expected increase in the ABC transporter homologue was only significant BLaER1 cells. The reasons for this are twofold and consist of a limitation of the experimental setup and the gene regulation of *Leishmania*. First, the infection experiment was performed in a micro-reaction tube, thus, extracellular parasites could not be removed as efficiently by washing steps as in cell culture plates. Hence, RNA from residual non-phagocytosed promastigotes could have influenced the analysis of SHERP. Furthermore, cells did not have a cell culture-treated surface for adhesion within the micro-reaction tube i.e., were cultivated in suspension. It is well established that this negatively affects the viability of primary cell culture [158], thus, it is possible that the BLaER1 cells, due to their properties as tumor cell line, were more viable in these disadvantageous culture conditions and allowed more parasite transformations. The second reason is likely to be found in the gene regulation of *Leishmania* parasites, which mostly happens on a translational level and by varying the gene copy numbers rather than on a transcriptional level [10,171] Hence, it remains a topic of debate to which extend qPCR is a suitable method to determine the differential regulation of *Leishmania* in general (reviewed in [10]). Additionally, it has been shown that upon transformation to the amastigote form, *L. major* downregulates its transcription, which might explain the small effect size of the ABC transporter homologue upregulation [171]. Yet, taken together with increasing fluorescence intensity over time from infection experiments, both BLaER1 cells and either type of hMDM support the transformation and proliferation of the parasite.

5.1.4 BLaER1 cells show an overall lower cytokine response than hMDMs

As a final step of the establishment of the BLaER1 cells as infection model, the response to *L. major* infection was compared in regard to cytokine secretion. However, this comparison was complicated by the lack of strong and specific cytokine secretion of hMDMs in response to in vitro infections with *Leishmania*. The reason for this is primarily the low immunogenicity of *Leishmania ssp.*. Based on reports, that hMDMs infected with PS-negative *L. major* promastigotes purified from stationary-phase culture or logarithmic-phase promastigotes induce higher TNF-α [155] and IL-10 [172] secretions than hMDMs infected with an unpurified stationary-phase promastigotes, these two cytokines were chosen for the comparison. Initially, IL-12 secretion was also analyzed, due to its crucial role as a key cytokine of the T_h1 response [48,50], but was excluded from analysis due to repeated lack of detectability in any tested cell type irrespective of infection and stimulus (data not shown).While BLaER1 cells, GM-CSF-derived hMDMs and M-CSF-derived hMDMs displayed a strong secretion of both cytokines upon LPS treatment, the response to *L. major* infection was weak and ambivalent. Thie response to LPS stimulation corresponds well with established literature that describes TNF-α secretion by macrophages upon contact with a plethora of PAMPs including LPS [29] and recognizes the secretion of IL-10 upon pro-inflammatory stimulation as an important negative feedback mechanism to limit immunopathogenic tissue damage (reviewed in [173]). The response to *L. major* infection in general was well in line with the low immunogenicity of *L. major* [174]. Notably, BLaER1 cells displayed an overall lower TNF-α response compared to hMDMs. The lower cytokine response, however, appeared to be limited to TNF-α secretion, as the IL-10 secretion was on par with GM-CSF-derived hMDMs. This is assumption is supported by *Gaidt et al.*, who demonstrated a similar secretion of IL-1β and IL-6 of BLaER1 cells in comparison to primary human blood monocytes [77]. Interestingly, GM-CSF-derived hMDMs, unlike M-CSF-derived hMDMs, did not show a significant increase in their IL-10 secretion, suggesting that even though their phenotype is highly similar, some noticeable phenotypic differences between GM-CSF-derived hMDMs and M-CSF-derived hMDMs do exist and need to be considered.

Taking it all together, the systematic comparison of BLaER1 cells with GM-CSF-derived hMDMs and M-CSF-derived hMDMs showed that BLaER1 cells closely resemble these primary human macrophages in their response to *L. major* infection. Hence, the establishment of BLaER1 cells as an infection model for the infection of primary human macrophages with *L. major* was successful.

5.2 Characterization of the human NLRP3 inflammasome activation in response to *L. major* infection

Through the sensing of multiple PAMPs and DAMPs, the NLRP3 inflammasome plays a crucial role in the innate immune response against intracellular parasites including leishmaniasis [139,140]. However, effect of NLRP3 inflammasome activation on the outcome of cutaneous leishmaniasis remains unclear due to species-specific differences between mice and men in this pathway and between human and murine macrophages in general (see 1.5.3). So far, no mechanistical analyses of the NLRP3 inflammasome response of human host cells to *L. major* infection have been conducted, even though this data is imperative to elucidate the role of the NLRP3 inflammasome in cutaneous leishmaniasis and to evaluate its suitability as a drug target. Therefore, after the successful establishment of the BLaER1 infection model, I utilized the reverse genetic possibilities of the BLaER1 model to characterize the human NLRP3 inflammasome response to *L. major* infection. For this, I analyzed whether the two main activating pathways, (I): The canonical inflammasome activation with phagolysosomal NADPH oxidase-mediated ROS production as a second stimulus and (II): The non-canonical inflammasome activation by the interaction of cytosolic LPG with the sensor caspases-4/5, are also the main activating pathways in a human background.

5.2.1 *L. major* does activate the human NLRP3 inflammasome

I tested whether *L. major* infection does activate the human NLRP3 inflammasome. For this, BLaER1 cells were primed with LPS or the TLR7/8 agonist R848, followed by infection with *L. major*. Priming with two different stimuli was performed to isolate the effect caused by *Leishmania* infection (R848 priming) from the compounded effect of alternative inflammasome activation and *Leishmania* infection (LPS priming). The latter was included because it is the physiological most relevant priming stimulus as introduction of LPS through sand fly saliva and skin microbiome has been previously demonstrated [138,175]. *L. major* infection did result in a strong increase in IL-1β secretion for both priming stimuli demonstrating that *L. major* infection did activate the inflammasome by acting as a second stimulus of the canonical inflammasome activation pathway. This finding was well in line with previous reports of NLRP3 inflammasome activation by *L. major* infection in THP-1 cells [176] and mice [128,130]. As expected, the compounded alternative inflammasome activation by prolonged LPS stimulation and canonical activation by *L. major* infection led to an overall higher secretion of IL-1β by LPS-primed cells than by R848-primed cells. Interestingly, *L. major* infection did not result in any prolonged NLRP3 inflammasome activation, as no elevated IL-1β levels were detected at 24 h p.i.. This finding contrasts previous reports from experiments in mice, which showed high levels of IL-1β at 42

h p.i. for. in vitro-generated *L. amazonensis*-infected macrophages [128] and increased IL-1β levels of in vivo *L. infantum*-infected TRMs obtained from infected mice at 14 days p.i. [137]. While it would be tempting to attribute this to species-specific differences in the innate immunity to *Leishmania,* it should be noted that a decrease of IL-1β levels could be caused by a combination of transient inflammasome activation and uptake of IL-1β by BLaER1 cells via the IL-1R. This would correspond well with findings of *Lima-Junior et al.*, who demonstrated that murine macrophages showed an autocrine pro-inflammatory activation by taking up secreted IL-1β via the IL-1R [128]. The IL-1R is also abundantly expressed by primary human monocytes and THP-1 cells [177]. Another important consideration is that *L. major* has been reported to induce a weaker NLRP3 inflammasome activation than other *Leishmania* species like *L. mexicana* and *L. braziliensis* [178].

L. major-mediated NLRP3 inflammasome activation was further corroborated by measurement of caspase-1 activity, which showed NLRP3-specific caspase-1 activity upon *L. major* infection. Interestingly, caspase-1 activity induced by *L. major* infection, unlike activation by LPS and nigericin treatment, could not be completely inhibited by treatment with the pan-caspase inhibitor ZVAD. One possible reason for this could be that *L. major* induces caspase-2 activity in host cells, as this caspase is not inhibited by ZVAD [179]. However, caspase-2 is predominantly located in the nucleus and although some evidence for an involvement in IL1-β exists, the exact function of caspase-2 remains enigmatic (reviewed in [180,181]). Therefore, caspase-2 seems to be an unlikely reason for the residual 660-YVAD signal. Another possible reason could be the active cleavage of the 660-YVAD-FMK probe by *L. major*, as the observed fluorescence signal of 660-YVAD-FMK was detected in proximity to the internalized parasites. The mechanism of fluorescent caspase probes is suicidal inhibition of the active caspase by interaction of the active enzyme with a peptide containing the caspase-specific cleavage sequence. Hence, the surface metalloprotease gp63 of *Leishmania ssp.,* which has previously been shown to cleave the caspase-1 substrate pro-IL-1β [176], might be able to cleave the YVAD-sequence of the caspase-1 probe, too.

5.2.2 NLRP3 inflammasome activation by phagolysosomal ROS production

One signaling pathway for *Leishmania*-mediated activation of the NLRP3 inflammasome is the production of phagolysosomal ROS upon uptake of parasites via CLR receptors. Two non-redundant signaling axes have been reported by *Levefre et al.* (I): Uptake via Dectin-1 leads to activation of Syk kinase and subsequent activation of the NADPH oxidase complex, (II): Uptake via MR leads to release of arachnidonic acid from the inner leaflet of the plasma membrane, which controls the assembly of

the NADPH oxidase complex [137]. Treatment with DPI completely ablated the IL-1β secretion of *L. major* infected BLaER1 cells. However, the measurement of intracellular ROS by superoxide (O_2^-) and hydrogen peroxide (H_2O_2) probe DHE was equivocal. While the determination of ROS levels showed that *L. major* uptake, irrespective of prior stimulation, did cause the production of ROS by the host cell, treatment with DPI caused a high baseline level of ROS in the uninfected control. In follow-up experiments this high baseline level of ROS was shown to occur for other inhibitors (apocynin, NOX VII), too, and to be independent of DMSO. Despite the high baseline, however, DPI treatment successfully abrogated any increase in ROS levels caused by *L. major* infection in addition to the LPS stimulation. Hence, it can be assumed that DPI treatment, despite the observed off-target effects, successfully inhibited the ROS production induced by phagocytosis of *L. major* parasites, thereby demonstrating that phagocytosis-mediated ROS production plays a role in the activation of the human NLRP3 inflammasome. Even though these findings confirm reports of *Levefre et al.* and *Lima-Junior et al.,* which showed that inhibition of ROS abrogates *Leishmania ssp.*-mediated NLRP3 inflammasome action, the high baseline ROS levels compared to untreated controls are in contrast to these studies [137,141]. In general, the role of ROS in the activation of the NLRP3 inflammasome remains controversial. While some studies support the findings of *Levefre et al., Lima-Junior et al.* [137,141] and this thesis [117,182], others found the NLRP3 inflammasome activation to be independent of NADPH oxidase-mediated phagolysosomal ROS [116,183–185]. A possible explanation for this controversy could be that all studies that reported an independence of NLRP3 inflammasome activation from ROS production used second stimuli like monosodium urate, silica, or liposomes i.e., substances that induce lysosomal rupture [116,183–185]. Lysosomal rupture is an alternative second stimulus of the NLRP3 inflammasome and presumably activates NLRP3 via H^+ release and lysosomal enzymes, like cathepsins [115,120]. In line with this speculation, *Hornung et al.* reported that monosodium urate-mediated, ROS-independent inflammasome activation was abrogated by treatment with the H^+ ATPase inhibitor bafilomycin A, required for lysosome acidification [116]. It could therefore be speculated that lysosomal rupture circumvents NADPH oxidase-dependent NLRP3 inflammasome activation pathways. Finally, it should be noted that DPI [186], and likely other NADPH oxidase inhibitors due to the high structural similarity of this type of enzymes, increase mitochondrial ROS levels, which have also been implicated in the activation of the NLRP3 inflammasome [114,187]. These findings, however, have in turn been disputed by other reports [109,188,189], hence, the role of ROS in the NLRP3 inflammasome activation remains elusive.

5.2.3 Non-canonical inflammasome activation by parasite LPG

The second signaling pathway for *Leishmania*-mediated activation of the NLRP3 inflammasome is the non-canonical activation of the NLRP3 inflammasome by detection of LPG by the murine cytosolic sensor caspase-11 [142]. Therefore, I tested whether the human orthologs of caspase-11, caspase-4 and caspase-5, could detect LPG upon *L. major* infection and activate the NLRP3 inflammasome. Infection of BLaER1 cells with LPG-deficient *L. major* T7/Cas9 DsRed *LPG1*$^{-/-}$ led to a complete abrogation of the NLRP3 inflammasome activation. This finding confirmed the hypothesis that the *L. major* LPG is an important activator of the human NLRP3 inflammasome and confirms the findings of *de Carvalho et al.* from *L. amazonensis*-infected murine macrophages, who could show similar results [142]. Furthermore, this experiment points towards a recognition of LPG by the human orthologs of caspase-11, caspase-4 and caspase-5. This would be expected, as caspase-11 and caspase-4 have previously been shown to have highly similar properties in the direct binding of LPS by their CARD domain [123,142].

To elucidate the role of caspase-4/5 in the detection of *L. major* LPG, BLaER1 *Casp4*$^{-/-}$ and BLaER1 *Casp5*$^{-/-}$ cells were infected with *L. major* T7/Cas9 DsRed and *L. major* T7/Cas9 DsRed *LPG1*$^{-/-}$ parasites. Interestingly, knockout of caspase-4 or caspase-5 did not reduce the IL-1β secretion to the level of cells infected with *L. major* T7/Cas9 DsRed *LPG1*$^{-/-}$ parasites. This suggests either a redundancy of these caspases in human cells or the involvement of other receptors in the recognition of LPG. The latter would be well in line with findings showing that recombinant caspase-4/11 does not directly bind LPG, raising the question how LPG is detected by these caspases [142]. The data on caspase-5 is scarce, presumably due to the lack of caspase-5 expression by the frequently used cell lines THP-1 and U937 [123] and its role in the non-canonical inflammasome seems to originate from its homology to caspase-4.

5.2.4 Inflammasome activation in hMDMs is subject to high donor variation

To account for eventual differences in the NLRP3 inflammasome response of BlaER1 cells and hMDMs, I explored whether some experiments that compared BLaER1 cells to BLaER1 *Casp1*$^{-/-}$ and BLaER1 *NLRP3*$^{-/-}$ cells, could be performed in primary human cells using hMDMs and the small molecule NLRP3 inhibitor MCC950. Except for nigericin-treated cells – the positive control for inflammasome competence, no significant results in primary hMDMs were observed. This was due to the high donor variance as the differences in IL-1β secretion between the lowest and highest responding donors varied between 40fold (R848 stimulated GM-CSF-derived hMDMs) to 97fold (LPS stimulated GM-CSF-derived

hMDMs. This data corresponds well with IL-1β concentrations measured in patient material from CL lesions, which showed high donor variances in several reports [148,149,190]. Moreover, several authors reported a considerable higher IL-1β production of human peripheral blood monocytes compared to in vitro-differentiated hMDMs [191,192]. Hence, observed differences in the inflammasome activation might also arise from different differentiation efficiencies between different donors. In summary, despite their functional NLRP3 inflammasome, the effect of the NLRP3 inflammasome on *L. major* infection could not be investigated in hMDMs due to the low IL-1β secretion of in vitro differentiated hMDMs and the conservative experimental design, which treated donor-derived cells as unpaired data.

5.2.5 Inflammasome-mediated parasite restriction

NLRP3 inflammasome activation has been shown to be a potent leishmanicidal effector mechanism of murine macrophages. Killing of intracellular parasites is mediated by NO production induced by autocrine stimulation with secreted IL-1β [128]. Since strong iNOS-mediated NO production is a hallmark of murine macrophages, I tested whether NLRP3 inflammasome activation induces the restriction of intracellular parasites in human BLaER1 cells. While a strong NLRP3 inflammasome-specific IL-1β secretion could be observed for BLaER1 cells upon *L. major* infection, no differences in infection rate and parasite burden were observed compared to inflammasome-deficient BLaER1 *CASP1*^{-/-} cells or BLaER1 *NLRP3*^{-/-} cells. The reason for this is likely a lack of a strong NO production upon *L. major* infection, as human cells rely more on ROS as an innate antimicrobial effector mechanism [19,59,61]. However, it is well established that human macrophages do not effectively restrict *L. major* parasites in the absence of T_h1 T cells [46,193,194]. This is underlined by the fact that *Lima-Junior et al.* also managed to induce parasite restriction by murine macrophages via pro-inflammatory stimulation with IFN-γ, a key cytokine of the T_h1 immune response [128]. In contrast to the aforementioned findings, pro-inflammatory stimulation with LPS and IFN-γ or IFN-γ alone did not induce parasite restriction by BLaER1 cells, despite an increase in the production of the effector ROS. Interestingly, my results also did not correspond well with results from experiments with human cells, which demonstrated the NO-independent, IFN-γ-induced restriction of *L. braziliensis* in human monocytes [74]. Another group even reported the restriction of *L. braziliensis* in human monocytes without any stimulation [195]. However, it should be noted that in this study, PBMCs from CL patients or healthy donors were infected with *L. braziliensis* without prior isolation of monocytes, which were discriminated by anti-CD14 immunostaining in the subsequent flow cytometric analysis [195]. Since PBMCs contain NK cells, which upon stimulation with IL-12 and IL-18 become strong producers of IFN-γ [29], it is likely that parasite restriction in that work was also the result of IFN-γ stimulation.

Considering a study by *Müller et al.*, who demonstrated that T_h1 cells activate macrophages within a 80 µm radius [51], thereby suggesting a strong concentration dependency of IFN-γ-mediated parasite restriction, it is possible that the use of a higher IFN-γ concentration could have achieved restriction of *L. major* in human BLaER1 cells.

Macrophages are a highly plastic cell type and can change their phenotype based on the stimuli they receive from their respective microenvironment [35,38,40]. Consequently, the exact immunophenotype of human macrophage subsets is a topic of ongoing debate and very dependent of the used experimental conditions [36]. In an attempt to establish an easy validation of the pro-inflammatory polarization of BLaER1 cells, I tested the CD86 expression level and IL-12 secretion of pro-inflammatorily polarized BLaER1 cells as possible activation markers. However, irrespective of the pro-inflammatory stimulus and infection, no upregulation of CD86 nor a secretion of IL-12 could be detected.This finding contradicts reports of significant increases in CD86 expression level by pro-inflammatory macrophages [196–198] However, it should be considered that CD86 expression of unpolarized BLaER1 cells was already high, thus, the additional increase by pro-inflammatory activation might have been too small to reach the level of significance. Immunophenotyping experiments of polarized hMDMs previously performed by the lab have shown a strong upregulation of CD86 by pro-inflammatory hMDMs (unpublished data), hence, high baseline expression of CD86 could be a divergent behavior of BLaER1 cells that should be tested in future experiments.

The lack of IL-12 secretion clearly contradicted reports from pro-inflammatory murine macrophages, which produce IL-12 [199,200]. On the other hand, it overall corresponded well with data from human cells, which show that IL-12 is primarily secreted by monocytes or DCs [196,201,56,202], and only at low levels by macrophages irrespective of polarization [197,198]. In contrast to findings by *Smith et al.* that pointed towards M-CSF treatment as a possible reason for the absent IL-12 secretion of human macrophages [203], transdifferentiation of BLaER1 cells with GM-CSF instead of M-CSF did not result in IL-12 production upon infection of either unpolarized or upon IFN-γ treated BLaER1 cells. The reason for this is likely, that *Smith et al.* did not compare M-CSF-derived macrophages to GM-CSF-derived macrophages but to in vitro-generated DCs, which are potent and producers of IL-12 [56,203–205]. However, they are also a different cell type, hence, the conclusion of *Smith et al.* was unwarranted.

5.2.5.1 Parasite restriction by NO treatment

Strong, iNOS-mediated NO production is a hallmark of the murine innate immune response, but absent or extremely low in human phagocytes (see 1.3.4). Furthermore, NO is a very strong leishmanicidal effector mechanism of macrophages against intracellular pathogens and likely responsible for the efficient parasite restriction of many *Leishmania* species by murine macrophages compared to human macrophages [59,68]. Accordingly, the analysis of iNOS expression by qPCR showed no significant upregulation for either cell type. Notably, the cycle threshold values (Ct), which allow some conclusions about basal expression of iNOS, ranged from 30-32 for BLaER1 cells and hMDMs compared to Ct values of 17 observed for LPS+IFN-γ-stimulated murine macrophages used for the validation of the primer efficiency (Appendix A). This result was expected, because the detection of iNOS by qPCR was shown to be inconsistent and the observed expression always very low (for a comprehensive overview see table 1 in [59]). However, it has previously been reported that [206] upregulation of iNOS mRNA did not necessarily lead to NO secretion, hence, it can not be ruled out that the absence of pronounced upregulation necessarily indicates a lack of iNOS protein. Therefore, BLaER1 cells and hMDMs could have potentially expressed a sufficient amount of iNOS and simply not have responded to *L. major* infection with a higher iNOS gene expression.

Analysis of infected BLaER1 cells by flow cytometry and Griess reaction, showed that infection with *L. major* did not induce any production of NO, while the treatment with 80 µM SNI-1 increased the NO concentration in the supernatant by approx. 50 µM. Treatment with SNI-1 significantly reduced the parasite burden, but not the infection rate in BLaER1 cells as early as 24 h p.i. and the reduction became stronger with longer incubation times and increased number of SNI-1 treatments. Since the parasite burden in this experiment was assessed by flow cytometric analysis of the DsRed intensity of the intracellular parasites, it is possible that NO did not kill the parasites, but impaired their intracellular proliferation. This would be well in line with results of *Müller et al.* who showed a primarily sublethal effect of NO on intracellular *L. major* parasites in a murine infection model [207]. While the same study also reported that a share of the parasites was killed by NO production, this was not observed here. This could have been due to lower local concentrations of NO in the phagolysosome, because the SNI-1 treatment relied on the diffusion of the gaseous NO into the phagolysosome while NO production in murine cells takes place at the phagolysosome membrane [207]. Another explanation could be phases of recovery in between of the SNI-1 treatments caused by the short half-life of the compound. This problem was partially addressed by the repeated addition of fresh SNI-1, but constitutes a notable difference to murine cells.

To confirm these results in hMDMs, I repeated the experiment with GM-CSF-derived and M-CSF-derived hMDMs. A reduction of the parasite burden was observed for GM-CSF-derived hMDMs, but not M-CSF-derived hMDMs. Another interesting observation was a significant increase in the infection rate of M-CSF-derived hMDMs upon *L. major* infection. *Heyde et al.* reported first evidence that *L. major* parasites transmitted to new host cells in an pro-inflammatory microenvironment show a higher proliferation than other intracellular parasites [50]. Hence, it could be speculated that the NO treatment in M-CSF-derived hMDM lead to parasite spread by NO-induced cell death, which might have stimulated parasite growth and, therefore, also an increase in DsRed abundance upon uptake by a previously uninfected macrophage. In summary, however, the lack of parasite restriction in M-CSF-derived hMDMs compared to GM-CSF-derived hMDMs and BLaER1 cells was equally unexpected and enigmatic and further experiments are needed to shed light on the characteristics of these cells that led to this different outcome.

Taking it all together, I successfully utilized the BLaER1 infection model to confirm the activation of the human NLRP3 inflammasome by *L. major* infection. Analysis of the ROS and LPG dependency of the inflammasome activation largely confirmed the findings of the murine model, but pointed towards a human-specific convergence of the non-canonical inflammasome pathway and the ROS-mediated activation upstream of caspases-4/5. In sharp contrast to findings from murine cells, no inflammasome-mediated parasite restriction could be found in human cells. This is an important species-specific difference that needs to be considered for the development of drugs targeting the inflammasome.

5.3 Pyroptosis as a mechanism of parasite spread to new host cells

Over the course of an infection with intracellular pathogen, host-to-host transmission of the pathogen is required to maintain and spread the infection to new previously uninfected host cells. While this part of the pathogen life-cycle has been often neglected in the past, interest in the mechanisms of cell-to-cell spread has increased in recent years (reviewed in [26]). The mechanism of host-to-host transmission of *Leishmania* in particular is poorly understood. The egress of *Leishmania* amastigotes has often been attributed to cell membrane rupture of the host cell caused by increasing numbers of intracellular amastigotes. However, this assumption has been challenged by recent studies that showed the capability of macrophages to tolerate extremely high parasite burdens of greater than 70 parasites per cell both in vitro and in vivo [22]. Therefore, in the final part of the thesis, I used the

BLaER1 model to test whether pyroptosis, a downstream effector mechanism of strong NLRP3 inflammasome activation, plays a role in the spread of *L. major* infection to new host cells.

Harnessing the possibilities of reverse genetics by this cell line model, a BLaER1 knockout cell line that is resistant to pyroptotic cell death had to be found and functionally validated. Based on its role as the predominant pore-forming protein in pyroptosis [105,106], gasdermin D was chosen as a candidate. Comparison of inflammasome activation and cell death of BLaER1 *GSDMD*^{-/-} cells and BLaER1 wild type cells showed that BLaER1 *GSDMD*^{-/-} cells were significantly more resistant to pyroptosis induction than BLaER1 wild type cells. Despite pyroptosis resistance BLaER1 *GSDMD*^{-/-} cells started to show signs of lytic cell death at 4 h post nigericin treatment. This was unexpected, but corresponded well with *He et al.,* who showed that *GSDMD*^{-/-} RAW264.7-asc cells show increased caspase-3/7/8 activity and undergo apoptosis upon pyroptosis induction [208]. Possible inducers of apoptosis in this experimental setting could have been cell stress by prolonged K^+-efflux, or the priming step with LPS, which could have triggered the extrinsic, caspase-8 dependent apoptosis pathway [44,209,210]. At the first glance, apoptosis would contradict the observed increase in IL-1β secretion by BLaER1 *GSDMD*^{-/-} cells, however, several reports have shown that caspase-3/6/7 activity can induce pyroptosis by cleavage of gasdermin-E and gasdermin D [210–212]. This is also not the only crosstalk between pyroptosis and apoptosis, as mitochondrial depolarization by the proteins BAX and BAK releases mitochondrial contents into the cytoplasm, activating NLRP3 [44,209]. The pro-inflammatory nature of BLaER1 *GSDMD*^{-/-} cell death involving IL-1β secretion, could also point towards necroptosis. This type of pro-inflammatory lytic cell death has multiple intersections with both pyroptosis and apoptosis and acts as an alternative cell death mechanism if apoptosis is impaired [44,209,213]. However, necroptosis, like pyroptosis results in an "explosion-like" lytic cell death and thereby contradicted the morphological characteristics of BLaER1 *GSDMD*^{-/-} cell death observed by live-cell imaging. In summary, I could show that BLaER1 *GSDMD*^{-/-} cells, despite their ultimate cell death under pyroptosis-inducing conditions, were refractory to pyroptosis creating a sufficiently large time window to study the involvement of pyroptosis in cell-to-cell spread of *L. major* parasites.

To characterize pyroptosis as an exit mechanism, the release of parasites from BLaER1 cells and *GSDMD*^{-/-} cells under pyroptosis-inducing conditions was analyzed. The live-cell imaging data showed that induction of pyroptosis led to a rapid release of intracellular parasites from a large share of BLaER1 cells, but not from BLaER1 *GSDMD*^{-/-} cells. This finding was well in line with a previous report from the murine system in which induction of pyroptosis led to a rapid release of *L. amazonensis* amastigotes

from murine macrophages [214]. Notably, neither in murine [214] nor in human macrophages did NLRP3 inflammasome activation affect the viability of intracellular amastigotes. While this was expected for human host cells, due to the lack of NO induction discussed earlier, it is quite important for the murine system, because in murine host cells a potent leishmanicidal induction of NO downstream of NLRP3 inflammasome activation has been reported [128]. The reason for this is likely the rapid onset of pyroptosis by treatment with nigericin that limits the time of NO production. This raises the question, if parasite viability would be impaired by NO in an in vivo experiment conducted in mice, because of the slower induction of pyroptosis by physiological stimuli and the concomitant prolonged exposure to NO. This could possibly lead to an underestimation of pyroptosis-mediated parasite spread in this system.

After demonstrating pyroptosis-mediated parasite exit, it was analyzed whether this phenomenon would lead to parasite spread in a co-incubation assay. Flow cytometric analysis demonstrated that induction of pyroptosis led to strong and significant increases in the secondary infection rate for BLaER1 *GSDMD*^{-/-} cells co-incubated with BLaER1 eGFP^{-/-} cells, but not for BLaER1 *GSDMD*^{-/-} cells co-incubated with BLaER1 *GSDMD*^{-/-} x eGFP^{-/-} cells. This finding showed that pyroptotic release of parasites can facilitate the spread to new host cells within the same pro-inflammatory microenvironment in which the parasite exit occurred, which is a pre-requisite for this mechanism to play a role in vivo at the infection site. In summary, the co-incubation assay confirmed the hypothesis that pyroptosis can facilitate cell-to-cell spread of *L. major*. Notably, I observed a strong, pyroptosis-dependent increase in the secondary infection rate of amastigote infected BLaER1 *GSDMD*^{-/-} cells co-incubated with BLaER1 eGFP^{-/-} cells, which were stimulated with LPS alone. Therefore, pyroptosis of these cells was likely induced through the alternative activation pathway of the NLRP3 inflammasome. Since the alternative activation of the inflammasome i.e., by LPS stimulation alone, does not exist in murine cells [77] and is non-functional in THP-1 cells, this finding would have not been possible in any other experimental system. These observations, are in contrast to earlier speculations that cell-to-cell spread of *Leishmania* must necessarily involve direct cell-to-cell transfer, due to the susceptibility of *Leishmania* to complement-mediated lysis [4,215]. However, they are well in line with recent studies, that showed a strong recruitment of monocytes to the infection site during the acute infection phase [47,48,50]. Since *Carneiro et al.* showed upregulation of IL1-β during this phase of the infection [48] it is tempting to speculate that pyroptosis might play a role in the spread of parasites to new host cells. However, it should be considered that other groups previously have demonstrated the involvement of apoptosis in the cell-to-cell spread of *L. major* under these pro-inflammatory conditions [50]. Interestingly, transcriptomic profiling of tissue from lesions of cutaneous leishmaniasis patients infected with *L.*

braziliensis revealed an upregulation of inflammasome as well as apoptosis-associated genes, suggesting the activation of both pathways during leishmaniasis [147]. Considering the heterogenous polarization of macrophages at the infection site [48], and the substantial crosstalk of apoptosis, pyroptosis and necroptosis mentioned earlier, it is likely that several forms of cell death contribute to the spread of *Leishmania* parasites at the infection site.

5.4 Conclusions and outlook

In summary, this thesis provided important insights into the role of the NLRP3 inflammasome in cutaneous leishmaniasis. By establishment of the transdifferentiating cell line BLaER1 as an infection model for the infection of hMDMs with *L. major* fast and easy genetic alteration of human phagocytes, mechanistic insights into the role of the human NLRP3 inflammasome in could be obtained. Investigation of the PAMPs and DAMPs that facilitate *L. major*-mediated inflammasome activation largely confirmed the findings from murine models that phagolysosomal ROS production and LPG are the key stimuli. Interestingly, inhibition of ROS and absence of LPG abrogated the NLRP3 inflammasome activation in human cell, hence, pointing towards a convergence of these pathways upstream of the ROS production. Notably, an absence of parasite restriction in human phagocytes was discovered in this thesis. This is an extraordinarily important species-specific difference to murine models that must be considered during the translation of pre-clinical inflammasome research to clinical stages. Lastly, pyroptosis was identified as a mechanism of cell-to-cell spread of *L. major* parasites.

Increasingly powerful in vivo imaging techniques have greatly improved the understanding of TRMs and the role of different macrophage subsets [25,50,195]. However, this also poses a challenge for the research in human macrophages that rarely transcends mostly unactivated GM-CSF-derived and M-CSF-derived hMDMs and few strongly pro- or anti-inflammatory polarizations. Future experimentations of the BLaER1 model should, therefore, focus on the polarization of these cells to mimic important TRM subsets. A possible approach for this could the transcriptomic comparison with macrophages of murine origin and validation of new polarization protocols on primary human macrophages/monocytes or induced pluripotent stem cells.

While this thesis provided important insights into the *L. major*-mediated activation of the NLRP3 inflammasome, I could not examine all aspects of this mechanism, due to the broad range of stimuli

that activate the inflammasome. Particularly, the role of ROS remains enigmatic, not just in the context of *Leishmania* infection but also in the context of NLRP3 inflammasome activation in general. All aspects of ROS, that is, the particular species of ROS, the compartment in which it is produced, and whether it activates NLRP3 directly or by oxidizing other molecules, are subjects of ongoing debate [103] Regarding *Leishmania* infection, microscopic approaches that, in contrast to flow cytometry, provide structural information should be used to elucidate the role of ROS. The high-throughput microscopy approach established in this thesis is well suited for this, and allows sample sizes close to the ones of flow cytometric experiments. By using fluorescent probes, the compartment of ROS production and phagolysosome acidification could be revealed. Additionally, the information about the localization of ROS production could clarify the high background ROS levels and allow a more unequivocal inhibition of *L. major*-induced ROS production than flow cytometric approaches. Future experiments in regard to caspase-4/5 signaling should aim to investigate the potential redundancy of caspase-4 and caspase-5 by using a BLaER1 *CASP4*$^{-/-}$ x *CASP5*$^{-/-}$ cell line. Lastly, this thesis demonstrated that the inflammasome-mediated parasite restriction observed in murine cells does not occur in human phagocytes. This finding has strong implications for the use of the NLRP3 inflammasome as a drug target, because it highlights that a protective effect cannot be achieved by innate parasite restriction, but will likely occur on a T cell level. Hence future experiments should focus not so much on parasite restriction but on the cytokine secretion and the effect of altered inflammasome activation on the T cell response. A possible approach could be a combination of established T cell activation assays [216] with small molecule inhibitors of the NLRP3 inflammasome like MCC950. Furthermore, the comprehensive comparison of cytokine responses during altered inflammasome activation should be conducted using Luminex and Legendplex technologies.

Lastly, the demonstration of pyroptosis as a mechanism of parasite exit, showed that inflammatory forms of programmed cell death can play a role in the cell-to-cell spread of *Leishmania* and should not be disregarded in favor of apoptosis. Furthermore, the successful generation of cell lines refractory against certain types of cell death, has been shown as a powerful tool to analyze the mechanisms of pathogen spread. With a smart selection of targets, this approach could be applied to other forms of cell death, like apoptosis and allow mechanistic insights into the role of other forms of cell death in the spread of *Leishmania*.

References

1. WHO (2022) Leishmaniasis. Key facts. Available: https://www.who.int/news-room/fact-sheets/detail/leishmaniasis.

2. Murray HW, Berman JD, Davies CR, Saravia NG (2005) Advances in leishmaniasis. The Lancet 366 (9496): 1561–1577.

3. Handman E (2001) Leishmaniasis: current status of vaccine development. Clinical microbiology reviews 14 (2): 229–243.

4. Kumar A (2013) Leishmania and Leishmaniasis. New York, NY: Springer New York.

5. Torres-Guerrero E, Quintanilla-Cedillo MR, Ruiz-Esmenjaud J, Arenas R (2017) Leishmaniasis: a review. F1000Research 6: 750.

6. van Griensven J, Diro E (2012) Visceral leishmaniasis. Infectious disease clinics of North America 26 (2): 309–322.

7. (2010) Control of the leishmaniases. Report of a meeting of the WHO Expert Committee on the Control of Leishmaniases, Geneva, 22-26 March 2010. Geneva: World Health Organization. 186 p.

8. Sunter J, Gull K (2017) Shape, form, function and Leishmania pathogenicity: from textbook descriptions to biological understanding. Open biology 7 (9).

9. Guerrant R. L., Walker D. H., Weller P. F. (2006) Tropical infectious diseases. Principles, pathogens, & practice. Philadelphia, Pa.: Churchill Livingstone Elsevier.

10. Clos J, Grünebast J, Holm M (2022) Promastigote-to-Amastigote Conversion in Leishmania spp.- A Molecular View. Pathogens (Basel, Switzerland) 11 (9).

11. Wikimedia Foundation (2023) Leishmaniasis. Wikipedia article. Available: https://en.wikipedia.org/wiki/Leishmaniasis. Accessed 17 February 2023.

12. Kaye P, Scott P (2011) Leishmaniasis: complexity at the host-pathogen interface. Nature reviews. Microbiology 9 (8): 604–615.

13. Ueno N, Wilson ME (2012) Receptor-mediated phagocytosis of Leishmania: implications for intracellular survival. Trends in parasitology 28 (8): 335–344.

14. Horta MF, Andrade LO, Martins-Duarte ÉS, Castro-Gomes T (2020) Cell invasion by intracellular parasites - the many roads to infection. Journal of cell science 133 (4).

15. Blackwell JM (1985) Receptors and recognition mechanisms of Leishmania species. Transactions of the Royal Society of Tropical Medicine and Hygiene 79 (5): 606–612.

16. Chauhan P, Shukla D, Chattopadhyay D, Saha B (2017) Redundant and regulatory roles for Toll-like receptors in Leishmania infection. Clinical and experimental immunology 190 (2): 167–186.

17. Laskay T, van Zandbergen G, Solbach W (2003) Neutrophil granulocytes--Trojan horses for Leishmania major and other intracellular microbes. Trends in Microbiology 11 (5): 210–214.

18. van Zandbergen G, Klinger M, Mueller A, Dannenberg S, Gebert A et al. (2004) Cutting edge: neutrophil granulocyte serves as a vector for Leishmania entry into macrophages. J Immunol 173 (11): 6521–6525. Available: https://journals.aai.org/jimmunol/article/173/11/6521/2129/Cutting-Edge-Neutrophil-Granulocyte-Serves-as-a.

19. Scott P, Novais FO (2016) Cutaneous leishmaniasis: immune responses in protection and pathogenesis. Nature reviews. Immunology 16 (9): 581–592.

20. Handman E, Spira DT (1977) Growth of Leishmania amastigotes in macrophages from normal and immune mice. Zeitschrift fur Parasitenkunde (Berlin, Germany) 53 (1): 75–81.

21. HAWKING F (1948) Growth of protozoa in tissue culture; Leishmania donovani. Transactions of the Royal Society of Tropical Medicine and Hygiene 41 (4): 545–554.

22. Lecoeur H, Zhang S, Varet H, Legendre R, Proux C et al. (2022) Leishmania amazonensis controls macrophage-regulated cell death to establish chronic infection in vitro and in vivo.

23. Blank C, Fuchs H, Rappersberger K, Röllinghoff M, Moll H (1993) Parasitism of epidermal Langerhans cells in experimental cutaneous leishmaniasis with Leishmania major. The Journal of infectious diseases 167 (2): 418–425.

24. Locksley RM, Heinzel FP, Fankhauser JE, Nelson CS, Sadick MD (1988) Cutaneous host defense in leishmaniasis: interaction of isolated dermal macrophages and epidermal Langerhans cells with the insect-stage promastigote. Infection and immunity 56 (2): 336–342.

25. Chaves MM, Lee SH, Kamenyeva O, Ghosh K, Sacks D (2020) The role of dermis resident macrophages and their interaction with neutrophils in the early establishment of Leishmania major infection transmitted by sand fly bite. 24 p.

26. Flieger A, Frischknecht F, Häcker G, Hornef MW, Pradel G (2018) Pathways of host cell exit by intracellular pathogens. Microbial cell (Graz, Austria) 5 (12): 525–544.

27. Mosser DM, Hamidzadeh K, Goncalves R (2021) Macrophages and the maintenance of homeostasis.

28. Metchnikoff E (1893) Lectures on the Comparative Pathology.

29. Murphy KM, Weaver C (2017) Janeway's immunobiology. New York, London: GS Garland Science Taylor & Francis Group. 904 p.

30. Gordon S, Martinez-Pomares L (2017) Physiological roles of macrophages. Pflugers Archiv : European journal of physiology 469 (3-4): 365–374.

31. Gautier EL, Shay T, Miller J, Greter M, Jakubzick C et al. (2012) Gene-expression profiles and transcriptional regulatory pathways that underlie the identity and diversity of mouse tissue macrophages. Nature immunology 13 (11): 1118–1128.

32. Mills CD, Kincaid K, Alt JM, Heilman MJ, Hill AM (2000) M-1/M-2 macrophages and the Th1/Th2 paradigm. J Immunol 164 (12): 6166–6173.

33. Heinzel FP, Sadick MD, Holaday BJ, Coffman RL, Locksley RM (1989) Reciprocal expression of interferon gamma or interleukin 4 during the resolution or progression of murine leishmaniasis. Evidence for expansion of distinct helper T cell subsets. The Journal of experimental medicine 169 (1): 59–72.

34. Kloc M (2017) Macrophages 62.

35. Mosser DM, Edwards JP (2008) Exploring the full spectrum of macrophage activation. Nature reviews. Immunology 8 (12): 958–969.

36. Murray PJ, Allen JE, Biswas SK, Fisher EA, Gilroy DW et al. (2014) Macrophage activation and polarization: nomenclature and experimental guidelines. Immunity 41 (1): 14–20.

37. Sans-Fons MG, Yeramian A, Pereira-Lopes S, Santamaría-Babi LF, Modolell M et al. (2013) Arginine transport is impaired in C57Bl/6 mouse macrophages as a result of a deletion in the promoter of Slc7a2 (CAT2), and susceptibility to Leishmania infection is reduced. The Journal of infectious diseases 207 (11): 1684–1693.

38. Sica A, Mantovani A (2012) Macrophage plasticity and polarization: in vivo veritas. The Journal of clinical investigation 122 (3): 787–795.

39. Takata K, Kozaki T, Lee CZW, Thion MS, Otsuka M et al. (2017) Induced-Pluripotent-Stem-Cell-Derived Primitive Macrophages Provide a Platform for Modeling Tissue-Resident Macrophage Differentiation and Function. Immunity 47 (1): 183-198.e6.

40. Murray PJ (2017) Macrophage Polarization.

41. Ginhoux F, Guilliams M (2016) Tissue-Resident Macrophage Ontogeny and Homeostasis. Immunity 44 (3): 439–449.

42. Xue J, Schmidt SV, Sander J, Draffehn A, Krebs W et al. (2014) Transcriptome-based network analysis reveals a spectrum model of human macrophage activation. Immunity 40 (2): 274–288.

43. Davis BK, Wen H, Ting JP-Y (2011) The inflammasome NLRs in immunity, inflammation, and associated diseases. Annual review of immunology 29: 707–735.

44. Huang Y, Xu W, Zhou R (2021) NLRP3 inflammasome activation and cell death. Cellular & molecular immunology 18 (9): 2114–2127.

45. Mills CD (2015) Anatomy of a discovery: m1 and m2 macrophages. Frontiers in immunology 6: 212.

46. Bogdan C (2020) Macrophages as host, effector and immunoregulatory cells in leishmaniasis: Impact of tissue micro-environment and metabolism. Cytokine: X 2 (4): 100041.

47. M D Sadick, C S Nelson, J E Fankhauser, F P Heinzel, R M Locksley Cutaneous host defense in leishmaniasis: interaction of isolated dermal macrophages and epidermal Langerhans cells with the insect-stage promastigote.

48. Carneiro MB, Lopes ME, Hohman LS, Romano A, David BA et al. (2020) Th1-Th2 Cross-Regulation Controls Early Leishmania Infection in the Skin by Modulating the Size of the Permissive Monocytic Host Cell Reservoir. Cell host & microbe 27 (5): 752-768.e7.

49. Romano A, Carneiro MBH, Doria NA, Roma EH, Ribeiro-Gomes FL et al. (2017) Divergent roles for Ly6C+CCR2+CX3CR1+ inflammatory monocytes during primary or secondary infection of the skin with the intra-phagosomal pathogen Leishmania major. PLOS Pathogens 13 (6): e1006479.

50. Heyde S, Philipsen L, Formaglio P, Fu Y, Baars I et al. (2018) CD11c-expressing Ly6C+CCR2+ monocytes constitute a reservoir for efficient Leishmania proliferation and cell-to-cell transmission. PLOS Pathogens 14 (10): e1007374. Available: https://journals.plos.org/plospathogens/article?id=10.1371/journal.ppat.1007374.

51. Müller AJ, Filipe-Santos O, Eberl G, Aebischer T, Späth GF et al. (2012) CD4+ T cells rely on a cytokine gradient to control intracellular pathogens beyond sites of antigen presentation. Immunity 37 (1): 147–157.

52. Suzue K, Kobayashi S, Takeuchi T, Suzuki M, Koyasu S (2008) Critical role of dendritic cells in determining the Th1/Th2 balance upon Leishmania major infection. International immunology 20 (3): 337–343.

53. Ashok D, Schuster S, Ronet C, Rosa M, Mack V et al. (2014) Cross-presenting dendritic cells are required for control of Leishmania major infection. European journal of immunology 44 (5): 1422–1432.

54. Brewig N, Kissenpfennig A, Malissen B, Veit A, Bickert T et al. (2009) Priming of CD8+ and CD4+ T cells in experimental leishmaniasis is initiated by different dendritic cell subtypes. The Journal of Immunology 182 (2): 774–783.

55. Mestas J, Hughes CCW (2004) Of mice and not men: differences between mouse and human immunology. J Immunol 172 (5): 2731–2738.

56. Stafford JL, Neumann NF, Belosevic M (2002) Macrophage-mediated innate host defense against protozoan parasites. Critical reviews in microbiology 28 (3): 187–248.

57. Schneemann M, Schoedon G (2002) Species differences in macrophage NO production are important. Nature immunology 3 (2): 102.

58. Bogdan C (2001) Nitric oxide and the immune response. Nature immunology 2 (10): 907–916.

59. Weinberg JB Human Mononuclear Phagocyte Nitric Oxide Production and Inducible Nitric Oxide Synthase Expression: 95–150.

60. Schneemann M, Schoeden G (2007) Macrophage biology and immunology: man is not a mouse. Journal of leukocyte biology 81 (3): 579.

61. Bronte V, Zanovello P (2005) Regulation of immune responses by L-arginine metabolism. Nature reviews. Immunology 5 (8): 641–654.

62. Deffert C, Cachat J, Krause K-H (2014) Phagocyte NADPH oxidase, chronic granulomatous disease and mycobacterial infections. Cellular microbiology 16 (8): 1168–1178.

References

63. Tsuji S, Iharada A, Taniuchi S, Hasui M, Kaneko K (2012) Increased production of nitric oxide by phagocytic stimulated neutrophils in patients with chronic granulomatous disease. Journal of pediatric hematology/oncology 34 (7): 500–502.

64. Nathan C, Shiloh MU (2000) Reactive oxygen and nitrogen intermediates in the relationship between mammalian hosts and microbial pathogens. Proceedings of the National Academy of Sciences of the United States of America 97 (16): 8841–8848.

65. Patil T, More V, Rane D, Mukherjee A, Suresh R et al. (2018) Pro-inflammatory cytokine Interleukin-1β (IL-1β) controls Leishmania infection. Cytokine 112: 27–31.

66. Colotti G, Ilari A (2011) Polyamine metabolism in Leishmania: from arginine to trypanothione. Amino acids 40 (2): 269–285.

67. Natoli G, Pileri F, Gualdrini F, Ghisletti S (2021) Integration of transcriptional and metabolic control in macrophage activation. EMBO reports 22 (9): e53251.

68. Stebut E von, Tenzer S (2018) Cutaneous leishmaniasis: Distinct functions of dendritic cells and macrophages in the interaction of the host immune system with Leishmania major. International journal of medical microbiology : IJMM 308 (1): 206–214.

69. Solbach W, Lohoff M., Streck H., Rohwer P., Röllinghoff M. (1987) Kinetics of cell-mediated immunity developing during the course of Leishmania major infection in "healer" and "non-healer" mice: progressive impairment of response to and generation of interleukin 2. Immunology.

70. Hau J, Schapiro SJ, editors (2011) Handbook of laboratory animal science. Volume 1, Essential principles and practices. Boca Raton, FL: CRC Press.

71. Copeland S, Warren HS, Lowry SF, Calvano SE, Remick D (2005) Acute inflammatory response to endotoxin in mice and humans. Clinical and diagnostic laboratory immunology 12 (1): 60–67.

72. Schroder K, Irvine KM, Taylor MS, Bokil NJ, Le Cao K-A et al. (2012) Conservation and divergence in Toll-like receptor 4-regulated gene expression in primary human versus mouse macrophages. Proceedings of the National Academy of Sciences of the United States of America 109 (16): E944-53.

73. Gantt KR, Goldman TL, McCormick ML, Miller MA, Jeronimo SM et al. (2001) Oxidative responses of human and murine macrophages during phagocytosis of Leishmania chagasi. Journal of immunology (Baltimore, Md. : 1950) 167 (2): 893–901.

74. Novais FO, Nguyen BT, Beiting DP, Carvalho LP, Glennie ND et al. (2014) Human classical monocytes control the intracellular stage of Leishmania braziliensis by reactive oxygen species. The Journal of infectious diseases 209 (8): 1288–1296.

75. Crauwels P, Bank E, Walber B, Wenzel UA, Agerberth B et al. (2019) Cathelicidin Contributes to the Restriction of Leishmania in Human Host Macrophages. Frontiers in immunology 10: 2697.

76. Lee H, Da Yoon E, Kim K (2020) Genome editing methods in animal models. Animal cells and systems 24 (1): 8–16.

77. Gaidt MM, Ebert TS, Chauhan D, Schmidt T, Schmid-Burgk JL et al. (2016) Human Monocytes Engage an Alternative Inflammasome Pathway. Immunity 44 (4): 833–846.

78. Baker PJ, Masters SL (2018) Generation of Genetic Knockouts in Myeloid Cell Lines Using a Lentiviral CRISPR/Cas9 System. Methods in molecular biology (Clifton, N.J.) 1714: 41–55.

79. Stratmann SA, Morrone SR, van Oijen AM, Sohn J (2015) The innate immune sensor IFI16 recognizes foreign DNA in the nucleus by scanning along the duplex. eLife 4: e11721.

80. Schumann K, Lin S, Boyer E, Simeonov DR, Subramaniam M et al. (2015) Generation of knock-in primary human T cells using Cas9 ribonucleoproteins. Proceedings of the National Academy of Sciences of the United States of America 112 (33): 10437–10442.

81. Hultquist JF, Schumann K, Woo JM, Manganaro L, McGregor MJ et al. (2016) A Cas9 Ribonucleoprotein Platform for Functional Genetic Studies of HIV-Host Interactions in Primary Human T Cells. Cell reports 17 (5): 1438–1452.

82. Seki A, Rutz S (2018) Optimized RNP transfection for highly efficient CRISPR/Cas9-mediated gene knockout in primary T cells. The Journal of experimental medicine 215 (3): 985–997.

83. Hiatt J, Cavero DA, McGregor MJ, Zheng W, Budzik JM et al. (2021) Efficient generation of isogenic primary human myeloid cells using CRISPR-Cas9 ribonucleoproteins. Cell reports 35 (6): 109105.

84. Xiao Q (2021) Generation of macrophage models to investigate the effect of host factors restricting HIV and HSV infection.

85. Lee JS, Reiner NE, editors (2009) Stable lentiviral vector-mediated gene silencing in human monocytic cell lines.

86. Kloke B-P, Schüle S, Mühlebach MD, Wolfrum N, Cichutek K et al. (2010) Functional HIV-2- and SIVsmmPBj- derived lentiviral vectors generated by a novel polymerase chain reaction-based approach. The journal of gene medicine 12 (5): 446–452.

87. Abrink M, Gobl AE, Huang R, Nilsson K, Hellman L (1994) Human cell lines U-937, THP-1 and Mono Mac 6 represent relatively immature cells of the monocyte-macrophage cell lineage. Leukemia 8 (9): 1579–1584.

88. Minciacchi VR, Kumar R, Krause DS (2021) Chronic Myeloid Leukemia: A Model Disease of the Past, Present and Future. Cells 10 (1).

89. Schepers H, Wierenga ATJ, van Gosliga D, Eggen BJL, Vellenga E et al. (2007) Reintroduction of C/EBPalpha in leukemic CD34+ stem/progenitor cells impairs self-renewal and partially restores myelopoiesis. Blood 110 (4): 1317–1325.

90. Schwende H, Fitzke E, Ambs P, Dieter P (1996) Differences in the state of differentiation of THP-1 cells induced by phorbol ester and 1,25-dihydroxyvitamin D 3. Journal of leukocyte biology 59 (4): 555–561.

91. Ziemba BP, Burke JE, Masson G, Williams RL, Falke JJ (2016) Regulation of PI3K by PKC and MARCKS: Single-Molecule Analysis of a Reconstituted Signaling Pathway. Biophysical journal 110 (8): 1811–1825.

92. Lund ME, To J, O'Brien BA, Donnelly S (2016) The choice of phorbol 12-myristate 13-acetate differentiation protocol influences the response of THP-1 macrophages to a pro-inflammatory stimulus. Journal of immunological methods 430: 64–70.

93. Starr T, Bauler TJ, Malik-Kale P, Steele-Mortimer O (2018) The phorbol 12-myristate-13-acetate differentiation protocol is critical to the interaction of THP-1 macrophages with Salmonella Typhimurium. PloS one 13 (3): e0193601.

94. Daigneault M, Preston JA, Marriott HM, Whyte MKB, Dockrell DH (2010) The identification of markers of macrophage differentiation in PMA-stimulated THP-1 cells and monocyte-derived macrophages. PloS one 5 (1): e8668.

95. Tedesco S, Majo F de, Kim J, Trenti A, Trevisi L et al. (2018) Convenience versus Biological Significance: Are PMA-Differentiated THP-1 Cells a Reliable Substitute for Blood-Derived Macrophages When Studying in Vitro Polarization. Frontiers in pharmacology 9: 71.

96. Bosshart H, Heinzelmann M (2016) THP-1 cells as a model for human monocytes. Annals of translational medicine 4 (21): 438.

97. Sharif O, Bolshakov VN, Raines S, Newham P, Perkins ND (2007) Transcriptional profiling of the LPS induced NF-kappaB response in macrophages. BMC immunology 8: 1.

98. Jack I., Seshadri R., Garson M., Michael P., Callen D., Zola H., Morley A. (1986) RCH-ACV: A lymphoblastic leukemia cell line with chromosome translocation 1;19 and trisomy 8. Cancer Genet. Cytogenet. (19).

99. Rapino F, Robles EF, Richter-Larrea JA, Kallin EM, Martinez-Climent JA et al. (2013) C/EBPα induces highly efficient macrophage transdifferentiation of B lymphoma and leukemia cell lines and impairs their tumorigenicity. Cell reports 3 (4): 1153–1163.

100. Gaidt MM, Rapino F, Graf T, Hornung V (2018) Modeling Primary Human Monocytes with the Trans-Differentiation Cell Line BLaER1. Methods in molecular biology (Clifton, N.J.) 1714: 57–66.

101. Vierbuchen T, Bang C, Rosigkeit H, Schmitz RA, Heine H (2017) The Human-Associated Archaeon Methanosphaera stadtmanae Is Recognized through Its RNA and Induces TLR8-Dependent NLRP3 Inflammasome Activation. Frontiers in immunology 8: 1535.

102. Franchi L, Eigenbrod T, Muñoz-Planillo R, Nuñez G (2009) The inflammasome: a caspase-1-activation platform that regulates immune responses and disease pathogenesis. Nature immunology 10 (3): 241–247.

103. Kelley N, Jeltema D, Duan Y, He Y (2019) The NLRP3 Inflammasome: An Overview of Mechanisms of Activation and Regulation. International journal of molecular sciences 20 (13).

104. Bergsbaken T, Fink SL, Cookson BT (2009) Pyroptosis: host cell death and inflammation. Nature reviews. Microbiology 7 (2): 99–109.

105. Ding J, Wang K, Liu W, She Y, Sun Q et al. (2016) Pore-forming activity and structural autoinhibition of the gasdermin family. Nature 535 (7610): 111–116.

106. Heilig R, Dick MS, Sborgi L, Meunier E, Hiller S et al. (2018) The Gasdermin-D pore acts as a conduit for IL-1β secretion in mice. European journal of immunology 48 (4): 584–592.

107. Bauernfeind FG, Horvath G, Stutz A, Alnemri ES, MacDonald K et al. (2009) Cutting edge: NF-kappaB activating pattern recognition and cytokine receptors license NLRP3 inflammasome activation by regulating NLRP3 expression. The Journal of Immunology 183 (2): 787–791.

108. Lin K-M, Hu W, Troutman TD, Jennings M, Brewer T et al. (2014) IRAK-1 bypasses priming and directly links TLRs to rapid NLRP3 inflammasome activation. Proceedings of the National Academy of Sciences of the United States of America 111 (2): 775–780.

109. Muñoz-Planillo R, Kuffa P, Martínez-Colón G, Smith BL, Rajendiran TM et al. (2013) K^+ efflux is the common trigger of NLRP3 inflammasome activation by bacterial toxins and particulate matter. Immunity 38 (6): 1142–1153.

110. Mariathasan S, Weiss DS, Newton K, McBride J, O'Rourke K et al. (2006) Cryopyrin activates the inflammasome in response to toxins and ATP. Nature 440 (7081): 228–232.

111. Walev I, Reske K, Palmer M, Valeva A, Bhakdi S (1995) Potassium-inhibited processing of IL-1 beta in human monocytes. The EMBO journal 14 (8): 1607–1614.

112. Lee G-S, Subramanian N, Kim AI, Aksentijevich I, Goldbach-Mansky R et al. (2012) The calcium-sensing receptor regulates the NLRP3 inflammasome through Ca2+ and cAMP. Nature 492 (7427): 123–127.

113. Zhong Z, Liang S, Sanchez-Lopez E, He F, Shalapour S et al. (2018) New mitochondrial DNA synthesis enables NLRP3 inflammasome activation. Nature 560 (7717): 198–203.

114. Zhou R, Yazdi AS, Menu P, Tschopp J (2011) A role for mitochondria in NLRP3 inflammasome activation. Nature 469 (7329): 221–225.

115. Gupta R, Ghosh S, Monks B, DeOliveira RB, Tzeng T-C et al. (2014) RNA and β-hemolysin of group B Streptococcus induce interleukin-1β (IL-1β) by activating NLRP3 inflammasomes in mouse macrophages. The Journal of biological chemistry 289 (20): 13701–13705.

116. Hornung V, Bauernfeind F, Halle A, Samstad EO, Kono H et al. (2008) Silica crystals and aluminum salts activate the NALP3 inflammasome through phagosomal destabilization. Nature immunology 9 (8): 847–856.

117. Dostert C, Pétrilli V, van Bruggen R, Steele C, Mossman BT et al. (2008) Innate immune activation through Nalp3 inflammasome sensing of asbestos and silica. Science (New York, N.Y.) 320 (5876): 674–677.

172

118. Duewell P, Kono H, Rayner KJ, Sirois CM, Vladimer G et al. (2010) NLRP3 inflammasomes are required for atherogenesis and activated by cholesterol crystals. Nature 464 (7293): 1357–1361.

119. Halle A, Hornung V, Petzold GC, Stewart CR, Monks BG et al. (2008) The NALP3 inflammasome is involved in the innate immune response to amyloid-beta. Nature immunology 9 (8): 857–865.

120. Orlowski GM, Colbert JD, Sharma S, Bogyo M, Robertson SA et al. (2015) Multiple Cathepsins Promote Pro-IL-1β Synthesis and NLRP3-Mediated IL-1β Activation. The Journal of Immunology 195 (4): 1685–1697.

121. Baker PJ, Boucher D, Bierschenk D, Tebartz C, Whitney PG et al. (2015) NLRP3 inflammasome activation downstream of cytoplasmic LPS recognition by both caspase-4 and caspase-5. European journal of immunology 45 (10): 2918–2926.

122. Hagar JA, Powell DA, Aachoui Y, Ernst RK, Miao EA (2013) Cytoplasmic LPS activates caspase-11: implications in TLR4-independent endotoxic shock. Science (New York, N.Y.) 341 (6151): 1250–1253.

123. Shi J, Zhao Y, Wang Y, Gao W, Ding J et al. (2014) Inflammatory caspases are innate immune receptors for intracellular LPS. Nature 514 (7521): 187–192.

124. Piccini A, Carta S, Tassi S, Lasiglié D, Fossati G et al. (2008) ATP is released by monocytes stimulated with pathogen-sensing receptor ligands and induces IL-1beta and IL-18 secretion in an autocrine way. Proceedings of the National Academy of Sciences of the United States of America 105 (23): 8067–8072.

125. Yang D, He Y, Muñoz-Planillo R, Liu Q, Núñez G (2015) Caspase-11 Requires the Pannexin-1 Channel and the Purinergic P2X7 Pore to Mediate Pyroptosis and Endotoxic Shock. Immunity 43 (5): 923–932.

126. Pedra JHF, Sutterwala FS, Sukumaran B, Ogura Y, Qian F et al. (2007) ASC/PYCARD and caspase-1 regulate the IL-18/IFN-gamma axis during Anaplasma phagocytophilum infection. J Immunol 179 (7): 4783–4791.

127. Mencacci A, Bacci A, Cenci E, Montagnoli C, Fiorucci S et al. (2000) Interleukin 18 restores defective Th1 immunity to Candida albicans in caspase 1-deficient mice. Infection and immunity 68 (9): 5126–5131.

128. Lima-Junior DS, Costa DL, Carregaro V, Cunha LD, Silva ALN et al. (2013) Inflammasome-derived IL-1β production induces nitric oxide-mediated resistance to Leishmania. Nature medicine 19 (7): 909–915.

129. Ben-Sasson SZ, Hu-Li J, Quiel J, Cauchetaux S, Ratner M et al. (2009) IL-1 acts directly on CD4 T cells to enhance their antigen-driven expansion and differentiation. Proceedings of the National Academy of Sciences of the United States of America 106 (17): 7119–7124.

130. Charmoy M, Hurrell BP, Romano A, Lee SH, Ribeiro-Gomes F et al. (2016) The Nlrp3 inflammasome, IL-1β, and neutrophil recruitment are required for susceptibility to a nonhealing strain of Leishmania major in C57BL/6 mice. European journal of immunology 46 (4): 897–911.

131. Franchi L, Muñoz-Planillo R, Núñez G (2012) Sensing and reacting to microbes through the inflammasomes. Nature immunology 13 (4): 325–332.

132. Zhang Y, Yang W, Li W, Zhao Y (2021) NLRP3 Inflammasome: Checkpoint Connecting Innate and Adaptive Immunity in Autoimmune Diseases. Frontiers in immunology 12: 732933.

133. Shao B-Z, Xu Z-Q, Han B-Z, Su D-F, Liu C (2015) NLRP3 inflammasome and its inhibitors: a review. Frontiers in pharmacology 6: 262.

134. Jorgensen I, Miao EA (2015) Pyroptotic cell death defends against intracellular pathogens. Immunological reviews 265 (1): 130–142.

135. Wang H, Mao L, Meng G (2013) The NLRP3 inflammasome activation in human or mouse cells, sensitivity causes puzzle.

136. Delfino D, Chiofalo MS, Riggio G, Angelici MC, Gramiccia M et al. (1995) Induction of interleukin 1 alpha in murine macrophages infected in vitro with different species and strains of Leishmania. Microbial pathogenesis 18 (2): 73–80.

137. Lefèvre L, Lugo-Villarino G, Meunier E, Valentin A, Olagnier D et al. (2013) The C-type lectin receptors dectin-1, MR, and SIGNR3 contribute both positively and negatively to the macrophage response to Leishmania infantum. Immunity 38 (5): 1038–1049.

138. Dey R, Joshi AB, Oliveira F, Pereira L, Guimarães-Costa AB et al. (2018) Gut Microbes Egested during Bites of Infected Sand Flies Augment Severity of Leishmaniasis via Inflammasome-Derived IL-1β. Cell host & microbe 23 (1): 134-143.e6.

139. Carvalho RVH de, Zamboni DS (2020) Inflammasome Activation in Response to Intracellular Protozoan Parasites. Trends in parasitology 36 (5): 459–472.

140. Zamboni DS, Sacks DL (2019) Inflammasomes and Leishmania: in good times or bad, in sickness or in health. Current opinion in microbiology 52: 70–76.

141. Lima-Junior DS, Mineo TWP, Calich VLG, Zamboni DS (2017) Dectin-1 Activation during Leishmania amazonensis Phagocytosis Prompts Syk-Dependent Reactive Oxygen Species Production To Trigger Inflammasome Assembly and Restriction of Parasite Replication. Journal of immunology (Baltimore, Md. : 1950) 199 (6): 2055–2068.

142. Carvalho RVH de, Andrade WA, Lima-Junior DS, Dilucca M, Oliveira CV de et al. (2019) Leishmania Lipophosphoglycan Triggers Caspase-11 and the Non-canonical Activation of the NLRP3 Inflammasome. Cell reports 26 (2): 429-437.e5.

143. Gurung P, Karki R, Vogel P, Watanabe M, Bix M et al. (2015) An NLRP3 inflammasome-triggered Th2-biased adaptive immune response promotes leishmaniasis. The Journal of clinical investigation 125 (3): 1329–1338.

144. Ohne Y, Silver JS, Thompson-Snipes L, Collet MA, Blanck JP et al. (2016) IL-1 is a critical regulator of group 2 innate lymphoid cell function and plasticity. Nature immunology 17 (6): 646–655.

145. Lee SH, Charmoy M, Romano A, Paun A, Chaves MM et al. (2018) Mannose receptor high, M2 dermal macrophages mediate nonhealing Leishmania major infection in a Th1 immune environment. The Journal of experimental medicine 215 (1): 357–375.

146. Anderson CF, Mendez S, Sacks DL (2005) Nonhealing infection despite Th1 polarization produced by a strain of Leishmania major in C57BL/6 mice. J Immunol 174 (5): 2934–2941.

147. Novais FO, Carvalho LP, Passos S, Roos DS, Carvalho EM et al. (2015) Genomic profiling of human Leishmania braziliensis lesions identifies transcriptional modules associated with cutaneous immunopathology. The Journal of investigative dermatology 135 (1): 94–101.

148. Carvalho RVH de, Lima-Junior DS, Da Silva MVG, Dilucca M, Rodrigues TS et al. (2019) Leishmania RNA virus exacerbates Leishmaniasis by subverting innate immunity via TLR3-mediated NLRP3 inflammasome inhibition. Nature communications 10 (1): 5273.

149. Fernández-Figueroa EA, Rangel-Escareño C, Espinosa-Mateos V, Carrillo-Sánchez K, Salaiza-Suazo N et al. (2012) Disease severity in patients infected with Leishmania mexicana relates to IL-1β. PLoS neglected tropical diseases 6 (5): e1533.

150. Christensen SM, Belew AT, El-Sayed NM, Tafuri WL, Silveira FT et al. (2019) Host and parasite responses in human diffuse cutaneous leishmaniasis caused by L. amazonensis. PLoS neglected tropical diseases 13 (3): e0007152.

151. Sinha S, Fernández G, Kapila R, Lambert WC, Schwartz RA (2008) Diffuse cutaneous leishmaniasis associated with the immune reconstitution inflammatory syndrome. International journal of dermatology 47 (12): 1263–1270.

152. Velasco O, Savarino SJ, Walton BC, Gam AA, Neva FA (1989) Diffuse cutaneous leishmaniasis in Mexico. The American Journal of Tropical Medicine and Hygiene 41 (3): 280–288.

153. Schindelin J, Arganda-Carreras I, Frise E, Kaynig V, Longair M et al. (2012) Fiji: an open-source platform for biological-image analysis. Nature methods 9 (7): 676–682.

154. Beneke T, Madden R, Makin L, Valli J, Sunter J et al. (2017) A CRISPR Cas9 high-throughput genome editing toolkit for kinetoplastids. Royal Society open science 4 (5): 170095.

155. van Zandbergen G, Bollinger A, Wenzel A, Kamhawi S, Voll R et al. (2006) Leishmania disease development depends on the presence of apoptotic promastigotes in the virulent inoculum. Proceedings of the National Academy of Sciences of the United States of America 103 (37): 13837–13842.

156. Späth GF, Beverley SM (2001) A lipophosphoglycan-independent method for isolation of infective Leishmania metacyclic promastigotes by density gradient centrifugation. Experimental parasitology 99 (2): 97–103.

157. Cunningham F, Allen JE, Allen J, Alvarez-Jarreta J, Amode MR, Armean IM, Austine-Orimoloye O, Azov AG, Barnes I, Bennett R, Berry A, Bhai J, Bignell A, Billis K, Boddu S, Brooks L, Charkhchi M, Cummins C, Da Rin Fioretto L, Davidson C, Dodiya K, Donaldson S, El Houdaigui B, El Naboulsi T, Fatima R, Giron CG, Genez T, Martinez JG, Guijarro-Clarke C, Gymer A, Hardy M, Hollis Z, Hourlier T, Hunt T, Juettemann T, Kaikala V, Kay M, Lavidas I, Le T, Lemos D, Marugán JC, Mohanan S, Mushtaq A, Naven M, Ogeh DN, Parker A, Parton A, Perry M, Piližota I, Prosovetskaia I, Sakthivel MP, Salam AIA, Schmitt BM, Schuilenburg H, Sheppard D, Pérez-Silva JG, Stark W, Steed E, Sutinen K, Sukumaran R, Sumathipala D, Suner M-M, Szpak M, Thormann A, Tricomi FF, Urbina-Gómez D, Veidenberg A, Walsh TA, Walts B, Willhoft N, Winterbottom A, Wass E, Chakiachvili M, Flint B, Frankish A, Giorgetti S, Haggerty L, Hunt SE, IIsley GR, Loveland JE, Martin FJ, Moore B, Mudge JM, Muffato M, Perry E, Ruffier M, Tate J, Thybert D, Trevanion SJ, Dyer S, Harrison PW, Howe KL, Yates AD, Zerbino DR, Flicek P (2022) Ensembl 2022.

158. Gstraunthaler G, Lindl T (2013) Zell- und Gewebekultur. Berlin, Heidelberg: Springer Berlin Heidelberg. 331 p.

159. Akilov OE, Kasuboski RE, Carter CR, McDowell MA (2007) The role of mannose receptor during experimental leishmaniasis. Journal of leukocyte biology 81 (5): 1188–1196.

160. Polando RE, Jones BC, Ricardo C, Whitcomb J, Ballhorn W et al. (2018) Mannose receptor (MR) and Toll-like receptor 2 (TLR2) influence phagosome maturation during Leishmania infection. Parasite immunology 40 (4): e12521.

161. Lacey DC, Achuthan A, Fleetwood AJ, Dinh H, Roiniotis J et al. (2012) Defining GM-CSF- and macrophage-CSF-dependent macrophage responses by in vitro models. The Journal of Immunology 188 (11): 5752–5765.

162. Forestier C-L, Machu C, Loussert C, Pescher P, Späth GF (2011) Imaging host cell-Leishmania interaction dynamics implicates parasite motility, lysosome recruitment, and host cell wounding in the infection process. Cell host & microbe 9 (4): 319–330.

163. Dey P (2010) Cancer nucleus: morphology and beyond. Diagnostic cytopathology 38 (5): 382–390.

164. Fischer EG (2020) Nuclear Morphology and the Biology of Cancer Cells. Acta cytologica 64 (6): 511–519.

165. Nilsson K, Sundström C (1974) Establishment and characteristics of two unique cell lines from patients with lymphosarcoma. International journal of cancer 13 (6): 808–823.

166. Wenzel UA, Bank E, Florian C, Förster S, Zimara N et al. (2012) Leishmania major parasite stage-dependent host cell invasion and immune evasion. FASEB journal : official publication of the Federation of American Societies for Experimental Biology 26 (1): 29–39.

167. Elliott MR, Koster KM, Murphy PS (2017) Efferocytosis Signaling in the Regulation of Macrophage Inflammatory Responses. The Journal of Immunology 198 (4): 1387–1394.

168. Ariel A, Serhan CN (2012) New Lives Given by Cell Death: Macrophage Differentiation Following Their Encounter with Apoptotic Leukocytes during the Resolution of Inflammation. Frontiers in immunology 3: 4.

169. Fredman G, Li Y, Dalli J, Chiang N, Serhan CN (2012) Self-limited versus delayed resolution of acute inflammation: temporal regulation of pro-resolving mediators and microRNA. Scientific reports 2: 639.

170. Stenger S, van Zandbergen G (2011) Measuring the killing of intracellular pathogens: Leishmania. Current protocols in immunology Chapter 14: Unit14.23.

171. Bifeld E, Lorenzen S, Bartsch K, Vasquez J-J, Siegel TN et al. (2018) Ribosome Profiling Reveals HSP90 Inhibitor Effects on Stage-Specific Protein Synthesis in Leishmania donovani. mSystems 3 (6).

172. Crauwels P, Bohn R, Thomas M, Gottwalt S, Jäckel F et al. (2015) Apoptotic-like Leishmania exploit the host's autophagy machinery to reduce T-cell-mediated parasite elimination. Autophagy 11 (2): 285–297.

173. Ma X, Yan W, Zheng H, Du Q, Zhang L et al. (2015) Regulation of IL-10 and IL-12 production and function in macrophages and dendritic cells. F1000Research 4.

174. Reiner SL, Locksley RM (1995) The regulation of immunity to Leishmania major. Annual review of immunology 13 (1): 151–177.

175. Gimblet C, Meisel JS, Loesche MA, Cole SD, Horwinski J et al. (2017) Cutaneous Leishmaniasis Induces a Transmissible Dysbiotic Skin Microbiota that Promotes Skin Inflammation. Cell host & microbe 22 (1): 13-24.e4.

176. Shio MT, Christian JG, Jung JY, Chang K-P, Olivier M (2015) PKC/ROS-Mediated NLRP3 Inflammasome Activation Is Attenuated by Leishmania Zinc-Metalloprotease during Infection. PLoS neglected tropical diseases 9 (6): e0003868.

177. Spriggs MK, Lioubin PJ, Slack J, Dower SK, Jonas U et al. (1990) Induction of an interleukin-1 receptor (IL-1R) on monocytic cells. Evidence that the receptor is not encoded by a T cell-type IL-1R mRNA. The Journal of biological chemistry 265 (36): 22499–22505.

178. Sá KSG de, Amaral LA, Rodrigues TS, Ishimoto AY, Andrade WAC de et al. (2023) Gasdermin-D activation promotes NLRP3 activation and host resistance to Leishmania infection. Nature communications 14 (1): 1049.

179. Upton J-P, Austgen K, Nishino M, Coakley KM, Hagen A et al. (2008) Caspase-2 cleavage of BID is a critical apoptotic signal downstream of endoplasmic reticulum stress. Molecular and cellular biology 28 (12): 3943–3951.

180. Krumschnabel G, Sohm B, Bock F, Manzl C, Villunger A (2009) The enigma of caspase-2: the laymen's view. Cell death and differentiation 16 (2): 195–207.

181. Sladky VC, Villunger A (2020) Uncovering the PIDDosome and caspase-2 as regulators of organogenesis and cellular differentiation. Cell death and differentiation 27 (7): 2037–2047.

182. Cruz CM, Rinna A, Forman HJ, Ventura ALM, Persechini PM et al. (2007) ATP activates a reactive oxygen species-dependent oxidative stress response and secretion of proinflammatory cytokines in macrophages. The Journal of biological chemistry 282 (5): 2871–2879.

183. Moon J-S, Nakahira K, Chung K-P, DeNicola GM, Koo MJ et al. (2016) NOX4-dependent fatty acid oxidation promotes NLRP3 inflammasome activation in macrophages. Nature medicine 22 (9): 1002–1012.

184. van Bruggen R, Köker MY, Jansen M, van Houdt M, Roos D et al. (2010) Human NLRP3 inflammasome activation is Nox1-4 independent. Blood 115 (26): 5398–5400.

185. Zhong Z, Zhai Y, Liang S, Mori Y, Han R et al. (2013) TRPM2 links oxidative stress to NLRP3 inflammasome activation. Nature communications 4: 1611.

186. Zavadskis S, Weidinger A, Hanetseder D, Banerjee A, Schneider C et al. (2020) Effect of Diphenyleneiodonium Chloride on Intracellular Reactive Oxygen Species Metabolism with Emphasis on NADPH Oxidase and Mitochondria in Two Therapeutically Relevant Human Cell Types. Pharmaceutics 13 (1).

187. Nakahira K, Haspel JA, Rathinam VAK, Lee S-J, Dolinay T et al. (2011) Autophagy proteins regulate innate immune responses by inhibiting the release of mitochondrial DNA mediated by the NALP3 inflammasome. Nature immunology 12 (3): 222–230.

188. Allam R, Lawlor KE, Yu EC-W, Mildenhall AL, Moujalled DM et al. (2014) Mitochondrial apoptosis is dispensable for NLRP3 inflammasome activation but non-apoptotic caspase-8 is required for inflammasome priming. EMBO reports 15 (9): 982–990.

189. Bauernfeind F, Bartok E, Rieger A, Franchi L, Núñez G et al. (2011) Cutting edge: reactive oxygen species inhibitors block priming, but not activation, of the NLRP3 inflammasome. The Journal of Immunology 187 (2): 613–617.

190. Santos D, Campos TM, Saldanha M, Oliveira SC, Nascimento M et al. (2018) IL-1β Production by Intermediate Monocytes Is Associated with Immunopathology in Cutaneous Leishmaniasis. The Journal of investigative dermatology 138 (5): 1107–1115.

191. Pazár B, Ea H-K, Narayan S, Kolly L, Bagnoud N et al. (2011) Basic calcium phosphate crystals induce monocyte/macrophage IL-1β secretion through the NLRP3 inflammasome in vitro. The Journal of Immunology 186 (4): 2495–2502.

192. Netea MG, Nold-Petry CA, Nold MF, Joosten LAB, Opitz B et al. (2009) Differential requirement for the activation of the inflammasome for processing and release of IL-1beta in monocytes and macrophages. Blood 113 (10): 2324–2335.

193. Sacks D, Noben-Trauth N (2002) The immunology of susceptibility and resistance to Leishmania major in mice. Nature reviews. Immunology 2 (11): 845–858.

194. Wakil AE, Wang ZE, Ryan JC, Fowell DJ, Locksley RM (1998) Interferon gamma derived from CD4(+) T cells is sufficient to mediate T helper cell type 1 development. The Journal of experimental medicine 188 (9): 1651–1656.

195. Carneiro PP, Conceição J, Macedo M, Magalhães V, Carvalho EM et al. (2016) The Role of Nitric Oxide and Reactive Oxygen Species in the Killing of Leishmania braziliensis by Monocytes from Patients with Cutaneous Leishmaniasis. PloS one 11 (2): e0148084.

196. Mia S, Warnecke A, Zhang X-M, Malmström V, Harris RA (2014) An optimized protocol for human M2 macrophages using M-CSF and IL-4/IL-10/TGF-β yields a dominant immunosuppressive phenotype. Scandinavian journal of immunology 79 (5): 305–314.

197. Iqbal S, Kumar A (2015) Characterization of In vitro Generated Human Polarized Macrophages. J Clin Cell Immunol 06 (06).

198. Hickman E, Smyth T, Cobos-Uribe C, Immormino R, Rebuli ME et al. (2023) Expanded characterization of in vitro polarized M0, M1, and M2 human monocyte-derived macrophages: Bioenergetic and secreted mediator profiles. PloS one 18 (3): e0279037.

199. Edwards JP, Zhang X, Frauwirth KA, Mosser DM (2006) Biochemical and functional characterization of three activated macrophage populations. Journal of leukocyte biology 80 (6): 1298–1307.

200. Hrčková G, Mačak Kubašková T, Mudroňová D, Jurčacková Z, Ciglanová D (2023) Co-Treatment with Human Leukocyte Extract and Albendazole Stimulates Drug's Efficacy and Th1 Biased Immune Response in Mesocestoides vogae (Cestoda) Infection via Modulation of Transcription Factors, Macrophage Polarization, and Cytokine Profiles. Pharmaceutics 15 (2).

201. Trinchieri G (2003) Interleukin-12 and the regulation of innate resistance and adaptive immunity. Nature reviews. Immunology 3 (2): 133–146.

References

202. Sypek JP, Chung CL, Mayor SE, Subramanyam JM, Goldman SJ et al. (1993) Resolution of cutaneous leishmaniasis: interleukin 12 initiates a protective T helper type 1 immune response. The Journal of experimental medicine 177 (6): 1797–1802.

203. Smith W, Feldmann M, Londei M (1998) Human macrophages inducedin vitroby macrophage colony-stimulating factor are deficient in IL-12 production. Eur. J. Immunol. 28 (8): 2498–2507.

204. Erlich Z, Shlomovitz I, Edry-Botzer L, Cohen H, Frank D et al. (2019) Macrophages, rather than DCs, are responsible for inflammasome activity in the GM-CSF BMDC model. Nature immunology 20 (4): 397–406.

205. Chapuis F, Rosenzwajg M, Yagello M, Ekman M, Biberfeld P et al. (1997) Differentiation of human dendritic cells from monocytes in vitro. European journal of immunology 27 (2): 431–441.

206. Reiling N, Ulmer AJ, Duchrow M, Ernst M, Flad HD et al. (1994) Nitric oxide synthase: mRNA expression of different isoforms in human monocytes/macrophages. European journal of immunology 24 (8): 1941–1944.

207. Müller AJ, Aeschlimann S, Olekhnovitch R, Dacher M, Späth GF et al. (2013) Photoconvertible pathogen labeling reveals nitric oxide control of Leishmania major infection in vivo via dampening of parasite metabolism. Cell host & microbe 14 (4): 460–467.

208. He W, Wan H, Hu L, Chen P, Wang X et al. (2015) Gasdermin D is an executor of pyroptosis and required for interleukin-1β secretion. Cell research 25 (12): 1285–1298.

209. Khoury MK, Gupta K, Franco SR, Liu B (2020) Necroptosis in the Pathophysiology of Disease. The American journal of pathology 190 (2): 272–285.

210. Taabazuing CY, Okondo MC, Bachovchin DA (2017) Pyroptosis and Apoptosis Pathways Engage in Bidirectional Crosstalk in Monocytes and Macrophages. Cell chemical biology 24 (4): 507-514.e4.

211. Wang Y, Gao W, Shi X, Ding J, Liu W et al. (2017) Chemotherapy drugs induce pyroptosis through caspase-3 cleavage of a gasdermin. Nature 547 (7661): 99–103.

212. Zhang Z, Zhang Y, Xia S, Kong Q, Li S et al. (2020) Gasdermin E suppresses tumour growth by activating anti-tumour immunity. Nature 579 (7799): 415–420.

213. Frank D, Vince JE (2019) Pyroptosis versus necroptosis: similarities, differences, and crosstalk. Cell death and differentiation 26 (1): 99–114.

214. Rosazza T, Lecoeur H, Blisnick T, Moya-Nilges M, Pescher P et al. (2020) Dynamic imaging reveals surface exposure of virulent Leishmania amastigotes during pyroptosis of infected macrophages. Journal of cell science 134 (5).

215. Hoover DL, Berger M, Hammer CH, Meltzer MS (1985) Complement-mediated serum cytotoxicity for Leishmania major amastigotes: killing by serum deficient in early components of the membrane attack complex. The Journal of Immunology 135 (1): 570–574.

216. Filippis C, Arens K, Noubissi Nzeteu GA, Reichmann G, Waibler Z et al. (2017) Nivolumab Enhances In Vitro Effector Functions of PD-1+ T-Lymphocytes and Leishmania-Infected Human Myeloid Cells in a Host Cell-Dependent Manner. Frontiers in immunology 8: 1880.

Appendix

Appendix A

Table 6 Ct and ΔCt values of iNOS determined by qPCR for LPS+IFN-γ stimulated murine macrophages.

gene	Ct value	dCt values (HK=GAPDH)	dCt values (HK=HNRNPAB)
GAPDH	32.25	0	10.03
HNRNPAB	22.22	-10.03	0
NOS2	17.31	-14.94	-4.91

Declaration of Authorship

I hereby certify that I have written the present dissertation with the title

Use of genome editing in human phagocytic cells to elucidate the role of the NLRP3 inflammasome in *L. major* infection

independently, using no other aids then those I have cited. I have clearly mentioned the source of the passages that are taken word for word or paraphrased from other works.

The presented thesis has not been submitted in this or any other form to another faculty or examination institution.

Eidesstattliche Versicherung

Hiermit versichere ich, dass ich die vorgelegte Dissertation mit dem Titel

Use of genome editing in human phagocytic cells to elucidate the role of the NLRP3 inflammasome in *L. major* infection

Selbstständig verfasst habe und keine anderen als die angegebenen Quellen und Hilfsmittel verwendet habe. Die Stellen der Dissertation, die anderen Werken oder Veröffentlichungen dem Wortlaut oder dem Sinn nach entnommen wurden, sind durch Quellenangaben gekennzeichnet.

Diese Dissertation wurde in der jetzigen oder in ähnlicher Form noch an keiner anderen Hochschule eingereicht und hat noch keinen sonstigen Prüfungszwecken gedient.

Darmstadt, 26.04.2023

Kerren Volkmar